Tampere University

EERO KOIVUSALO

Advancing the Fundamentals in Molecular Beam Epitaxy of GaAs-based Nanowires

Tampere University Dissertations 339

Tampere University Dissertations 339

EERO KOIVUSALO

Advancing the Fundamentals in Molecular Beam Epitaxy of GaAs-based Nanowires

ACADEMIC DISSERTATION
To be presented, with the permission of
the Faculty of Engineering and Natural Sciences
of Tampere University,
for public discussion in the auditorium S2
of the Sähkötalo Building, Korkeakoulunkatu 3, Tampere,
on 20 October 2020 at 12 o'clock.

ACADEMIC DISSERTATION
Tampere University, Faculty of Engineering and Natural Sciences
Finland

Responsible supervisor and Custos	Professor Mircea Guina Tampere University Finland	
Supervisor	Dr. Teemu Hakkarainen Tampere University Finland	
Pre-examiners	Professor Ray LaPierre McMaster University Canada	Dr. Lutz Geelhaar Paul-Drude-Institut für Festkörperelektronik, Germany
Opponent	Professor Lucia Sorba NEST, Istituto Nanoscienze-CNR Italy	

The originality of this thesis has been checked using the Turnitin OriginalityCheck service.

Cover design: Roihu Inc.

ISBN 978-952-03-1760-7 (print)
ISBN 978-952-03-1761-4 (pdf)
ISSN 2489-9860 (print)
ISSN 2490-0028 (pdf)
http://urn.fi/URN:ISBN:978-952-03-1761-4

PunaMusta Oy – Yliopistopaino
Vantaa 2020

ACKNOWLEDGEMENTS

The research presented in this thesis was carried out at the Optoelectronics Research Centre (ORC) at Tampere University during the years 2016-2020. This work was funded by the Academy of Finland projects NESP (#294630), NanoLight (#310985) and QuantSi (#323989). I would like to personally thank the Väisälä Fund of Finnish Academy of Science and Letters for working grants and to acknowledge the HPY Research Foundation. I also thank EU Horizon 2020 program and the project MIREGAS (#644192) for giving the chance to expand my expertise to the world of laser diodes and antimonides.

Working at ORC has truly been a great privilege to which I thank Prof. Mircea Guina. Your never-ending drive and enthusiasm to push the photonics technology, ORC and its people forward keep up our spirit as a group in the constantly changing academic rollercoaster. The freedom you have given me to experiment with a molecular beam epitaxy (MBE) reactor has truly been a unique opportunity. However, I would have been completely lost with all this freedom without my supervisor, Dr. Teemu Hakkarainen. Your unparalleled insights on the physics of MBE and even more importantly, resilience to dig down deeper in the results, find the most profound conclusions and take time to design experiments has set a great example to my journey into the depths of epitaxy of nanostructures. Some could call this "scientific sisu", and I thank you for sharing it with me.

The results of this thesis would not be the same without our international collaborators. The same nanowires might lie in the bottom of a drawer in a laboratory, but without the scientific community knowing their value. The largest gratitude I owe to Prof. Vladimir Dubrovskii from the Ioffe Institute, St. Petersburg, Russia. Your models raised many of our publications to completely different level. But most importantly, the discussions with you have been invaluable source of insight to the phenomena of the nanowire growth. I would also like to express my gratitude to Prof. Yara G. Gobato and Prof. Helder V.A. Galeti from UFSCAR, Brazil. I thank you for the great interest towards our samples and all the hard work you have done to characterize the nanowires.

Dr. Marcelo Rizzo Piton, I thank you for the vast amount of nanowire processing work, Raman measurements and analysis. Your nanowire handling skills are beyond

comparison, and some of the most advanced characterizations presented in this work are your contribution. I respect your integrity in the laboratory. It has been a privilege and incredibly fun to do science with you.

Superior MBE know-how at ORC is the key to all my scientific results. For this, I want to express my deepest gratitude to Dr. Soile Suomalainen and Mr. Riku Koskinen for guiding me to the secrets of MBE. Soile, I still take care of our loved SS10-2 reactor and leave her in good hands someday. I want to also thank the rest of the MBE-team. Mr. Joonas Hilska, your incredible understanding on what is happening inside the reactor and on the substrate has been priceless for the nanowire work, this thesis and the SS10-2 reactor. Dr. Sanna Ranta, our profound discussions on the spiritual life of our 10-port reactors may have led to more questions than answers. But I believe they have helped us more than the reactors. Thankfully, Dr. Jari Lyytikäinen, our bedrock of MBE knowledge has been there for us. Mr. Riku Isoaho, I thank you for being there for me at the early hours when the worst MBE disasters are found and at the other occasions of (equipment?) breakdowns. I cannot list everyone deserving thanks in here, but thank you all, who have been there for the MBE team!

The spirit at ORC arises from the wonderful co-workers. Support and fun are always available. Thank you Riku, Marcelo and Jarno, my dudes, for all the academic and less academic activities, whether being reasonable or less so. You know what I mean. My office friend Maija, you have made the days at the office so much brighter. Solar cell and MECSEL teams, your laughter still echoes in my ears while I write this at the silence of my home office. Vexlum and Picophotonics people, your enthusiasm is contagious, keep on going.

Finally, I want to thank my family and friends. Mom, Dad, you have given me the positive attitude towards education and all the support I could have hoped for. And here I am, school is almost finished. Laura, my dear wife, you are the beacon that has guided me through the shallows during these years. And thank you to all my friends, the boys from Tavi, Jaakko, Muusi-crew and all the other crazy people I've sailed with. You have given me distractions to put my mind in ease when I have needed it the most.

Kangasala, October 2020
Eero Koivusalo

ABSTRACT

Semiconductor nanowires (NWs) allow epitaxial integration of III–V semiconductors directly on Si platform, offering an intriguing pathway towards integration of photonic and microelectronic functionalities. NW growth using internal metal catalyst, so called self-catalyzed growth, is a complicated physical process resulting from the interplay of the supersaturations and chemical potentials in vapor, liquid and solid phases of the elements present during the growth. Although many aspects of the epitaxy have been addressed during the recent years, advancing the NWs technology towards practical applications requires significant developments to guarantee high crystal purity, uniform size distributions, precise definition of doped heterostructures as well as improve ability to control the incorporation mechanisms of different elements. Accessing these properties requires detailed information on the physics controlling the NW growth and their relation to the technological control steps.

To this end, the thesis contributes to the development of NW technology by investigating the physical phenomena behind the self-catalyzed gallium arsenide-based NW growth but also by offering concrete pathways towards the desired NW functionality. The NW growth is investigated by molecular beam epitaxy growth on lithography-free templates. The templates provide a robust tool to focus on the NW growth mechanism while offering possibility to grow comparable samples. The crystal structure of these NWs is shown to be excellent. The first demonstration of sub-Poissonian length distribution is presented in this thesis providing evidence of the so-called nucleation antibunching in a large NW ensemble. Nucleation antibunching causes the nucleation events during NW growth be temporally anticorrelated. Furthermore, incorporation of Be and Te dopant atoms, and Sb as a ternary element have been studied; this is a significant step towards realization of practical structures yet marginally addressed before due to the early stage of development of the field overall. Details on the incorporation mechanisms of these elements into the NWs have been revealed for the first time. Moreover, the role of As species in the molecular beam epitaxy of NWs was clarified; the selection of As species was found to be a practical tool for NW grower to adjust the dimensions of NWs, but also select the primary incorporation mechanisms of elements.

TIIVISTELMÄ

III-V yhdistepuolijohteita voidaan valmistaa suoraan piille nanolankojen muodossa, mikä puolestaan mahdollistaa fotoniikan ja mikroelektroniikan saumattoman integraation. Nanolankojen kasvatuksessa käytettävä itsekatalysoitu menetelmä, jossa kasvua tukeva katalyyttipisara koostuu samoista alkuaineista kuin nanolanka, on monimutkainen fysikaalinen prosessi. Se perustuu eri faasien, kaasun, nesteen ja kiinteän aineen keskinäisiin kemiallisiin potentiaaleihin ja aineiden supersaturaatioihin. Käytännön näkökulmasta näitä parametreja voidaan hallita molekyylisuihkuepitaksiakasvatuksen aikana muuttamalla III– ja V–ryhmän alkuaineiden vuosuhteita ja kasvatuslämpötilaa. Vaikka monet nanolankojen kasvatukseen liittyvät ilmiöt ovat jo hyvin tunnettuja, niiden kehitys käytännön sovelluksiin vaatii vielä tutkimusta kidelaadun, kapean kokojakauman, seostuksen sekä useiden alkuaineiden inkorporaation ymmärtämiseksi.

Tässä työssä pureudutaan näihin seikkoihin tutkimalla fysikaalisia ilmiöitä itse-katalysoitujen galliumarsenidipohjaisten nanolankojen molekyylisuihkuepitaksiassa. Nanolankojen kasvuprosessin ymmärryksen lisäksi työ tarjoaa konkreettisia menetelmiä nanolankojen toiminnallisuuden kasvattamiseksi kohti käytännön sovelluksia. Tässä työssä osoitetaan, että kehittämällämme menetelmällä kasvatettujen nanolankojen kidelaatu on erinomainen ja että sillä pystytään saavuttamaan Poissonin jakaumaa kapeampi kokojakauma. Tämä on ensimmäinen havainto nanolankajoukossa nähdystä atomikerrosten nukleaation ajallisesta antikorrelaatiosta. Puhtaan galliumarsenidin lisäksi työssä tutkitaan nanolankojen seostusta sähköä johtavaksi berylliumin ja telluurin avulla sekä vyöaukon kontrollointia antimonin avulla. Nämä yksityiskohtaiseen inkorporaatiomekanismien ymmärrykseen johtaneet tulokset ovat merkittäviä askeleita nanolankarakenteiden toiminnallisuuden lisäämiseksi käytännön sovelluksia varten. Eri alkuaineiden inkorporaation lisäksi työssä tutkittiin myös kasvatuksessa käytetyn arseenivuon molekyylityypin vaikutusta nanolankakasvuun. Molekyylityypin valinnan osoitettiin olevan käytännöllinen kasvatustyökalu, jolla voidaan säätää niin nanolankojen pituuden ja paksuuden suhdetta sekä kasvunopeutta kuin hallita eri alkuaineiden inkorporaatiomekanismeja.

CONTENTS

ABBREVIATIONS

MBE	Molecular beam epitaxy
NW	Nanowire
GR	Growth rate
PIC	Photonic integrated circuit
VLS	Vapor-liquid-solid
VS	Vapor-solid
UHV	Ultra-high vacuum
ML	Monolayer
BEP	Beam equivalent pressure
ZB	Zincblende
WZ	Wurtzite
HR-TEM	High-resolution transmission electron microscopy
SAED	Selected area electron diffraction
DE	Droplet epitaxy
RMS	Root mean square
LT	Low temperature
TPL	Triple phase line
HR-XRD	High-resolution x-ray diffractometer/diffractometry
μ-PL	Micro-photoluminescence
PL	Photoluminescence
RSM	Reciprocal space map
SEM	Scanning electron microscope
1D	one-dimensional
2D	two-dimensional

ORIGINAL PUBLICATIONS

Publication I E. Koivusalo, T. Hakkarainen, and M. Guina, "Structural investigation of uniform ensembles of self-catalyzed GaAs nanowires fabricated by a lithography-free technique" Nanoscale Res. Lett., vol. 12, no. 1, pp. 192, Sep. 2017.

Publication II E. Koivusalo, T. Hakkarainen, M. Guina, and V. G. Dubrovskii, "Sub-Poissonian Narrowing of Length Distributions Realized in Ga-Catalyzed GaAs Nanowires" Nano Lett., vol. 17, no. 9, 2017

Publication III E. Koivusalo, T. Hakkarainen, H. V. A. Galeti, Y. G. Gobato, V. G. Dubrovskii, and M. Guina, "Deterministic Switching of the Growth Direction of Self-Catalyzed GaAs Nanowires," Nano Lett., vol. 19, no. 1, pp. 82–89, Jan. 2019

Publication IV E. Koivusalo, J. Hilska, H. V. A. Galeti, Y.G. Gobato, M. Guina, and T. Hakkarainen, "The role of As species in self-catalyzed growth of GaAs and GaAsSb nanowires" Nanotechnology, 2020, https://doi.org/10.1088/1361-6528/abac34

Publication V M. Rizzo Piton, E. Koivusalo, T. Hakkarainen, H.V.A. Galeti, A. De Giovanni Rodrigues, S. Talmila, S. Souto, D. Lupo, Y. Galvão Gobato and M. Guina, "Gradients of Be-dopant concentration in self-catalyzed GaAs nanowires" Nanotechnology, vol. 30, no. 33, pp. 335709, 2019

AUTHOR'S CONTRIBUTIONS

The results included in this thesis were obtained as teamwork. The Author, Eero Koivusalo, conducted most of the molecular beam epitaxy steps, scanning electron microscopy, high-resolution x-ray diffractometry, and photoluminescence measurements. All authors contributed to writing of the manuscripts. The specific details of Author's contribution and other key contributions are listed below:

[P1] The Author was responsible for writing the manuscript. The experiment was planned with Teemu Hakkarainen. The Author conducted the scanning electron microscopy, x-ray diffractometry and micro-photoluminescence measurements, and collected and interpreted the dimensional data of the NWs.

[P2] The Author had the main responsibility of writing the manuscript. The section describing the kinetic model was provided by prof. Vladimir Dubrovskii, who also created the model. The Author was responsible of designing the samples with Dr. Hakkarainen, growing the samples, conducting the scanning electron microscopy and measuring the nanowire dimensions.

[P3] The Author had the main responsibility of writing the manuscript and interpretation of the results. The section describing the kinetic model was provided by prof. Vladimir Dubrovskii. The Author had the main responsibility for designing the samples and grew all the samples. The Author conducted the scanning electron microscopy and prepared the samples with removed droplets and participated in the transmission electron microscopy measurements.

[P4] The Author was responsible for writing the manuscript. The samples were designed together with Dr. Hakkarainen and Dr. Rizzo Piton. The Author conducted all the molecular beam epitaxy and scanning electron microscopy, as well as the photoluminescence and x-ray diffraction measurements. The Author also participated in the energy dispersive x-ray spectroscopy measurements.

[P5] The Author designed the samples and experiments with Dr. Rizzo Piton and Dr. Hakkarainen. The Author conducted the molecular beam epitaxy and scanning electron microscopy characterization of the as-grown samples. Dr. Rizzo Piton corresponded from the fabrication and measurement of the single-nanowire devices and Raman spectroscopy. Dr. Rizzo Piton analyzed the Raman and current-voltage measurements obtained from single nanowires. The Author had a major role in interpretation of the results within the framework of dopant incorporation mechanisms during the nanowire growth. The Author wrote the molecular beam epitaxy section and participated actively in writing the discussion of beryllium incorporation mechanisms. This manuscript was included also in the thesis of Dr. Rizzo Piton.

1 INTRODUCTION

Nanowires (NWs) are one-dimensional (1D) nanostructures having many peculiar properties. They can be fabricated from various materials either by top-down method, i.e. sculpting them from bulk using lithography, or by bottom-up growth with different chemical or physical deposition methods. This thesis focuses on an important paradigm in the vast spectrum of NWs, namely self-catalyzed III–V semiconductor NWs grown epitaxially on silicon. The introduction aims at briefly answering the questions: **why would anyone ever grow NWs, and what is the motivation behind this work in this field of science that lies somewhere between physics, material science, and photonics?**

The basic reason for the NW research lies in fundamental differences between different types of semiconductors and their intrinsic limitations, for example in terms of lattice constant and band-gap coverage, which impact their application. Silicon is an excellent material to fabricate microelectronics and waveguides used in photonic integrated circuits (PICs), and as such dominates the world of electronics and passive PICs. However, Si has an indirect band gap, which makes it a poor material to fabricate light sources, requiring hybrid integration of light sources to Si platform. On the other hand, III–V semiconductors composing of stoichiometric amounts of group III and group V materials provide a broad tunability of direct band gaps, thus making them efficient and versatile materials for all photonic applications. Unfortunately, direct epitaxial integration of III–V and Si material systems is difficult due to different lattice and thermal expansion coefficients. Yet this issue is alleviated when growing the III–V material on Si in 1D NW geometry. This is largely because NWs have so small footprint that the strain induced by lattice mismatch may relax horizontally without introducing dislocations in the growth direction.

Moreover, the dimensions of NWs are in the scale of the wavelength of visible and near infrared light making them to act as photonic waveguides. The NW geometry, and the photonic properties of III-V semiconductors have led to fabrication of several NW-based devices integrated on Si, for instance lasers [1], [2], light emitting diodes [3], photodetectors [4], [5] and solar cells [6]. While these proof-of-concept devices have been experimentally realized, fundamental research on the

physics behind NW growth is an active field, in particular when it comes to the development of more complex heterostructures requiring doping and a good control of the geometry and crystallography. To this end, the work presented in this thesis has contributed to this development from the viewpoint of fundamental growth phenomena including size controllability, doping, and NW geometry, and by providing practical guidelines for the growth of more complex NW-based heterostructures.

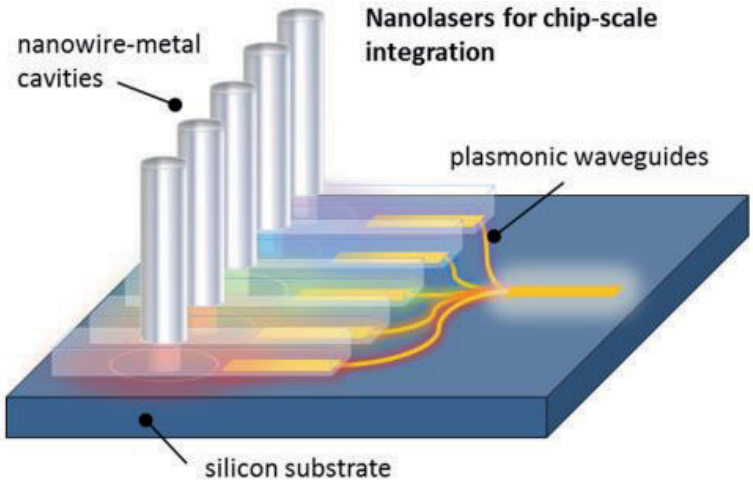

Figure 1. Schematic illustration of NW lasers monolithically integrated in waveguides. © [2012] IEEE, [7]

The contribution of this work to the overall framework of NW research is summarized by the key research questions presented in Figure 2. The publications [P1]-[P5], and [8] all contribute to the physics of NW growth which includes theoretical approaches focusing on the NW growth kinetics and practical approaches offering tools that NW growers can directly utilize. Moreover, photonic properties of the NWs are interlinked to their dimensional properties which result from the NW growth kinetics. Thus, the NW photonic properties are the very least related to results of each publication or utilized as a characterization method. Modifying the NW electrical properties by doping with Be and Te is investigated as a final step towards NW functionality in [P4]-[P5] and [8], whereas the NW crystal structure investigated in [P1] is also a major contributor in NW electrical properties.

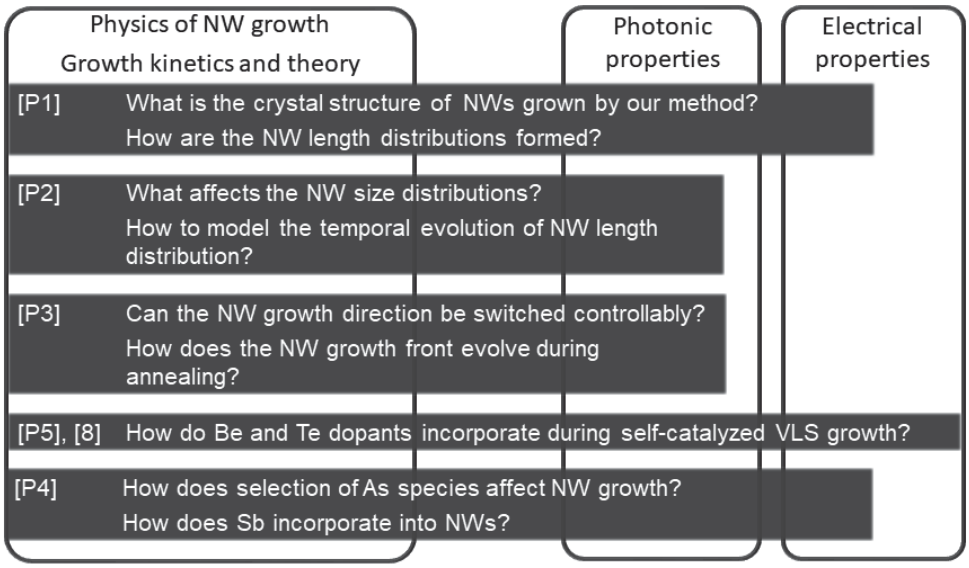

Figure 2. Research questions discussed in papers [P1]-[P5] and [8].

The thesis starts with a description of the technology and the basics of NW growth modes and structure in Chapter 2. This is followed by a comparison of common NW growth methods with the growth on lithography-free oxide patterns used in this work. Moreover, unpublished results on effects related to the yield of successful NWs are discussed. Chapter 3 focuses on more detailed physics explaining the formation of NW crystal structure and size distributions. The NW crystal structure is first discussed within the scope of [P1] followed by the effects of dopants and Sb incorporation investigated in [P4],[P5] and [8] which is an additional study conducted as parallel research to this thesis. These chapters answer to the first research question of [P1] and expand the results to GaAsSb material system and doped NWs. The intrinsic GaAs NWs are shown to exhibit pure zincblende structure, Be and Sb are found to reduce twinning and polytypic sections, and Te is shown to induce twinning superlattices. The discussion is then expanded to include the whole NW ensemble, when narrowing length distributions [P2] and the role of As species [P4] are discussed. The mechanisms behind NW length distribution formation are identified according to the second research question of [P1]. This understanding is then utilized in [P2] to achieve sub-Poissonian narrowing of the NW length distribution. The narrowing of length distribution is further modeled by a detailed kinetic model answering the second research question of [P2]. Answering the first research question of [P4] concerning the role of As species gives a practical and efficient tool

for NW growers to adjust the NW dimensions and the incorporation mechanisms of additional elements, Be, Te and Sb. Furthermore, new NW horizons are opened by presenting the methodology to controllably switch the NW growth direction [P3]. The key to the controllable switching of the growth direction is the understanding of the evolving NW growth front, answering to both research questions of [P3]. Chapter 4 focuses on developing the NW growth mechanisms essential for practical applications, namely dopant [P5], [8] and Sb [P4] incorporation, which allow tuning the electrical properties and band gap, respectively. Incorporation mechanism of each element is identified according to the research questions of [P5],[P4] and [8].

2 MOLECULAR BEAM EPITAXY AND NANOWIRE GROWTH

Molecular beam epitaxy (MBE) is a semiconductor growth method developed during the 1960's, and first introduced in 1970 by Cho et al. [9]. It was designed for the fabrication of high-quality single crystal films as other deposition methods did not provide high enough material quality. To this date, MBE is a standard crystal growth method for many commercial applications that demand high–purity crystalline materials and continues to be largely used for the research and development of new materials and heterostructures. [9]–[12]

2.1 Technological overview

The concept of MBE is rather simple regardless of the technical complexity. High purity elemental materials are evaporated as directional beams in ultra-high vacuum (UHV) to the surface of a heated substrate, where the atoms are physisorbed and migrate to a favorable site leading to material growth. When the grown material replicates the crystal structure of the substrate, the process is referred as epitaxy.

2.1.1 MBE equipment

A typical schematic of an MBE reactor is shown in Figure 3. demonstrating the location and angle of the material sources with respect to the substrate. In MBE of III–V materials used in this thesis, group III-elements are evaporated from crucibles, and the atomic flux is controlled by the crucible temperature. The material flux is switched on and off by a magnetic shutter plate. The dopant elements are evaporated from cells, similar to those used for the group III elements, but as the dopant fluxes are too low for direct monitoring, the cell temperatures are calibrated using separate samples characterized by Hall-measurements. Group V-elements are evaporated in heated bulk zones with overpressure of the group V vapor from which the group V material is released as molecular flux of tetramers As_4/Sb_4. The group V flux

magnitude is controlled by a needle valve. Following the needle valve, the tetramers pass into a heated cracking zone in which, based on the temperature, the tetramers are either dissociated into dimers (As_2 or Sb_2) or remain as tetramers. Typical cracking zone temperatures for tetramers and dimers are 620 °C and 920 °C, respectively. Due to the higher incorporation rate in typical planar MBE, dimers are typically used [13], [14], the use of tetramers may be beneficial for NW growth, as shown in [P4].

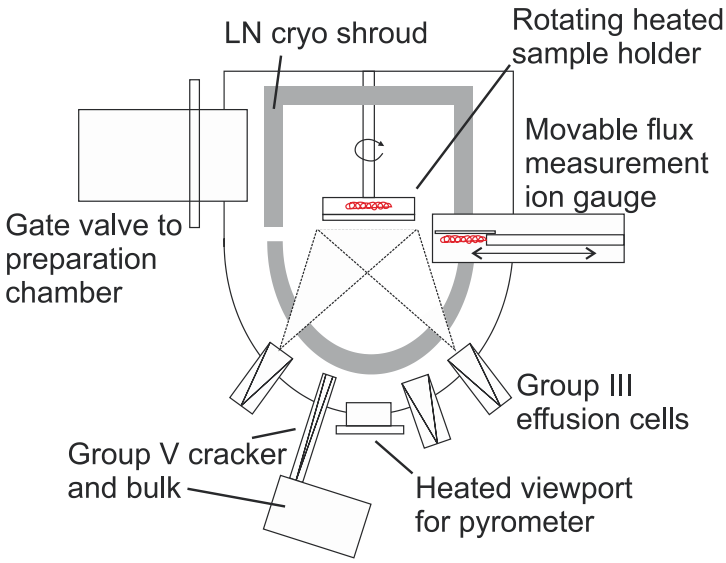

Figure 3. Schematic illustration of an MBE reactor.

2.1.2 Growth modes

The most broadly utilized epitaxial growth mode is the Frank-van der Merve mode which is used largely in device applications. In Frank-van der Merve growth, the physisorbed atoms grow as two-dimensional (2D) layers yielding in extremely flat surfaces, where ideally only monoatomic steps are found. The atoms migrate to these monoatomic steps, and often high-quality MBE grown surfaces are referred to exhibit step-edge growth. This growth mode allows adjusting the layer thickness down to monolayer (ML) precision using growth rates around 1 μm/h. To obtain high-quality single crystals via the Frank-van der Merve growth the lattice constants of the substrate and the thick epitaxial layers must be closely matched. Otherwise, the crystal structure breaks, leading to the formation of dislocations that degrade the optical and electrical properties of the material. However, successful methods have

been developed to relieve the inherent strain for facilitating direct epitaxial integration of high quality 2D layers of III-V materials on Si. [15] Frank-van der Merve growth occurs under a group V overpressure that inhibits the formation of metallic droplets. Other typical MBE growth modes are Volmer-Weber and Stranski-Krastanow, where 3-dimensional islands are formed due to strain induced by lattice mismatch between the substrate and epitaxial layer. They are used, for example, to grow quantum dots. [16]

More unconventional growth modes are utilized in NW growth. VLS growth is described in Section 2.2, which gives the basic understanding of the 1D growth of NWs, whereas droplet epitaxy is described in Section 2.4.2 as a tool for fabrication of NW templates.

2.1.3 Determining the material fluxes

Accurate measurement of the fluxes arriving on the substrate is an essential step in the MBE. While the group V is provided in excess for 2D MBE growth, the growth rate is solely determined by the group III flux. The fluxes are measured by a monitoring ion gauge. The group III fluxes are calibrated to correspond to a certain growth rate, and thus typically given in the units of a growth rate. For example, in [P3], the Ga flux is given in micrometers per hour (μm/h), whereas in [P1] monolayers per second (ML/s), both referring to thickness of GaAs layer grown on (100) surface in a time unit. By using the lattice constant and the atomic density, the flux can be also turned into a more physical unit of atoms/cm^2·s. In this unit system, the typical Ga flux used for NW growth throughout the whole work [P1]-[P4] is 0.3 μm/h, which equals 18.4·10^{13} atoms/cm^2·s.

The group V fluxes, on the other hand, are often given in units of pressure (mbar or Torr). However, the pressure is dependent on the ion gauge and reactor geometry. Furthermore, the sensitivity of the ion gauge is different for different elements and to the group V species. Thus, the pressure as such tells relatively little about the amount of available group V atoms with respect to the amount of group III atoms. To give more accurate information, beam equivalent pressure (BEP) ratio comparing the measured group V and III fluxes (BEP of group V flux divided by group III flux) is used in [P1]-[P3] to denote the group V flux. For [P4], the As and Sb fluxes were determined as atomic flux ratios with respect to the Ga flux as described in Puustinen et al. [17]. The determination was based on growth of low temperature GaAs and GaSb films and tracking down the threshold V/III BEP ratio for Ga droplet

formation. At low growth temperature, the formation of Ga droplets necessitates that the true atomic V/III flux ratio is below one as the group V sticking coefficient is near unity and any excess Ga material does not evaporate from the surface. The excess Ga forms droplets, and the size of the droplets is decreased by increasing the atomic flux ratio closer to one. When the atomic V/III flux ratio is >1, no excess Ga is available to form droplets. Therefore, finding the minimum V/III BEP ratio where Ga droplets are formed corresponds to the stoichiometric (1:1) atomic V/III ratio, allowing for accurate As and Sb atomic flux calibration. The resulting 1:1 V/III BEP ratios were found to be 3 for GaAs and 2.3 for GaSb. Thus, the atomic As/Ga flux ratio is determined by dividing the measured As_2/Ga BEP ratio with 3 and atomic Sb/Ga flux ratio by dividing the Sb_2/Ga BEP ratio by 2.3.

2.2 Vapor–Liquid-Solid growth – From 2D to 1D

The history of 1D VLS growth extends beyond MBE technology, as Wagner and Ellis introduced this growth mode for fabrication of Au-catalyzed Si whiskers in 1964 [18]. VLS growth occurs when a liquid-phase catalyst droplet is exposed to vapor-phase material fluxes. As the vapor-phase material accumulates into the droplet, the droplet becomes supersaturated with the accumulated material, driving precipitation of solid material under the droplet. As this process continues, one dimensional growth proceeds under the catalyst droplet, as shown in Figure 4. [18]

The VLS process may be catalyzed by an external constituent, such as gold or an internal metal such as Ga for GaAs growth. The latter process is referred to as self-catalyzed, and the details of VLS growth within its framework are discussed in detail. Au-catalyzed NW growth is generally an easier process compared to the self-catalyzed growth, due to a broad eutectic temperature window where liquid Au-Ga droplets can be formed and easier supersaturation by As flux compared to pure Ga droplets. However, self-catalyzed VLS growth is often favored over the Au-catalyzed process when aiming for Si-integration, as gold diffuses into the Si substrate forming deep-level traps. [19], [20]

As the VLS process occurs under the influence of liquid metallic droplets, the growth conditions differ quite significantly from 2D Frank-van der Merve growth. Formation of droplets is supported by low group V fluxes, which are not adequate to crystallize the droplets immediately. Simultaneously, the low group V flux enhances diffusion of group III elements [21], which is also the effect seen at higher growth temperatures. Thus, low group V flux and high growth temperature are used

to ensure adequate diffusion length for the metal to feed the droplets up to few μm distance from each other. For example, typical 2D GaAs growth is done under a V/III BEP ratio of 15 and at temperature of 580 °C, as determined by an optical pyrometer, whereas the corresponding "standard" parameters for self-catalyzed NW growth most commonly used in this work are V/III BEP ratio 9, corresponding to atomic flux ratio of 3, and temperature of 640 °C.

The growth conditions described above allow the group III elements to have long diffusion lengths on the typical NW sidewalls. From the surface, Ga may be re-emitted or diffuse over short distances [22]–[25] The chemical potential of the droplet drives the group III elements to the droplet. A similar effect is seen in the so called vapor-solid (VS) growth of NWs, where the catalyst, instead of a droplet, is the preferable growth facet on the NW tip. [26] The group V species, however, have short diffusion lengths, both on the substrate and on the NW sidewall. [27]–[29] Thus, majority of the group V flux impinging the substrate or NW sidewall is re-emitted, and the major sources of group V material to the droplet are direct flux from the vapor and secondary flux from the substrate surface and sidewalls of other NWs, as sketched in Figure 4. [30]

As the self-catalyzed VLS NW growth occurs under Ga rich conditions, it is more sensitive to the group V flux than 2D Frank-van der Merve growth. Too small group V flux leads to swelling of the droplet, whereas too high group V flux consumes the droplet. This may form (inverse) tapered structures [31], [32], which consists of atomic step edges on the NW sidewall. These step edges support 2D radial growth on the NW sidewalls. This radial growth may completely or partially compensate for the droplet swelling resulting in untapered NWs, as illustrated in Figure 4. c), and as witnessed in [P1], [P2], [P5] and [8]. By careful selection of growth parameters, the radial growth can also be suppressed [30], although the growth window for vertical sidewalls in absence of radial growth was found to be very narrow in [33].

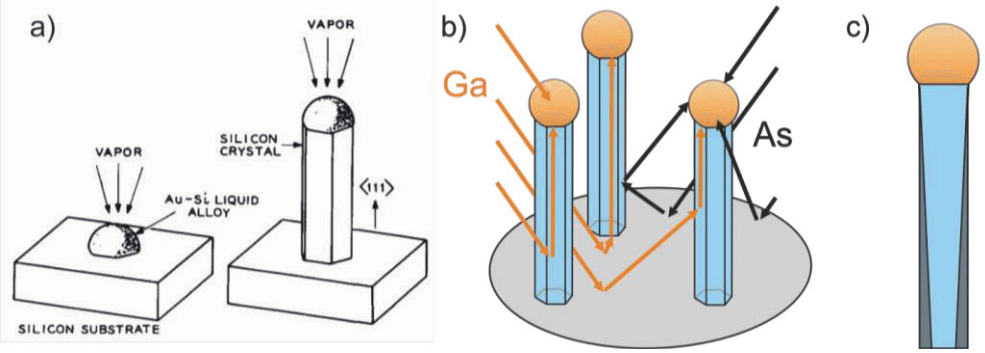

Figure 4. a) The original description of VLS growth by Wagner and Ellis in 1964 [18]. b) shows the material incorporation pathways to the droplet. Ga directly impinges the droplet, hits NW sidewalls and diffuses to the droplet or hits the substrate surface where it may diffuse to a NW or be re-emitted. As either directly impinges the droplet or is re-emitted from substrate or NW sidewall surfaces. c) VLS growth with increasing droplet size and continuous VS growth filling up the tapered space.

2.3 Crystal structure of nanowires

Due to the complex energetics of the VLS growth mode, the resulting crystal structure may vary from the commonly observed bulk structures. The typical bulk crystal structure or III–V semiconductors is zincblende (ZB), but in NWs, metastable wurtzite (WZ) structure is also present. [34] As NWs grown in self-catalyzed mode grow in the [111]B direction, the ZB and WZ stacking can be described by three different types of monolayers (MLs), most commonly labeled as A, B and C, according to the position of Ga (or As) atoms in the lattice planes. ZB structure consists of consecutive ABC stacking, whereas WZ consists of simpler ABAB-stacking. Often, the ZB NW stacking is not completely phase pure. The simplest exception from the ZB stacking is a twin plane, where the ZB stacking rotates by 180°. This can be described by a single ML of WZ stacking as ABCBAC. More complex and random stacking sequences are also often found in NWs, referred to as stacking faults, whereas short sections of altering ZB/WZ stacking are referred to as polytypism.

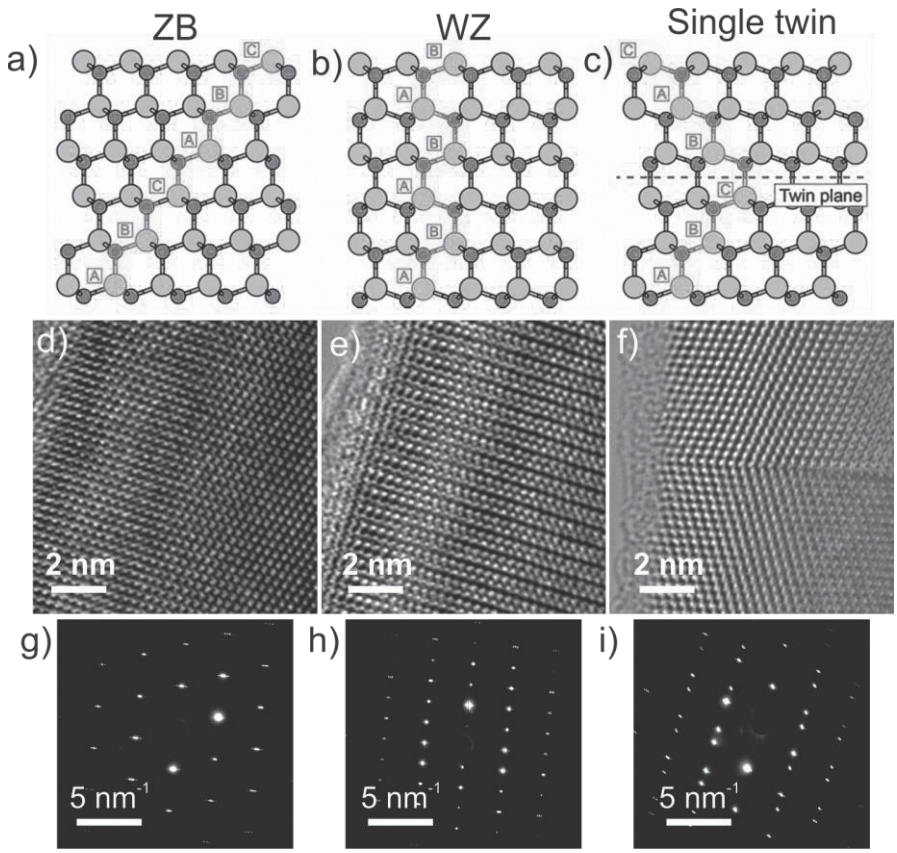

Figure 5. The crystal structure of III–V semiconductors in ZB [111] and WZ [1000] directions. a)-b) show schematics of the sequence of ZB, WZ crystal structures and c) a formation of a single twin plane. Reproduced from [35]. d)-f) show HR-TEM micrographs of the corresponding structures and g)-i) SEAD-patterns from similar regions. d), e), g) and h) are from the 60 min growth duration sample, and f) and i) from the 40 min growth duration sample in in [P1].

The NW crystal structure is commonly studied by transmission electron microscopy (TEM). Typical imaging mode used in this work is the high-resolution transmission electron microscopy (HR-TEM) (Figure 5. d)-e)), revealing the lattice structure. Note that the images do not show individual atoms, but rather the resulting amplitude of the electron wave passing through the medium being imaged. Another common TEM imaging mode is selective area electron diffraction (SAED) which, similarly to x-ray diffraction, shows the reciprocal of the lattice that diffracts waves passing through it. In this case, the waves are high energy electrons instead of x-rays. The short wavelength of electrons results in seeing multiple reciprocal lattice points in small angle patterns. This makes distinction of crystal structures by SAED patterns

straightforward. Typical SAED patterns of ZB, WZ, and ZB with a single twin plane are shown in Figure 5. The twin plane mirrors the ZB pattern with respect to the [111] zone axis.

2.4 Surface preparation and nucleation

Epitaxial NWs can be grown on various substrates due to the relaxed lattice matching condition. However, the typical GaAs NW growth direction <111>B (and for WZ NWs with hexagonal lattice structure, <1000>) determines the substrate orientation when the goal is to grow vertical NWs. However, some work has been done also on NW growth on (111)A surface. [31] Moreover, significant work has been done on GaAs(111)B wafers [36], [37], but the most common wafer choice is Si(111), as it enables various surface preparation schemes, as described in the following. The surface supporting NW growth should have three fundamental functionalities: offering preferential nucleation sites for NWs, suppressing planar growth and minimizing the amount of parasitic growth between the nucleation sites. Parasitic growth refers to random mounds, most often growing in VS mode, in areas between the NWs, as seen as example in Figure 7. b). Furthermore, the number of nucleation sites should be tunable to control the NW density, which affects the growth kinetics significantly, as discussed in Section 2.2.

2.4.1 The common surface preparation methods

Silicon oxide (SiO_x) layer covering the Si substrates offers several ways to fulfill the purpose of ensuring a suitable surface for NWs growth. This is due to the fact that Ga tends to easily diffuse on SiO_x at moderate temperatures [21], while at higher temperature, where NW growth is performed, sticking of both group III and group V species sticking is reduced. [14], [22], [23] Both properties prevent planar growth and parasitic nucleation between the NWs while supporting material collection to the catalyst droplet. On the other hand, the oxide layer can be modified by several methods to form preferential nucleation sites for NWs, as described in the following.

When a high level of control over the nucleation site density and the inter-NW distance is required, a thermally-grown, relatively thick (~10-30 nm) oxide layer with lithographic hole patterning can be used. [22], [23], [38]–[43] This is a common method for studying NW growth kinetics as a function of intermediate NW distance

[22], [23], [41], but also commonly accepted method for NWs aiming for device applications [39].

Another common approach with less control over NW position is to form pinholes via annealing and depositing Ga on a thin SiO_x layer, which may be the native oxide of an epi-ready substrate, chemically fabricated [44], or modified by controlled oxidation of oxide-free substrates [45]. These processes have the practical benefit of being simple wafer scale steps providing NW material for a multitude of experiments and processes. The large NW ensembles allow, for example, the utilization of standard high-resolution x-ray diffractometers, which require large (several mm) measurement areas. However, the simplest method of using the native oxide without any modifications lacks precise control of the nucleation time, leading to broadening of NW length distributions. This unwanted effect can be reduced by precise control of the oxide thickness. [44], [45] Another method to control and reduce the nucleation time is to decouple the two roles of Ga droplets: etching the pinholes to the oxide and nucleating the NW. This can be done by using in-situ droplet etching procedure to prepare the oxide pinholes acting as nucleation sites, and removing the droplets by annealing before the actual NW growth. [46], [47]

The nucleation sites may also be determined by Ga droplet epitaxy, as in the work of Somaschini and Bietti et al. [48], [49], where NWs are grown on top of GaAs islands mediated by droplet epitaxy. This method is closely related to the lithography-free oxide patterning method used in this work [P1],[50]].

2.4.2 Droplet epitaxy mediated lithography-free oxide patterns

The NWs studied in this work are grown on lithography-free oxide patterns mediated by droplet epitaxy. This template fabrication method was introduced by Hakkarainen et al. in [50]. The method combines the ease of template fabrication without lithography with precise control over the nucleation site density while enabling growth of large NW ensembles for various characterization methods.

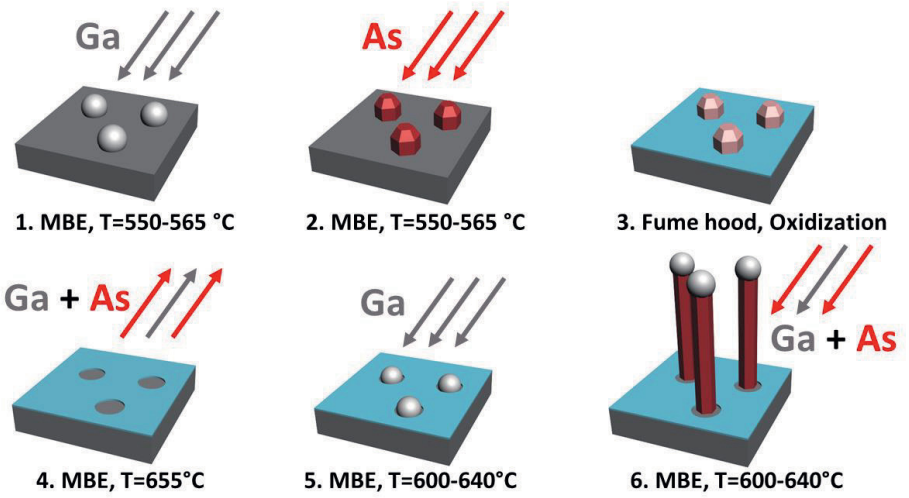

Figure 6. The principle of lithography-free oxide patterns as NW templates.1. Ga droplet epitaxy on oxide-free Si(111) substrate, 2. Droplet crystallization under As flux, 3. Oxidization in ambient conditions, 4. Nanocrystal evaporation revealing the nucleation sites, 5. Ga pre-deposition 6. NW growth.

As evident from the method's name, the templates are fabricated by droplet epitaxy. In droplet epitaxy a small amount of metal (Ga) is evaporated on an oxide-free substrate, where it diffuses to form droplets. The droplets can be subsequently crystallized under a group V (As) flux to form nanocrystals. The nanocrystal density can be controlled by the substrate temperature during the Ga deposition, although it is also weakly dependent on the Ga flux. [51], [52] The purpose of the nanocrystals is to protect the substrate locally from oxidization to create nanopatterns for NW nucleation. The oxidation is conducted in a fume hood in ambient conditions after the droplet epitaxy. At this phase, the nanocrystal density is characterized by SEM, after which the 2" Si(111) substrates are cut to six pieces offering comparable templates for investigating the effects of changing NW growth parameters. The method is illustrated step by step in Figure 6.

In the author's MSc thesis [53], the nanocrystal density resulting from the droplet epitaxy was found to exhibit significant random variations. The variations were closely related to the root mean square (RMS) roughness of the Si surface, which was further found to correlate with the heat treatment temperature preceding the Ga deposition. Lower heat treatment temperature induced higher substrate RMS roughness and denser nanocrystals. Several oxide removal methods, n-and p-type substrates, also with thick thermally grown oxide, and lowering the substrate

temperature between Ga deposition and crystallization under As flux were tested. This research led to the common droplet epitaxy parameters used in this work: oxide removal using a 10 s dip in 2.5 % hydrofluoric acid followed by 2 and 5 s rinsing in separate beakers of de-ionized water and fast transfer into MBE vacuum. In the MBE growth chamber the samples are annealed without As flux for 10 min at 700 °C, after which 0.091 or 0.19 nm Ga is deposited at 550-565 °C followed by instant crystallization under As flux with a V/III BEP ratio >20 with respect to the already shut Ga flux. These parameters enable nanocrystal densities ranging from $4 \cdot 10^7$ cm^{-2} to $2 \cdot 10^9$ cm^{-2} and diameters ranging from 20 to 111 nm. Even though, the exact density has not been fully reproducible from template to template, 50% of the fabricated templates exhibit a useful combination of nucleation site density and size for different purposes. As the selected templates have offered repeatable NW growth, and the template growth is relatively simple, the lithography-free oxide patterning has proven itself to be an efficient template to investigate NW growth and the resulting NW properties.

2.4.3 Nanowire nucleation and resulting yield

The NW nucleation is discussed within the framework of Ga-catalyzed GaAs NWs. However, similar group III metal droplet induced nucleation occurs in other material systems, such as Ga(As)P [54]–[56] or GaAsSb and may also be dominant in In-V NWs, which can be grown in VLS mode or in catalyst-free VS-growth mode [56]–[60].

The typical NW nucleation begins with the formation of Ga droplets on the wafer surface. The Ga droplets may be formed by a separate pre-wetting step under Ga flux, or it may occur spontaneously under the low V/III ratio used in NW growth. After the droplet formation, the As concentration in the droplets starts to increase until supersaturation is reached and the first NW monolayer nucleates. The droplet formation and reaching supersaturation form a so called incubation time of NW nucleation which can be tuned by the growth conditions [61] or by modifying the pre-wetting procedure as in [P2]. The incubation time has also a significant effect on the NW length distribution [62], which will be discussed in more detail in Section 3.2.

When NWs are grown on an intact native oxide or controllably-grown SiOx surface, in addition to reaching supersaturation during the incubation time, the droplets etch nanoscale pinholes through the oxide where the first ML nucleation

occurs on the bare Si surface. [63] Thus, the oxide thickness and roughness are crucial parameters for simultaneous and effective nucleation of NWs. [44], [45], [64]–[66] The oxide thickness also needs to be considered as it varies from batch to batch. [46] In [46], [47] Tauchnitz et al. showed that the oxide thickness and Ga pre-deposition (referred to as surface modification procedure) were closely related to the pinhole size in the oxide which was further found to affect the yield of vertical NWs.

Similarly, the NW yield is related to the hole size and oxide properties when lithographically patterned thicker oxide layers are used. However, nucleation in lithographical patterns is made even more complicated by a thin oxide often covering the holes fabricated in the thick thermal oxide. [38], [42], [67]–[69] The effect of oxide thickness and hole size are related to the Ga wetting, which determines the manner of nucleation of the first MLs. If the first nucleation event occurs under non-preferential wetting condition determined by the contact angle of the droplet and the substrate or oxide surface, two effects may take place yielding tilted NWs and parasitic growth expanding on the SiO_x surface. The first is three-dimensional multiple order twinning which mainly induces tilted NWs, whereas nucleation at multiple locations within the same droplet induces parasitic growth, as fitting the crystal structure of the multiple nuclei yields complex twinning instead of controlled vertical growth. [63], [70], [71]

In NW templates fabricated by the lithography-free oxide patterning, the nanocrystals protect the nucleation sites from oxidation, thus diminishing the need of the droplets to etch pinholes through the oxide during the incubation time preceding the nucleation of the first ML. In our initial work on NW growth [50], a 60 s Ga wetting was used to form the Ga-catalyst droplets for the NW growth. The same wetting has been used as such for [P1], and with 40 s duration in [P4]. In [P1], the NW incubation time was found to be 68 s after opening the As needle valve. However, the target to narrow down the NW length distribution for [P2], created a need to investigate the effect of reducing the wetting time. The aim was to form smaller droplets with narrower absolute size distribution, and thus exhibiting simultaneous nucleation. Simultaneously, the incubation time was expected to be reduced as smaller absolute amount of As would be needed to supersaturate the smaller droplets. A template with small nanocrystal diameter of 34 nm was selected to test Ga wetting times of 0, 1, 2 and 60 s, and a separate Ga re-evaporation step. In the Ga re-evaporation method, Ga droplets are formed in a 60 s pre-wetting step similarly to the regular growth procedure and then removed by annealing for 10 min in 655-660 °C. The annealing is followed by NW nucleation with simultaneous opening of Ga and As fluxes. The purpose of the pre-wetting combined with the re-

evaporation resembles the common scheme of etching pinholes in the native oxide layer, to reveal the oxide- free Si surface to support fast epitaxial nucleation. The shorter pre-wetting times were found to induce significantly enhanced NW nucleation yield compared to the 60 s wetting. The yield of NWs is determined by the ratio of vertical NWs with respect to all nucleation present on the wafer. The yield was further improved by the re-evaporation procedure as shown in Figure 7. Thus, the re-evaporation procedure was used in the NW growths throughout the growths conducted for [P2] and [P3].

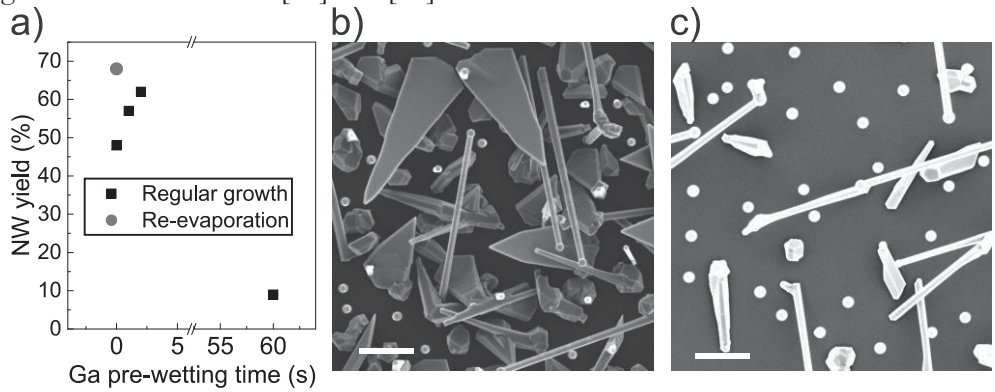

Figure 7. The effect of wetting time on the yield of successful NWs on a template with 34 nm nanocrystals a). Regular growth refers to pre-wetting for 0, 1, 2 and 60 s without re-evaporation. In b) top-view SEM images of the sample with 60 s pre-wetting and in c) with the re-evaporation step. The scale bars are 1 μm.

However, as the number of available NW samples for collective yield analysis increased to 140 samples during the growths for [P3], it was found that the yield of NWs following the re-evaporation was not completely reproducible. The yield of vertical NWs is plotted as a function of nanocrystal diameter in samples with regular pre-wetting of 60 or 40 s in Figure 8. a) and in samples with re-evaporation procedure in Figure 8. b). In both cases, the maximum NW yield increases with smaller template nanocrystal size but below 35 nm the reproducibility starts to decrease. The yield is also found to be relatively independent of several variables, such as presence of doping during NW growth, using experimental GaSb nanocrystals instead of GaAs, low temperature crystallization during DE, or the MBE reactor used. The low-yield sample with 60 s Ga pre-wetting in Figure 7. a) is shown as a random variation of the lowest yield sample in Figure 8. a), thus diminishing the 60 s wetting results of the yield test in Figure 7. a). Following these observations, majority of the samples in [P4] were grown using a 40 s pre-wetting without the re-evaporation procedure.

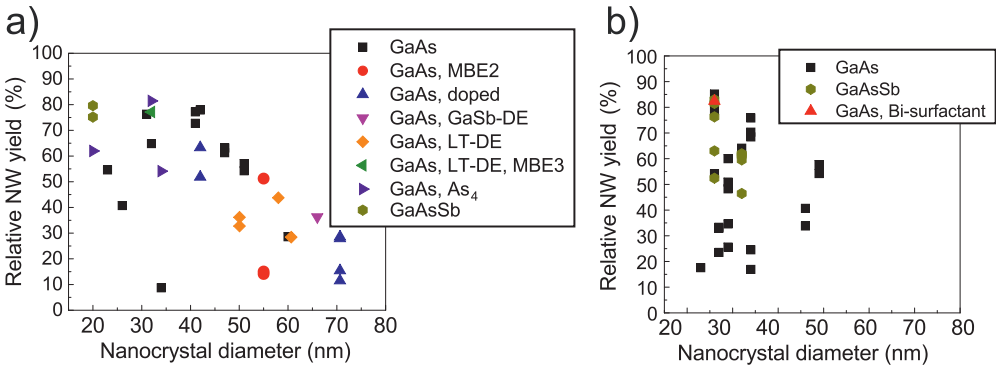

Figure 8. The yield of NW nucleation as a function of nanocrystal diameter for regular pre-wetting procedure a) and pre-wetting and re-evaporation procedure b). In a) MBE2, doped and As_4 refer to the NW growth in another MBE reactor, under the influence of dopants and using As_4 instead of typically used As_2 species, whereas GaSb-DE, LT-DE and LT-DE, MBE3 refer to template fabricated by GaSb nanocrystals, low temperature crystallization of the droplets and low temperature crystallization in a third MBE reactor, respectively. In b) Bi-surfactant refers to introducing Bi as a surfactant during the NW growth.

As discussed in this section, mainly summarizing unpublished results, a significant amount of optimization needs to be done so that all is not lost in terms of successful NW growth even before the NWs growth is initiated. The following sections will focus on the NW growth itself, often concluding that the NW growth is stable and repeatable, almost easy. Thus, the importance of surface preparation for achieving successful NW growth cannot be stressed enough.

3 THE DROPLET – CONTROLLING GROWTH FROM SINGLE NANOWIRE TO ENSEMBLES

Since the first demonstration of Si whiskers in 1964 [18], the role of catalyst droplet in the VLS growth mode has been known to be crucial for NW growth. This has led to describing the NW growth via detailed models that focus on the droplet behavior. The models guide the growers, while also providing explanations to the various effects that growers have come across in their experiments. The NW growth is described in this chapter by relying on the models found in literature and used in [P1]-[P3]. Section 3.1. introduces the most common models used to describe the NW growth, Section 3.2. shows how they can be applied to explain the NW crystal structure relying mainly on the results of [P1], whereas in Section 3.3. the NW length distributions are discussed based on [P2]. Section 3.4. shows how this understanding can be utilized to control the NW geometry beyond 1D approach by controllably switching the NW growth direction as in [P3].

3.1 The growth models

The first models concerning NW growth were focused around the metastable WZ phase found in Au-catalyzed III-V NWs. The very first approaches considered the bulk and surface energies of the atomic bonds in already grown NW concluding that extremely thin NWs (5-20 nm in diameter) should be more stable in the WZ crystal structure, even in materials predominantly seen in the ZB phase. [72], [73] However, as NW growth is a kinetic process, the model should also be kinetic and describe the nucleation energetics instead of the energetics of the final structure. Glas et al. published pioneering work describing Au-catalyzed GaAs NW growth with a kinetic approach in 2007 [34]. This work will be described in the following to give an idea of the energetic parameters affecting the NW growth, as these are the very same parameters in terms of which the results of [P1]-[P5] will be discussed. Other noteworthy publications that describe the "macroscopic" parameters of the NW growth, such as vertical and radial growth rate, continuity of the growth and preferential faceting of the NWs, can be found in [24], [32], [74]–[76]. Moreover,

models based on describing individual nucleation events can be found in [77]–[81]. Finally, a more comprehensive description of nucleation theory is provided by Dubrovskii in [82].

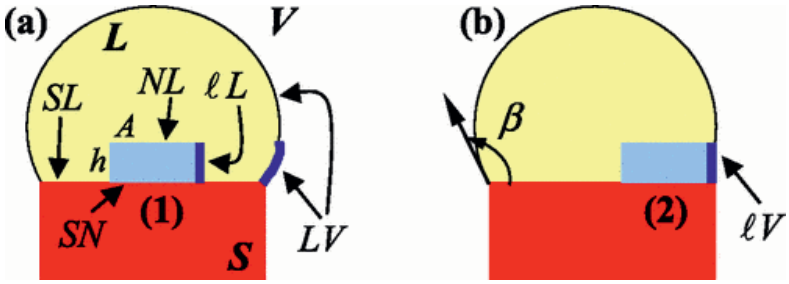

Figure 9. The schematics of a mononuclear nucleation event in a VLS NW describing a) nucleation away from the TPL and b) at the TPL. The symbols are described in the main text. Reproduced with permission from: F. Glas, J.-C. Harmand, and G. Patriarche, "Why Does Wurtzite Form in Nanowires of III-V Zinc Blende Semiconductors?" Phys. Rev. Lett., vol. 99, no. 14, p. 146101, 2007, Copyright 2007 American Physical Society [34].

In [34], a critical, and later validated assumption, was mononuclear growth, where NW grows a ML at a time with only a single nucleus initiating the ML growth. The change in free enthalpy ΔG of the system during formation of a nucleus of area A, perimeter P and having a ML height h is described in terms of the chemical potential difference of a GaAs pair in liquid and in solid phase $\Delta\mu$, and the surface energies of lateral-liquid interface γ_{lL}, substrate-liquid γ_{SL}, substrate-nucleus γ_{SN}, nucleus-liquid γ_{NL}, and lateral-vapor γ_{lV} with substrate being the top facet of the NW. This consideration gives ΔG for nucleation away from the triple phase line (TPL), where the NW top facet, droplet and vapor phase meet (Figure 9. a)):

$$\Delta G = -Ah\Delta\mu + Ph\gamma_{lL} + A(\gamma_{NL} - \gamma_{SL} + \gamma_{SN}). \quad (1)$$

When considering nucleation on the TPL as in Figure 9. b), the fraction of nucleus perimeter in nucleus-vapor interface α and droplet contact angle β will affect the change in the size of liquid-vapor interface and the free enthalpy becomes:

$$\Delta G(\alpha) = -Ah\Delta\mu + Ph[(1-\alpha)\gamma_{lL} + \alpha(\gamma_{lV} - \tau\gamma_{LV})] + A\gamma_{SN}), \quad (2)$$

where $\tau = \sin\beta$.

This gives difference in formation enthalpies away $\Delta G(0)$ and at the TPL $\Delta G(\alpha)$:

$$\Delta G(\alpha) - \Delta G(0) = \alpha P h(\gamma_{IV} - \gamma_{IL} - \tau\gamma_{LV}). \quad (3)$$

Since, α, P and h are positive, Eq. 3 gives a simple condition for nucleation to be preferable at the TPL:

$$\gamma_{IV} - \gamma_{IL} - \gamma_{LV} \sin\beta < 0. \quad (4)$$

In [34], equation (4) and computational surface energies for MBE conditions under As-rich conditions from [83] showed that GaAs NWs preferentially grow in WZ structure even in self-catalyzed growth. However, as there was only little experimental data available for ZB NWs, they were considered to have {111}-type sawtooth side facets, instead of the vertical {110} side facets typically witnessed in self-catalyzed GaAs NWs. Nevertheless, this model still gives valid base for evaluating the NW crystal structure and is used as basis for qualitative understanding the NW crystal structure throughout Section 3.2.

One significant effect not included in the model presented above, is truncation of the growth front. This effect was found by in-situ TEM growth which is used to visualize the growth and crystal structure formation of NWs by recording NW growth with sub-ML precision. These growth experiments were first conducted in other material systems, such as Si and sapphire [84]–[86] followed by Au-catalyzed [76], [87]–[89] and finally self-catalyzed GaAs [33]. The volume of the truncated corner oscillates periodically during the growth, as illustrated in Figure 10. a). [84]–[86] The presence of oscillating truncated volume has two significant implications to ML nucleation in self-catalyzed NWs discussed in the Sections 3.2.1 and 3.3.1, respectively:

1. The monolayer nucleation begins inside the droplet, on liquid-solid interface.
2. The monolayer nucleation events are temporally anticorrelated.

The first implication, has the effect given in the Glas' model described above [34], i.e. the self-catalyzed GaAs NWs grow predominantly in ZB structure. The effect of implication 2. is more complex. The supersaturation cycle and nucleation probability as a function of time is illustrated in Figure 10. b) and c), respectively. The ML nucleation cycle starts with truncated volume slowly filling up as the supersaturation in the droplet increases. This represents the increasing chemical potential in Figure 10. b). Simultaneously, the probability of nucleation starts to increase as shown in Figure 10. c). The actual ML nucleation event that follows the droplet filling is quasi-instantaneous compared to the filling time. During the ML nucleation, the truncation

returns to the original state. [33], [84] This creates a temporal anticorrelation creating a self-regulated growth regime discussed in [P2] and Section 3.3.1.

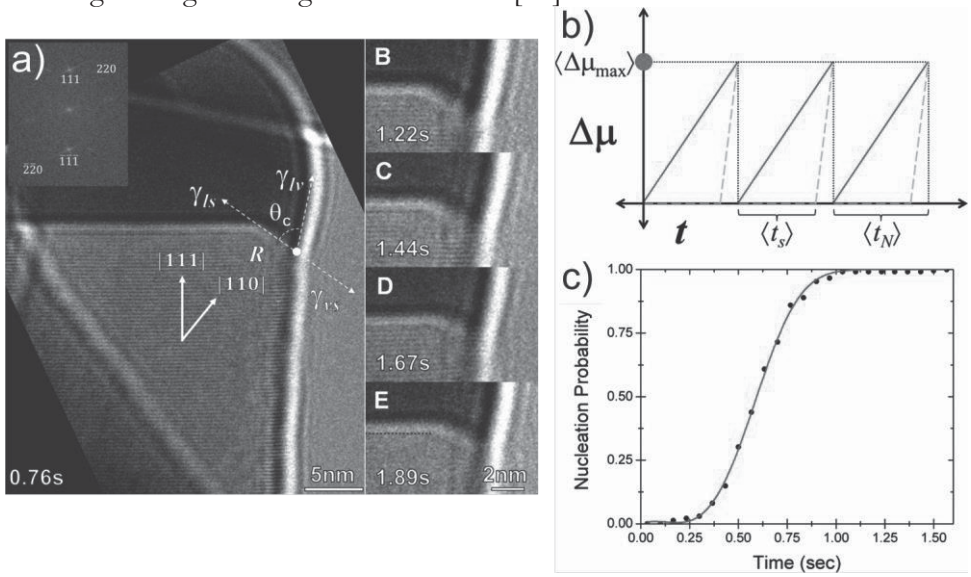

Figure 10. In-situ TEM growth of Au-catalyzed Ge NW under the influence of truncation a). The cyclic temporal evolution of supersaturation (red curve) and hypothetical supersaturation (blue dashed line) with $\Delta\mu=0$ until the filling the truncated volume are shown in b). The time dependence of ML nucleation probability is shown in c). [84] Adapted and reprinted with permission from A. D. Gamalski et al., "Cyclic Supersaturation and Triple Phase Boundary Dynamics in Germanium Nanowire Growth," J. Phys. Chem. C, vol. 115, no. 11, pp. 4413–4417, 2011. Copyright 2011 American Chemical Society [84].

3.2 Crystal structure

The crystal structure of the self-catalyzed GaAs NWs is predominantly ZB [90], whereas Au-catalyzed GaAs NWs often exhibit hexagonal WZ structure [34]. However, in the pure ZB NWs, stacking faults and rotational twin planes, which can be described as single MLs of WZ, are often present, evidenced also in [P1]. As discussed in Section 3.1, the crystal structure of a nucleating ML is determined by the location of the initial nucleus of the ML. If the nucleus is inside the droplet, ML is ZB, and if the nucleation occurs on TPL, the ML is WZ. [34] This has been commonly accepted as a general guideline by the NW growers and models even before the final confirmation by various in-situ TEM studies. [33], [76], [87], [88] The starting point of ML nucleation is further controlled by two interlinked parameters, which are accessible by the NW growth conditions, namely the droplet

contact angle and the surface energetics. These are the same parameters that control the presence of truncation. [33], [76], [79] The crystal structure of self-catalyzed NWs is investigated from the viewpoint of the contact angle in [P1] (Section 3.2.1), whereas the effects of surface energetics under the influence of Te and Be dopants and Sb incorporation are discussed in [P4] and [P5] (Sections 3.2.2, 3.2.3 and 3.2.4, respectively).

3.2.1 GaAs nanowires, effects of contact angle and supersaturation

In [P1], the evolution of the crystal structure was studied in a NW growth time series. The following discussion of these samples demonstrates the applicability of VLS growth models on the self-catalyzed NW growth and give a practical approach on the physical phenomena and quantities behind the self-catalyzed VLS growth. Samples with 60, 40, 20 and 5 min growth duration (samples NW1-NW4, respectively) were grown using Ga flux corresponding to 0.3 μm/h growth rate on GaAs(100) surface, a 60 s Ga pre-wetting, V/III BEP ratio of 9, and growth temperature 640 °C. The droplets were crystallized in samples NW2-NW4 grown for 5-40 min by exposing them to As flux during cooldown from the growth temperature, whereas the droplets in sample NW1 grown for 60 min were preserved by closing the As needle valve during the rapid cooldown (45 °C/min).

The HR-TEM analysis in Figure 11. shows the resulting crystal structure throughout a NW from sample NW1. Figure 12. shows the effect of droplet crystallization of a NW from sample NW2. In both cases, the NW bottom exhibits polytypism and stacking faults followed by up to 2 μm long twin-free sections with increasing but still sparse twinning towards the NW tip. In NW1 a short, few nm long, WZ section is found just below the droplet. Figure 12. reveals that during the droplet crystallization a short section with stacking faults followed by 150 nm long section of pure WZ ending with 20 nm of pure ZB is formed.

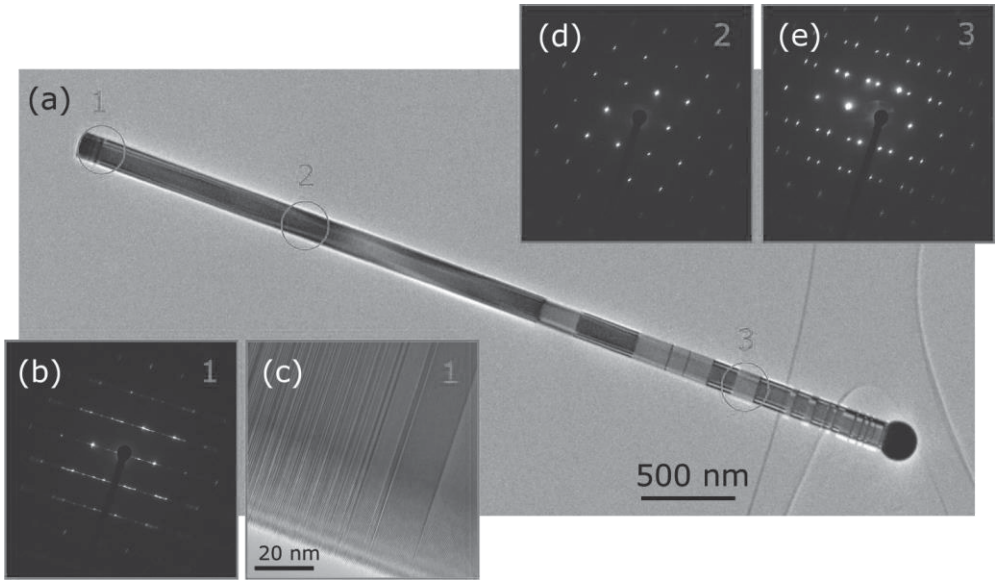

Figure 11. HR-TEM analysis of a NW from sample NW1 with preserved Ga droplet. Low magnification image is shown in a), and SAED patterns from the bottom, middle and top part in b), d) and e), respectively. HR-micrograph from the NW bottom is shown in c). [P1]

The polytypism in the bottom part of the NW was assigned to the relatively long Ga pre-deposition time creating large droplets which take relatively long time to achieve stable growth. [P1] However, during the HR-TEM analysis of NWs for [P3], similar polytypic section was found in the bottom of the NWs even though the re-evaporation procedure was used. Thus, the large pre-wetted droplets are not the cause for the polytypic section, but rather general instability during the first minute(s) of the growth. The droplet has not yet reached the steady-state conditions of As concentration and contact angle during this transient time. Thus, pinpointing a single reason for the polytypic section in NW bottom is challenging.

After the polytypic section in the bottom of the NWs, the droplet stabilizes, and NW growth continues in steady-state conditions. Thus, the crystal structure becomes completely predictable by the contact angle. As a basis for this discussion, the surface energies of different NW morphologies and crystal structures are compared to vertical {110} sidewall surface energies of a ZB NW, shown in Figure 13. a). The droplet contact angle is the parameter which determines the favorable NW morphology and crystal structure. [33] At this point it should be noted, that the models and in-situ TEM give information in terms of the contact angle during the NW growth, whereas only post-growth contact angle is accessible for NWs grown in regular MBE. The post-growth contact angle is affected by nucleation with

residual As, and possibly by other effects, such as material evaporation. Furthermore, reliable determination of the contact angle, even from high-quality SEM images, is rather unreliable, as illustrated in Figure 13. Thus, the discussion relies on the evolution of the contact angle, rather than its absolute values. However, the rough value of post-growth contact angle is usable parameter to validate assumptions of NW growth and can be used to compare different samples of a growth series, as done in [P4] (Sections 3.2.2 and 3.2.4.).

In the early stages of growth, the NW is still thin, which supports large contact angle. As seen in Figure 13. large contact angles support ZB growth with widening sidewall geometry. This is exactly the case in our NWs, where the NW diameter grows constantly. This results in the long pure ZB section. Eventually, the droplet swelling lags the diameter growth and contact angle decreases toward the transition to WZ phase. In [33] this was found to reduce the amount of truncated growth front corners, which slowly starts to increase the twinning probability. However, our NWs are not tapered due to finite radial growth as shown in Figure 4. and the radial growth is eventually terminated by shadowing effects, as discussed in Section 3.3.1.

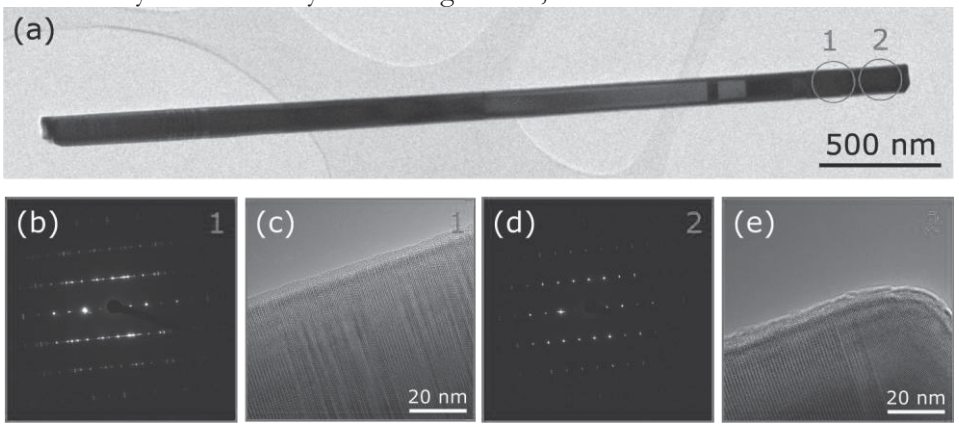

Figure 12. HR-TEM analysis of a NW from sample NW2 with crystallized Ga droplet. Low magnification image is shown in a) and SAED patterns and HR-micrographs from the marked areas 1 and 2 in b)-e), respectively. [P1]

The crystal structure of the NW section formed during the droplet crystallization is also well described by the changes in the contact angle. First, the polytypic section forms when the contact angle decreases very close to the critical angle of WZ formation (125° in Figure 13. a)). When the critical angle is reached, the 150 nm long WZ section begins to grow. As the droplet is consumed, and the contact angle further decreases, a limit for ZB growth with narrowing side facets is reached, as witnessed by the narrowing of the ZB tip of the NW in Figure 12. e).

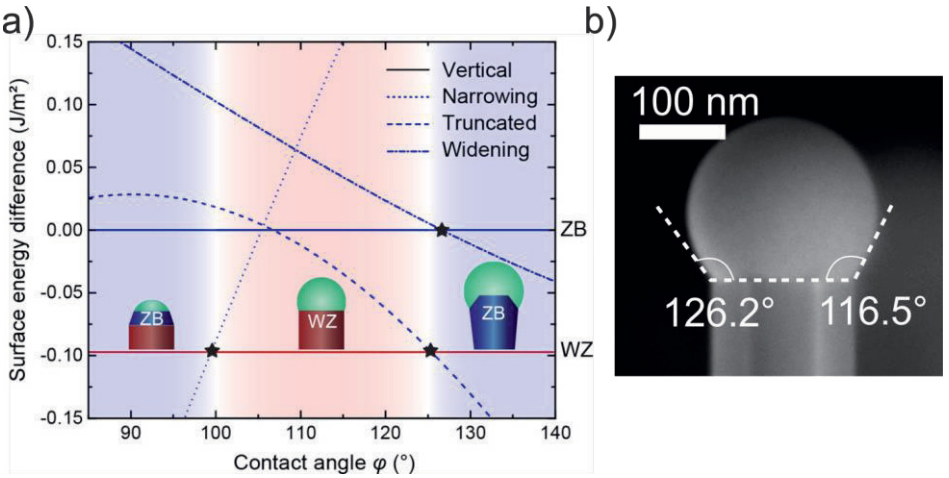

Figure 13. In a) the effect of contact angle on the NW crystal structure, shape of the facets and truncated growth is described in terms of the surface energy difference with respect to vertical ZB {110} side facets, as presented in [33]. The solid lines represent the energy of vertical WZ {1-100} and ZB {110} side facets. The black stars mark the transition contact angle to different growth regime. Starting from small contact angles, the narrowing ZB structure has lowest surface energy, making this the favorable NW morphology. As the contact angle increases to 100° change to vertical WZ {1-100} sidewall morphology occurs, followed by a brief section where truncated growth front with vertical ZB {110} sidewalls are favored from 125° to 127°. After this, truncation remains favorable, but with widening side facets which yield in inversely tapered NW morphology. Reprinted with permission from F. Panciera et al., "Phase Selection in Self-catalyzed GaAs Nanowires," Nano Lett., vol. 20, no. 3, pp. 1669–1675, Mar. 2020. Copyright 2020 American Chemical Society. [33] b) describes the difficulty of visual estimation of the post-growth droplet contact angle in SEM images of the droplet-NW interface. The NW is from the Te-doped sample used in [8].

In [P1], the GaAs NW crystal structure was studied in addition to HR-TEM by complementary methods, HR-XRD and micro-photoluminescence (μ-PL). It was shown that HR-XRD can be used to investigate the crystal structure of large NW ensembles collectively and that reciprocal space maps (RSMs) can be utilized to determine the lattice constant of the NWs with high precision. HR-XRD became an important tool used later in [P4] to analyze the Sb composition and crystal structure of GaAsSb NWs. μ-PL, on the other hand, enabled to correlate the NW crystal structure with its emission properties via indirect localized transitions at sections with stacking faults and polytypism.

3.2.2 Tellurium dopant as a surfactant – twinning superlattices

We have earlier shown that high Te dopant fluxes were shown to induce NW structure consisting of twinning superlattice with a sawtooth {111} sidewall faceting. [37] These NWs were grown on (111)B GaAs substrate, under conditions differing significantly for the ones used in growth on Si. However, the same effect was witnessed in NWs grown on Si in [8]. In [P4], the effect of As species on NW growth was investigated with one approach focusing on effects of Te dopant. The presence of Te was found to induce similar twinning superlattices as in [37] irrespective of selection of As species, As/Ga flux ratio and growth temperature as revealed by the HR-TEM analysis in Figure 14. Simultaneously, the NW sidewalls were found to consist of {111} facets [37]. This is caused by Te surfactant effect, which reduces the surface energy of {111} facets below the energy of regular vertical (or widening) {110} sidewalls shown in Figure 13.

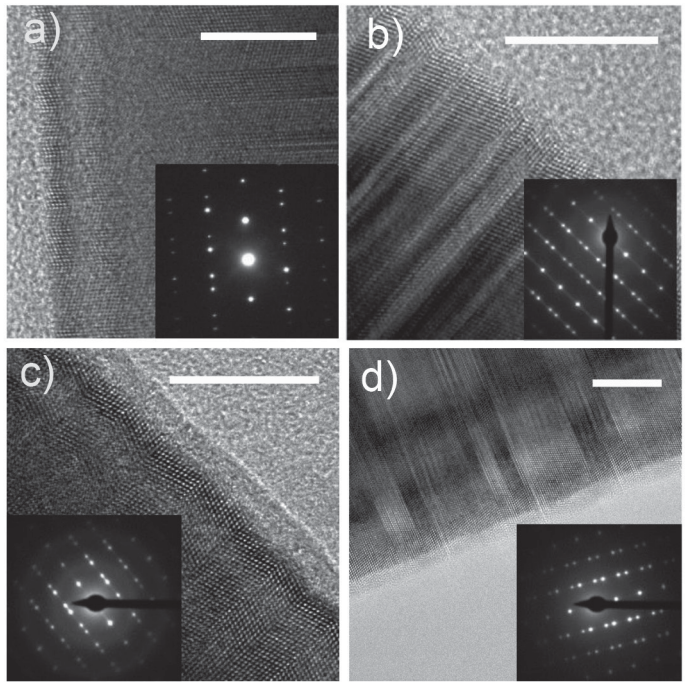

Figure 14. HR-TEM analysis of Te-doped NWs grown by As_2 in a), with As_4 in b)-d). NWs in c)-d) are grown with low As/Ga flux ratio of 2.3 and in d) the growth temperature is reduced to 620°. Reprinted from [P4].

The droplet contact angle is found to remain unmodified by the presence of Te in [P4] indicating that the increased probability of twin nucleation at TPL is not caused by a simple change in the contact angle. However, Te might increase the probability of TPL nucleation, as the sidewall configuration changes to {111} configuration.

A similar twinning superlattice has been found in other material systems [91], [92], and later explained by a detailed model for self-catalyzed doped GaAs NWs [93]. In all cases, the presence of the superlattice is explained by the nonvertical sidewalls. The nonparallel sidewalls reshape the droplet-NW interface towards a triangular shape while the NW grows. This distorts the shape of the droplet which increases its surface energy until a twin plane reverses the reshaping of the droplet-NW interface. The direct implication of this growth mode is that the twinning in Te doped NWs cannot be avoided unless a way is found to tune the sidewall surface energetics so that the regular vertical {110} sidewalls become energetically favorable. In Section 3.2.4, Sb is shown to have the opposite effect offering a possible pathway towards twin-free Te-doped NWs. [94]

3.2.3 Beryllium dopant – Reducing supersaturation and twinning

The growth and characterization of Be-doped NWs grown during the course of this thesis is described with details in [P5] and summarized in Sections 4.1.1 and 4.1.2. Be was found to reduce the amount of twinning in the upper parts of the NWs, and in high concentrations also shorten the polytypic sections in the early and final stages of growth, as shown in Figure 15. Simultaneously, the dimensions and droplet contact angle of the Be-doped NWs is comparable to the undoped reference. To suppress twinning or polytypic layer formation by TPL nucleation Be must affect the interface energies according to Eq. 4. The change may be increase of the lateral nucleus-vapor energy γ_{lV}, or decrease of the lateral nucleus-liquid γ_{lL} or liquid-vapor γ_{LV} energies.

In [95], the presence of Be in the droplet was found to destabilize the droplet and reshape the droplet-NW interface similarly to annealing done in [P3]. This strongly implies that the supersaturation in the droplet is reduced by Be. Decreased supersaturation further implies that the liquid-NW surface energies, including γ_{lL}, are reduced which supports nucleation away from the TPL yielding a phase pure, almost twin-free ZB NWs.

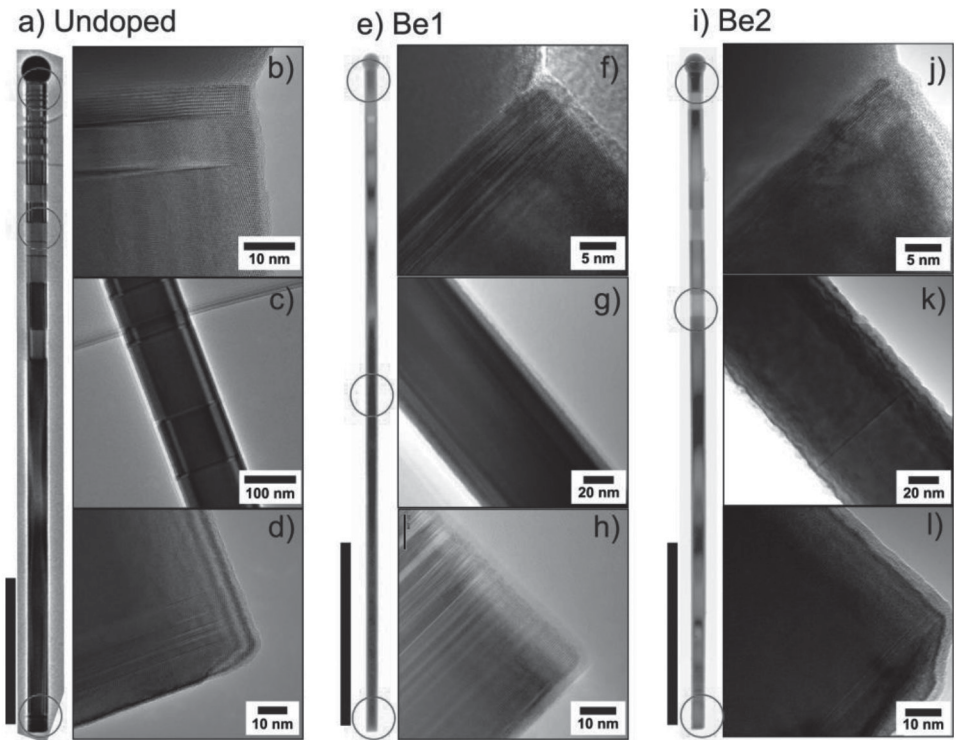

Figure 15. HR-TEM analysis of undoped, and Be doped NWs from [P5]. The nominal Be concentrations of NWs Be1 and Be2 are $2 \cdot 10^{18}$ cm^{-3} and $2 \cdot 10^{19}$ cm^{-3}, respectively. The scale bars in a), e) and i) are 1 µm. [P5]

3.2.4 Antimonide-based ternaries – Complete suppression of twinning

GaAsSb NWs were investigated in [P4]. The growth, characterization methods and compositional and dimensional analysis are summarized in Section 4.2.1. Similarly to Be, Sb was found to reduce twinning, but up to the point where the ZB GaAsSb NWs are completely untwinned. This is witnessed in Figure 16. revealing a TEM analysis of a single NW from sample GaAsSb9 (see Table 1. on page 51 for details of the sample). The graph in Figure 16. d) shows the twinning ratio of the GaAsSb NWs as a function of relative Sb flux. The twinning ratio is determined by HR-XRD analysis described in Section 4.2.1. The twinning approaches zero already at relative Sb flux of 20 % from the total group V flux and is independent on the As species used in the NW growth.

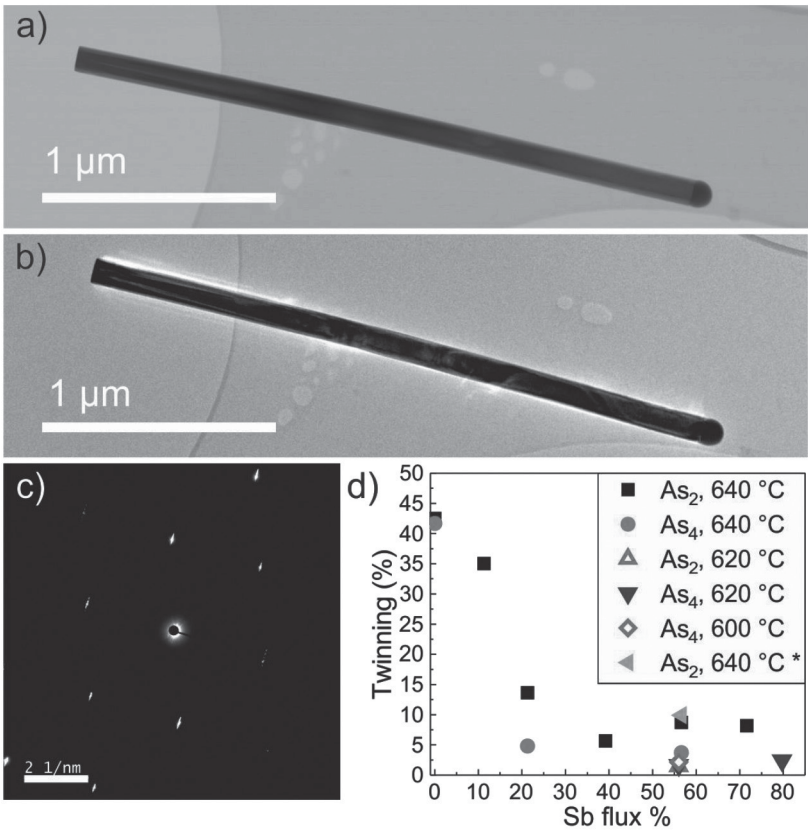

Figure 16. STEM a) and HR-TEM b) micrographs and a SAED pattern c) of a GaAsSb NW from sample GaAsSb9. The sample was grown using As_4 under relative Sb flux of 57% at temperature of 640 °C. d) shows the twinning ratio of the GaAsSb NWs with respect to the relative Sb flux and is determined by HR-XRD (220)-phi scans. See Section 4.2.1. for details on the NW sample and HR-XRD phi-scans. Adapted from [P4].

The reduction of twinning in GaAsSb NWs is explained by modified energetics of the VLS system. [P4] The contact angle of the GaAsSb NWs decreases with Sb flux (Figure 31.) below values which in GaAs NWs should result in significant twinning and even pure WZ growth according to [33]. Thus, the reason for lack of twinning must be the reduced supersaturation in the droplet, as described in detail in [29].

However, the energetics do not fully explain the lack of twinning in GaAsSb NWs, as some of them grow fully or partially in VS mode (Figure 30.). The VS grown NWs exhibit complex faceting with three-fold rotational symmetry of the NW tip. A 180° rotational twin would thus reform the NW growth front completely, which is a large deviation to a stable growth.

Once more, the simple energetic model described in Section 3.2.1 [34] combined with qualitative considerations based on SEM analysis has explained an interesting effect in NW crystal structure. The phase purity and lack of twinning in GaAsSb NWs implicates that similar effect could be achieved in other material systems by modifying the energetics of the VLS system with a suitable surfactant.

3.3 Dimensional control

The requirement for dimensional control of NWs is driven by the photonic waveguiding properties of the NWs, i.e. identical NWs have identical properties which can be controllably tuned by the NW dimensions. Simultaneously, the various incorporation pathways for dopants and ternary elements discussed in Chapter 4 may lead into compositional variations unless the axial and radial growth are not controlled.

3.3.1 Narrowing the length distribution

Inspired by the narrow NW length distribution observed in [P1], investigations were initiated to narrow down the NW length distribution further and to identify the mechanisms which broaden the distributions. Yet another growth duration series of 3, 6, 20, 40, 50 and 80 min was fabricated. The growth conditions followed the standard established in [P1] but the re-evaporation step introduced in Section 2.4.3 was utilized, and all the droplets were preserved. NW densities were $0.7\text{-}1.5 \cdot 10^8$ cm^{-2}. SEM images of the resulting NW ensembles and data of the evolving dimensions are shown in Figure 17. The length distributions are found to be remarkably narrow already in the SEM images. Simultaneously, the NW length data shows that the growth is linear. Note also saturation of the radial growth witnessed in the 80 min sample in Figure 17. g).

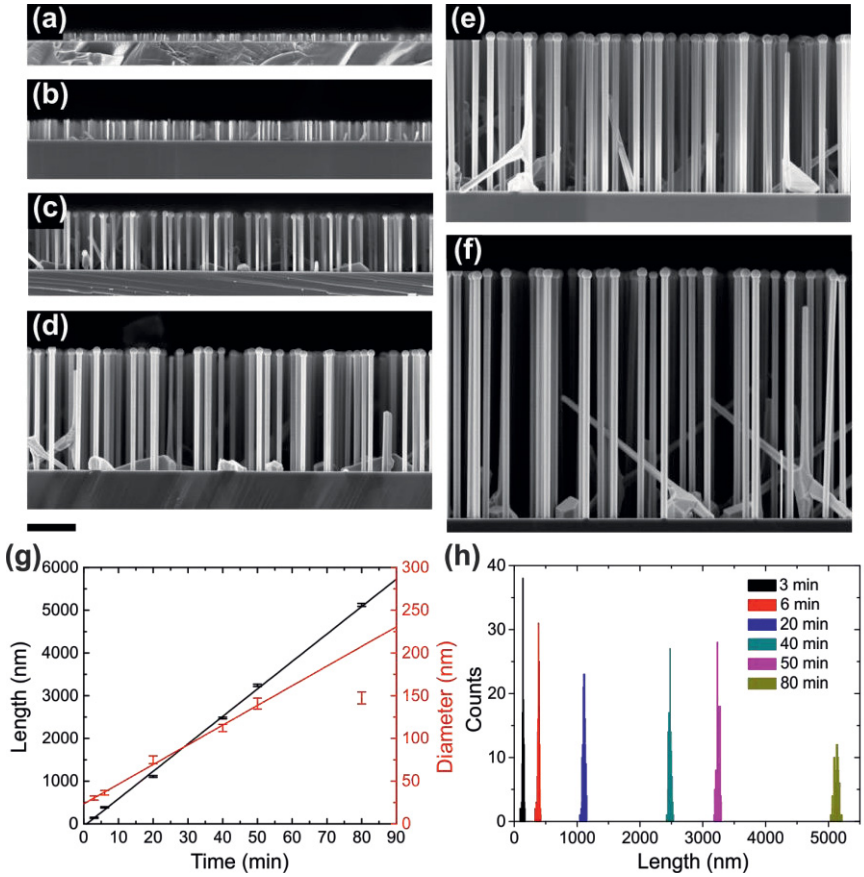

Figure 17. SEM images of samples grown for 3, 6, 20, 40, 50 and 80 min in a)-f), respectively. All images have the same scale bar of 1 µm. The time dependent dimensions in g) and the measured length histograms in h). Adapted from [P2].

During continuous growth, the NW length distribution is expected to slowly broaden. In NWs growing from directly impinging fluxes without any nucleation delays or secondary nucleation, the length distribution is expected to follow the Gaussian Green's function due to kinetic fluctuations [77], [96]:

$$F(L,\langle L\rangle) = \frac{1}{\sqrt{2\pi}\sigma_P}\exp\left[-\frac{(L-\langle L\rangle)^2}{2\sigma_P^2}\right], \quad (5)$$

where L is the NW length, $\langle L\rangle$ is the mean length, and

$$\sigma_P^2 = h\langle L\rangle \quad (6)$$

is the Poisson variance. Here h is the ML height in the NW growth direction and for <111> ZB GaAs, $h = 0.326$ nm. However, due to the low As concentration of

only few percent in the droplet [24], and truncation [33], the ML nucleation events are temporally anticorrelated because each nucleation event temporarily fills the truncation and depletes the droplet from As species. Similar temporal anticorrelation has been shown to induce sub-Poissonian nucleation statistics within a single NW. [78] In [P2], it was shown how this temporal anticorrelation saturates the length distribution of a NW ensemble to a constant value after ~6 min of NW growth. The saturated length distribution variance was estimated to be negligibly small based on the measured values of contact angle (133°) and NW radius of 25.5 nm after 5 min growth. Comparing to the growth model in Figure 13. a), our NWs grow in the region of highest contact angle with truncated growth front and widening sidewall configuration. However, after 50 min of growth, the radial growth suppresses, and the narrow window of ZB growth with truncated growth front and vertical sidewalls is reached. This can be caused by the fact that the amount of Ga required to increase the diameter of long and thick NW becomes constantly larger, when the NW grows, and thus the amount of available Ga starts to limit the radial growth. [23]

In [P2], the length distributions were found to be extremely narrow with only 367 nm^2 variance after 40 min growth, when the Poisson variance is 808 nm^2. In comparison, in [P1] the corresponding values after 60 min growth were 1024 nm^2 and 1406 nm^2. However, as seen in Figure 17. and Figure 18. some broadening mechanisms still affects the length distribution in the early stages of the NW growth and after ~50 min growth. The broadening mechanisms were identified as initial nucleation randomness and shadowing. They were added up into a single model with the stationary regime, resulting in the "Model fit" for the experimental length distribution variances shown in Figure 18.

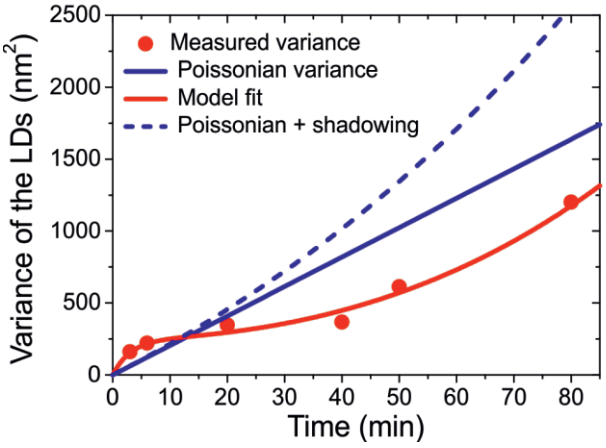

Figure 18. Measured variance of the length distributions in [P2] compared to the fitted model, Poissonian variance and combined Poissonian broadening and shadowing effect.

The NW length distribution sums up into variance

$$\sigma^2 = \sigma_*^2 \left(1 - e^{-\langle L \rangle / L_*}\right) + hL_0 \left(e^{\langle L \rangle / L_0} - 1 - \langle L \rangle / L_0\right), \quad (7)$$

where the first term describes the nucleation randomness and the second term the shadowing effect. σ_*^2 is the saturation variance of the initial nucleation randomness at the characteristic saturation length L_*, L_0characteristic length of shadowing, $\langle L \rangle$ is the mean NW length, and h is the ML height in NW growth direction. Values for σ_*^2, L_* and L_0 were found to be 250 nm^2, 200 nm and 6000 nm, respectively. The shadowing length is large compared to the geometrical shadowing, which initiates already at 1000 nm long NWs with the average inter-NW distance of 550 nm and flux angle of 35°. However, the random nature of nearest neighbor statistic resulting from the template affects how each NW experiences the shadowing. Also the re-emission of group V species from NW sidewalls and substrate, and the re-emission of group III species from the substrate make the shadowing effect much more complex than the simple geometrical shadowing from the nearest NWs. Thus, it should be investigated in more detail in symmetric NW arrays as in [23].

The broadening of the length distribution can be suppressed either by focusing on the random nucleation or the shadowing. Significant progress was done to shorten the incubation time from [P1] to [P2] by introducing the re-evaporation step and nucleating the NWs without a Ga wetting. However, in [97] Bastiman et al. showed that the NW incubation time is almost independent of the Ga pre-wetting time and that it can be reduced by lower growth temperature and higher group V partial pressure. This forms a clear path towards faster nucleation and likely towards more simultaneous nucleation. The shadowing effect, on the other hand, is straightforward to be reduced or postponed by growing sparser NWs. The opposite effect can be demonstrated by investigating an additional dense NW sample ($7.1 \cdot 10^8$cm^{-2}). The length distribution broadening can be visually seen from the SEM image in Figure 19. The variance of the 5925 nm long NWs is 3546 nm^2, which is clearly higher than the Poissonian variance of 1931 nm^2. Unfortunately, the droplets in this sample are crystallized during cooldown, which has some unknown contribution to the length distribution. Furthermore, significantly shorter NWs are seen in the image, implying that the shadowing may have almost completely suppressed their growth when the Ga flux reaching them is prevented by the surrounding NWs. The shorter NW population is not taken into account in the variance.

Figure 19. Side-view images of NWs high density of $7.1 \cdot 10^8 cm^{-2}$ demonstrating the broadening length distribution in dense NW arrays.

Since the publication of [P2], similar results have been obtained by the combination of Ga wetting and annealing in [47]. Narrow length distributions had been demonstrated also by other methods [44], [45]. The results presented above, and the fact that nucleation antibunching results from stable growth in self-catalyzed GaAs NWs, suggest that negligible broadening of length distributions is a common effect and achievable with broad range of growth parameters. Thus, it is the simultaneous nucleation which makes the NWs grown within this work unique. Therefore, after understanding the details of NW growth mechanism, it can be concluded that the template preparation and suitable initial nucleation conditions have yielded the main results concerning length distributions in [P1] and [P2].

3.3.2 The role of As species

During writing of [P1]-[P3], discussions in various events with NW grower community led to understanding that there is a consensus that using As_4 is beneficial for self-catalyzed NW growth. While the vast majority of reports on self-catalyzed NW growth are done using As_4, no real comparison of growth with As_2 and As_4 was found in literature. However, a single report recommended using As_4 to achieve longer and thinner Au-catalyzed NWs [98].

To investigate the effect of As species, a series of samples with atomic V/III ratios of 2.3, 3 and 3.7 (corresponding to BEP-ratios of 7, 9 and 11 for As_2) was grown with both As species. The established 0.3 µm/h Ga growth rate was used for all samples. All samples were grown on the same high-density template yielding NW densities around $2 \cdot 10^8$ cm^{-2}. The resulting NWs are shown in Figure 20. The visual inspection tells that As_4 induces longer and thinner NWs. This is further confirmed

in the dimensional analysis provided in Figure 21. The effect of As species is evidently significant, as the NWs grown by As_4 are longer and thinner.

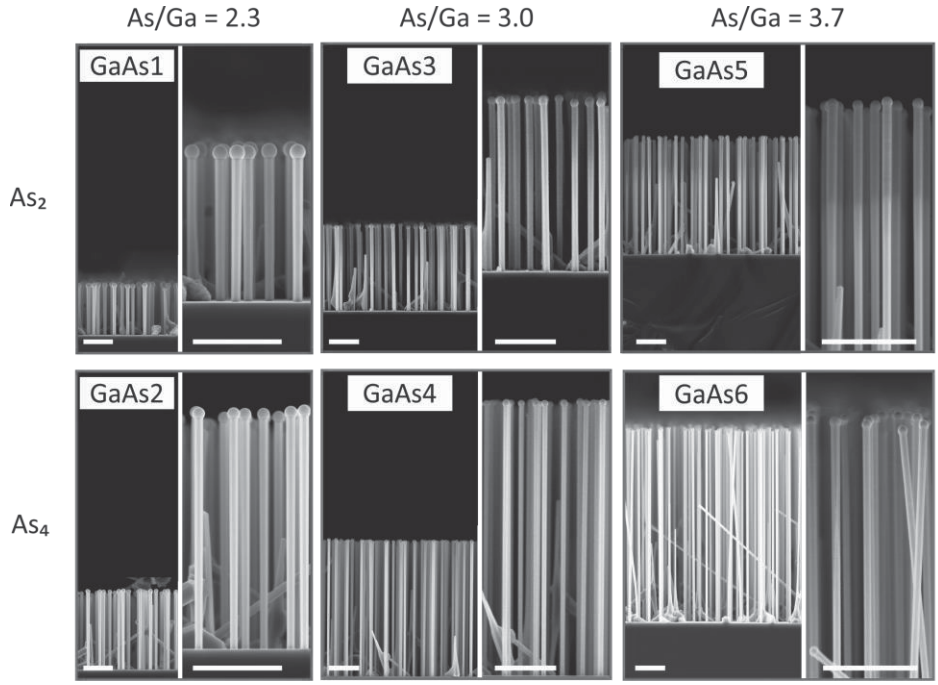

Figure 20. Comparison of GaAs NWs grown with different As species and V/III ratios. All scale bars are 1 µm. [P4]

The higher axial growth rate of NWs grown with As_4 was found to be a result of the incorporation mechanism of As from different species. As_4 has lower sticking coefficient on GaAs surface due to its incorporation mechanism. As_4-molecule first dissociates into dimers upon chemisorption, which is followed by desorption or diffusion of the second dimer. [14], [99] Since As re-evaporation is known to be a major source of As into the droplet [30], the higher growth rate is direct consequence of higher local V/III ratio at the droplet. Simultaneously, lower sticking of As_4 on GaAs(110) surfaces suppresses the radial growth effectively and allows Ga on the sidewalls to diffuse to the droplet.

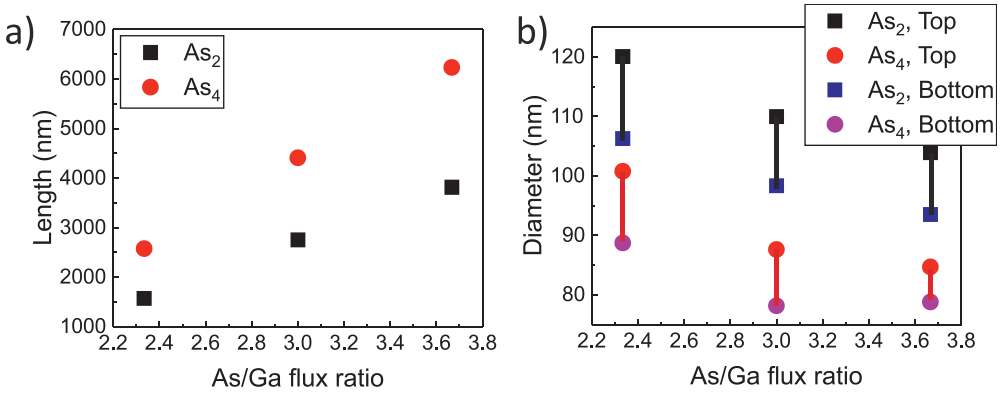

Figure 21. The dimensions of samples GaAs1-GaAs6. The different top and bottom diameters indicate inverse tapering. Adapted from [P4].

The longer and thinner NWs formed by growth with As_4 supports the general understanding that NWs would be "easier" to grow using As_4-species, even though no effect on the actual yield of successful NWs was found. Moreover, the selection of As species offers a tool to independently adjust the vertical and radial growth rate which can be used to tune incorporation of ternary elements, as discussed in Section 4.2.

The NW growth could also be conducted using various intermediate cracker temperatures where a mixture of both As species is present. The transition between As_4 and As_2 is a continuous function of the cracker temperature. Thus, the broad cracker temperature range should give adequate control for precise tuning of the As_2-fraction.

3.4 Beyond 1D – Switching the growth direction

Switching the NW growth direction has been proven to be a useful tool in fabrication of nanocrosses. [100] They can be further utilized in low dimensional quantum devices. [101] Extreme control of the Ga droplet and droplet-NW interface reshaping is required to form this kind of bent nanostructures.This was demonstrated in [P3] discussed in this section. The importance of these results does not lie solely in these particular structures but in the generalizable methodology and detailed understanding of the phenomena behind it.

3.4.1 Modifying the droplet-nanowire interface

Precise understanding and identification of truncated facets was the first step in controlling the growth direction switching mechanism used to form the bent NWs in [P3]. Droplets dropping towards NW sidewall were observed close to the growth edge of the 20 min grown sample in [P2]. The sample edge is close to the sample holder with large thermal capacity, and thus the droplet dropping was considered a thermal effect. In order to test this theory, a NW sample with 20 min growth duration was grown but a 45 s annealing at the 640 °C growth temperature without any fluxes was added prior to the regular rapid cooldown of 45 °C/min. This annealing yielded 100% of the Ga droplets tilting towards one of the {110} side facets as witnessed in Figure 22.

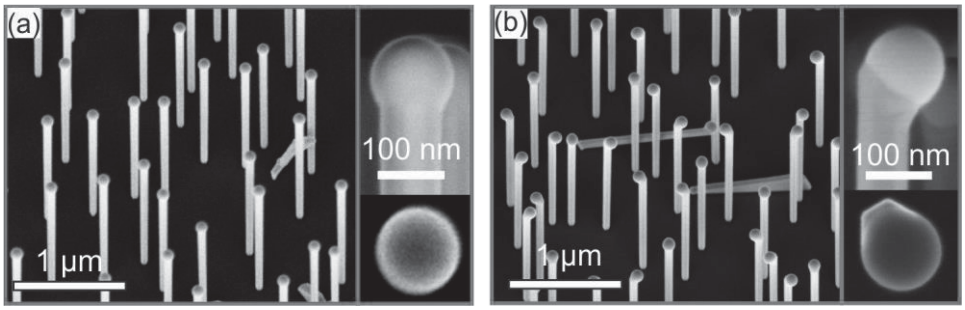

Figure 22. SEM images of 20 min grown NWs without (a) and with (b) post-growth annealing.

To understand this facet reformation, HR-TEM analysis was conducted. The observations are compiled in Figure 23. The NW top-facet was found to be truncated from two of the corners between top-facet and {112} corners of the sidewalls. Three low index facets in addition to the original top facet were identified: wetted {111}A and {100} facets which support the droplet, and a {111}B facet at the NW sidewall. In addition, multiple smaller higher index facets were found as seen in Figure 23. Furthermore, a vast amount of SEM analysis was conducted on annealed NWs with droplets removed by HCl etching (10% HCl in IPA for 30 s with stirring) to perceive the shape of the NW tip. Simultaneously, it was statistically confirmed that the wetted {111}A and {100} facets are present in all the NWs, and are not just different structures.

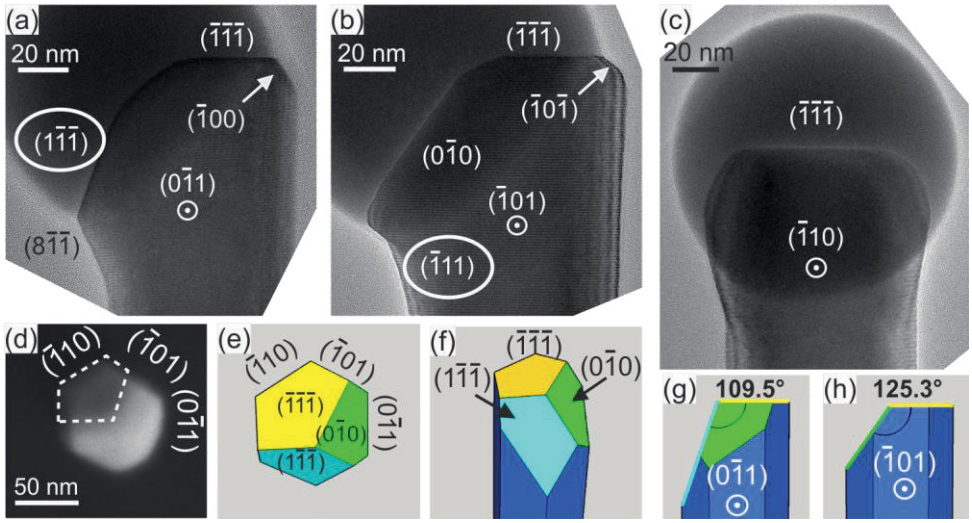

Figure 23. HR-TEM analysis and illustration of the reshaped NW top. All facet indices are marked to represent one exemplary NWs, but the threefold symmetry would justify also two different set of indices. (a)-(c) show three different NWs from different viewpoint to the droplet-NW interface. (d) shows a SEM image of a NW with droplet etched away using HCl. Numerous images were taken with different imaging settings and detectors to form a comprehensive understanding of the shape of the NW top. Part of these images are shown also in the supporting information of [P3]. (e)-(h) show a schematic illustration of the NW top structure.

The multitude of facets was explained via a kinetic model in [P3]. During the annealing, As depletes from the droplet by a certain rate and the chemical potential difference $\Delta\mu$ per GaAs pair in liquid and solid GaAs approaches to quasi-equilibrium $\Delta\mu = 0$. This process was found to take roughly 60 s for NWs with 50 nm radius. At this state, both wetted facets, {111}A and {100} are energetically favorable. When the horizontal growth is initiated, the dimensional ratio of these facets determines the type of the growing structure as discussed in Section 3.4.2. It should also be noted that the analysis of the reshaped droplet-NW interface was conducted in post-growth conditions, and the structure at the end of the annealing may be significantly different. According to the model, the {111}A facets form slower than the {100} facet, and thus the resumed growth primarily occurs on {111}A facet after long annealing times. The equalizing of the sizes of the {111}A and {100} facets seen in post-growth analysis may have partly taken place during the cooldown. This is why we need the model to give further insights on the process.

3.4.2 Nucleating horizontal growth

Following the annealing described in the Section 3.4.1, horizontal growth on the reshaped droplet-NW interface was nucleated by simultaneous opening of Ga and As. The same 0.3 μm/h Ga impingement rate was used also in the horizontal growth. This resulted in two main structure types differentiated by fundamentally different nucleation mechanism. Type 1 structure is analyzed by SEM and HR-TEM in Figure 24. and type 2 structure in Figure 25.

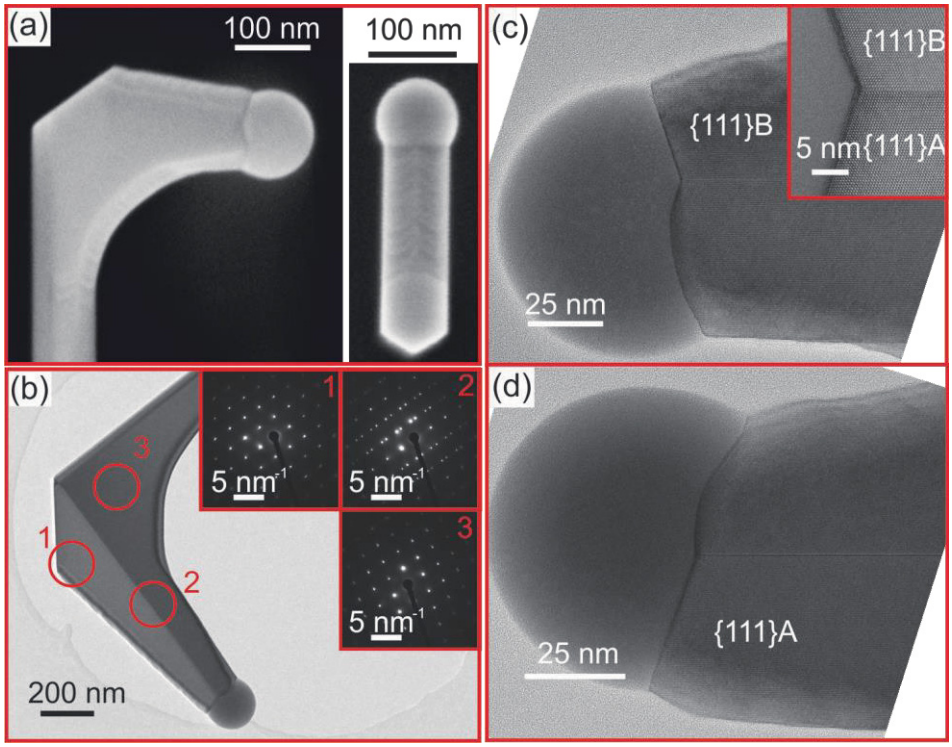

Figure 24. SEM image of Type 1 structure (a) showing the horizontal growth after 5 min. The TEM-analysis is done after 10 min horizontal growth showing a pure ZB structure with a single twin extending along the horizontal growth direction (b). Two different growth front configurations of the horizontal growth are shown in (c) and (d). Both have {111} A and B facets next to the twin, as shown in the inset of (c). Note the periodical structuring on the top of the horizontal growth best visible in top-view inset in (a) and in (d). Adapted from [P3].

The Type 1 growth initiates on the {111}A facet identified in Figure 23. When the horizontal growth nucleates, a twin plane is formed, most likely by TPL nucleation on the small contact angle edge of the dropped droplet. The twin plane nucleation

creates a {111}B facet, which opposes the {111}A facet formed during the annealing. The twin plane pins the droplet to a stable position between the {111}A and {111}B facets.

As with Type 1 structures, in Type 2 structures, a twin plane is formed when the growth is resumed. However, now the droplet tends towards the {100} facet which does not support the growth and instead of being pinned by the twin plane, the droplet slides to the {111}B facet found under the {100} facet seen in Figure 23. The downward growth was found to consist of a twinning superlattice by additional TEM analysis in [117] zone axis. The twinning is also visible in high contrast SEM micrograph in Figure 27. g).

The dependence of nucleation yield of Type 1 and 2 structures was investigated by varying the annealing time, III/V ratio during the horizontal growth and initial NW diameter. The set of samples was designed to confirm the hypothesis that lower chemical potential at the end of the annealing supports growth of the {111}A facet and hence type 1 nucleation. The results are plotted in Figure 26. Only one parameter was changed at a time, and the intermediate data point is same for all the graphs. For example, the annealing time series is done with NWs having 83 nm diameter, and with V/III BEP ratio of 9. The diameter series was prepared simply by growing a growth time series of 20, 22.5, 25 and 30 min. The 25 min and 30 min sample resulted in roughly the same diameter of 90 nm due to different NW densities.

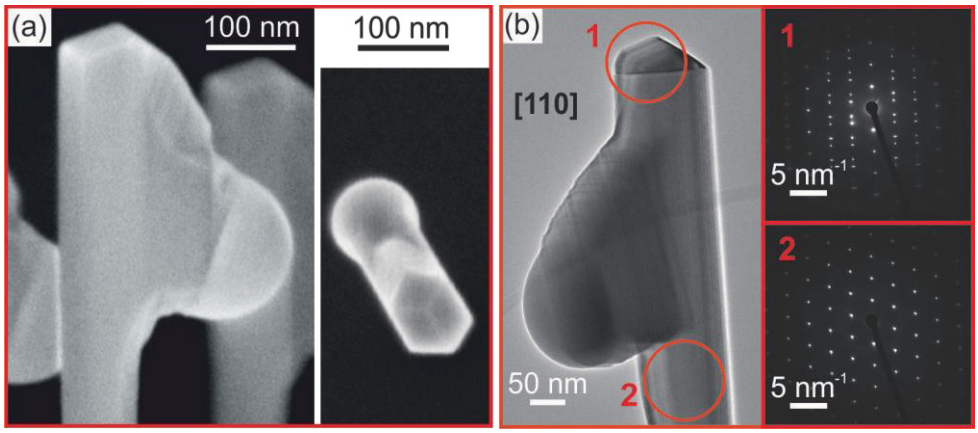

Figure 25. Type 2 structure grows slightly downward from the horizontal direction, as visible in the SEM image in (a). In (b) the NW is aligned so that the downward growth points 60° towards the detector. A single twin is identified in the tip of the NW in otherwise twin-free vertical part. In this configuration twinning of the horizontal growth is not visible as a twin would turn the duplicate set of [110] diffraction away from zone axis. Adapted from [P3].

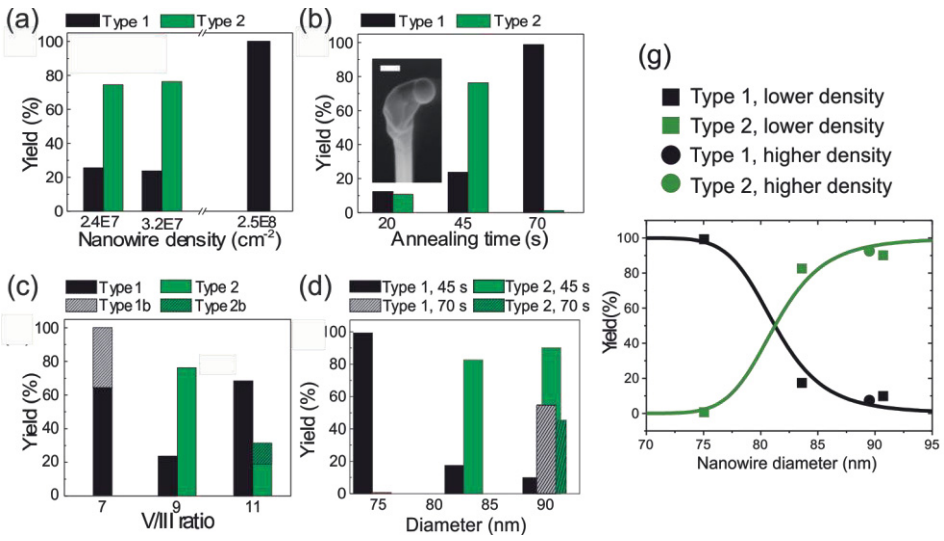

Figure 26. The resulting yields of Type 1 and Type 2 structures as a function of NW density (a), Annealing time (b), V/III BEP ratio (c) and NW diameter (d). In (d) also longer, 70 s annealing is tested for NWs with 90 nm diameter. The intermediate data point is same for each graph. (g) shows the yield of different structures fitted with the model. The lower and higher densities represent total surface structure densities of 1.26 and $1.91 \cdot 10^8$ cm^{-2}.

The behavior with annealing time is just as predicted by the model, the yield of Type 1 structures approaches 100% with the 70 s annealing. Similarly, with low BEP ratio, the supersaturation increases slower after resuming the growth, and again Type 1 structures nucleate with highest yield. However, the growth is destabilized as it proceeds forming structures labeled Type 1b, where the droplets begin to wet the sidewall of the horizontal growth. Furthermore, the smallest diameter sample experienced almost 100% yield of Type 1 structures. This is simply caused the faster As depletion from smaller droplet. The absolute amount of As in the droplet is smaller in the smaller droplets, while the As depletion rate is not size dependent. The diameter effect lies also behind the 100% Type 1 yield of the high-density sample. The high-density NWs experience 75 nm diameter similarly to the thinnest sample of the diameter series. Yet again, understanding the theory behind the VLS growth mode and carefully conducting a growth experiment have shown their worth.

3.4.3 Stable horizontal growth

The horizontal and downward growth modes were investigated with a growth time series of horizontal growth durations 5, 10 and 20 min. SEM images and the linear growth with constant growth rate of the Type 1 horizontal section is shown in Figure 27. Moreover, the droplet size remains constant in both structures throughout the 20 min growth which is a strong indicator of a stable growth mode. Thus, both growth modes were found to be stable and continuous under the typical NW growth conditions.

The twin-mediated growth mode of Type 1 structures is known for other type of structures, as it was observed in Ge ingots already in 1950's [102], [103], and later in Au-catalyzed group IV [104], [105] and III-V [106] NWs. However, the v-shaped growth front formed by opposing {111}A and B facets is unique within III-V material system. Furthermore, the growth front was speculated to oscillate between the configuration with a flat {111}A facet below the twin and microfacets above the twin (Figure 24. d)), and a configuration with a flat {111}B facet above the twin and microfacets below the twin (Figure 24. c)). The presence of this novel growth mode is supported by the periodical roughness of the top facet of the Type 1 structures. Furthermore, extensive SEM analysis was conducted on Type 1 structures with droplets removed by HCl etching, which revealed random occurrence for both growth fronts. Furthermore, the {111}B facet is known to have lower surface energy than the {111}A facet in contact with As species [83], whereas the {111}A is energetically preferable at low chemical potential difference between liquid and solid GaAs pair (i.e. low As concentration). Together these energetics create optimal conditions for pulsed nucleation, similar to the truncated growth front discussed in Section 3.1. The As filled droplet supports growth on flat {111}B facet followed by rapid nucleation which depletes the droplet from As making the growth front configuration with flat {111}A facet energetically favorable.

The downward growth mode of Type 2 NWs, on the other hand, was found to be dominated by a flat {111}B growth front. This growth mode fits perfectly the known facts of self-catalyzed VLS growth. As shown in Section 3.2.1, contact angles below 100° supports growth of ZB GaAs, which is clearly the case for the top and bottom part of the downward section in Type 2 structures. However, on side facets, the contact angle is larger as seen for instance in top-view SEM in Figure 25. This combination of different contact angles is most likely the reason behind the dense twinning in the downward growth.

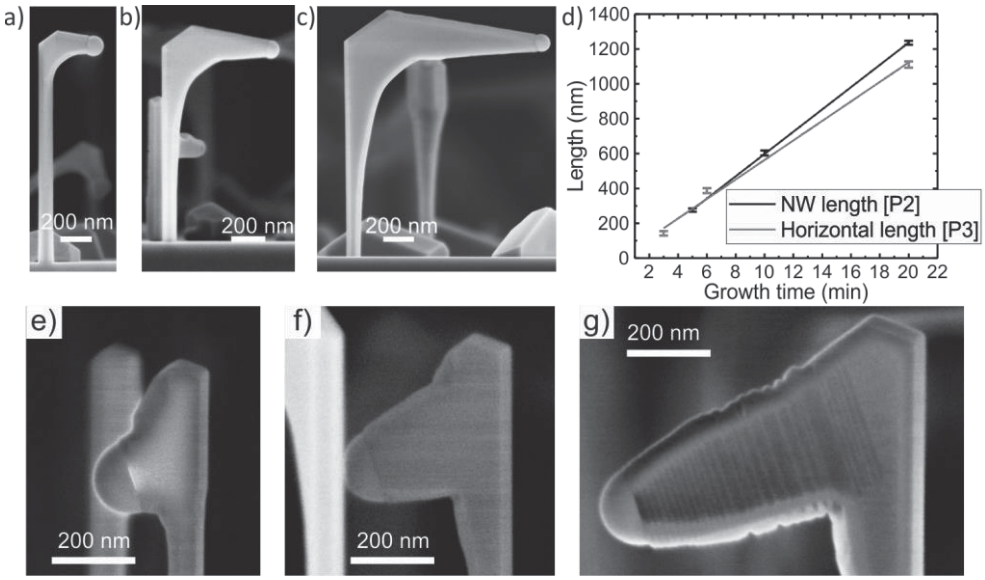

Figure 27. The evolution of type 1 (a-c) and type 2 (e-g) structures after 5, 10 and 20 min growth, respectively. The length of type 1 horizontal section after each growth time is compared to vertical NWs from [P2] in d).

4 DOPING AND TERNARIES – TOWARDS FUNCTIONALITY

The goal of NW research in general is to create something that has technological significance. When discussing semiconductors, the first thing making them useful in device applications is tunability of their electric properties which can be controlled by introducing dopant impurities in the lattice. The electrical properties can be utilized for example to make diodes or solar cells. For compound semiconductors, such as the III–V semiconductors, another important functionality arises from the tunability of the band gap by changing the material composition. The tunable, and often direct, band gap offers a broad spectrum of possibilities for efficient light generation and detection at different wavelengths. Combining the NW geometry which relaxes the lattice matching conditions and tunable direct band gap, III–V NWs are a well-suited option for direct integration with silicon photonics. Both the dopant incorporation and growth of ternaries are, however, relatively challenging tasks in VLS mode compared to planar 2D growth. This is due to the different incorporation rates via the droplet and sidewalls, and the diffusion of atoms in the solid phase at the typically high NW growth temperatures. In the following sections, first the dopant incorporation and then the band gap tuning in NWs are discussed focusing on the dopant/ternary incorporation mechanisms, compositional gradients and how to avoid the gradients.

4.1 Dopant incorporation

The dopant incorporation into NWs is an interesting topic, as there are several incorporation pathways for the dopant atoms. Furthermore, the reports on preferential dopant incorporation pathways are often contradicting. For example, Be-dopant incorporation was reported to occur predominantly via VS sidewall incorporation in [107], whereas [95], [108] report preferential incorporation via droplet. A recent model describes general thermodynamics of dopant incorporation and preferential lattice site for dopant incorporation in VLS system [109], but is still

not capable to explain the dopant incorporation arising from the simultaneous VLS and VS growth mode.

4.1.1 Growth and characterization methods of the doped nanowires

Both p- and n-type doped NWs were grown within the course of this thesis, and investigated in detail in the works of Rizzo Piton et al. [P5], [110], [111] and Hakkarainen et al. [8]. The doped NWs were grown similarly to the undoped NWs in [P1]. The NWs from the 60 min growth duration sample in [P1] were used as a reference sample throughout [P5] and [110], whereas the 80 min growth duration sample from [P2] was used as reference in [8]. For doping, the dopant cell was opened simultaneously with the As cracker. The doping levels were calibrated using 1 μm thick Hall samples grown on semi-insulating (100) GaAs wafers and adjusted to correspond the Ga flux of 0.3 μm/h used in NW growth. The droplets were preserved to distinguish the NW growth direction easily. Additional Te-doped NWs were grown capped by Al(0.3)GaAs shell for atom probe tomography and off-axis electron holography investigation of the doped core. The shells were grown by ramping the substrate temperature to 540 °C under As flux to crystallize the droplets. After the ramp, Ga and Al fluxes were opened, and the As valve was kept open also during the cooldown. The growth rate on NW sidewalls is 23 % of the vertical 2D growth rate, as determined in Author's MSc thesis [53].

As the purpose of growing the doped NWs was to investigate the incorporation mechanisms of the dopants, spatially resolved characterization techniques needed to be utilized. One of the most crucial achievements for characterization was fabrication of multiple ohmic contacts with adequately low contact resistance to a single NW [P5], [8], [110], [111]. The contacts were then used for current-voltage (IV) measurements. Another important technique was micro-Raman spectroscopy, which was extensively used to study the free carrier concentration and mobility in the NWs. Both methods provide information on the number of carriers in the semiconductor, hence describing the number of activated dopants. In [8], atom probe tomography and off-axis electron holography were used as complementary techniques to micro-Raman and electrical characterization. Atom probe tomography is an extremely sensitive mass-spectroscopic technique where the NW is evaporated by voltage or laser pulsing. The atoms are collected and counted creating 3D profiles of atomic concentrations with sensitivity easily down to low dopant levels of $1 \cdot 10^{17}$ cm^{-3}. [112] Off-axis electron holography, on the other hand, is TEM based

technique, where the phase difference between an electron beam passing through a sample and a known reference give information on the mean inner potential of the material. The mean inner potential further correlates to the number of free carriers. Thus, atom probe tomography combined with off-axis electron holography, μ-Raman spectroscopy and electrical measurements give complementary information on the incorporation and activation of the dopant atoms.

4.1.2 Beryllium – Saturation of vapor-solid incorporation

The incorporation of Be in NWs was investigated in [P5] with two p-doped NW samples having nominal Be concentrations of $2.0 \cdot 10^{18}$ cm^{-3} and $2.0 \cdot 10^{19}$ cm^{-3} referred to as Be1 and Be2, respectively. First, the resulting carrier concentrations were determined by micro-Raman spectroscopy giving incorporation yields of 60% for Be1 and 35% for Be2 with respect to the nominal doping. Furthermore, the hole mobility in Be2 was found to be significantly lower than in corresponding bulk GaAs sample, whereas Be1 experienced almost bulk-like mobility. As the Be-doped NWs are almost twin-free, as discussed in Section 3.2.3, the decreased mobility is not a consequence of twin-induced potential barriers, but surface scattering. The surface depletion region width is reduced by higher carrier concentration in sample Be2. Thus, the carriers in Be2 NWs move closer to the surface and are more prone to surface effects. As a consequence, mobility in NWs decreases even faster with doping level than in bulk semiconductor. The effect could be compensated either by growing thicker NWs or using passivating shells that prevent the carriers to experience the surface effects.

The dopant gradients in Be-doped NWs was primarily investigated by IV measurements. Data from single NW IV measurements is shown in Figure 28. The four-contact geometry allows distinguishing that in Be1 NWs the resistivity is much higher in between the top contacts (CD) than in bottom (AB). In Be2 NWs, however, the differences become much smaller while the trend becomes opposite. The top contacts have lower resistivity in Be2.

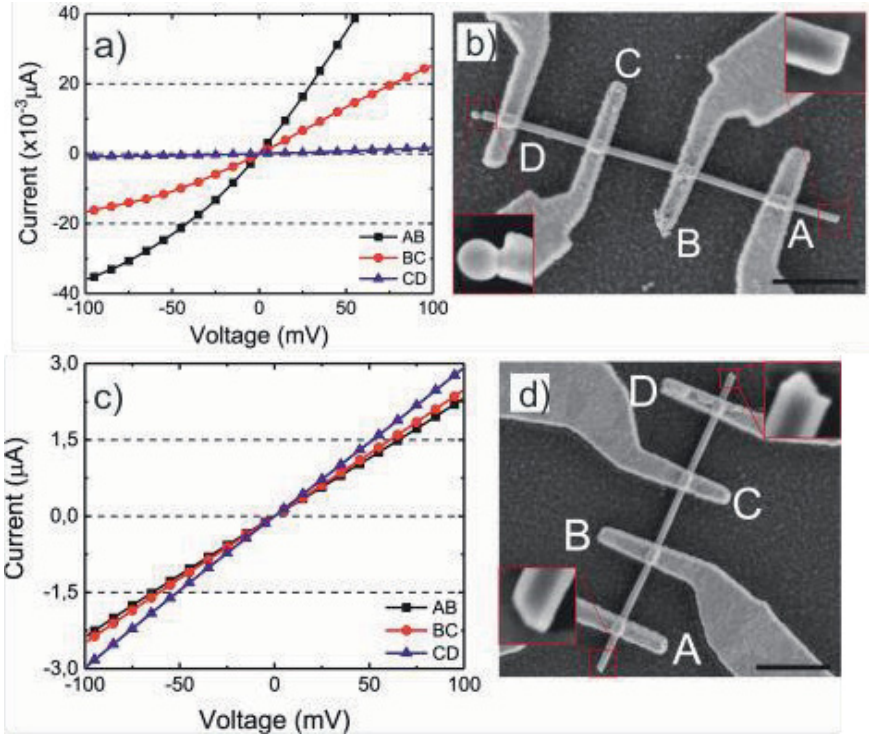

Figure 28. IV-measurements and SEM images of corresponding devices of a NW from Be1 in a) and b), and from Be 2 in c) and d). [P5] The scale bars are 1 µm. Adapted from [P5]

These results indicate a higher Be incorporation in the bottom part of the NWs with lower Be fluxes, whereas higher Be-fluxes allow higher incorporation to the top part of the NWs. This observation indicates that Be incorporation under low Be fluxes (Be1) is higher in VS growth mode of the NW sidewalls. As more VS grown material forms in the bottom part of the NWs (see Figure 4.), the dopant in the bottom part is higher. Moreover, the amount of Be atoms impinging the droplet is limited compared to the high axial growth rate, whereas the sidewall growth is extremely slow (~70 nm/h in [P2]), making the Be flux on the sidewalls large compared to the growth rate.

On the other hand, the total incorporation efficiency was found to be lower in sample Be2 grown under higher Be flux. Thus, we concluded that the incorporation via the VS mechanism saturates under high Be fluxes rather than the VLS efficiency increases. The surface of the Be-doped NWs was found to be rough in the TEM analysis presented in Figure 15. The surface roughness implies that the cause of saturating VS incorporation is surface segregation of Be. The segregation is known to be pronounced in high temperatures and low V/III-ratios, both matching to the

NW growth conditions. [113] Thus, growth conditions supporting VS growth in general, also support VS incorporation of Be and homogeneous Be compositions could thus be achieved in core-shell NWs primarily via shell growth as suggested in [107]. Moreover, these results agree with the preferential VLS incorporation reported in [95], [108], especially in [108], where negligible sidewall growth is reported.

4.1.3 Tellurium – Dominating vapor-liquid-solid incorporation

Te is commonly used in GaAs NWs as an n-type dopant instead of Si. This is due to amphoteric nature of Si which may act as a donor or an acceptor depending on the incorporation mechanism and growth conditions. [109], [114], [115] However, successful n-type doping using Si has been reported in Au-catalyzed GaAs NWs grown by hydride vapor phase epitaxy. [109], [115] The Te-doped NWs grown within the course of this thesis [8] revealed a dopant gradient where Te concentration increases towards the NW tip. The gradient was observed by micro-Raman spectroscopy, transport measurements and off-axis electron holography. Due to volume limitations, APT only scanned the inner core of the NW's upper part where a uniform dopant concentration was found. A model was developed to confirm the assumption that Te primarily incorporates via the droplet and then out-diffuses to the VS grown shell driven by the high temperature of NW growth. The model resulted in good fit with the off-axis electron holography measurements conducted in cross-sectional NW slices taken from bottom and top parts of the n-GaAs/AlGaAs core-shell NWs described in Section 4.1.1.

Thus, it was concluded that Te predominantly incorporates via the VLS growth, and the VS grown shell doping mainly results from the out-diffusing Te species. This is an expected conclusion due to the high vapor pressure of Te. [116] Te easily re-evaporates from the NW sidewalls and substrate surface at NW growth temperatures. Thus, Te doesn't stick to the NW sidewalls for VS incorporation and simultaneously, an increased secondary Te flux is supplied to the droplet similarly to re-emitted group V species.

The weak sidewall incorporation of Te created the need to suppress the radial growth using As_4, as described in Section 3.3.2. However, electrical characterization of the Te-doped NWs grown using As_4 is not yet concluded, and the success of suppressing the compositional gradient along with the radial growth remains an open question.

4.2 GaAsSb nanowires – Tuning the band gap

GaAsSb provides a full range of direct band gaps extending from GaAs emission at 870 nm to GaSb emission at 1700 nm. [117] This spectrum covers the whole telecommunication wavelength band making GaAsSb an interesting material for photonic integration on Si. However, GaAsSb can be grown as 2D layers only with very narrow composition ranges on GaAs, GaSb or InP substrates due to strain. NW geometry can be used to detour these limitations. Thus, GaAsSb NWs have been widely studied, even though they still exhibit several issues reducing their practicality. Introduction of Sb into the NW growth reduces the NW aspect ratio and as the Sb flux increases, axial NW growths starts to deplete completely. This has restricted the Sb composition from the group V species of conventionally grown GaAsSb NWs to 44%. [29] However, growth with residual As flux or on GaAs stems has led to higher compositions of 80% [118] and 93% [119], [120], respectively. In addition to the depletion of 1D growth, GaAsSb NWs typically suffer from compositional gradients with lower Sb composition in the bottom part and outer shell of the NW. The gradients are typically related to Sb out-diffusion and As-to-Sb exchange reaction. [121]–[123] These issues are addressed in the following sections by investigating the role of As species on the growth of GaAsSb NWs while mapping the growth parameter space.

4.2.1 Growth and characterization of the GaAsSb nanowires

In total 12 different GaAsSb NW samples were investigated in [P4] to assess the effects of Sb on the resulting NW dimensions and the compositional Sb gradients. The growths were conducted similarly to GaAs NWs, but Sb was used in addition to As. Both As species were used with atomic flux ratios of 2.3 and 3 (corresponding to BEP-ratios of 7 and 9 for As_2). Furthermore, an As/Ga atomic flux ratio of 1.7 was used for the highest Sb containing sample grown with As_4. The Ga growth rate was 0.3 μm/h. The Sb flux % was determined as the fraction of atomic Sb flux from the total atomic group V flux. See Section 2.1.3 for description of the methods used for determining the atomic flux ratios. The GaAsSb NW samples are described in Table 1.

Table 1. Details of the GaAsSb NW samples. Sb% are determined by HR-XRD RSMs, or as average EDS compositions when denoted by *. D is the NW diameter and L is the length.

Sample	As species	Sb flux%	Growth T (°C)	As/ Ga	Growth	Sb %	D (nm)	L (nm)	Aspect ratio L/D	Contact angle (°)
Ref1	As2	-	640	3	VLS	0	102	4550	45	127
Ref2	As4	-	640	3	VLS	0	84	5870	70	123
GaAsSb1	As2	11	640	3	VLS	4.7	109	3230	30	121
GaAsSb2	As2	21	640	3	VLS	9.6*	118	1930	16	118
GaAsSb3	As2	39	640	3	VLS	14.1	136	2320	17	114
GaAsSb4	As2	57	640	3	VLS	14.2*	156	910	5.8	111
GaAsSb5	As2	72	640	3	VLS	19.5	178	750	4.2	107
GaAsSb6	As2	56	620	2.3	VS	23.6*	218	1190	5.5	-
GaAsSb7	As2	56	600	2.3	VS	-	204	175	0.86	-
GaAsSb8	As4	21	640	3	VLS	14.6*	91	3940	43	120
GaAsSb9	As4	57	640	3	VLS	21.3*	105	3160	30	108
GaAsSb10	As4	56	620	2.3	VLS	32.0*	135	3430	25	-
GaAsSb11	As4	56	600	2.3	VS	33.4*	177	1480	8.4	-
GaAsSb12	As4	80	620	1.7	VLS	38.1*	158	1530	9.7	-

The composition of GaAsSb NWs was initially investigated by HR-XRD RSMs around the symmetric (111) diffraction. An exemplary RSM of sample GaAsSb6 is shown in Figure 29. The data was corrected with reference to the theoretical value of Si(111) diffraction and integrated along the Q_x-axis. The center of gravity of the integrated GaAsSb(111) diffraction was used to determine the separation of the GaAsSb and Si peaks and the Sb composition as shown in Figure 29. a). Additionally, energy-dispersive x-ray spectroscopy (EDS) was conducted in SEM to determine the Sb composition and study the compositional gradients in the axial direction. For EDS, the NWs were transferred on Cu-carbon TEM grids. The NWs were released into IPA by sonicating an as grown sample piece in IPA for 3 min in ultrasound bath and drop casting 10 µl of the IPA-NW solution on the grid.

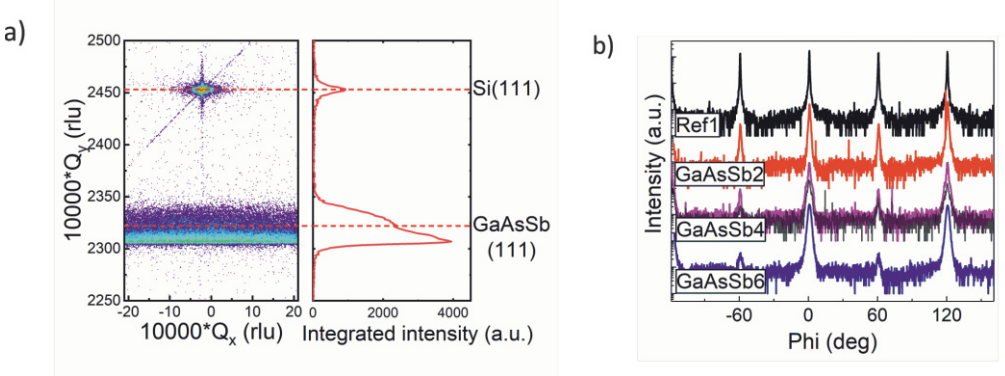

Figure 29. Reciprocal space map around the symmetric (111) diffraction of the sample GaAsSb6 and the intensity integrated along the Q_x-direction a). Both intensities are given in logarithmic scale. Dashed lines mark the center of gravity for each peak. b) shows 280° sections of the rotational (220) phi-scans.

Crystal structure of the GaAsSb NWs was studied by HR-TEM and HR-XRD. The XRD analysis relied on rotational phi-scans around the (220) diffraction. The (220) diffraction tilted 35.26° degree from the (111) diffraction has a three-fold rotational symmetry. As a rotational twin plane turns the crystal direction by 180°, twinned NWs create duplicate peaks every 60°. Thus, randomly twinned ensemble of NWs should produce a six-fold rotational symmetry. It should be noted that just a single twin plane allows the NW to contribute to the duplicate peaks. Thus, even a small amount of twinning should be directly visible in the phi-scans.

4.2.2 Dimensions and composition of the GaAsSb nanowires

Sb has a strong tendency to reduce the NW aspect ratio as seen in SEM images of Figure 30. the data summarized in Table 1. and Figure 31. This is an expected result based on previous reports that describe the energetics of GaAsSb NW growth. The enhanced radial growth in GaAsSb NWs is caused by the long diffusion length of Sb on the {110} sidewall surface. It gives Ga atoms more time to interact and form bonds on the NW sidewalls compared to bare GaAs NWs. This also limits the Ga diffusion into the droplet and reduces the axial growth rate. [29]

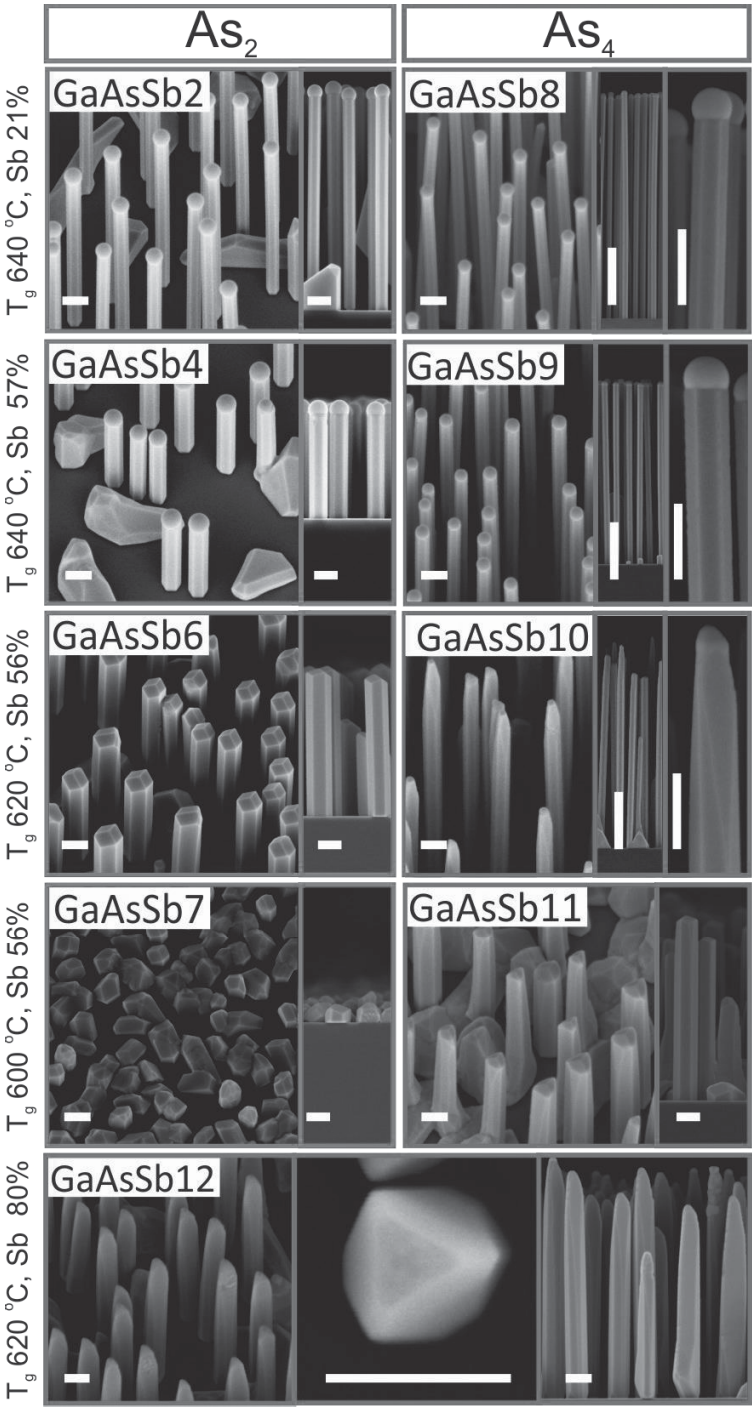

Figure 30. SEM analysis of the GaAsSb NWs. All scale bars are 200 nm, except the lower magnification insets of GaAsSb8-10 have 1 μm long sale bars.

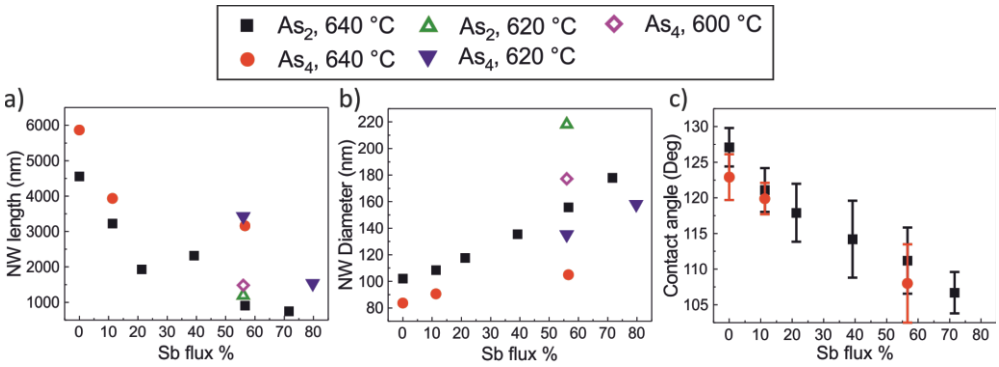

Figure 31. Dimensional data of the GaAsSb NWs. NW length in a), diameter in b) and droplet contact angle with standard deviation resulting from both wire-to-wire variation and measurement error in c).

The significant result in the perspective of NW dimensions is that As_4 suppresses the reduction of aspect ratio as seen in the SEM images of Figure 30. and numerical data in Figure 31. and Table 1. Simultaneously, As_4 extends the growth window towards lower temperatures, down to 600 °C, where growth by As_2 results only in parasitic mounding (samples GaAsSb11 and GaAsSb7, respectively). Another interesting observation is that the axial growth mode of the GaAsSb changes to VS growth when the growth temperature is reduced. At 620 °C, growth with As_2 yields dimensionally uniform NWs without any evidence of presence of a Ga droplet (GaAsSb6), whereas NWs grown with As_4 exhibit broad length distributions and partially consumed droplets (GaAsSb11). With As_4, the GaAs NWs grow fully in VS mode at 600 °C (GaAsSb10 and GaAsSb12).

The extended growth window obtained by using As_4 was utilized to increase the Sb composition % in the NWs. The GaAsSb NWs grown with As_4 exhibit higher Sb composition % than the ones grown with As_2. Moreover, the axial NW growth is sustained in lower growth temperatures and under higher relative Sb fluxes. Both changes enhance the Sb incorporation, as witnessed in Figure 32. The Sb composition furthermore increases towards the NW tip in most of the samples. The compositional gradient is, however, significantly reduced in NWs which grow in VS mode. The increasing Sb composition % toward NW tip and the reduced gradient in NWs imply that the compositional gradient might be caused by similar effect as proposed for Te-doped NWs in Section 4.1.3. The Sb incorporation is easier via VLS growth and thus the radially grown shell is Sb poor. This is not seen in the NWs that

grow in VS mode which suggests that the Sb incorporation is equally efficient via the facets at the NW tip and sidewalls. However, based on this data it is not possible to exclude contribution of the commonly reported Sb out-diffusion and As-to-Sb exchange reaction.

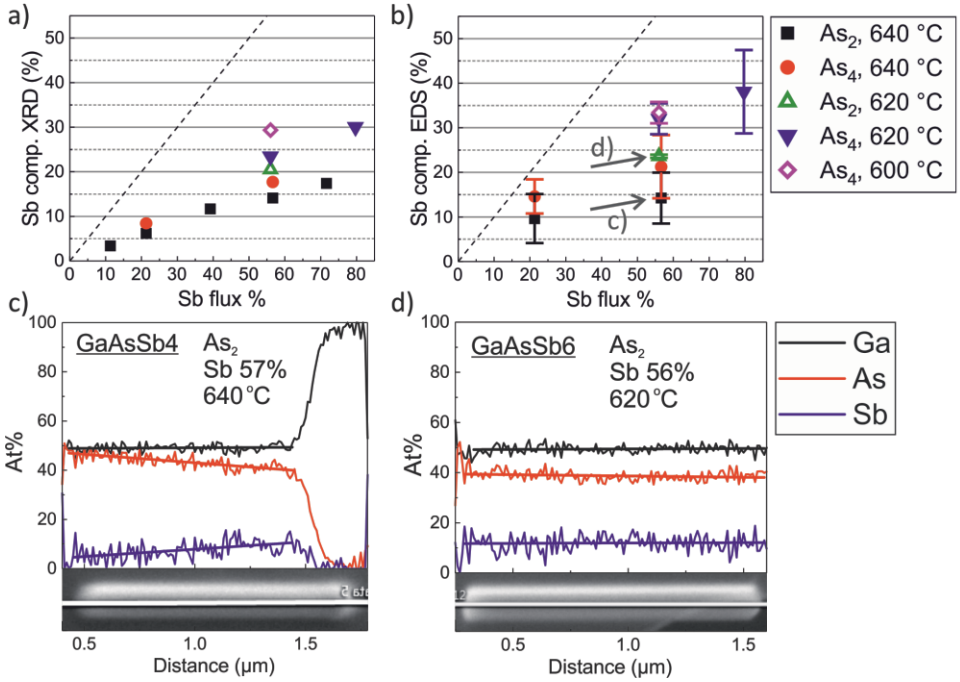

Figure 32. Compositional analysis of the GaAsSb NWs. a) shows the compositions obtained by HR-XRD method, and b) show average EDS compositions with the error bars depicting the composition gradients with lower Sb composition in the bottom part of the NW. The dashed lines in a) and b) are reference lines describing equal incorporation for Sb and As. The EDS line scans in sample c) and d) are from samples GaAsSb4 and GaAsSb6, respectively, marked in b). The VLS grown NW from GaAsSb4 in c) shows a clearly increasing Sb composition towards the droplet, whereas the VS grown NW from sample GaAsSb6 in d) shows no evidence of Sb gradient nor presence of Ga droplet.

Independent of the mechanism that suppresses the gradient in VS grown GaAsSb NWs, the highest Sb composition % reported so far by traditional NW growth methods is achieved in the tip of VLS grown NWs of sample GaAsSb12 [P4]. Furthermore, the growth window with As_4 should extend beyond the growth temperature of 620 °C, As/Ga atomic flux ratio of 1.7 and relative Sb flux of 80%. The high Sb composition % has allowed extending the PL emission in the sample GaAsSb12 to 1400 nm at telecom E-band (Figure 33.) demonstrating the great promise of this material system for photonic integration.

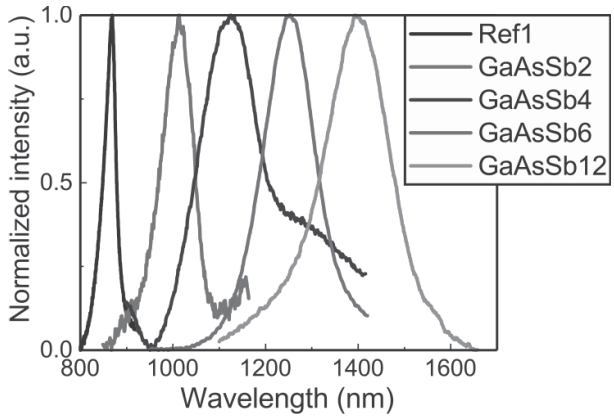

Figure 33. Normalized room temperature PL spectra of different GaAsSb NW samples showing the wavelength shift with increasing Sb composition.

5 CONCLUSIONS

The goal of this thesis was to advance the physics and methodology of NW growth. As a general summary, the results of the publications discussed within this thesis are compared to the original research questions in Figure 34. All the publications contribute to advancing fundamental understanding of the physics of NW growth. On the other hand, aspects related to doping, controllability of size distribution, density, and geometry place some clear steps advancing the functionality of NWs towards device heterostructures and applications.

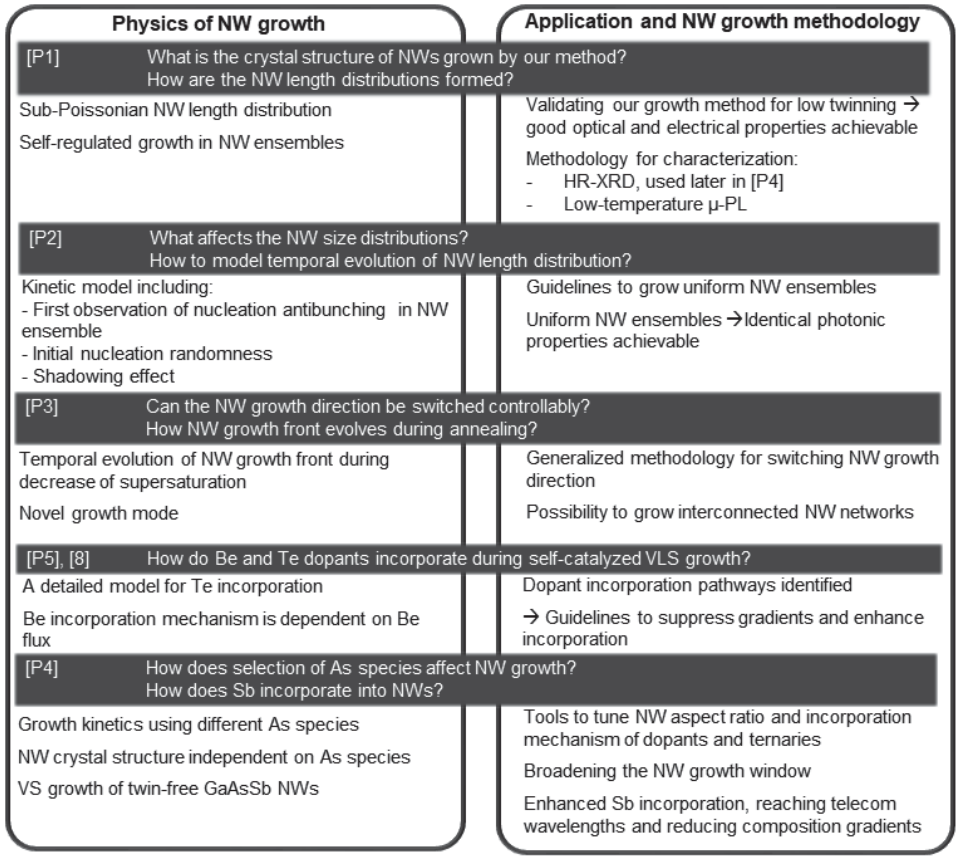

Figure 34. The most important results discussed in this thesis compared with the research questions described in the introduction. The results are distributed into fundamental results describing the physics of NW growth and results related directly to applications or development of the NW growth methodology.

The structure of self-catalyzed GaAs NWs grown on lithography-free oxide patterns was investigated in [P1]. The crystal purity of the NWs was found to be high while HR-XRD and μ-PL were validated as valuable characterization methods for NW crystal structure complimentary to the commonly used HR-TEM.

Moreover, sub-Poissonian length distribution was observed in [P1]. This led to further investigations of narrowing the NW length distributions in [P2], which also introduced a practical methodology to achieve narrow NW length distributions in large NW ensembles. This achievement was explained by a detailed kinetic model including nucleation delay, shadowing effects and temporal anticorrelation of NW nucleation events, so called nucleation antibunching. [P1] and [P2] were also the first demonstration of nucleation antibunching effect in a NW ensemble. This result interlinked observations made in the microstructure of individual NWs to a whole NW ensemble. These results are useful to adjust the photonic properties of the NWs.

Temporal evolution of NW-droplet interface during annealing was investigated in [P3]. Continuing the NW growth on the reshaped growth front led to the most important result of [P3], i.e. the growth direction of NW could be switched controllably. A thermodynamic model was introduced to explain this effect. Furthermore, a new growth mode was found in the horizontal growth following the annealing.

Important steps towards utilizing NWs in practical applications were made in [P5], [8], [110], [111], where the dopant incorporation mechanisms to the NWs were investigated. Both Be and Te doped NWs grown within the course of this thesis revealed dopant gradients and details on the primary incorporation mechanisms. As highlights of the results on doped NWs, full activation of Te dopants was observed in [8], whereas the primary mechanism of Be incorporation was found to be dependent on the Be flux in [P5].

The goal to suppress dopant gradients led to the investigation of the role of As species in the self-catalyzed NW growth [P4]. The dimensional effect of using As_4 was found to be significant and extend to Te doped GaAs NWs and GaAsSb material system. As_4 was found to enhance the axial NW growth yielding longer and thinner NWs, while extending the NW growth window towards lower temperatures and V/III ratios. The growth of GaAsSb NWs with As_4 led to high Sb composition % of up to 47% in phase pure, twin-free ZB NWs with room temperature PL emission extending to the telecommunication wavelengths.

The effects of different growth parameters on the resulting NW properties are explained in Table 2. This growth guide offers a practical view to tune the NW growth parameters to obtain the required properties.

Table 2. Growth guide for NWs. The first column describes which parameter is increased followed by description on how the increase of the parameter affects the most important NW properties investigated in this work. As_4 in the first column refers to using As_4 instead of As_2.

Increased	Aspect ratio	Contact angle	Twinning	Sb incorporation
As/III ratio	Increases supersaturation and accelerates axial growth. Local V/III ratio has the same effect	Eventually decreases, and under high enough As flux, droplet gets fully consumed	Eventually increases according to change in contact angle [33].	Unclear, highest Sb % achieved with low As fluxes [120] but As_4 (=higher local As/III ratio) increases the incorporation [P4]
Growth temperature	Increases, As evaporates easier from sidewalls	Increases, at low T the droplet crystallizes due to low As evaporation	Should decrease according to change in contact angle [33].	Decreases, out-diffusion, As-to-Sb exchange reaction and evaporation from sidewalls increase
As_4	Increases due to lower sticking on sidewalls from As_4	No effect	No effect	Increases
NW density	Increases, high enough density causes inverse tapering due to shadowing	No effect	Not investigated. Based on contact angle, no effect is expected	Not investigated, but could increase, weaker radial growth reduces the Sb-poor shell

Sb flux	Decreases, enhances sidewall growth which suppresses Ga diffusion to droplet	Decreases	Decreases, completely twin-free NWs obtained easily	Incorporated fraction eventually decreases, while absolute incorporation increases
Te flux	Decreases	No effect	Increases, twinning superlattices with (111) sidewalls	Not investigated
Be flux	Not investigated, but increase is expected due to ML nucleation with lower supersaturation [95]	No effect	Reduces due to reducing liquid-NW surface energy	Not investigated

In terms of future work, the understanding gained here, particularly in respects with doping incorporation that is essential for many functional device heterostructures, should be used for demonstrating unique device applications. To this end, an obvious path is to integrate NWs with Si-waveguides enabling nanoscale integrated light sources. This opens several new research questions, part of which expand beyond the growth of NWs requiring also expertise on processing of Si waveguides. How to monolithically integrate NW devices to Si waveguides? How to inject or collect carriers into or out of these NWs? In terms of NW growth, these developments require NW design, for example, capable of lasing under electrical pumping. Pathway towards lasing is paved by passivating the NWs by higher band gap shells, such as GaAs/AlGaAs/GaAs core-shell NWs grown in the Author's MSc thesis [53]. Moreover, the understanding of dopant incorporation mechanisms achieved in this work should be sufficient to grow both radial and axial p-i-n junctions. Another requirement towards using the full potential of NWs, is the utilization of band-gap engineering enabled by GaAsSb NWs. The first questions in this path are, how to grow passive shells to GaAsSb NWs and how to cover the full Sb composition range. These areas are already active topics in the research groups and will be further continued.

6 BIBLIOGRAPHY

[1] B. Mayer *et al.*, "Lasing from individual GaAs-AlGaAs core-shell nanowires up to room temperature," *Nat Commun*, vol. 4, p. 2931, 2013, doi: https://doi.org/10.1038/ncomms3931.

[2] B. Mayer *et al.*, "Monolithically Integrated High-β Nanowire Lasers on Silicon," *Nano Lett.*, vol. 16, no. 1, pp. 152–156, Jan. 2016, doi: 10.1021/acs.nanolett.5b03404.

[3] K. Tomioka, J. Motohisa, S. Hara, K. Hiruma, and T. Fukui, "GaAs/AlGaAs Core Multishell Nanowire-Based Light-Emitting Diodes on Si," *Nano Lett.*, vol. 10, no. 5, pp. 1639–1644, 2010, doi: 10.1021/nl9041774.

[4] X. Dai *et al.*, "GaAs/AlGaAs Nanowire Photodetector," *Nano Lett.*, vol. 14, no. 5, pp. 2688–2693, May 2014, doi: 10.1021/nl5006004.

[5] R. R. LaPierre, M. Robson, K. M. Azizur-Rahman, and P. Kuyanov, "A review of III–V nanowire infrared photodetectors and sensors," *J. Phys. D. Appl. Phys.*, vol. 50, no. 12, p. 123001, 2017, doi: 10.1088/1361-6463/aa5ab3.

[6] P. Krogstrup *et al.*, "Single-nanowire solar cells beyond the Shockley-Queisser limit," *Nat Phot.*, vol. 7, no. 4, pp. 306–310, 2013, doi: https://doi.org/10.1038/nphoton.2013.32.

[7] D. Saxena, S. Mokkapati, and C. Jagadish, "Semiconductor Nanolasers," *IEEE Photonics J.*, vol. 4, no. 2, pp. 582–585, 2012, doi: 10.1109/JPHOT.2012.2189201.

[8] T. Hakkarainen *et al.*, "Te incorporation and activation as n-type dopant in self-catalyzed GaAs nanowires," *Phys. Rev. Mater.*, vol. 3, no. 8, p. 86001, Aug. 2019, doi: 10.1103/PhysRevMaterials.3.086001.

[9] A. Y. Cho, M. B. Panish, and I. Hayashi, "Molecular beam epitaxy of

GaAs, AlGaAs and GaP," in *3rd Int. Symp. on Gallium Arsenide and Related Com; The Institute of Physics; Conference Series Number 9*, 1970, pp. 18–29.

[10] S. Franchi, "Molecular beam epitaxy: fundamentals, historical background and future prospects," in *Molecular Beam Epitaxy From Research to Mass Production*, M. Henini, Ed. Oxford: Elsevier, 2013, pp. 1–46, 2013, doi: https://doi.org/10.1088/0022-3727/46/31/313001

[11] A. Y. Cho, "How molecular beam epitaxy (MBE) began and its projection into the future," *J. Cryst. Growth*, vol. 201–202, pp. 1–7, May 1999, doi: 10.1016/S0022-0248(98)01265-2.

[12] F. Jabeen, S. Rubini, and F. Martelli, "Growth of III–V semiconductor nanowires by molecular beam epitaxy," *Microelectronics J.*, vol. 40, no. 3, pp. 442–445, 2009, doi: //dx.doi.org/10.1016/j.mejo.2008.06.001.

[13] V. V Preobrazhenskii, M. A. Putyato, O. P. Pchelyakov, and B. R. Semyagin, "Experimental determination of the incorporation factor of As4 during molecular beam epitaxy of GaAs," *J. Cryst. Growth*, vol. 201–202, pp. 170–173, May 1999, doi: 10.1016/S0022-0248(98)01308-6.

[14] E. S. Tok, J. H. Neave, J. Zhang, B. A. Joyce, and T. S. Jones, "Arsenic incorporation kinetics in GaAs(001) homoepitaxy revisited," *Surf. Sci.*, vol. 374, no. 1–3, pp. 397–405, Mar. 1997, doi: 10.1016/S0039-6028(97)01241-7.

[15] I. George, F. Becagli, H. Y. Liu, J. Wu, M. Tang, and R. Beanland, "Dislocation filters in GaAs on Si," *Semicond. Sci. Technol.*, vol. 30, no. 11, p. 114004, 2015, doi: 10.1088/0268-1242/30/11/114004.

[16] M. Henini, Ed., *Molecular Beam Epitaxy: From research to mass production*. Elsevier, 2013, doi: //dx.doi.org/10.1016/B978-0-12-387839-7.00001-4

[17] J. Puustinen, J. Hilska, and M. Guina, "Analysis of GaAsBi growth regimes in high resolution with respect to As/Ga ratio using stationary MBE growth," *J. Cryst. Growth*, vol. 511, pp. 33–41, 2019, doi: https://doi.org/10.1016/j.jcrysgro.2019.01.010.

[18] R. S. Wagner and W. C. Ellis, "Vapor-Liquid-Solid Mechanism of Single Crystal Growth," *Appl. Phys. Lett.*, vol. 4, no. 5, pp. 89–90, 1964, doi: //dx.doi.org/10.1063/1.1753975.

[19] C. B. Collins, R. O. Carlson, and C. J. Gallagher, "Properties of Gold-Doped Silicon," *Phys. Rev.*, vol. 105, no. 4, pp. 1168–1173, 1957, doi: https://doi.org/10.1103/PhysRev.105.1168.

[20] M. Hill, M. Lietz, and R. Sittig, "Diffusion of Gold in Silicon," *J. Electrochem. Soc.*, vol. 129, no. 7, pp. 1579–1587, Jul. 1982, doi: 10.1149/1.2124212.

[21] M. Hata, A. Watanabe, and T. Isu, "Surface diffusion length observed by in situ scanning microprobe reflection high-energy electron diffraction," *J. Cryst. Growth*, vol. 111, no. 1, pp. 83–87, 1991, doi: https://doi.org/10.1016/0022-0248(91)90951-Z.

[22] S. J. Gibson and R. R. LaPierre, "Model of patterned self-assisted nanowire growth," *Nanotechnology*, vol. 25, no. 41, p. 415304, 2014, doi: 10.1088/0957-4484/25/41/415304.

[23] F. Oehler, A. Cattoni, A. Scaccabarozzi, G. Patriarche, F. Glas, and J.-C. Harmand, "Measuring and Modeling the Growth Dynamics of Self-Catalyzed GaP Nanowire Arrays," *Nano Lett.*, vol. 18, no. 2, pp. 701–708, Feb. 2018, doi: 10.1021/acs.nanolett.7b03695.

[24] P. Krogstrup *et al.*, "Advances in the theory of III–V nanowire growth dynamics," *J. Phys. D. Appl. Phys.*, vol. 46, no. 31, p. 313001, 2013, doi: https://doi.org/10.1088/0022-3727/46/31/313001.

[25] M. Shibata, S. S. Stoyanov, and M. Ichikawa, "Selective growth of nanometer-scale Ga dots on Si(111) surface windows formed in an ultrathin SiO2 film," *Phys. Rev. B*, vol. 59, no. 15, pp. 10289–10295, Apr. 1999, doi: 10.1103/PhysRevB.59.10289.

[26] D. Rudolph *et al.*, "Direct Observation of a Noncatalytic Growth Regime for GaAs Nanowires," *Nano Lett.*, vol. 11, no. 9, pp. 3848–3854, 2011, doi: 10.1021/nl2019382.

[27] V. Pankoke, S. Sakong, and P. Kratzer, "Role of sidewall diffusion in GaAs nanowire growth: A first-principles study," *Phys. Rev. B*, vol. 86, no. 8, p. 85425, Aug. 2012, doi: 10.1103/PhysRevB.86.085425.

[28] J. N. Shapiro, A. Lin, D. L. Huffaker, and C. Ratsch, "Potential energy surface of In and Ga adatoms above the (111)A and (110) surfaces of a

GaAs nanopillar," *Phys. Rev. B*, vol. 84, no. 8, p. 85322, Aug. 2011, doi: 10.1103/PhysRevB.84.085322.

[29] D. Ren *et al.*, "New Insights into the Origins of Sb-Induced Effects on Self-Catalyzed GaAsSb Nanowire Arrays," *Nano Lett.*, vol. 16, no. 2, pp. 1201–1209, 2016, doi: 10.1021/acs.nanolett.5b04503.

[30] M. R. Ramdani, J. C. Harmand, F. Glas, G. Patriarche, and L. Travers, "Arsenic Pathways in Self-Catalyzed Growth of GaAs Nanowires," *Cryst. Growth Des.*, vol. 13, no. 1, pp. 91–96, 2013, doi: 10.1021/cg301167g.

[31] V. G. Dubrovskii, Y. Berdnikov, and N. V Sibirev, "Regimes of radial growth for Ga-catalyzed GaAs nanowires," *Appl. Phys. A*, vol. 122, no. 7, p. 671, 2016, doi: 10.1007/s00339-016-0179-4.

[32] J. Tersoff, "Stable self-catalyzed growth of III-V nanowires," *Nano Lett*, vol. 15, no. 10, pp. 6609-6613, Sept. 2015, doi: 10.1021/acs.nanolett.5b02386.

[33] F. Panciera *et al.*, "Phase Selection in Self-catalyzed GaAs Nanowires," *Nano Lett.*, vol. 20, no. 3, pp. 1669–1675, Mar. 2020, doi: 10.1021/acs.nanolett.9b04808.

[34] F. Glas, J.-C. Harmand, and G. Patriarche, "Why Does Wurtzite Form in Nanowires of III-V Zinc Blende Semiconductors?," *Phys. Rev. Lett.*, vol. 99, no. 14, p. 146101, 2007, doi: https://doi.org/10.1103/PhysRevLett.99.146101.

[35] T. Ito and T. Akiyama, "Recent Progress in Computational Materials Science for Semiconductor Epitaxial Growth," *Crystals*, vol. 7, no. 2, p. 46, 2017, doi: https://doi.org/10.3390/cryst7020046.

[36] C. Colombo, D. Spirkoska, M. Frimmer, G. Abstreiter, and A. Fontcuberta i Morral, "Ga-assisted catalyst-free growth mechanism of GaAs nanowires by molecular beam epitaxy," *Phys. Rev. B*, vol. 77, no. 15, p. 155326, 2008, doi: https://doi.org/10.1103/PhysRevB.77.155326.

[37] S. Suomalainen *et al.*, "Te-doping of self-catalyzed GaAs nanowires," *Appl. Phys. Lett.*, vol. 107, no. 1, p. 12101, 2015, doi: //dx.doi.org/10.1063/1.4926494.

[38] A. M. Munshi *et al.*, "Position-Controlled Uniform GaAs Nanowires on Silicon using Nanoimprint Lithography," *Nano Lett.*, vol. 14, no. 2, pp. 960–966, 2014, doi: 10.1021/nl404376m.

[39] K. Tomioka, T. Tanaka, S. Hara, K. Hiruma, and T. Fukui, "III–V Nanowires on Si Substrate: Selective-Area Growth and Device Applications," *Sel. Top. Quantum Electron. IEEE J.*, vol. 17, no. 4, pp. 1112–1129, 2011, doi: 10.1109/JSTQE.2010.2068280.

[40] S. Hertenberger, D. Rudolph, M. Bichler, J. J. Finley, G. Abstreiter, and G. Koblmüller, "Growth kinetics in position-controlled and catalyst-free InAs nanowire arrays on Si(111) grown by selective area molecular beam epitaxy," *J. Appl. Phys.*, vol. 108, no. 11, p. 114316, 2010, doi: //dx.doi.org/10.1063/1.3525610.

[41] V. G. Dubrovskii *et al.*, "Self-equilibration of the diameter of Ga-catalyzed GaAs nanowires," *Nano Lett*, vol. 15, no. 8, pp. 5580-5584, 2015, doi: 10.1021/acs.nanolett.5b02226.

[42] S. Plissard, G. Larrieu, X. Wallart, and P. Caroff, "High yield of self-catalyzed GaAs nanowire arrays grown on silicon via gallium droplet positioning," *Nanotechnology*, vol. 22, no. 27, p. 275602, 2011, doi: 10.1088/0957-4484/22/27/275602.

[43] J. Vukajlovic-Plestina *et al.*, "Fundamental aspects to localize self-catalyzed III-V nanowires on silicon," *Nat. Commun.*, vol. 10, no. 1, p. 869, 2019, doi: 10.1038/s41467-019-08807-9.

[44] S. L. Tan, Y. Genuist, M. I den Hertog, E. Bellet-Amalric, H. Mariette, and N. T. Pelekanos, "Highly uniform zinc blende GaAs nanowires on Si(111) using a controlled chemical oxide template," *Nanotechnology*, vol. 28, no. 25, p. 255602, 2017, doi: https://doi.org/10.1088/1361-6528/aa7169.

[45] P. Krogstrup, R. Popovitz-Biro, E. Johnson, M. H. Madsen, J. Nygård, and H. Shtrikman, "Structural Phase Control in Self-Catalyzed Growth of GaAs Nanowires on Silicon (111)," *Nano Lett.*, vol. 10, no. 11, pp. 4475–4482, 2010, doi: 10.1021/nl102308k.

[46] T. Tauchnitz *et al.*, "Decoupling the Two Roles of Ga Droplets in the Self-Catalyzed Growth of GaAs Nanowires on SiOx/Si(111) Substrates,"

Cryst. Growth Des., vol. 17, no. 10, pp. 5276–5282, 2017, doi: 10.1021/acs.cgd.7b00797.

[47] T. Tauchnitz, Y. Berdnikov, V. G. Dubrovskii, H. Schneider, M. Helm, and E. Dimakis, "A simple route to synchronized nucleation of self-catalyzed GaAs nanowires on silicon for sub-Poissonian length distributions," *Nanotechnology*, vol. 29, no. 50, p. 504004, 2018, doi: 10.1088/1361-6528/aae361.

[48] C. Somaschini *et al.*, "Control over the Number Density and Diameter of GaAs Nanowires on Si(111) Mediated by Droplet Epitaxy," *Nano Lett.*, vol. 13, no. 8, pp. 3607–3613, 2013, doi: 10.1021/nl401404w.

[49] S. Bietti *et al.*, "Self-assisted GaAs nanowires with selectable number density on Silicon without oxide layer," *J. Phys. D. Appl. Phys.*, vol. 47, no. 39, p. 394002, 2014, doi: https://doi.org/10.1088/0022-3727/47/39/394002.

[50] T. V Hakkarainen, A. Schramm, J. Mäkelä, P. Laukkanen, and M. Guina, "Lithography-free oxide patterns as templates for self-catalyzed growth of highly uniform GaAs nanowires on Si(111)," *Nanotechnology*, vol. 26, no. 27, p. 275301, 2015, doi: https://doi.org/10.1088/0957-4484/26/27/275301.

[51] C. Somaschini, S. Bietti, N. Koguchi, F. Montalenti, C. Frigeri, and S. Sanguinetti, "Self-assembled GaAs islands on Si by droplet epitaxy," *Appl. Phys. Lett.*, vol. 97, no. 5, p. 53101, 2010, doi: //dx.doi.org/10.1063/1.3475923.

[52] S. Sanguinetti and N. Koguchi, "Chapter 4 - Droplet epitaxy of nanostructures," in *Molecular Beam Epitaxy From Research to Mass Production*, M. Henini, Ed. 1, Oxford: Elsevier, pp. 95–111, 2013, doi: //dx.doi.org/10.1016/B978-0-12-387839-7.00004-X

[53] E. Koivusalo, "Epitaxial III-V semiconductor nanowires," 2016.

[54] G. Priante, G. Patriarche, F. Oehler, F. Glas, and J.-C. Harmand, "Abrupt GaP/GaAs Interfaces in Self-Catalyzed Nanowires," *Nano Lett.*, vol. 15, no. 9, pp. 6036–6041, 2015, doi: 10.1021/acs.nanolett.5b02224.

[55] Y. Zhang, M. Aagesen, J. V Holm, H. I. JÃ¸rgensen, J. Wu, and H. Liu,

"Self-Catalyzed GaAsP Nanowires Grown on Silicon Substrates by Solid-Source Molecular Beam Epitaxy," *Nano Lett.*, vol. 13, no. 8, pp. 3897–3902, 2013, doi: 10.1021/nl401981u.

[56] B. Mandl *et al.*, "Growth Mechanism of Self-Catalyzed Group III-V Nanowires," *Nano Lett.*, vol. 10, no. 11, pp. 4443–4449, 2010, doi: 10.1021/nl1022699.

[57] E. Dimakis *et al.*, "Self-Assisted Nucleation and Vapor-Solid Growth of InAs Nanowires on Bare Si(111)," *Cryst. Growth Des.*, vol. 11, no. 9, pp. 4001–4008, 2011, doi: 10.1021/cg200568m.

[58] T. Grap, T. Rieger, C. Blömers, T. Schäpers, D. Grützmacher, and M. I. Lepsa, "Self-catalyzed VLS grown InAs nanowires with twinning superlattices," *Nanotechnology*, vol. 24, no. 33, p. 335601, 2013, doi: 10.1088/0957-4484/24/33/335601.

[59] T. Rieger, D. Grützmacher, and M. I. Lepsa, "Si substrate preparation for the VS and VLS growth of InAs nanowires," *Phys. status solidi – Rapid Res. Lett.*, vol. 7, no. 10, pp. 840–844, Oct. 2013, doi: 10.1002/pssr.201307229.

[60] U. P. Gomes *et al.*, "Nucleation and growth mechanism of self-catalyzed InAs nanowires on silicon," *Nanotechnology*, vol. 27, no. 25, p. 255601, 2016, doi: 10.1088/0957-4484/27/25/255601.

[61] M. Federico, V. G. Dubrovskii, D. Rüffer, G. Tütüncüoğlu, Y. Fontana, and I. M. A. Fontcuberta, "Tailoring the diameter and density of self-catalyzed GaAs nanowires on silicon," *Nanotechnology*, vol. 26, no. 10, p. 105603, 2015, doi: https://doi.org/10.1088/0957-4484/26/10/105603.

[62] V. G. Dubrovskii, "Length distributions of nanowires: Effects of surface diffusion versus nucleation delay," *J. Cryst. Growth*, vol. 463, pp. 139–144, 2017, doi: https://doi.org/10.1016/j.jcrysgro.2017.02.014.

[63] E. Russo-Averchi *et al.*, "Suppression of three dimensional twinning for a 100% yield of vertical GaAs nanowires on silicon," *Nanoscale*, vol. 4, no. 5, pp. 1486–1490, 2012, doi: 10.1039/C2NR11799A.

[64] C. García Núñez, A. F. Braña, N. López, and B. J. García, "GaAs nanowires grown by Ga-assisted chemical beam epitaxy: Substrate preparation and growth kinetics," *J. Cryst. Growth*, vol. 430, pp. 108–115,

Nov. 2015, doi: 10.1016/J.JCRYSGRO.2015.08.008.

[65] F. Matteini, G. Tütüncüoglu, H. Potts, F. Jabeen, and A. Fontcuberta i Morral, "Wetting of Ga on SiOx and Its Impact on GaAs Nanowire Growth," *Cryst. Growth Des.*, vol. 15, no. 7, pp. 3105–3109, Jul. 2015, doi: 10.1021/acs.cgd.5b00374.

[66] F. Matteini, G. Tütüncüoğlu, D. Rüffer, E. Alarcón-Lladó, and A. F. i Morral, "Ga-assisted growth of GaAs nanowires on silicon, comparison of surface SiOx of different nature," *J. Cryst. Growth*, vol. 404, pp. 246–255, 2014, doi: //dx.doi.org/10.1016/j.jcrysgro.2014.07.034.

[67] S. J. Gibson, J. P. Boulanger, and R. R. LaPierre, "Opportunities and pitfalls in patterned self-catalyzed GaAs nanowire growth on silicon," *Semicond. Sci. Technol.*, vol. 28, no. 10, p. 105025, 2013, doi: 10.1088/0268-1242/28/10/105025.

[68] E. Russo-Averchi *et al.*, "High Yield of GaAs Nanowire Arrays on Si Mediated by the Pinning and Contact Angle of Ga," *Nano Lett.*, vol. 15, no. 5, pp. 2869–2874, May 2015, doi: 10.1021/nl504437v.

[69] H. Küpers *et al.*, "Surface preparation and patterning by nano imprint lithography for the selective area growth of GaAs nanowires on Si(111)," *Semicond. Sci. Technol.*, vol. 32, no. 11, p. 115003, 2017, doi: 10.1088/1361-6641/aa8c15.

[70] E. Uccelli *et al.*, "Three-Dimensional Multiple-Order Twinning of Self-Catalyzed GaAs Nanowires on Si Substrates," *Nano Lett.*, vol. 11, no. 9, pp. 3827–3832, 2011, doi: 10.1021/nl201902w.

[71] F. Matteini *et al.*, "Impact of the Ga Droplet Wetting, Morphology, and Pinholes on the Orientation of GaAs Nanowires," *Cryst. Growth Des.*, vol. 16, no. 10, pp. 5781–5786, Oct. 2016, doi: 10.1021/acs.cgd.6b00858.

[72] T. Akiyama, K. Sano, K. Nakamura, and T. Ito, "An Empirical Potential Approach to Wurtzite-Zinc-Blende Polytypism in Group III-V Semiconductor Nanowires," *Jpn. J. Appl. Phys.*, vol. 45, no. No. 9, pp. L275–L278, 2006, doi: 10.1143/jjap.45.l275.

[73] R. Leitsmann and F. Bechstedt, "Surface influence on stability and structure of hexagon-shaped III-V semiconductor nanorods," *J. Appl.*

Phys., vol. 102, no. 6, p. 63528, Sep. 2007, doi: 10.1063/1.2783899.

[74] V. G. Dubrovskii *et al.*, "Gibbs-Thomson and diffusion-induced contributions to the growth rate of Si, InP, and GaAs nanowires," *Phys. Rev. B*, vol. 79, no. 20, p. 205316, May 2009, doi: 10.1103/PhysRevB.79.205316.

[75] F. Glas, M. R. Ramdani, G. Patriarche, and J.-C. Harmand, "Predictive modeling of self-catalyzed III-V nanowire growth," *Phys. Rev. B*, vol. 88, no. 19, p. 195304, 2013, doi: //doi.org/10.1103/PhysRevB.88.195304.

[76] D. Jacobsson *et al.*, "Interface dynamics and crystal phase switching in GaAs nanowires," *Nature*, vol. 531, p. 317, 2016, doi: http://dx.doi.org/10.1038/nature17148.

[77] V. G. Dubrovskii, "Self-regulated pulsed nucleation in catalyzed nanowire growth," *Phys Rev B*, vol. 87, 2013, doi: 10.1103/PhysRevB.87.195426.

[78] F. Glas, J. Harmand, and G. Patriarche, "Nucleation antibunching in catalyst-assisted nanowire growth," *Phys Rev Lett*, vol. 104, no 13, p. 135501, 2010, doi: 10.1103/PhysRevLett.104.135501.

[79] V. G. Dubrovskii, "Development of Growth Theory for Vapor–Liquid–Solid Nanowires: Contact Angle, Truncated Facets, and Crystal Phase," *Cryst. Growth Des.*, vol. 17, no. 5, pp. 2544–2548, 2017, doi: 10.1021/acs.cgd.7b00076.

[80] F. Glas, "Statistics of sub-Poissonian nucleation in a nanophase," *Phys Rev B*, vol. 90, 2014, doi: 10.1103/PhysRevB.90.125406.

[81] N. V Sibirev, "Statistics of nucleation associated with the growth of whisker nanocrystals," *Tech. Phys. Lett.*, vol. 39, no. 7, pp. 660–663, 2013, doi: 10.1134/S1063785013070237.

[82] V. G. Dubrovskii, *Nucleation Theory and Growth of Nanostructures*. Springer, Berlin, Heidelberg, 2013, doi: https://doi.org/10.1007/978-3-642-39660-1

[83] N. Moll, A. Kley, E. Pehlke, and M. Scheffler, "GaAs equilibrium crystal shape from first principles," *Phys. Rev. B*, vol. 54, no. 12, pp. 8844–8855, 1996, doi: 10.1103/PhysRevB.54.8844.

[84] A. D. Gamalski, C. Ducati, and S. Hofmann, "Cyclic Supersaturation and Triple Phase Boundary Dynamics in Germanium Nanowire Growth," *J. Phys. Chem. C*, vol. 115, no. 11, pp. 4413–4417, Mar. 2011, doi: 10.1021/jp1095882.

[85] C.-Y. Wen *et al.*, "Periodically Changing Morphology of the Growth Interface in Si, Ge, and GaP Nanowires," *Phys. Rev. Lett.*, vol. 107, no. 2, p. 25503, Jul. 2011, doi: 10.1103/PhysRevLett.107.025503.

[86] S. H. Oh *et al.*, "Oscillatory Mass Transport in Vapor-Liquid-Solid Growth of Sapphire Nanowires," *Science (80-.).*, vol. 330, no. 6003, pp. 489 LP – 493, Oct. 2010, doi: 10.1126/science.1190596.

[87] C. B. Maliakkal *et al.*, "In situ analysis of catalyst composition during gold catalyzed GaAs nanowire growth," *Nat. Commun.*, vol. 10, no. 1, p. 4577, 2019, doi: 10.1038/s41467-019-12437-6.

[88] C. B. Maliakkal *et al.*, "Independent Control of Nucleation and Layer Growth in Nanowires," *ACS Nano*, vol. 14, no. 4, pp. 3868–3875, Apr. 2020, doi: 10.1021/acsnano.9b09816.

[89] M. Tornberg, C. B. Maliakkal, D. Jacobsson, K. A. Dick, and J. Johansson, "Limits of III–V Nanowire Growth Based on Droplet Dynamics," *J. Phys. Chem. Lett.*, vol. 11, no. 8, pp. 2949–2954, Apr. 2020, doi: 10.1021/acs.jpclett.0c00387.

[90] G. E. Cirlin *et al.*, "Self-catalyzed, pure zincblende GaAs nanowires grown on Si(111) by molecular beam epitaxy," *Phys. Rev. B*, vol. 82, no. 3, p. 35302, 2010, doi: 10.1103/PhysRevB.82.035302.

[91] F. M. Ross, J. Tersoff, and M. C. Reuter, "Sawtooth Faceting in Silicon Nanowires," *Phys. Rev. Lett.*, vol. 95, no. 14, p. 146104, Sep. 2005, doi: 10.1103/PhysRevLett.95.146104.

[92] R. E. Algra *et al.*, "Twinning superlattices in indium phosphide nanowires," *Nature*, vol. 456, no. 7220, pp. 369–372, 2008, doi: 10.1038/nature07570.

[93] N. I. Goktas, A. Sokolovskii, V. G. Dubrovskii, and R. R. LaPierre, "Formation Mechanism of Twinning Superlattices in Doped GaAs Nanowires," *Nano Lett.*, vol. 20, no. 5, pp. 3344–3351, Apr. 2020, doi:

10.1021/acs.nanolett.0c00240.

[94] E. Ahmad *et al.*, "Te incorporation in GaAs1−xSbxnanowires and p-i-n axial structure," *Semicond. Sci. Technol.*, vol. 31, no. 12, p. 125001, 2016, doi: 10.1088/0268-1242/31/12/125001.

[95] Y. Zhang *et al.*, "Doping of Self-Catalyzed Nanowires under the Influence of Droplets," *Nano Lett.*, vol. 18, no. 1, pp. 81–87, 2017, doi: 10.1021/acs.nanolett.7b03366.

[96] V. G. Dubrovskii, "Fluctuation-induced spreading of size distribution in condensation kinetics," *J. Chem. Phys.*, vol. 131, no. 16, p. 164514, Oct. 2009, doi: 10.1063/1.3254384.

[97] F. Bastiman, H. Küpers, C. Somaschini, V. G. Dubrovskii, and L. Geelhaar, "Analysis of incubation time preceding the Ga-assisted nucleation and growth of GaAs nanowires on Si(111)," *Phys. Rev. Mater.*, vol. 3, no. 7, p. 73401, Jul. 2019, doi: 10.1103/PhysRevMaterials.3.073401.

[98] C. Sartel, D. L. Dheeraj, F. Jabeen, and J. C. Harmand, "Effect of arsenic species on the kinetics of GaAs nanowires growth by molecular beam epitaxy," *Journal of Crystal Growth*, vol. 312, no. 14. pp. 2073–2077, 2010, doi: //doi.org/10.1016/j.jcrysgro.2010.04.027.

[99] B. A. Tok, E.S.; Neave, J.H.; Allegretti, F.E.; Zhang, J.; Jones, T-S-; Joyce, "Incorporation kinetics of As2 and As4 on GaAs (110)," *Surface science*, vol. 371, no. 2–3. North-Holland Pub Co, Amsterdam :, p. 277, 1997, doi: 10.1016/S0039-6028(96)01085-0.

[100] F. Krizek *et al.*, "Growth of InAs Wurtzite Nanocrosses from Hexagonal and Cubic Basis," *Nano Lett.*, vol. 17, no. 10, pp. 6090–6096, 2017, doi: 10.1021/acs.nanolett.7b02604.

[101] S. Gazibegovic *et al.*, "Epitaxy of advanced nanowire quantum devices," *Nature*, vol. 548, p. 434, 2017, doi: https://doi.org/10.1038/nature23468.

[102] E. Billig, "Growth of monocrystals of germanium from an undercooled melt," *Proc. R. Soc. London.Series A.Mathematical Phys. Sci.*, vol. 229, no. 1178, pp. 346–363, 1955, doi: 10.1098/rspa.1955.0090.

[103] D. R. Hamilton and R. G. Seidensticker, "Propagation Mechanism of

Germanium Dendrites," *J. Appl. Phys.*, vol. 31, no. 7, pp. 1165–1168, 1960, doi: 10.1063/1.1735796.

[104] A. J. Shahani and P. W. Voorhees, "Twin-mediated crystal growth," *J. Mater. Res.*, vol. 31, no. 19, pp. 2936–2947, 2016, doi: 10.1557/jmr.2016.308.

[105] A. D. Gamalski, P. W. Voorhees, C. Ducati, R. Sharma, and S. Hofmann, "Twin Plane Re-entrant Mechanism for Catalytic Nanowire Growth," *Nano Lett.*, vol. 14, no. 3, pp. 1288–1292, 2014, doi: 10.1021/nl404244u.

[106] D. S. Oliveira *et al.*, "Interaction between lamellar twinning and catalyst dynamics in spontaneous core–shell InGaP nanowires," *Nanoscale*, vol. 7, no. 29, pp. 12722–12727, 2015, doi: 10.1039/C5NR02747K.

[107] A. Casadei *et al.*, "Doping incorporation paths in catalyst-free Be-doped GaAs nanowires," *Appl. Phys. Lett.*, vol. 102, no. 1, p. 13117, 2013, doi: 10.1063/1.4772020.

[108] M. H. T. Dastjerdi *et al.*, "Three-fold Symmetric Doping Mechanism in GaAs Nanowires," *Nano Lett.*, vol. 17, no. 10, pp. 5875–5882, Oct. 2017, doi: 10.1021/acs.nanolett.7b00794.

[109] V. G. Dubrovskii, H. Hijazi, N. I. Goktas, and R. R. LaPierre, "Be, Te, and Si Doping of GaAs Nanowires: Theory and Experiment," *J. Phys. Chem. C*, Jul. 2020, doi: 10.1021/acs.jpcc.0c04061.

[110] M. Rizzo Piton *et al.*, "Optimization of Ohmic Contacts to p-GaAs Nanowires," *Nanoscale Res. Lett.*, vol. 14, no. 1, p. 344, 2019, doi: 10.1186/s11671-019-3175-8.

[111] M. Rizzo Piton, "Development of Semiconductor Nanowire Materials for Electronic and Photonic Applications," Tampere University, 2019.

[112] T. F. Kelly and M. K. Miller, "Atom probe tomography," *Rev. Sci. Instrum.*, vol. 78, no. 3, p. 31101, Mar. 2007, doi: 10.1063/1.2709758.

[113] S. V Ivanov, P. S. Kop'ev, and N. N. Ledentsov, "Interplay of beryllium segregation and diffusion in heavily doped GaAs and AlGaAs grown by molecular beam epitaxy (thermodynamic analysis)," *J. Cryst. Growth*, vol. 108, no. 3, pp. 661–669, 1991, doi: https://doi.org/10.1016/0022-

0248(91)90246-2.

[114] M. Hilse, M. Ramsteiner, S. Breuer, L. Geelhaar, and H. Riechert, "Incorporation of the dopants Si and Be into GaAs nanowires," *Appl. Phys. Lett.*, vol. 96, no. 19, p. 193104, 2010, doi: 10.1063/1.3428358.

[115] H. Hijazi *et al.*, "Si Doping of Vapor–Liquid–Solid GaAs Nanowires: n-Type or p-Type?," *Nano Lett.*, vol. 19, no. 7, pp. 4498–4504, Jul. 2019, doi: 10.1021/acs.nanolett.9b01308.

[116] D. M. Collins, J. N. Miller, Y. G. Chai, and R. Chow, "Sn and Te doping of molecular beam epitaxial GaAs using a SnTe source," *J. Appl. Phys.*, vol. 53, no. 4, pp. 3010–3018, Apr. 1982, doi: 10.1063/1.331042.

[117] I. Vurgaftman, J. R. Meyer, and L. Ram-Mohan, "Band parameters for III-V compound semiconductors and their alloys," *J Appl Phys*, vol. 89, no. 11, pp. 5815-5875, 2001, doi: 10.1063/1.1368156.

[118] P. Deshmukh, M. Sharma, S. Nalamati, C. L. Reynolds, Y. Liu, and S. Iyer, "Molecular beam epitaxial growth of high quality Ga-catalyzed GaAs1–x Sb x (x > 0.8) nanowires on Si (111) with photoluminescence emission reaching 1.7 μm," *Semicond. Sci. Technol.*, vol. 33, no. 12, p. 125007, 2018, doi: 10.1088/1361-6641/aae7b8.

[119] E. Alarcón-Lladó, S. Conesa-Boj, X. Wallart, P. Caroff, and A. Fontcuberta i Morral, "Raman spectroscopy of self-catalyzed GaAs 1− x Sb x nanowires grown on silicon," *Nanotechnology*, vol. 24, no. 40, p. 405707, 2013, doi: https://doi.org/10.1088/0957-4484/24/40/405707.

[120] L. Li *et al.*, "Near Full-Composition-Range High-Quality GaAs1–xSbx Nanowires Grown by Molecular-Beam Epitaxy," *Nano Lett.*, vol. 17, no. 2, pp. 622–630, Feb. 2017, doi: 10.1021/acs.nanolett.6b03326.

[121] R. Kaspi and K. R. Evans, "Sb-surface segregation and the control of compositional abruptness at the GaAsSb/GaAs interface," *Journal of Crystal Growth*, vol. 175–176. pp. 838–843, 1997, doi: //doi.org/10.1016/S0022-0248(96)00948-7.

[122] J. Huh *et al.*, "Rectifying Single GaAsSb Nanowire Devices Based on Self-Induced Compositional Gradients," *Nano Lett.*, vol. 15, no. 6, pp. 3709–3715, 2015, doi: 10.1021/acs.nanolett.5b00089.

[123] H. Kauko *et al.*, "Near-surface depletion of antimony during the growth of GaAsSb and GaAs/GaAsSb nanowires," *J. Appl. Phys.*, vol. 116, no. 14, p. 144303, 2014, doi: 10.1063/1.4896904.

PUBLICATIONS

PUBLICATION 1

Structural investigation of uniform ensembles of self-catalyzed GaAs nanowires fabricated by a lithography-free technique

E. Koivusalo, T. Hakkarainen, and M. Guina

Nanoscale Res. Lett., vol. 12, no. 1, pp. 192, 2017
10.1186/s11671-017-1989-9

Koivusalo et al. Nanoscale Research Letters (2017) 12:192
DOI 10.1186/s11671-017-1989-9

Nanoscale Research Letters

NANO EXPRESS Open Access

Structural Investigation of Uniform Ensembles of Self-Catalyzed GaAs Nanowires Fabricated by a Lithography-Free Technique

Eero Koivusalo*, Teemu Hakkarainen and Mircea Guina

Abstract

Structural analysis of self-catalyzed GaAs nanowires (NWs) grown on lithography-free oxide patterns is described with insight on their growth kinetics. Statistical analysis of templates and NWs in different phases of the growth reveals extremely high-dimensional uniformity due to a combination of uniform nucleation sites, lack of secondary nucleation of NWs, and self-regulated growth under the effect of nucleation antibunching. Consequently, we observed the first evidence of sub-Poissonian GaAs NW length distributions. The high phase purity of the NWs is demonstrated using complementary transmission electron microscopy (TEM) and high-resolution X-ray diffractometry (HR-XRD). It is also shown that, while NWs are to a large extent defect-free with up to 2-μm-long twin-free zincblende segments, low-temperature micro-photoluminescence spectroscopy reveals that the proportion of structurally disordered sections can be detected from their spectral properties.

Keywords: Nanowires, GaAs, Molecular beam epitaxy, Microstructure

Background

Semiconductor nanowires (NWs) offer versatile possibilities for the realization of future electronic and photonic devices. For example, owing to their small footprint, one-dimensional NWs enable integration of highly lattice or thermally mismatched materials on dissimilar substrates [1]. Combination of the excellent optical and electronic properties of III–V semiconductors and low-cost Si platform is technologically very tempting. The development of NW-based technologies has already led to integration of III–V NW-based lasers [2, 3] and light-emitting diodes [4, 5] on Si. Furthermore, the large absorption cross section of NWs can be exploited by NW solar cells [6, 7], or NWs can be used as building blocks for high-mobility transistors [8, 9] and single-photon emitters [10, 11]. To this end, it is important to minimize crystal defects such as polytypism and stacking faults which could affect the device performance. For example, zincblende (ZB)–wurtzite (WZ) interfaces in GaAs NWs have type II band alignment which causes carrier localization along the NW axis and localized recombination at the interfaces [12, 13]. Many applications also require homogeneous NW arrays with narrow size distributions as the NW dimensions significantly affect their optical properties [14, 15] and cause difficulties in device fabrication.

Self-catalyzed NWs are often grown via self-assembled method on porous SiO_x or native-oxide-covered wafers. Disadvantages of this method include coupling of the NW nucleation and growth conditions as well as variations in nucleation time for different NWs, which significantly broadens their size distribution [16, 17]. Furthermore, the wafer-to-wafer variations and non-uniformity of the oxide properties lead to reproducibility issues in the NW growth [18]. Homogeneous NW arrays may be obtained by selective area growth in an array of holes in SiO_x layer formed using for instance nanoimprint [19] or electron beam lithography [14, 20]. However, lithographical techniques require a rather complex substrate preparation procedure while exposing it to various chemicals [19]. To mitigate these issues, we have recently introduced a lithography-

* Correspondence: eero.koivusalo@tut.fi
Optoelectronics Research Centre, Tampere University of Technology, Korkeakoulunkatu 3, FI-33720 Tampere, Finland

free droplet-epitaxy-based method for making Si/SiO_x patterns that allow self-catalyzed growth of highly uniform GaAs NWs [21]. In this letter, we provide detailed insight of the growth process of these NWs based on statistical analysis of feature sizes at different stages of the template fabrication and NW growth. The NW microstructure is then assessed by complementary high-resolution transmission electron microscopy (HR-TEM) and high-resolution X-ray diffraction (HR-XRD) techniques. Furthermore, we investigate the correlation between the structural defects and optical properties and show that the proportion of structurally disordered sections in mostly defect-free NWs increases the fine structure in the low-temperature micro-photoluminescence spectra.

Methods

Self-catalyzed GaAs NWs were grown on lithography-free oxide patterns using molecular beam epitaxy (MBE). The growth method was initiated with droplet epitaxy (DE) of GaAs nanocrystals on oxide-free p-type Si(111) substrates. The native oxide covering the substrates was removed by a dip in aqueous solution of hydrofluoric acid. After the oxide removal, the substrates were immediately transferred to the MBE reactor and degassed at 640 °C prior to Ga droplet formation at 545 °C by deposition of 0.7 monolayers (ML) of Ga with 0.1 ML/s growth rate calibrated for planar GaAs growth on GaAs(001). The droplets were then crystallized into GaAs by exposing them to As_2 flux for 10 min. Subsequently, the templates were removed from the MBE chamber and exposed to air for 18 h in order to form a thin oxide layer on the Si surface. During this time, the nanocrystal density and diameter were characterized by scanning electron microscopy (SEM). The NWs were grown in the second growth step which started with a 30-min thermal annealing at 655 °C for desorbing the GaAs nanocrystals, thus forming a template composed of oxide-free holes on otherwise SiO_x-covered Si(111) surface, which act as nucleation sites for the subsequent NW growth. Further details of the template properties and fabrication process can be found in [21]. A 60-s Ga predeposition at 640 °C with Ga flux corresponding to 0.3 ML/s was performed prior to the NW growth. The NW growth was then initiated in the same substrate temperature by providing an As_2 flux with a V/III ratio of 9. Four samples were grown with NW growth durations of 60, 40, 20, and 5 min, referred as NW1, NW2, NW3, and NW4, respectively. The GaAs nanocrystal densities of the templates used for NW growth were 2×10^8 cm^{-2}. In sample NW1, the growth was terminated by shutting the As_2 and Ga fluxes simultaneously, thus preserving the Ga catalyst droplets, whereas samples NW2, NW3, and NW4 were exposed to As_2-flux during the sample cooldown thus crystallizing the Ga catalyst droplets.

The crystal structure of the NWs in samples NW1 and NW2 was studied using HR-TEM and HR-XRD. Samples NW1 and NW2 were chosen for characterization in order to see the differences between NWs with preserved (NW1) and crystallized (NW2) Ga catalyst droplets.

A photoluminescence (PL) study was conducted in order to see the effect of Ga droplet crystallization and NW size on the optical properties of the NWs. Power-dependent micro-PL measurements were conducted at 10-K temperature using as-grown samples. A 640-nm diode laser with excitation power densities ranging from 0.1 to 960 W/cm^2 was used. The excitation beam spot size was 20 μm meaning that several NWs were excited simultaneously. The PL signal was collected using a 1024×256 pixel CCD detector through a spectrometer. Spatial resolution in one of the lateral directions was obtained by defining pixel rows as individual tracks, while for the other lateral direction, it was given by the slit placed in front of the spectrograph. The resulting spatial resolution was around 500 nm which allowed us to collect PL signal corresponding to an individual NW or few NWs.

Results and Discussion

SEM images of samples NW1–NW4 are shown in Fig. 1. Figure 1a represents sample NW1 that exhibits preserved Ga catalyst droplets; Fig. 1b–d shows samples NW2–NW4, respectively, which have crystallized droplets. The most prominent feature seen in the SEM images is the size uniformity of the NW arrays. This characteristic was further studied analyzing a minimum of 20 NWs from each sample. The length and diameter data of the NWs including the standard deviations are shown in Fig. 2. The growth of NW diameter and length is linear, and the NWs do not exhibit tapered morphology despite the finite radial growth. The standard deviations of the NW length and diameter in sample NW1 are 1.2 and 3.8%, respectively. These distributions are similar [19] or even narrower [22] than the ones obtained via selective area growth. It is noteworthy that the standard deviation of the NW length is around 40 nm for all the samples. Hence, the differences in the NW lengths are formed at a very early stage of the NW growth and can be attributed to differences in reaching the supersaturation condition of different size Ga droplets [23].

In order to further investigate the evolution of NWs throughout the growth process, we determined the statistics for GaAs nanocrystal diameter in the template material (Fig. 3a) and Ga catalyst droplet diameter after 60-s Ga pre-deposition (Fig. 3b), as well as NW and catalyst droplet diameters and NW length of sample NW1 with a 60-min growth duration (Fig. 3c, d), respectively. The catalyst droplet diameters after Ga pre-deposition (Fig. 3b) were

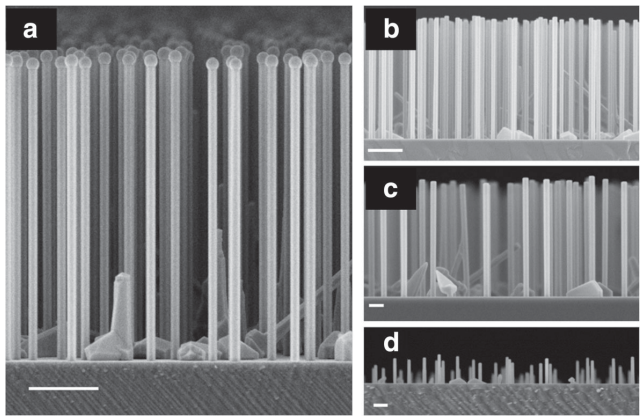

Fig. 1 SEM pictures of samples NW1–NW4 in **a**–**d**, respectively. The *scale bars* are 1 μm in **a**, **b** and 200 nm in **c**, **d**

determined from an additional sample with only pre-deposited Ga droplets, which were grown on a similar template as the NW samples. The densities of GaAs nanocrystal and pre-deposited Ga droplets were determined and found to be equal, which indicates that a Ga droplet is present in all holes in the oxide layer. The standard deviation of the diameter increases in the very beginning of the growth process from 2.3 nm of the pre-deposited Ga droplets (Fig. 3b) to 3.8 nm of the NWs grown for 5 min (NW4, Fig. 2). On the other hand, it can be immediately seen from Fig. 3 that the size distribution remains remarkably narrow throughout the growth process. The diameter of the GaAs nanocrystals is 51 ± 4.9 nm (Fig. 3a). In the beginning of the second growth step, they are thermally desorbed and replaced with Ga catalyst droplets having a diameter of 41 ± 2.3 nm (Fig. 3b), indicating reduction of the diameter distribution between these two stages. This is most likely caused by slight asymmetries observed in the shape of the nanocrystals. It should be also noted that the uncertainty in assessing the feature sizes from SEM pictures is approximately 1–2 nm. In Fig. 3c, d, the distributions of NW diameter and length after a 60-min growth duration are compared to Poissonian distributions

$$F(D, \langle D\rangle) \propto \exp\left[-\frac{(D-\langle D\rangle)^2}{2wD}\right], \tag{1}$$

and

$$F(L, \langle L\rangle) \propto \exp\left[-\frac{(L-\langle L\rangle)^2}{2h\langle L\rangle}\right], \tag{2}$$

where D and L are the NW diameter and length, $\langle\rangle$ denote the mean values, and h and w are the ML thicknesses to the NW growth direction (111) and side facet (110) directions, respectively. The Poissonian standard deviations σ_p for the diameter and length distributions are 5.3 and 37.5 nm, respectively. The diameter distribution (Fig. 3c) is almost Poissonian, whereas the length distribution (Fig. 3d) seems to be sub-Poissonian, thus further demonstrating the homogeneity of the NW length distribution. The inset in Fig. 3d shows a positive correlation of 0.5 between the NW length and droplet diameters after 60 min NW growth.

This data gives new insight into the NW growth kinetics on lithography-free oxide patterns. When the As cracker valve is opened, the droplets start to approach supersaturation and simultaneously compete for the amount of Ga with other droplets within the Ga diffusion length. At this point, the nearest neighbor distance, which is known to affect the NW diameters in site-selective growth [24], controls the Ga diffusion into the droplets. Simultaneously, the Gibbs–Thompson (G-T) effect [23] allows the larger

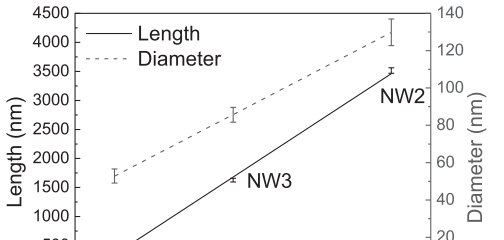

Fig. 2 NW length (*solid line*) and diameter (*dashed line*) data of samples NW2, NW3, and NW4 presented with the standard deviations

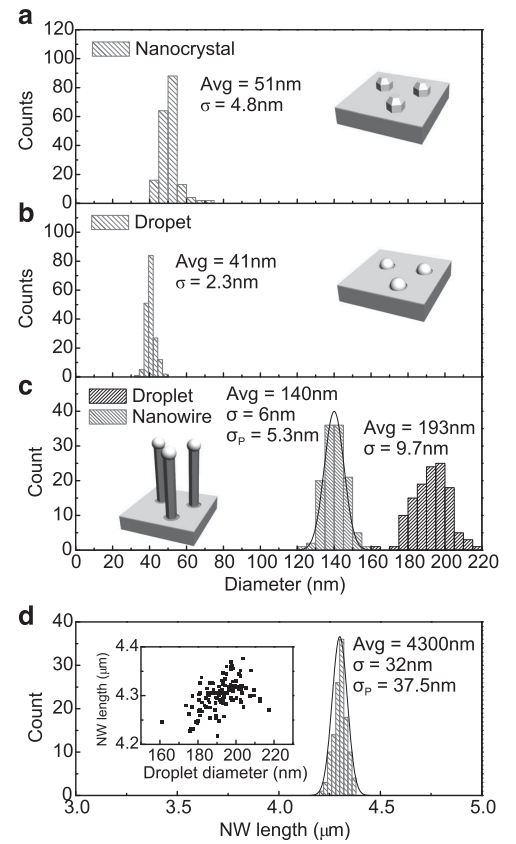

Fig. 3 Size distributions at different steps of the self-catalyzed GaAs NW growth on lithography-free Si/SiOx patterns. **a** Diameter of the GaAs nanocrystals grown on oxide-free Si(111) by droplet epitaxy. **b** Diameter of the Ga catalyst droplets deposited in oxide-free areas formed by thermal desorption of the GaAs nanocrystals. **c** Diameter of the NWs with a Poissonian fit and Ga catalyst droplet diameters after a 60-min growth duration of sample NW1. **d** NW length of sample NW1 with a Poissonian fit after a 60-min growth duration. The measured and calculated Poissonian standard deviations are denoted by σ and σ_P, respectively. The inset in **d** shows the correlation between NW length and Ga catalyst droplet diameter

droplets to supersaturate and start nucleating at lower As concentrations thus elongating them faster which leads to the initial NW size distribution. The droplets have a tendency to self-equilibrate their size distributions in certain growth conditions. This is because the Ga adatom diffusion length along the NW sidewall starts to limit the growth rate of long NWs faster than of short NWs. This partially cancels the G-T effect, which is observed as the correlation between NW length and catalyst droplet diameter (Fig. 3c, d) and could lead to constant length distributions throughout the whole NW growth as seen in Figs. 2 and 3d [24]. However, the self-equilibration process [25] offers only partial description of the growth kinetics of our NWs as it does not explain the finite sidewall growth. The linear growth of the NW length indicates that the growth occurs by random nucleation of monolayers, which is expected to induce Poissonian length distributions [26, 27]. However, the length distributions seem to be sub-Poissonian, which has not been demonstrated before either for self-catalyzed or Au-catalyzed NWs. Moreover, demonstrations of even Poissonian length distributions are limited to Au-catalyzed InAs NWs [28, 29] making this the first demonstration of sub-Poissonian length distribution in epitaxial III–As NWs. The sub-Poissonian distribution is attributed to self-regulated growth caused by nucleation antibunching where the nucleation of each ML consumes a significant amount of group V species from the droplet inducing a temporal anticorrelation between the nucleation events. This allows growth in self-regulated mode, which is expected to result in sub-Poissonian length distributions [26, 30, 31]. The constant and sub-Poissonian standard deviation of the NW length distribution indicates that the remarkable uniformity of the GaAs NWs grown on lithography-free Si/SiOx patterns is a result of (i) uniformity of the nucleation sites created by the DE of GaAs nanocrystals, spontaneous oxidation, and thermal desorption, (ii) lack of secondary nucleation, and (iii) growth under self-regulation caused by nucleation antibunching.

The crystal structure of NWs was studied by TEM to further understand the growth process. TEM images of a NW with preserved Ga droplets of sample NW1 are shown in Fig. 4. In the bottom part of the NW (Fig. 4b, c), a short, typically less than 150-nm-long section of stacking faults and polytypism is observed. It is followed by a remarkably long, up to 2 μm, section of completely twin-free ZB GaAs (Fig. 4d). The phase pure ZB ends to a section with sparse twin planes until the top of the NW (Fig. 4e). Furthermore, a short WZ segment is found just under the Ga droplets. The disordered section in the bottom part of the NW is formed during the beginning of the NW growth, which may be related to Ga pre-deposition. This assumption is supported by other reports of NWs with similar base structure and rather long Ga pre-deposition times [19] and the absence of the stacking faults when NWs are grown without Ga pre-deposition, or in short, under 5-s Ga pre-deposition is used [17, 32]. The 2-μm phase pure ZB segments show the excellent crystal quality of our NWs, even though longer ZB segments can be obtained by growing NWs under conditions which prefer growth of thinner NWs [33]. The twin plane formation after the phase pure ZB can be attributed to lateral NW growth. The contact angle between the Ga

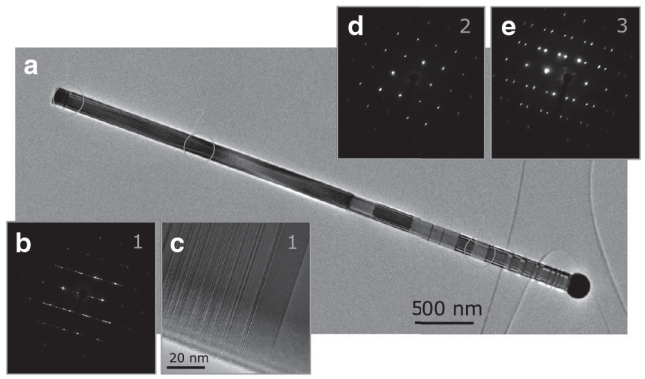

Fig. 4 TEM images of sample NW1. **a** HR-TEM low-magnification overview. **b**, **c** SAED pattern and HR-TEM micrograph of the disordered section at the root of the wire. **d** SAED pattern of the pure ZB section. **e** SAED pattern of the twinned ZB section

droplet and solid NW tip decreases towards 90°, and the spreading of the droplet over the edges of the NW tip reduces as the NW diameter grows. This is known to increase probability of nucleation at triple phase line which induces twin planes. Thus, more and more twinning is seen in the uppermost part of the NW [17, 34–36]. The WZ segment under the catalyst droplet, as the one seen in Fig. 4, is a typical feature in self-catalyzed GaAs NWs. It is associated with the rapid change in growth conditions as the material fluxes are terminated [17, 34, 37]. Some As species may still be present in the growth chamber after the Ga shutter has been closed as the As cracker needle valve operation is slower than the Ga shutter operation and group V materials are known to remain in longer time periods in the growth chamber. This rapidly increases the local V/III ratio at the droplet, which induces WZ formation in GaAs NWs [38]. Hence, this WZ segment is probably formed from the remaining As species after shutting the Ga flux.

TEM images of a NW with a crystallized Ga catalyst droplet from sample NW2 is shown in Fig. 5. The bottom parts of the NWs with crystallized Ga droplets exhibit similar crystal structure to the ones with preserved Ga droplets, as expected. The NW section formed during the Ga catalyst droplet crystallization begins with a short section of stacking faults (Fig. 5b, c) that is followed by a 150-nm-long section of pure WZ GaAs (Fig. 5d, e). A short section ~20 nm of ZB is found in the very end of the NWs (Fig. 5e). Similar characteristics are typical for self-catalyzed GaAs NWs with crystallized catalyst droplets [32, 37, 39]. Based on the TEM analysis, GaAs NWs grown on lithography-free Si/SiOx patterns exhibit typical characteristics of high-quality self-catalyzed GaAs NWs.

HR-XRD was used to obtain statistically meaningful data of the NW crystal structure. HR-XRD spectra of the samples NW1–NW4 are presented in Fig. 6a, and symmetric reciprocal space maps (RSMs) of samples

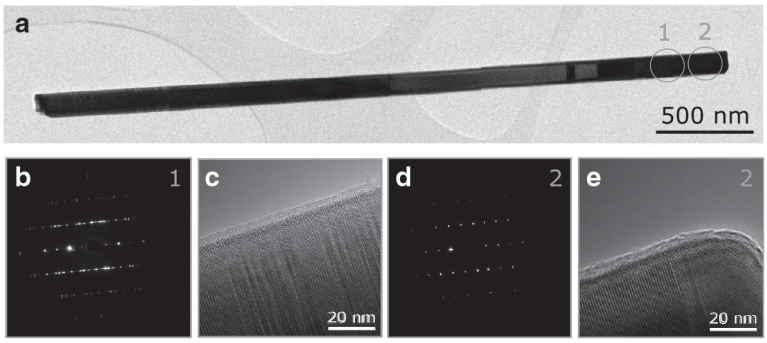

Fig. 5 TEM images of sample NW2. **a** HR-TEM low-magnification overview. **b**, **c** SAED pattern and HR-TEM micrograph of the disordered section close to the tip of the NW. **d** SAED pattern of the pure WZ section at the tip of the NW. **e** HR-TEM micrograph of the very tip of the NW

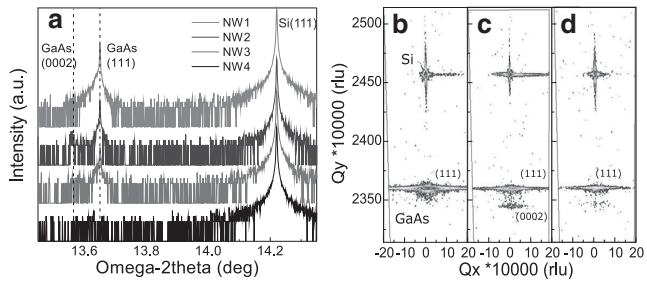

Fig. 6 HR-XRD spectra of samples NW1–NW4 from *top* to *bottom* in **a**. Reciprocal space maps of samples NW1–NW3 in **b**–**d**, respectively

NW1–NW3 are shown in Fig. 6b–d, respectively. The Si(111) and ZB GaAs(111) reflections are clearly seen in all of the spectra, disregarding spectrum of sample NW4 which has too small NWs to gain adequate intensity from GaAs(111) reflection. The GaAs(111) reflections in Fig. 6a show some degree of broadening towards low omega-2theta direction which can be attributed to the presence of short period polytypism [40] at the lower part of the NWs as well as in the upper part of samples NW2 and NW3. In addition to the GaAs(111) reflection, a weak peak can be observed in the smaller omega-2theta side of the GaAs(111) reflection in the spectra of samples NW2 and NW3 (Fig. 6a). The existence of this reflection is confirmed by the RSMs of samples with crystallized Ga catalyst droplets (NW2 and NW3 in Fig. 6c, d), and it is attributed to WZ GaAs(0002) reflection. Because the phase pure WZ segments in NW sections formed during droplet crystallization are 150 nm long, the WZ reflection is assumed to be strain-free which enables determination of WZ GaAs lattice constant *c*. We have obtained a WZ GaAs lattice constant $c = 6.5689$ Å by comparing the WZ GaAs(0002) reflection with the Si(111) reflection in RSM in Fig. 6b where WZ peak is most pronounced. This value is consistent with WZ GaAs lattice constant measured from Au-catalyzed WZ GaAs NWs using asymmetric RSMs 6.5701 Å [41]. As a test of the accuracy of the method, we determined also the ZB GaAs lattice constant and obtained value of 5.6524 Å which deviates from the literature value [42] by only 0.015%. These observations demonstrate that HR-XRD is a valuable tool for NW characterization providing complementary statistical information for TEM analysis performed for a small number of NWs per sample.

Furthermore, the optical properties of the NWs were studied using low-temperature micro-PL in order to correlate them with the crystalline structure. Power-dependent micro-PL spectra of samples NW1–NW3 are shown in Fig. 7. The peak wavelength is between 840 and 855 nm, which is significantly redshifted with respect to bulk GaAs band edge emission (816 nm) at 10 K. The spectra are broadened to longer wavelength side and the amount of fine structure in the spectra seems to increase as the NWs get smaller (from Fig. 6a–c). Possible reasons for the redshift are unintentional Si doping solute into the Ga catalyst droplet from the substrate [43], carbon, or other impurities [44] or band bending due to NW surface oxidation [45, 46]. The fine structure emission is most probably related to indirect and localized transitions at sections with polytypism and stacking faults [47, 48]. The spectra obtained from sample NW1 shows the least fine structure as it consists mostly of defect-free ZB except for the short disordered section at the bottom of the NW and the few twin planes in the upper part of the NWs. Furthermore, samples NW2 and NW3 have equally long polytypic sections at their bottom and top parts, but sample NW2 has a 1.5-μm longer pure ZB

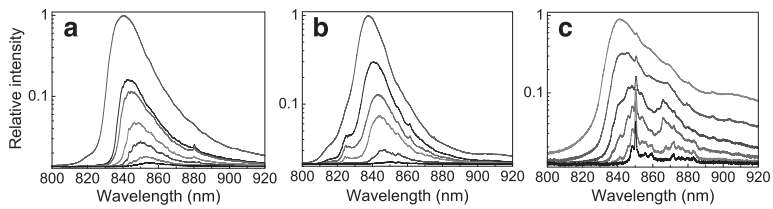

Fig. 7 Micro-photoluminescence spectra of samples NW1–NW3 in **a**–**c**, respectively. The used excitation power densities vary from 0.1 to 96 W cm^{-2} in **a** and **b** and in **c** from 1 to 960 W cm^{-2}

section. Hence, the fine structure emission becomes more prominent when the relative amount of stacking faults increases in shorter NWs, or in other words, the pure ZB segments become shorter in relation to the charge carrier diffusion length. Thus, we are able to associate the characteristics of the micro-PL spectra to the crystal structure of the NWs.

Conclusions

Based on the structural and optical analysis presented in this work, we have shown that the lithography-free oxide patterns provide a suitable template for growth of high-quality GaAs NWs by Ga-catalyzed technique. The sub-Poissonian length distribution of our NWs is a demonstration of their remarkable uniformity, which is attributed to the uniformity of the nucleation sites, lack of secondary nucleation, and self-regulated growth mode. However, further experiments are required for forming a complete understanding of the sub-Poissonian nature of the GaAs NWs grown on lithography-free oxide patterns. Furthermore, the HR-TEM and HR-XRD studies revealed that the GaAs NWs grown on lithography-free oxide patterns exhibit high crystalline quality characterized by up to 2-μm long defect-free ZB segments. The WZ segments formed during Ga catalyst droplet crystallization were used for the determination of lattice constant $c = 6.5689$ Å which corroborates the previously presented value obtained for phase pure WZ NWs. The micro-PL results correlated with the NW crystal structure so that the amount of fine structure PL emission relates to the proportion of disordered sections in the NWs. More generally speaking, our observations show that the non-destructive micro-PL and HR-XRD techniques are valuable tools for the characterization of NW crystal structure and, in particular, provide complementary statistically significant data to support the TEM results.

Abbreviations

HR-XRD: High-resolution X-ray diffractometry; MBE: Molecular beam epitaxy; NW: Nanowire; PL: Photoluminescence; SEM: Scanning electron microscopy; TEM: Transmission electron microscopy; WZ: Wurtzite crystal structure; ZB: Zincblende crystal structure

Acknowledgements

This work made use of Aalto University Nanomicroscopy Center (Aalto-NMC) facilities. Funding from the Academy of Finland Project NESP (decision number 294630) is acknowledged. We thank Dr. Soile Suomalainen for critical reading of the manuscript.

Funding

This work was funded by the Academy of Finland Project NESP (decision number 294630).

Availability of Data and Materials

The datasets supporting the conclusions of this article are included within the article.

Authors' Contributions

EK and TH were responsible for the NW growth and characterization. EK conducted the SEM imaging, HR-XRD, and PL measurements, whereas TH was responsible for the TEM analysis. MG initiated the research and was responsible for the supervision of the work. All authors read and accepted the final manuscript.

Competing Interests

The authors declare that they have no competing interests.

Publisher's Note

Received: 17 January 2017 Accepted: 9 March 2017
Published online: 16 March 2017

References

1. Glas F (2006) Critical dimensions for the plastic relaxation of strained axial heterostructures in free-standing nanowires. Phys Rev B 74:12
2. Mayer B, Janker L, Loitsch B, Treu J, Kostenbader T, Lichtmannecker S, Reichert T, Morkötter S, Kaniber M, Abstreiter G, Gies C, Koblmüller G, Finley JJ (2016) Monolithically integrated high-β nanowire lasers on silicon. Nano Lett 16:1
3. Couteau C, Larrue A, Wilhelm C, Soci C (2015) Nanowire lasers. Nanophotonics 4:90–107
4. Tomioka K, Motohisa J, Hara S, Hiruma K, Fukui T (2010) GaAs/AlGaAs core multishell nanowire-based light-emitting diodes on Si. Nano Lett 10:5
5. Lysov A, Offer M, Gutsche C, Regolin I, Topaloglu S, Geller M, Prost W, Tegude FJ (2011) Optical properties of heavily doped GaAs nanowires and electroluminescent nanowire structures. Nanotechnology 22:8
6. Wallentin J, Anttu N, Asoli D, Huffman M, Åberg I, Magnusson MH, Siefer G, Fuss-Kailuweit P, Dimroth F, Witzigmann B, Xu HQ, Samuelson L, Deppert K, Borgström MT (2013) InP nanowire array solar cells achieving 13.8% efficiency by exceeding the ray optics limit. Science 339:6123
7. Holm JV, Jørgensen HI, Krogstrup P, Nygård J, Liu H, Aagesen M (2013) Surface-passivated GaAsP single-nanowire solar cells exceeding 10% efficiency grown on silicon. Nat Commun 4:1498
8. Tomioka K, Yoshimura M, Fukui T (2012) A III-V nanowire channel on silicon for high-performance vertical transistors. Nature 488:7410
9. Dayeh S, Aplin DP, Zhou X, Yu PK, Yu E, Wang D (2007) High electron mobility InAs nanowire field-effect transistors. Small 3:2
10. Reimer ME, Bulgarini G, Akopian N, Hocevar M, Bavinck MB, Verheijen MA, Bakkers EPAM, Kouwenhoven LP, Zwiller V (2012) Bright single-photon sources in bottom-up tailored nanowires. Nat Commun 3:737
11. Holmes MJ, Choi K, Kako S, Arita M, Arakawa Y (2014) Room-temperature triggered single photon emission from a III-nitride site-controlled nanowire quantum dot. Nano Lett 14:2
12. Spirkoska D, Efros AL, Lambrecht WRL, Cheiwchanchamnangij T, Fontcuberta i Morral A, Abstreiter G (2012) Valence band structure of polytypic zinc-blende/wurtzite GaAs nanowires probed by polarization-dependent photoluminescence. Phys Rev B 85:4
13. Mukherjee A, Ghosh S, Breuer S, Jahn U, Geelhaar L, Grahn HT (2015) Spatially resolved study of polarized micro-photoluminescence spectroscopy on single GaAs nanowires with mixed zincblende and wurtzite phases. J Appl Phys 117:5
14. Heiss M, Russo-Averchi E, Dalmau-Mallorquí A, Tütüncüoğlu G, Matteini F, Rüffer D, Conesa-Boj S, Demichel O, Alarcon-Lladó E, Fontcuberta i Morral A (2014) III-V nanowire arrays: growth and light interaction. Nanotechnology 25:1
15. Larrue A, Wilhelm C, Vest G, Combrié S, De Rossi A, Soci C (2012) Monolithic integration of III-V nanowire with photonic crystal microcavity for vertical light emission. Opt Express 20:7
16. Colombo C, Spirkoska D, Frimmer M, Abstreiter G, Fontcuberta i Morral A (2008) Ga-assisted catalyst-free growth mechanism of GaAs nanowires by molecular beam epitaxy. Phys Rev B 77:15
17. Cirlin GE, Dubrovskii VG, Samsonenko YB, Bouravleuv AD, Durose K, Proskuryakov YY, Mendes B, Bowen L, Kaliteevski MA, Abram RA, Zeze D (2010) Self-catalyzed, pure zincblende GaAs nanowires grown on Si(111) by molecular beam epitaxy. Phys Rev B 82:3
18. Matteini F, Tütüncüoğlu G, Rüffer D, Alarcón-Lladó E, Fontcuberta i Morral A (2014) Ga-assisted growth of GaAs nanowires on silicon, comparison of surface SiOx of different nature. J Cryst Growth 404:246–255
19. Munshi AM, Dheeraj DL, Fauske VT, Kim DC, Huh J, Reinertsen JF, Ahtapodov L, Lee KD, Heidari B, van Helvoort AT, Fimland BO, Weman H

(2014) Position-controlled uniform GaAs nanowires on silicon using nanoimprint lithography. Nano Lett 14:2
20. Plissard S, Larrieu G, Wallart X, Caroff P (2011) High yield of self-catalyzed GaAs nanowire arrays grown on silicon via gallium droplet positioning. Nanotechnology 22:27
21. Hakkarainen TV, Schramm A, Mäkelä J, Laukkanen P, Guina M (2015) Lithography-free oxide patterns as templates for self-catalyzed growth of highly uniform GaAs nanowires on Si(111). Nanotechnology 26:27
22. Rudolph D, Schweickert L, Morkötter S, Loitsch B, Hertenberger S, Becker J, Bichler M, Abstreiter G, Finley JJ, Koblmüller G (2014) Effect of interwire separation on growth kinetics and properties of site-selective GaAs nanowires. Appl Phys Lett 105:3
23. Zhang Y, Sanchez AM, Sun Y, Wu J, Aagesen M, Huo S, Kim D, Jurczak P, Xu X, Liu H (2016) Influence of droplet size on the growth of self-catalyzed ternary GaAsP nanowires. Nano Lett 16:2
24. Dubrovskii VG, Xu T, Álvarez AD, Plissard SR, Caroff P, Glas F, Grandidier B (2015) Self-equilibration of the diameter of Ga-catalyzed GaAs nanowires. Nano Lett 15:8
25. Tersoff J (2015) Stable self-catalyzed growth of III-V nanowires. Nano Lett 15:10
26. Dubrovskii VG (2013) Self-regulated pulsed nucleation in catalyzed nanowire growth. Phys Rev B 87:19
27. Dubrovskii VG (2016) Kinetic narrowing of size distribution. Phys Rev B 93:17
28. Dubrovskii VG, Sibirev NV, Berdnikov Y, Gomes UP, Ercolani D, Zannier V, Sorba L (2016) Length distributions of Au-catalyzed and In-catalyzed InAs nanowires. Nanotechnology 27:37
29. Dubrovskii VG, Berdnikov Y, Schmidtbauer J, Borg M, Storm K, Deppert K, Johansson J (2016) Length distributions of nanowires growing by surface diffusion. Cryst Growth Des 16:4
30. Glas F, Harmand J, Patriarche G (2010) Nucleation antibunching in catalyst-assisted nanowire growth. Phys Rev Lett 104:13
31. Glas F (2014) Statistics of sub-Poissonian nucleation in a nanophase. Phys Rev B 90:12
32. Plissard S, Dick KA, Larrieu G, Godey S, Addad A, Wallart X, Caroff P (2010) Gold-free growth of GaAs nanowires on silicon: arrays and polytypism. Nanotechnology 21:38
33. Krogstrup P, Popovitz-Biro R, Johnson E, Madsen MH, Nygård J, Shtrikman H (2010) Structural phase control in self-catalyzed growth of GaAs nanowires on silicon (111). Nano Lett 10:11
34. Bauer B, Rudolph A, Soda M, Fontcuberta i Morral A, Zweck J, Schuh D, Reiger E (2010) Position controlled self-catalyzed growth of GaAs nanowires by molecular beam epitaxy. Nanotechnology 21:43
35. Glas F, Harmand J, Patriarche G (2007) Why does wurtzite form in nanowires of III-V zinc blende semiconductors? Phys Rev Lett 99:14
36. Krogstrup P, Curiotto S, Johnson E, Aagesen M, Nygård J, Chatain D (2011) Impact of the liquid phase shape on the structure of III-V nanowires. Phys Rev Lett 106:12
37. Yu X, Wang H, Lu J, Zhao J, Misuraca J, Xiong P, von Molnár S (2012) Evidence for structural phase transitions induced by the triple phase line shift in self-catalyzed GaAs nanowires. Nano Lett 12:10
38. Krogstrup P, Hannibal Madsen M, Hu W, Kozu M, Nakata Y, Nygård J, Takahasi M, Feidenhans'l R (2012) In-situ x-ray characterization of wurtzite formation in GaAs nanowires. Appl Phys Lett 100:9
39. Kim YH, Park DW, Lee JS (2012) Gallium-droplet behaviors of self-catalyzed GaAs nanowires: a transmission electron microscopy study. Appl Phys Lett 100:3
40. Schroth P, Köhl M, Hornung J, Dimakis E, Somaschini C, Geelhaar L, Biermanns A, Bauer S, Lazarev S, Pietsch U, Baumbach T (2015) Evolution of polytypism in GaAs nanowires during growth revealed by time-resolved *in situ* x-ray diffraction. Phys Rev Lett 114:5
41. Jacobsson D, Yang F, Hillerich K, Lenrick F, Lehmann S, Kriegner D, Stangl J, Wallenberg LR, Dick KA, Johansson J (2015) Phase transformation in radially merged wurtzite GaAs nanowires. Cryst Growth Des 15:10
42. Vurgaftman I, Meyer JR, Ram-Mohan LR (2001) Band parameters for III–V compound semiconductors and their alloys. J Appl Phys 89:11
43. Keck PH, Broder J (1953) The solubility of silicon and germanium in gallium and indium. Phys Rev 90:4
44. Scolfaro LMR, Pintanel R, Gomes VMS, Leite JR, Chaves AS (1986) Impurity levels induced by a C impurity in GaAs. Phys Rev B 34:10
45. Speckbacher M, Treu J, Whittles TJ, Linhart WM, Xu X, Saller K, Dhanak VR, Abstreiter G, Finley JJ, Veal TD, Koblmüller G (2016) Direct measurements of Fermi level pinning at the surface of intrinsically n-type InGaAs nanowires. Nano Lett 16:8
46. Songmuang R, Giang LTT, Bleuse J, Den Hertog M, Niquet YM, Dang LS, Mariette H (2016) Determination of the optimal shell thickness for self-catalyzed GaAs/AlGaAs core-shell nanowires on silicon. Nano Lett 16:6
47. Graham AM, Corfdir P, Heiss M, Conesa-Boj S, Uccelli E, Fontcuberta iM A, Phillips RT (2013) Exciton localization mechanisms in wurtzite/zinc-blende GaAs nanowires. Phys Rev B 87:12
48. Spirkoska D, Arbiol J, Gustafsson A, Conesa-Boj S, Glas F, Zardo I, Heigoldt M, Gass MH, Bleloch AL, Estrade S, Kaniber M, Rossler J, Peiro F, Morante JR, Abstreiter G, Samuelson L, Fontcuberta i Morral A (2009) Structural and optical properties of high quality zinc-blende/wurtzite GaAs nanowire heterostructures. Phys Rev B 80:24

PUBLICATION 2

Sub-Poissonian Narrowing of Length Distributions Realized in Ga-Catalyzed GaAs Nanowires

E. Koivusalo, T. Hakkarainen, M. Guina, and V. G. Dubrovskii

Nano Lett., vol. 17, no. 9, pp. 5350–5355, 2017
10.1021/acs.nanolett.7b01766

NANO LETTERS

Letter

pubs.acs.org/NanoLett

Sub-Poissonian Narrowing of Length Distributions Realized in Ga-Catalyzed GaAs Nanowires

Eero S. Koivusalo,*[,†] Teemu V. Hakkarainen,[†] Mircea D. Guina,[†] and Vladimir G. Dubrovskii[‡,§,∥]

[†]Optoelectronics Research Centre, Tampere University of Technology, Korkeakoulunkatu 3, FI 33720 Tampere, Finland

[‡]ITMO University, Kronverkskiy pr. 49, 197101 St. Petersburg, Russia

[§]St. Petersburg Academic University, Khlopina 8/3, 194021 St. Petersburg, Russia

[∥]Ioffe Physical Technical Institute of the Russian Academy of Sciences, Politekhnicheskaya 26, 194021 St. Petersburg, Russia

ABSTRACT: Herein, we present experimental data on the record length uniformity within the ensembles of semiconductor nanowires. The length distributions of Ga-catalyzed GaAs nanowires obtained by cost-effective lithography-free technique on silicon substrates systematically feature a pronounced sub-Poissonian character. For example, nanowires with the mean length $\langle L \rangle$ of 2480 nm show a length distribution variance of only 367 nm^2, which is more than twice smaller than the Poisson variance $h\langle L \rangle$ of 808 nm^2 for this mean length (with h = 0.326 nm as the height of GaAs monolayer). For 5125 nm mean length, the measured variance is 1200 nm^2 against 1671 nm^2 for Poisson distribution. A supporting model to explain the experimental findings is proposed. We speculate that the fluctuation-induced broadening of the length distribution is suppressed by nucleation antibunching, the effect which is commonly observed in individual vapor−liquid−solid nanowires but has never been seen for their ensembles. Without kinetic fluctuations, the two remaining effects contributing to the length distribution width are the nucleation randomness for nanowires emerging from the substrate and the shadowing effect on long enough nanowires. This explains an interesting time evolution of the variance that saturates after a short incubation stage but then starts increasing again due to shadowing, remaining, however, smaller than the Poisson value for a sufficiently long time.

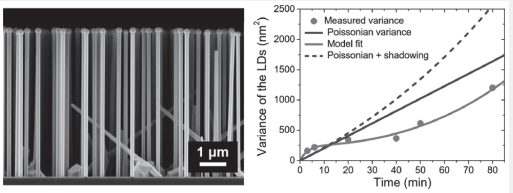

KEYWORDS: *Self-catalyzed VLS growth, molecular beam epitaxy, III−V nanowires, growth kinetics, size distribution*

Semiconductor nanowires (NWs) are widely considered as one of the most promising building blocks for nanoscience and nanotechnology.[1] Size uniformity within the NW ensembles in terms of both diameter and length is crucial for many applications and interesting from a fundamental viewpoint.[2] Particularly for III−V NWs, the self-catalyzed vapor−liquid−solid (VLS) method[3,4] enables Au-free growth of high quality NWs with a good vertical yield and high degree of spatial uniformity.[5−7] Unfortunately, however, most ensembles of VLS NWs (not only self-catalyzed III−V NWs, but in general) are not as uniform in length as they may look. It is common to compare the measured length distributions (LDs) to the Poisson distribution, which rapidly converges to a symmetric Gaussian with the variance scaling as $h\langle L \rangle$, where $\langle L \rangle$ is the mean length over the ensemble and h is the height of a NW monolayer in the growth direction.[2] While the diameter distributions of self-catalyzed III−V can be made remarkably narrow under the appropriate growth conditions (as shown theoretically in refs 8 and 9 and confirmed experimentally for Ga-catalyzed GaAs NWs in ref 9), the measured LDs of Au-catalyzed[10,11] and In-catalyzed[11] InAs NWs and Ga-catalyzed GaAs NWs[12] appear disappointingly broad, in fact, much broader than Poissonian in most cases. There are five main reasons for that: (i) nucleation randomness of NWs emerging from the substrate (meaning that different NWs start at different times and the initial length dispersion becomes larger for longer nucleation step[11−13]), (ii) fluctuation-induced broadening due to random character of growth,[11−14] (iii) diffusion-induced contributions into the NW elongation rate in the case of Au-catalyzed growth,[10,13] (iv) nucleation of secondary group III droplets in the self-catalyzed approach,[11,12] and (v) possible collective effects in the NW ensemble such as shadowing[15] in directional molecular beam epitaxy (MBE) growth.

Au-catalyzed InAs NWs growing by surface diffusion under group V rich conditions[10] showed broad LDs with variance σ^2 scaling with the mean length $\langle L \rangle$ as $\langle L \rangle^2$. Self-catalyzed InAs[11] and GaAs[12] NWs exhibited very broad LDs with a pronounced asymmetry toward a much longer left tail due to continuous nucleation of secondary In or Ga droplets. Au-catalyzed VLS InAs NWs described in ref 11 showed broad and asymmetrical LDs due to difficult nucleation of NWs from colloidal Au nanoparticles that were buried deep into the substrate in the annealing step. The measured Poissonian LDs with variance $h\langle L \rangle$ were reported only once in the case of Au-catalyzed InAs

Received: April 26, 2017
Revised: June 29, 2017
Published: August 7, 2017

DOI: 10.1021/acs.nanolett.7b01766
Nano Lett. 2017, 17, 5350−5355

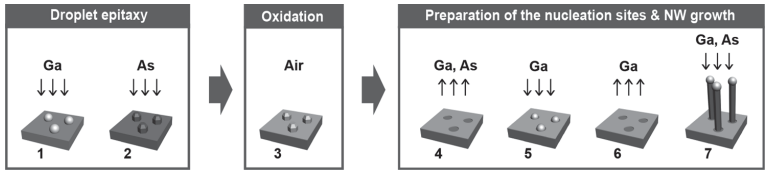

Figure 1. Description of the NW growth process. Steps 1 and 2: formation of GaAs nanocrystals on oxide-free Si(111) by droplet epitaxy. Step 3: spontaneous oxidation of the Si surface by air exposure. Step 4: removal of the GaAs nanocrystals by annealing. Steps 5 and 6: formation of Ga droplets inside the oxide-free holes and subsequent evaporation of the Ga droplets by annealing. Step 7: Ga-catalyzed NW growth.

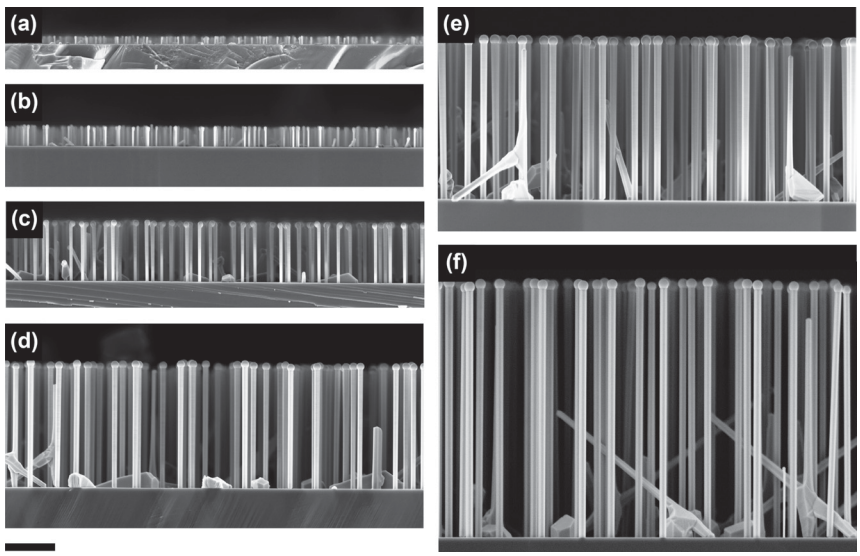

Figure 2. Cross-sectional SEM images of NWs grown for 3 (a), 6 (b), 20 (c), 40 (d), 50 (e), and 80 min (f). The scale bar is 1 μm.

NWs grown from thermally dewetted Au droplets.[11] Narrow LDs of Ga-catalyzed GaAs NWs were also obtained by a two-step MBE growth approach in ref 16 and by using growth on chemical oxide-covered Si substrates in ref 17. These LDs look close to the Poissonian shapes; however, no direct comparison with the Poissonian expectation was given. Until recently, Poisson distribution was therefore the narrowest NW LD observed experimentally. Our recent observations[18] revealed slightly sub-Poissonian LD only for one growth time corresponding to the longest Ga-catalyzed GaAs NWs studied in the work (with $\langle L \rangle$ = 4100 nm), where the measured variance of 1020 nm^2 was smaller than the Poisson value σ_P^2 of 1336 nm^2 at h = 0.326 nm for $\langle 111 \rangle$-oriented GaAs NWs.

Here, we for the first time demonstrate pronounced sub-Poissonian LDs and study the evolution of LD and NW dimensions during Ga-catalyzed growth of GaAs NWs fabricated on lithography-free Si/SiOx patterns. This NW fabrication technique provides control of the NW density by adjusting the density of the nucleation sites[19] and enables growth of NW ensembles having a remarkable size uniformity.[18,19] The size uniformity reveals new insight into the details of LD evolution, which are typically hidden by predominant broadening mechanisms, such as secondary nucleation. This allows us to theoretically separate the effects of different LD broadening mechanisms during the NW growth.

The NW samples were prepared on p-Si(111) wafers using a growth process, which is presented step-by-step in Figure 1. Before the first growth step, the Si wafers were dipped in HF in order to remove the native oxide and immediately transferred in vacuum where they were first annealed at 275 °C for 1 h and then at 700 °C for 10 min. Then GaAs nanocrystals were grown by droplet epitaxy;[20] (1) Ga droplets were first formed by depositing 0.3 monolayers (ML) of Ga at 550 °C and then (2) crystallized into GaAs by a 10 min As_2 exposure. The sample temperature in step 1 is a critical parameter that defines the density of the nucleation sites. Next, (3) the sample was removed from vacuum and exposed to air for 18 h in order to form an oxide layer on the Si(111) surface.[20] In the following step, (4) the sample was transferred back to vacuum where it was annealed at 660 °C for 30 min in order to remove the GaAs nanocrystals and reveal oxide free nucleation sites. In the final surface preparation steps, (5) Ga droplets were formed in the nucleation sites by depositing Ga for 60 s at 640 °C using a growth rate of 0.3 ML/s and (6) subsequently removed by annealing at 660 °C for 10 min. The purpose of steps 5 and 6 is to prepare the nucleation sites for subsequent NW growth. By infby eliminating the Ga predeposition step at the beginning oftroducing these additional steps to the process presented

DOI: 10.1021/acs.nanolett.7b01766
Nano Lett. 2017, 17, 5350−5355

before,[19] we obtain high vertical yield of 70% from all nucleation, without having to use Ga predeposition in the beginning of the NW growth. Finally, in step (7) the NW growth was initiated by simultaneously opening the Ga shutter and As valve and using sample temperature of 640 °C. The Ga growth rate was 0.3 ML/s, and the As_2/Ga beam equivalent pressure ratio was 9. Altogether six NW samples were grown using different growth durations: 3, 6, 20, 40, 50, and 80 min. The NW growth was terminated by switching off simultaneously the Ga and As supplies and rapidly ramping down the sample temperature. The 50 min sample was grown on a template having nucleation site density of 2×10^8 cm^{-2}, while a slightly higher density of 4×10^8 cm^{-2} was used for the other samples, resulting in NW densities of 0.7×10^8 and 1.5×10^8 cm^{-2}, respectively.

Figure 2 shows cross-sectional scanning electron microscope (SEM) images of the NWs after different growth durations. It is evident from the SEM images that the NWs obtained by our method remain remarkably uniform throughout the growth process from 3 min up to 80 min growth duration. The NW length was investigated quantitatively by measuring more than 100 NWs per sample using cross-sectional SEM. The diameter statistics were collected similarly by measuring more than 30 NWs per sample. The evolution of the length and diameter during growth are presented in Figure 3, which shows linear

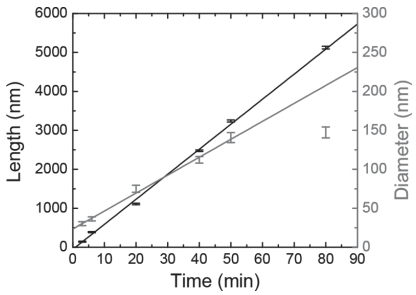

Figure 3. Mean values of the NW length and diameter presented with their standard deviations. Best linear fit to the mean length versus time yields a time-independent mean axial growth rate V of 62.8 nm/min.

time-dependence for the NW length. The NW diameter increases first linearly and then saturates as the NW length increases. This might be a sign of flux shadowing in directional MBE growth.[15] Furthermore, the standard deviation of the NW length in Figure 3 suggests extremely narrow LD, which will be discussed in detail in the following.

Theoretically, the Poisson LD is the best case regarding the length uniformity without one specific effect, which will be discussed later on. Indeed, in the absence of NW nucleation delays or secondary nucleation of catalyst droplets, the LD of NWs that grow by directly impinging the growth species from vapor is described by the Gaussian Green's function[14]

$$F(L, \langle L \rangle) = \frac{1}{\sqrt{2\pi}\,\sigma_p} \exp\left[-\frac{(L - \langle L \rangle)^2}{2{\sigma_p}^2}\right] \quad (1)$$

with the Poisson variance

$${\sigma_p}^2 = h\langle L \rangle \quad (2)$$

The measured LDs of our NWs after different growth times remain surprisingly narrow as shown in Figure 4, particularly

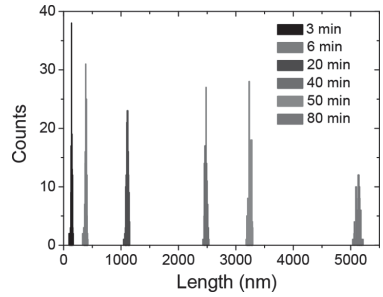

Figure 4. Measured length histograms of Ga-catalyzed GaAs NWs at t = 3, 6, 20, 40, 50, and 80 min.

for longer growth times. Figure 3 confirms that the mean NW length scales linearly with the growth time t, as it should be in Ga-catalyzed GaAs NWs whose axial growth rate is proportional to the As flux.[3,9,21] In our case, $\langle L \rangle = Vt$ with V = 62.8 nm/min as the effective influx of As atoms into the droplet. The measured LDs after 40, 50, and 80 min of growth are essentially sub-Poissonian, as shown in Figure 5. For example, the variance

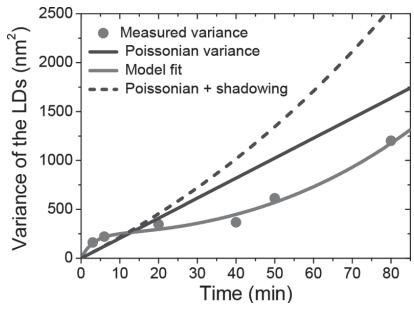

Figure 5. Measured variance of the GaAs NW LDs versus the growth time (symbols). Solid straight line shows the corresponding Poisson variance ${\sigma_p}^2 = h\langle L \rangle = hVt$, with V = 62.8 nm/min from Figure 3. The red line shows a theoretical fit by the model that includes the shadowing effect, and the dashed blue line corresponds to the Poissonian growth with shadowing as explained later.

of 2480 nm long NWs obtained after 40 min of growth is only 367 nm^2, which is more than twice smaller than the Poisson variance of 808 nm^2 for this mean length. This variance is also significantly smaller than the slightly sub-Poissonian value we reported in ref 18. We attribute the improved length uniformity to the modified growth process in which the incubation time before the first nucleation is shortened from 68 to 57 s. There is also a clear difference in the NW diameter during the early stage of growth, which appears smaller here than in ref 18, confirming that the NWs nucleate faster in the modified procedure.

Very importantly for our analysis, the measured variance in Figure 5 exhibits nonmonotonic time dependence. It increases faster than the Poissonian variance in the initial growth step (for 3 and 6 min growth times), then saturates to an almost time-independent value of ~350 nm^2 for 20 and 40 min growth

DOI: 10.1021/acs.nanolett.7b01766
Nano Lett. 2017, 17, 5350−5355

times and starts increasing again after that. However, it remains smaller than Poissonian also for 50 and 80 min growth times. In our technique for growing Ga-catalyzed GaAs NWs, the formation of secondary Ga droplets is safely avoided. The axial growth rate is limited by the impinging As species, as demonstrated by the linear time dependence of the mean length in Figure 3. Therefore, factors such as (iii) diffusion-induced effects on the NW growth rate and (iv) formation of secondary droplets for broadening are suppressed, and our LDs are influenced only by (i) nucleation randomness for NWs, (ii) Poissonian broadening, and (v) shadowing.

We will now try to understand the remarkable length uniformity that corresponds to the sub-Poissonian LDs after 20 min of growth. Qualitatively, the duration of the initial nucleation step for NWs is expected to determine the nucleation width of the LD,[2,22] which stays constant in the follow-up growth stage. Poissonian broadening of the LD is due to kinetic fluctuations[14,22] and may be suppressed by the so-called nucleation antibunching in individual III−V NWs[23] whereby mononuclear growth of a NW ML empties the droplet with its As, and the next nucleation becomes improbable until the droplet is refilled from vapor. Periodically changing supersaturation in the catalyst also leads to oscillations of truncated growth interfaces.[24,25] Glas[26] and Sibirev[27] showed that the nucleation statistics in individual NWs (which is related to Green's function of the LDs for the NW ensemble[28]) becomes sub-Poissonian in any NWs growing with nucleation antibunching.

The measure of the antibunching effect is given by the parameter[23,26−28]

$$\varepsilon = \frac{3\Omega_{Ga}}{\Omega_{GaAs} f(\beta)} \bar{c}_{As} \frac{\partial \Delta\mu}{\partial \bar{c}_{As}} i_*(\bar{c}_{As}) \frac{h}{\bar{c}_{As} R} \tag{3}$$

Here, $\Omega_{Ga} = 0.02$ nm^3 is the elementary volume of liquid gallium, $\Omega_{GaAs} = 0.0452$ nm^3 is the elementary volume of solid GaAs, $\bar{c}_{As}$ is the average concentration of As in the droplet (corresponding to the mean growth rate), $\partial\Delta\mu/\partial\bar{c}_{As}$ is the derivative of the chemical potential in the liquid phase with respect to the As concentration at $\bar{c}_{As}$, $i_*(\bar{c}_{As})$ is the number of GaAs pairs in the critical nucleus at $\bar{c}_{As}$, $f(\beta) = (1 - \cos\beta)(2 + \cos\beta)/[(1 + \cos\beta)\sin\beta]$ is the geometrical function relating the volume of spherical cap droplet to the cube of its base having the NW radius R through the contact angle β. Whenever the effect of nucleation antibunching is present (that is, for any positive ε), the variance of Green's function saturates with time rather than growing infinitely as in the Poissonian case.[26−28] The ε parameter controls the value of the variance at saturation (which equals $h^2/(2\varepsilon)$ for small $\varepsilon \ll 1$)[27,28] as well as the rate of saturation. We speculate that for large enough times, actually starting already from ∼6 min of growth in our case, sub-Poissonian LD narrowing by nucleation antibunching yields the time-independent variance instead of the Poisson value $h\langle L\rangle$. This discussion is limited to a simplified case of zero As evaporation from the catalyst. However, Sibirev and co-authors[29] showed that a similar convergence of the LDs to a time-independent shape is observed when the evaporation is included. We will therefore proceed with the model without evaporation for further estimates, which is acceptable because the contribution into the saturated variance due to antibunching appears negligible anyway.

Quasi-saturation of the variance is seen for our GaAs NWs for intermediate growth times (from 6 to 40 min in Figure 5). Taking for the estimate the mean value of the measured contact angle of 133° and the mean radius at 5 min of 25.5 nm, eq 3 at $\bar{c}_{As}\partial\Delta\mu/\partial\bar{c}_{As} = 1$ and $\bar{c}_{As} = 0.02$ yields $\varepsilon = 0.0885 \times i_*$, corresponding to a very small $h^2/(2\varepsilon) \approx 0.15$ nm^2 even for a small i_* of four GaAs pairs (corresponding to a small $\varepsilon = 0.35$). Therefore, the variance due to nucleation antibunching is much smaller than the saturated variance (reaching ∼300 nm^2) and can be neglected in the analysis of the observed LD width. Of course, our NWs grow radially with time, and hence, the ε parameter is a slow function of time. We speculate, however, that the suppression of kinetic fluctuations occurs in the initial stage with almost time-independent NW radii and once the LD is rendered into the self-regulated regime, there is no reason for its further Poissonian broadening.

Figure 5 shows that the measured variance starts to increase again after $t = 40$ min. We attribute this additional broadening to the shadowing effect[15] for As. In directional MBE growth, shorter NWs receive less As flux from vapor (including a large contribution of re-emitted species[30]) because they are blocked by the neighboring NWs that are longer. The observed broadening of the LDs for long NWs is the opposite of the self-regulation mechanism due to the cooperative effect of interwire exchange with the growth species, described in ref 31 in the case of Ga-limited non-VLS growth of GaN NWs. This effect leads, however, to bimodal LDs that are not seen in our experiments. Furthermore, the LDs of GaN NWs given in ref 31 are still much broader than Poissonian.

In order to quantify the statistical properties of the LDs shown in Figure 5, we use the rate equations for the normalized $(\sum_{s\geq 0} f_s = 1)$ probabilities $f_s(t)$ to observe a NW with the length of $s = L/h$ monolayers at time t, given by[10,11,13,14,28]

$$\frac{df_0}{dt} = -p_0 f_0, \quad \frac{df_s}{dt} = p_{s-1} f_{s-1} - p_s f_s, \quad s \geq 1 \tag{4}$$

For the growth rates p_s, we use the model of the form

$$p_s = v + u(s - \langle s\rangle), \quad s \geq 0 \tag{5}$$

Here, $v = V/h$ gives the length-independent average axial growth rate in MLs per min. The second term stands for the shadow effect in the linear approximation, with shorter NWs (with $s < \langle s\rangle$) growing slower and longer NWs (with $s < \langle s\rangle$) growing faster than the NWs having the mean length $\langle s\rangle = \langle L\rangle/h$. The parameter u describes the strength of the shadow effect. The mean length and variance in terms of the s variable are defined as

$$\langle s\rangle = \sum_{s=1}^{\infty} s f_s, \quad \sigma_s^2 = \langle s^2\rangle - \langle s\rangle^2 = \sum_{s=1}^{\infty} s^2 f_s - \langle s\rangle^2 \tag{6}$$

Differentiating eq 6 for the mean length with respect to time and using eq 4, we obtain $d\langle s\rangle/dt = v$, and hence, $\langle s\rangle = vt$. As expected, the shadow effect does not affect the expectation $\langle s\rangle$, which remains a linear function of time. Doing the same procedure with the variance, after some simple manipulations we find the exact result

$$\frac{d\sigma_s^2}{dt} = v + 2u\sigma_s^2 \tag{7}$$

Therefore, the variance of the LD exponentially increases with respect to the Poisson value $\langle s\rangle = vt$ due to the shadow effect. Of course, this property pertains only in the linear approximation for the instability and hence is valid only over a

DOI: 10.1021/acs.nanolett.7b01766
Nano Lett. 2017, 17, 5350−5355

limited range of the growth times. Integrating this and returning to the dimensional variance $\sigma^2 = h^2\sigma_s^2$, we obtain

$$\sigma^2 = hL_0(e^{\langle L\rangle/L_0} - 1) \quad (8)$$

with $\langle L\rangle = Vt$ as the mean length and $L_0 = h\nu/(2u) = V/(2u)$ as the characteristic length describing the shadow effect.

The variance given by Eq. 8 is reduced to the Poissonian value $\sigma_p^2 = h\langle L\rangle$ at $\langle L\rangle/L_0 \to 0$. We can rewrite it as $\sigma^2 = h\langle L\rangle + hL_0[\exp(\langle L\rangle/L_0) - 1 - \langle L\rangle/L_0]$, where the Poisson variance due to kinetic fluctuations is extracted explicitly in the linear term. According to our previous analysis, this term should be completely suppressed by nucleation antibunching (which does not change the mean length much[26−28]). However, the initial nucleation randomness[13,22] is not taken into account in eq 4, which applies uniformly for all lengths starting from $s = 0$ for free droplets. To access the nucleation-induced broadening of the LDs, clearly seen in Figure 5, we introduce the additional term that saturates to the nucleation variance σ_*^2 in the initial growth step, as in ref 19. As a result, our model expression for the variance takes the form

$$\sigma^2 = \sigma_*^2(1 - e^{-\langle L\rangle/L_*}) + hL_0(e^{\langle L\rangle/L_0} - 1 - \langle L\rangle/L_0) \quad (9)$$

This equation shows that, in the absence of Poissonian broadening, the length variation is determined by the two factors: the initial nucleation randomness of the NWs emerging from the substrate (leading asymptotically to a time-independent variance σ_*^2 with the characteristic saturation length L_*) and the additional broadening due to the shadow effect (which becomes important for long NWs having the mean length on the order of the shadowing length L_0). The line in Figure 5 demonstrates the excellent fit to the measured variance obtained from eq 9 with $\sigma_*^2 = 250$ nm^2, $L_* = 200$ nm, and $L_0 = 6000$ nm. The dotted line in Figure 5 corresponds to eq 8, that is, the Poissonian growth influenced by the shadow effect, with the same L_0 of 6000 nm and shows that the LDs without nucleation antibunching would be even broader than Poissonian in this case. Saturation of the variance in the intermediate growth stage requires that the nucleation step is fast (a short L_*) and that the shadowing length L_0 is large. We note that the value of $L_0 = 6000$ nm obtained from the fit is larger than the trivial geometrical shadowing length for the direct flux $A\cot\alpha$ (with A as the average distance between the neighboring NWs and α as the incident angle of the As beam), which is on the order of 1000 nm for our $A = 546$ nm and $\alpha = 35°$. This indicates weaker shadowing compared to the geometrical approach. The actual picture is much more complex as it includes re-emitted As species,[21,30−32] so the obtained L_0 is entirely possible. A more detailed investigation and modeling of the shadowing effect for different NW densities and growth conditions are underway. The nucleation variance σ_*^2 depends on the preparation technique used for Ga droplets, the type of the substrate/oxide, and the nucleation rate of stable NWs emerging from Ga droplets, which may be changed by the As flux. In comparison to our previous work,[15] by eliminating the Ga predeposition step at the beginning of the NW growth we were able to reduce the incubation time and significantly reduce the saturation level of the variance. Furthermore, the strength of the shadow effect for the long NWs could be reduced by increasing the nearest neighbor distance.

In summary, we have demonstrated for the first time the NW LDs that are narrower than Poissonian. Our Ga-catalyzed GaAs NWs grow with a time-independent elongation rate and reach the mean length of 5100 nm in 80 min. The variance of the LDs saturates to a time-independent value after the initial nucleation step due to suppression of the Poissonian broadening by nucleation antibunching. This effect was known for individual NWs but never seen in their ensembles. The saturated variance of less than 400 nm^2 is more than twice smaller than Poissonian (800 nm^2) for ∼2500 nm mean length. Further increase of the variance has been attributed to the shadow effect due to which shorter NWs receive smaller arsenic flux as they are surrounded by longer NWs. Overall, the LD widths remain smaller than Poissonian for growth times from 40 to 80 min, corresponding to the length from 2500 to 5100 nm. The obtained values of the relative LD widths $\sigma/\langle L\rangle$ of 0.00773, 0.00845, and 0.00676 for 40, 50, and 80 min growth times show record length homogeneity within the NW ensembles and may be further improved by optimizing the initial nucleation step and reducing the NW density.

AUTHOR INFORMATION

Corresponding Author

*E-mail: eero.koivusalo@tut.fi.

ORCID

Eero S. Koivusalo: 0000-0001-5029-4658
Teemu V. Hakkarainen: 0000-0001-6758-2496
Mircea D. Guina: 0000-0002-9317-8187
Vladimir G. Dubrovskii: 0000-0003-2088-7158

Notes

The authors declare no competing financial interest.

ACKNOWLEDGMENTS

Funding from the Academy of Finland Project NESP (decision no. 294630) is acknowledged. V.G.D. thanks the Ministry of Education and Science of the Russian Federation for financial support under grant 14.587.21.0040 (project ID RFMEFI58717X0040).

REFERENCES

(1) Zhang, A.; Zheng, G.; Lieber, C. M. *Nanowires: Building Blocks for Nanoscience and Nanotechnology*; Springer, 201610.1007/978-3-319-41981-7.

(2) Dubrovskii, V. G. *Nucleation Theory and Growth of Nanostructures*; Springer, 201410.1007/978-3-642-39660-1.

(3) Colombo, C.; Spirkoska, D.; Frimmer, M.; Abstreiter, G.; Fontcuberta i Morral, A. *Phys. Rev. B: Condens. Matter Mater. Phys.* **2008**, *77*, 155326.

(4) Jabeen, F.; Grillo, V.; Rubini, S.; Martelli, F. *Nanotechnology* **2008**, *19*, 275711.

(5) Plissard, S.; Larrieu, G.; Wallart, W.; Caroff, P. *Nanotechnology* **2011**, *22*, 275602.

(6) Munshi, A. M.; Dheeraj, D. L.; Fauske, V. T.; Kim, D. C.; Huh, J.; Reinertsen, J. F.; Ahtapodov, L.; Lee, K. D.; Heidari, B.; van Helvoort, A. T. J.; Fimland, B. O.; Weman, H. *Nano Lett.* **2014**, *14*, 960.

(7) Russo-Averchi, E.; Vukajlovic Plestina, J.; Tütüncüoglu, G.; Matteini, F.; Dalmau-Mallorquí, A.; de la Mata, M.; Rüffer, D.; Potts, H. A.; Arbiol, J.; Conesa-Boj, S.; Fontcuberta i Morral, A. *Nano Lett.* **2015**, *15*, 2869.

(8) Tersoff, J. *Nano Lett.* **2015**, *15*, 6609.

(9) Dubrovskii, V. G.; Xu, T.; Díaz Álvarez, A.; Plissard, S. R.; Caroff, P.; Glas, F.; Grandidier, B. *Nano Lett.* **2015**, *15*, 5580.

DOI: 10.1021/acs.nanolett.7b01766
Nano Lett. 2017, 17, 5350−5355

(10) Dubrovskii, V. G.; Berdnikov, Y.; Schmidtbauer, J.; Borg, M.; Storm, K.; Deppert, K.; Johansson, J. *Cryst. Growth Des.* **2016**, *16*, 2167.
(11) Dubrovskii, V. G.; Sibirev, N. V.; Berdnikov, Y.; Gomes, U. P.; Ercolani, D.; Zannier, V.; Sorba, L. *Nanotechnology* **2016**, *27*, 375602.
(12) Matteini, F.; Dubrovskii, V. G.; Rüffer, D.; Tütüncüoğlu, G.; Fontana, Y.; Fontcuberta i Morral, A. *Nanotechnology* **2015**, *26*, 105603.
(13) Dubrovskii, V. G. *J. Cryst. Growth* **2017**, *463*, 139.
(14) Dubrovskii, V. G. *Phys. Rev. B: Condens. Matter Mater. Phys.* **2013**, *87*, 195426.
(15) Sibirev, N. V.; Tchernycheva, M.; Timofeeva, M. A.; Harmand, J. C.; Cirlin, G. E.; Dubrovskii, V. G. *J. Appl. Phys.* **2012**, *111*, 104317.
(16) Küpers, H.; Bastiman, F.; Luna, E.; Somaschini, C.; Geelhaar, L. *J. Cryst. Growth* **2017**, *459*, 43.
(17) Tan, S. L.; Genuist, Y.; den Hertog, M. I.; Bellet-Amalric, E.; Mariette, H.; Pelekanos, N. T. *Nanotechnology* **2017**, *28*, 255602.
(18) Koivusalo, E.; Hakkarainen, T.; Guina, M. *Nanoscale Res. Lett.* **2017**, *12*, 192.
(19) Hakkarainen, T. V.; Schramm, A.; Mäkelä, J.; Laukkanen, P.; Guina, M. *Nanotechnology* **2015**, *26*, 275301.
(20) Sanguinetti, S.; Koguchi, N. Droplet epitaxy of nanostructures. In *Molecular Beam Epitaxy: From Research to Mass Production*; Henini, M., Ed.; Elsevier, 2012; Chapter 4, pp 100−10810.1016/B978-0-12-387839-7.00004-X.
(21) Glas, F.; Ramdani, M. R.; Patriarche, G.; Harmand, J. C. *Phys. Rev. B: Condens. Matter Mater. Phys.* **2013**, *88*, 195304.
(22) Dubrovskii, V. G. *J. Chem. Phys.* **2009**, *131*, 164514.
(23) Glas, F.; Harmand, J. C.; Patriarche, G. *Phys. Rev. Lett.* **2010**, *104*, 135501.
(24) Wen, C. Y.; Tersoff, J.; Hillerich, K.; Reuter, M. C.; Park, J. H.; Kodambaka, S.; Stach, E. A.; Ross, F. M. *Phys. Rev. Lett.* **2011**, *107*, 025503.
(25) Gamalski, A. D.; Ducati, C.; Hofmann, S. J. *J. Phys. Chem. C* **2011**, *115*, 4413.
(26) Glas, F. *Phys. Rev. B: Condens. Matter Mater. Phys.* **2014**, *90*, 125406.
(27) Sibirev, N. V. *Tech. Phys. Lett.* **2013**, *39*, 660.
(28) Dubrovskii, V. G.; Sibirev, N. V. J. *J. Phys. D: Appl. Phys.* **2017**, *50*, 254004.
(29) Sibirev, N. V.; Nazarenko, M. V.; Zeze, D. A.; Dubrovskii, V. G. *J. Cryst. Growth* **2014**, *401*, 51.
(30) Ramdani, M. R.; Harmand, J. C.; Glas, F.; Patriarche, G.; Travers, L. *Cryst. Growth Des.* **2013**, *13*, 91.
(31) Sabelfeld, K. K.; Kaganer, V. M.; Limbach, F.; Dogan, P.; Brandt, O.; Geelhaar, L.; Riechert, H. *Appl. Phys. Lett.* **2013**, *103*, 133105.
(32) Li, A.; Sibirev, N. V.; Ercolani, D.; Dubrovskii, V. G.; Sorba, L. *Cryst. Growth Des.* **2013**, *13*, 878.

DOI: 10.1021/acs.nanolett.7b01766
Nano Lett. 2017, 17, 5350−5355

PUBLICATION 3

Deterministic Switching of the Growth Direction of Self-Catalyzed GaAs Nanowires

E. Koivusalo, T. Hakkarainen, H. V. A. Galeti, Y. G. Gobato, V. G. Dubrovskii, and M. Guina

Nano Lett., vol. 19, no. 1, pp. 82–89, 2019
10.1021/acs.nanolett.8b03365

NANO LETTERS Cite This: Nano Lett. 2019, 19, 82–89

Letter

pubs.acs.org/NanoLett

Deterministic Switching of the Growth Direction of Self-Catalyzed GaAs Nanowires

Eero S. Koivusalo,*[,†] Teemu V. Hakkarainen,[†] Helder V. A. Galeti,[‡] Yara G. Gobato,[§] Vladimir G. Dubrovskii,[∥] and Mircea D. Guina[†]

[†]Optoelectronics Research Centre, Tampere University of Technology, P.O. Box 692, Tampere 33101, Finland

[‡]Electrical Engineering Department, Federal University of São Carlos, São Carlos, São Paulo13565-905, Brazil

[§]Physics Department, Federal University of São Carlos, São Carlos, São Paulo13565-905, Brazil

[∥]ITMO University, Kronverkskiy prospekt 49, St. Petersburg 197101, Russia

Supporting Information

ABSTRACT: The typical vapor–liquid–solid growth of nanowires is restricted to a vertical one-dimensional geometry, while there is a broad interest for more complex structures in the context of electronics and photonics applications. Controllable switching of the nanowire growth direction opens up new horizons in the bottom-up engineering of self-assembled nanostructures, for example, to fabricate interconnected nanowires used for quantum transport measurements. In this work, we demonstrate a robust and highly controllable method for deterministic switching of the growth direction of self-catalyzed GaAs nanowires. The method is based on the modification of the droplet–nanowire interface in the annealing stage without any fluxes and subsequent growth in the horizontal direction by a twin-mediated mechanism with indications of a novel type of interface oscillations. A 100% yield of switching the nanowire growth direction from vertical to horizontal is achieved by systematically optimizing the growth parameters. A kinetic model describing the competition of different interface structures is introduced to explain the switching mechanism and the related nanowire geometries. The model also predicts that the growth of similar structures is possible for all vapor–liquid–solid nanowires with commonly observed truncated facets at the growth interface.

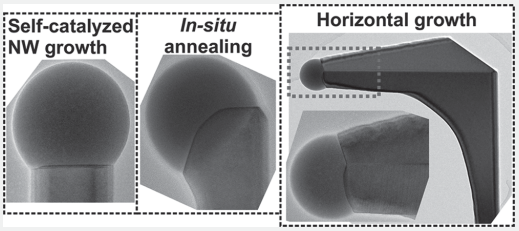

KEYWORDS: *Self-catalyzed GaAs nanowires, growth direction, crystal facets, surface energetics*

Precise shaping of III–V semiconductor nanowires (NWs) is paramount for their functionalization into electronic and photonic devices. In particular, GaAs/AlGaAs NW-based lasers integrated on silicon waveguides,[1] monolithic LEDs,[2,3] and functional NW array solar cells[4] have been important milestones in this development. All of these achievements have relied on the axial or radial heterostructures within one-dimensional (1D) NWs. Extension of the NW growth beyond 1D geometry provides a suitable template for delicate quantum transport measurements.[5,6] Several approaches have previously been used to form a versatility of three-dimensional NW-based structures. In particular, Au-catalyzed NW crosses have been grown on a (100) substrate producing rather random InAs NW meshes,[6] and in a more controllable way on a prepatterned substrate.[7] A ridged template covered by oxide with predetermined nucleation sites has provided another approach to grow more regular InAs[8,9] and InSb[5] NW crosses. Interconnected NWs can also be produced by switching the NW growth direction with respect to the typical <111> [or <0001> in the case of wurtzite (WZ) NWs] direction of the substrate normal. The most convenient 90° switching of the growth direction has been demonstrated for Au-catalyzed WZ InAs NWs[7] and catalyst-free InAs(Sb) NWs.[10] In optics and photonics, possible applications of such structures include circular dichroism in the optical response of chiral nanostructures,[11] exploiting the waveguiding properties of semiconductor NWs.[12,13] This effect further increases the interest in controlling the NW growth direction. To date, the yield of bent NWs has always been less than 100% within the framework of the self-catalyzed approach. Furthermore, not all of the horizontal growths start in the same horizontal plane, which is unfavorable for further contacting the NWs.

The simplest mechanism for switching the NW growth direction is driven by a catalyst droplet wetting one of the NW side facets.[7,10,14] After that, more complex growth effects may occur, including the formation of new facets or twin planes separating different facets. Using these effects, even reversible switching of the growth direction has been demonstrated in Au-catalyzed InP NWs.[15] In addition, twinning is known to facilitate the formation of kinks and other kinds of structures

Received: August 20, 2018
Revised: November 19, 2018
Published: December 11, 2018

DOI: 10.1021/acs.nanolett.8b03365
Nano Lett. 2019, 19, 82–89

such as nanomembranes,[16] flags,[14] and sails.[17] Very important information on the kinetics of kinking in Au-catalyzed NWs is provided by in situ transmission electron microscopy (TEM), as descried previously.[18,19] Despite the significant progress in understanding and controlling the NW growth direction by different methods, a simple and robust procedure for achieving 100% yield of horizontal self-catalyzed NW growth in one horizontal plane is still lacking. Consequently, this work reports a method to grow very regular ensembles of 90° bent GaAs NWs on silicon in the self-catalyzed approach.

By using lithography-free SiO_x patterns as templates for the self-catalyzed vapor−liquid−solid (VLS) growth, we have been able to obtain GaAs NWs with the controllable number density, high-quality zincblende (ZB) crystal structure, and remarkable sub-Poissonian length uniformity.[20−22] Here, we show that this growth method can be extremely suitable to induce bent NW structures with horizontal growth. The deterministic switching of the growth direction occurs in the same horizontal plane due to the narrow length distribution of the initial NWs. This is highly desirable for fabrication of interconnected NWs. A 100% yield of regularly bent NWs is achieved simply by a growth interruption, which determines a transition from vertical to horizontal growth. We investigate in detail the previously unknown growth mechanism in different stages and show that the NW morphology is generally sensitive to the duration of the growth interruption, the local V/III ratio, and the NW diameter. A longer growth interruption is found to deterministically switch the NW growth direction by 90° with a 100% yield. We develop a model, which describes the observed reshaping of the growth interface and shows that the deterministic transition from vertical to horizontal growth upon the growth interrupt must be a general phenomenon for all self-catalyzed III−V NWs under the appropriate conditions. Thus, the insights presented here may help to either avoid the unwanted kinking during the NW growth or deterministically switch the NW growth direction when required for particular applications.

The self-catalyzed GaAs NWs were grown by solid source molecular beam epitaxy (MBE) on lithography-free oxide pattern templates fabricated on p-Si(111) substrates via droplet epitaxy. The lithography-free templates are fabricated on HF etched, oxide-free Si substrates, by depositing Ga droplets on the substrate and crystallizing the droplets into GaAs under the As flux. After that, the templates are oxidized in air and loaded back into the MBE chamber, where the GaAs mounds are evaporated to form the lithography-free oxide patterns, on which the NWs are in situ grown, as described in refs 20 and 22. The NWs were grown on four different templates with the nucleation site densities varying from 5×10^7 cm^{-2} to 5×10^8 cm^{-2}. The vertical NW growth was initiated with a 40 s predeposition of Ga droplets, re-evaporation of the droplets, and simultaneously opening the Ga and As_2 fluxes. The NW growth was conducted at 640 °C, as determined by a pyrometer, the Ga deposition rate was 0.3 μm/h, as calibrated for (100) GaAs growth, and the V/III beam equivalent pressure (BEP) ratio was 9. The vertical NW growth time was 20 min, except for three samples with variable diameters, for which the growth durations from 20 to 30 min were used. More details on the template fabrication and the NW growth method can be found in refs 20−22. After growth of the vertical part, the NWs were annealed for 20−70 s at the growth temperature without any fluxes in order to reshape the droplet−NW interface. After the annealing, the NW growth was resumed by simultaneously providing the Ga and As fluxes. The V/III BEP ratio for the horizontal growth was varied from 7 to 11. After growth, the samples were rapidly cooled down. Additional samples with vertical NWs grown for 20 min and rapidly cooled down (template density 5×10^8 cm^{-2}) and NWs gone through 45 s annealing (template densities 2×10^8 cm^{-2}, 5×10^8 cm^{-2}, and 5×10^7 cm^{-2} and growth durations from 20 to 30 min) were also fabricated as the references to study the droplet−NW interface and the NW dimensions before the growth continuation.

The NW morphologies were studied using scanning electron microscopy (SEM). A typical NW sample after 20 min of vertical growth and immediate cool down without any fluxes is shown in Figures 1a,d. It is clearly seen that the Ga droplets

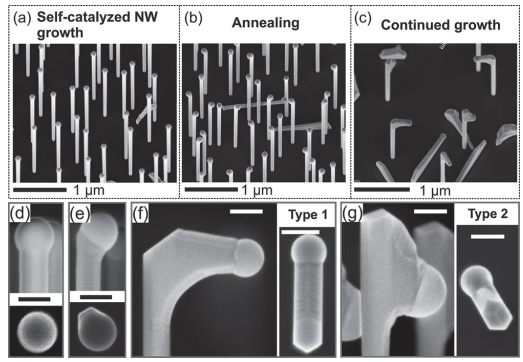

Figure 1. Growth of bent GaAs NWs. (a, d) Vertical NWs grown for 20 min and rapidly cooled down. (b, e) NWs annealed at the growth temperature for 45 s prior to cool down. (c) NWs grown for 5 min after 45 s annealing. Side- and top-view images of (f) type 1 horizontal and (g) type 2 downward growth. Scale bars in low-magnification 30° tilted images are 1 μm in parts a−c and 100 nm in parts d−g.

remain stationary on the NW tips just after growth. In contrast, the sample that was annealed for 45 s at the growth temperature prior to cool down [Figure 1b,e] exhibits 100% yield of droplets falling toward one of the (110) side facets. When the growth is resumed after annealing by simultaneously opening the Ga shutter and As valve, the NWs continue their growth perpendicular to their initial growth direction [Figures 1c,f], or slightly downward [Figure 1c,g]. Perpendicularly grown horizontal sections are referred to as type 1 and downward pointing sections as type 2. The azimuthal direction of the bent NW part is toward one of the <112> directions associated with the corners of the (110) sidewalls, in contrast to the droplet position after the annealing [see the top-view images in Figure 1e−g].

To further understand the formation mechanism of these structures, the postannealing droplet−NW interfaces were analyzed by SEM and high-resolution transmission electron microscopy (HR-TEM) [JEOL JEM-2200FS operated at 200 kV and FEI Tecnai G2-F20 operated at 200 kV for Figure 4b]. Two different droplet−NW interface shapes with respect to the [110] zone axis (ZA) were found by TEM, as shown in Figure 2a,b. The first shape is dominated by the A-polar (1−1−1) facet and the second type by the (0−10) facet. The third low index facet is the B-polar (−111) facet forming below the (0−10) one, as shown in Figure 2b. Otherwise, the structures

DOI: 10.1021/acs.nanolett.8b03365
Nano Lett. 2019, 19, 82−89

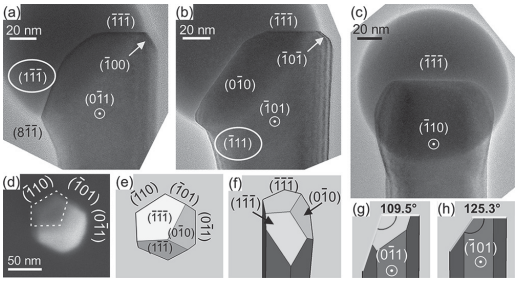

Figure 2. (a–c) TEM micrographs of three NWs annealed for 45 s at the growth temperature prior to cool down. The ZAs marked in the micrographs are also marked in the SEM image of the droplet-free NW top facet in part d and sketches e, g, and h. The SEM image (d) and top-view sketch (e) are aligned with respect to each other. The complementary SEM analysis of part d is presented in the Supporting Information.

compose of minor higher index facets. The facets are identified based on the assumption that the NW top facet is (−1−1−1) and the NW sidewalls are (110). The growth direction is identified as <111>B because it is the common growth direction of self-catalyzed GaAs NWs,[23,24] while A-polar GaAs NWs are rarely achieved and mainly use Au-catalyzed VLS growth.[25,26] It should also be noted that the radial symmetry of the NW is 3-fold. This symmetry yields three possible sets of [110] ZA that give equivalent results for the facet identification. The one presented here is an arbitrarily chosen example showing the droplet–NW interface of a particular NW.

Both dominating reshaped facets are inclined toward one of the <112> corner directions of the NW sidewalls, perpendicular to the [110] ZA used for imaging. However, back-view TEM [Figure 2c] and top-view SEM [Figure 1e] show that the droplets are tilted symmetrically toward one of the (110) side facets. The shape of the NW growth interface was imaged by SEM after removing the Ga droplets by HCl etching. SEM analysis revealed the pentagonal shape of the top facet marked by the dashed line in Figure 2d and that two of the sidewall corners are hidden under the reshaped facets. Based on these results, the interface configurations shown in Figure 2a,b are interpreted as different views of a similar structure, illustrated in the sketches in Figure 2e–h. More details on the SEM analysis of the droplet–NW interface are given in the Supporting Information.

Results of the TEM analysis of a type 1 NW structure, shown in Figure 3a,b, reveal a pure ZB structure throughout the whole NW, with a single twin plane extending along the horizontal section. HR-TEM images in Figure 3c–e are aligned in such a way that the top side of the horizontal section is facing upward. These images show two different interface configurations existing during growth of type 1 horizontal sections. Both configurations are dominated by a flat (111) plane on one side of the twin plane and feature a combination of smaller facets on the other. For the NW imaged in Figure 3c, the dominating flat (111) plane is B-polar as it is situated above the twin plane. For the NW in Figure 3d, the dominating (111) plane is A-polar and lies below the twin plane. This (111)A facet corresponds to the (1−1−1) plane marked in Figure 2a. The HR magnification shown in Figure 3e confirms that the (111) planes exist on both sides of the

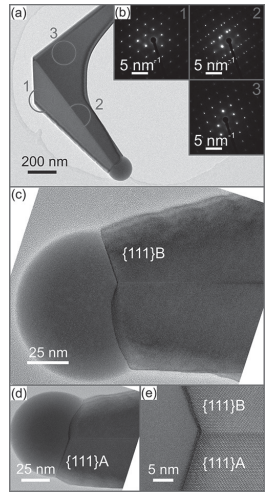

Figure 3. HR-TEM analysis of type 1 bent GaAs NWs. The low-magnification image in part a and selective area diffraction (SAED) patterns in part b reveal the excellent crystal purity in the ZB phase and a single twin plane present in the horizontal section. Two different droplet–NW interfaces are dominated by a flat (111)B plane in part c and (111)A plane in part d. Periodic faceting of the top of the horizontal NW section can clearly be seen in parts c and d. (e) HR magnification of the twin section that features both (111)A and (111)B facets.

twin plane. It should be noted that the defect-free ZB structure without twin planes was observed at the tip of all investigated NWs before and after the annealing step, as shown in the Supporting Information and Figure 2, respectively. On the basis of these observations, we conclude that type 1 growth is initiated by nucleation of the twin plane, which forms the (111)B plane to oppose the initial (1−1−1) plane seen in Figure 2a. The two (111)B and (111)A opposing facets pin the droplet to sustain the horizontal growth.

TEM analysis conducted on a type 2 NW structure reveals some similarities with type 1 growth. In particular, Figure 4a shows that type 2 downward growth occurs on a NW, where a single twin is present, as we saw earlier for type 1. However, in this case, the twin is found in the vertical part, above the downward type 2 growth [Figure 4a, SAED pattern 1], and is most likely formed when the growth is resumed. The downward growth continues directly along the <111> B direction [Figure 4b], pointing 109° away from the original NW growth direction. This is the direction of the (−111) facet marked in Figure 2b. Thus, type 2 downward growth is interpreted to start with nucleation of a single twin plane and the droplet sliding down from the (0−10) facet wetting the (−111) facet marked in Figure 2b, where the growth continues. During the downward growth, the (−111) facet remains flat and no microfacetting in the droplet–NW interface is witnessed [Figure 4b and Supporting Information].

The NW shown in Figure 4a is aligned to a [110] ZA, which is rotated by 60° around the NW axis from the direct side view [Figure 1g]. In this case, possible twinning of the downward part cannot be seen because a twin in that growth direction rotates the zone axis away from the [110]. Hence, only one set of the diffraction points would be seen in the SAED pattern

DOI: 10.1021/acs.nanolett.8b03365
Nano Lett. 2019, 19, 82–89

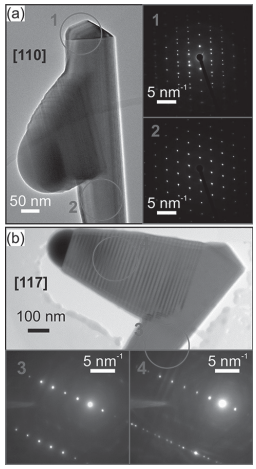

Figure 4. Type 2 downward growth of a GaAs NW. (a) The [110] ZA image of a type 2 structure with a downward section grown for 20 min shows the defect-free vertical section, with a single twin in the tip of the NW (SAED 1). (b) In the [117] ZA image of a structure with a 20 min downward growth, periodic twinning of the horizontal section is witnessed, corresponding to SAED 4. The evolution of type 2 structures during the downward growth is described in more detail in the Supporting Information.

even if the downward section were twinned. Therefore, an additional TEM analysis in a side-view configuration aligned to [117] ZA is shown in Figure 4b, demonstrating that the downward section is dominated by periodic twinning. The twinning is clearly seen as a contrast difference in Figure 4b and is also observable as roughness of the downward section in Figure 4a.

As type 1 structures grow precisely in the same horizontal plane (see the Supporting Information) and exhibit only a single twin plane, whereas type 2 structures consist of a periodic twinning superlattice, we carefully optimized the yield of higher quality type 1 structures. We studied the effects of the NW density, annealing time, V/III BEP ratio during the resumed growth, and NW diameter on the populations of type 1 and 2 NWs. For the annealing time, V/III BEP ratio, and NW density, all horizontal sections were grown on similar vertical NWs. The effect of each growth parameter was studied independently using the intermediate values of the other two parameters (the NW density = 3×10^7 cm^{-2}, the annealing time = 45 s, the V/III BEP ratio = 9). For the diameter series, the vertical growth time was varied in order to tune the size of the initial NWs (at a fixed V/III BEP ratio). The populations were characterized by analyzing top-view SEM images as described in more detail in the Supporting Information.

According to Figure 5a, increasing the NW surface density from 2.4×10^7 cm^{-2} to 2.5×10^8 cm^{-2} allowed us to increase the yield of type 1 structures from 20 to 100% . The effect of the annealing time is shown in Figure 5b. Very importantly, a 99% yield of type 1 structures was obtained with the longest annealing time of 70 s. For the shortest annealing time of 20 s, the horizontal growth was mostly suppressed by the formation of arbitrarily shaped bulges, showing that 20 s is not an adequate time for the deterministic switching of the NW growth direction. Figure 5c shows that altering the V/III ratio as the growth is resumed after the annealing step also had a significant effect on the yield of type 1 structures. For the lowest V/III ratio, all horizontal sections nucleated as type 1 structures. However, for 35% of these structures, the droplets wetted the horizontal NW sidewalls, terminating the original type 1 growth. The formation of these structures, referred to as type 1b in Figure 5e, is explained in the Supporting Information, where the top facets of such structures are analyzed in more detail based on SEM images. A higher V/III ratio of 11 produced up to 70% yield of type 1 structures.

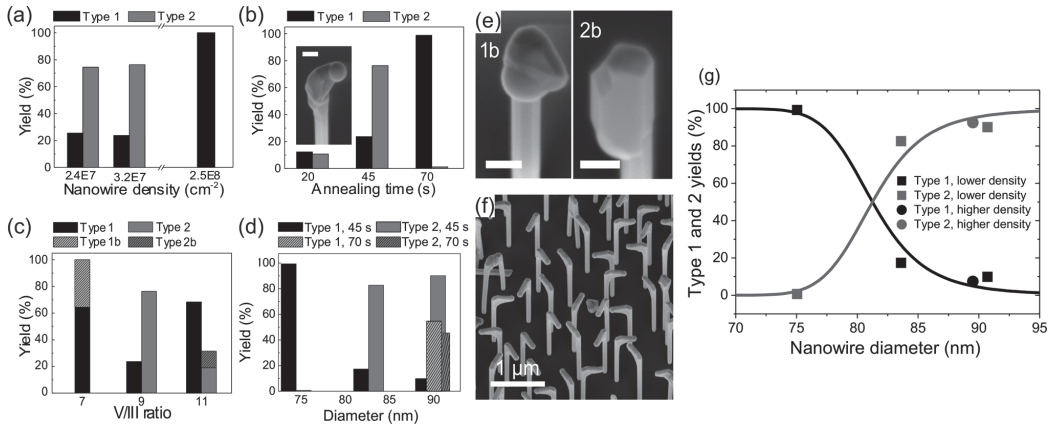

Figure 5. Effect of the growth parameter tuning on the yield of type 1 structures. (a) NW density, (b) annealing time, (c) V/III BEP ratio, and (d) NW diameter. Note that the intermediate data in histograms a–c are from the same sample. The inset in part b shows the typical random bulge formed when the annealing time is too short. The 30° tilted view SEM images in part e show type 1b and 2b structures as described in the text and Supporting Information. The scale bars are 100 nm. (f) The 30° tilted SEM image of the high-density sample with 100% yield of type 1 structures. (g) The NW diameter dependence of the type 1 and 2 populations at a fixed annealing time of 45 s (with a lower density of surface structures of 1.26×10^8 cm^{-2} and a higher density of 1.91×10^8 cm^{-2}), fitted by the model described below.

DOI: 10.1021/acs.nanolett.8b03365
Nano Lett. 2019, 19, 82–89

However, many droplets started shrinking during the subsequent horizontal growth, implying that such growth would eventually be terminated due to the droplet consumption. Furthermore, 40% of type 2 structures obtained with V/III = 11 exhibited growth directly downward along the sidewalls of vertical NWs. These structures have nucleated similarly to type 2 NWs and are referred to as type 2b in Figure 5e. The SEM analysis of these structures is given in the Supporting Information. No droplets were observed on top of type 2b structures.

Figure 5d shows the effect of the NW diameter on the yield of type 1 structures. For the narrowest NWs with the diameters of 75 nm, more than 99% yield of type 1 structures is achieved. Increasing the NW diameter leads to a rapid decrease of the type 1 population. For 84 nm diameter NWs, the type 1 yield becomes only 17.4% and drops below 10% for 91 nm diameter NWs. The additional data point for 90 nm diameter NWs but with the annealing time increased from 45 to 70 s demonstrates that the type 1 yield increases from less than 10% to 55% despite the large NW diameter. Therefore, increasing the annealing time has a similar effect as decreasing the NW diameter, both leading to a higher yield of type 1 structures. This will be important in what follows. Figure 5f shows an SEM image of the high-density sample with 100% yield of type 1 NWs.

We now compare these results with the previously published data. The droplet−NW interface reshaping shown in Figure 1e and analyzed in Figure 2 was observed in our previous work.[22] However, as these samples were immediately cooled down after the NW growth, the effect was not reproducible until the annealing step was introduced to achieve the deterministic switching of the NW growth direction as described above. A similar effect of the growth interface reshaping has previously been reported for Be-doped self-catalyzed GaAs NWs in ref 27, where Be was thought to lower the droplet surface energy and to cause a partial wetting of the NW sidewalls. In ref 28, the Ga flux was provided for 20−60 s after termination of the As input in order to inflate the droplet and let it wet the NW side facets. The multiple (111) facets observed in ref 27 form a similar structure to the one shown in Figure 2a. Similarly in ref 28, the (111)A facet dominated the reshaped droplet−NW interface, even though a few twin planes were formed above the droplets, one of which extended to the droplet−NW interface. This extended twin plane is likely to represent the very first steps of nucleation toward the type 1 structure. Thus, prior observations support the repeatability and generality of the (111)-dominated droplet−NW interface reshaping upon the growth interruption.

In addition to the reshaped (111)A [(1−1−1) in Figure 2a] facet, our NWs comprise a (100) facet, below which we always observe a (111)B facet [such as the (0−10) and (−111) facets in Figure 2b]. The reshaped (100) facet and the (111)B facet below it were not observed in refs 27 and 28. On the basis of the droplets tilting symmetrically in between the (1−1−1) and (0−10) facets [away from the (−110) NW side facet in Figure 2c] and taking into account the interface configuration observed on the NWs with the droplets removed, we conclude that the reshaped droplet−NW interface consists of a combination of the (111)A and (100) facets, as illustrated in Figure 2 e−h. According to this view, type 1 and type 2 structures nucleate from NWs having very similar droplet−NW interfaces. However, higher quality horizontal type 1 structures are dominated by the (111)A facets. Lower quality downward type 2 structures are dominated by the (100) facets and grow perpendicular to the (111)B facet situated below the (100) one. The difference between type 1 and 2 structures should then be explained by the fine-tuning of the interface geometry, namely, the probabilities of forming the (111)A and (100) reshaped facets. The reshaping of the growth interface should be due to an interplay of the surface energetics and kinetics, supported by the fact that the populations of type 1 and 2 structures can be tuned by the growth parameters and the NW diameters as shown in Figure 5.

We now present a model to explain and quantify the switching mechanism. According to refs 29 and 30, <111>B-aligned self-catalyzed GaAs NWs and even Au-catalyzed GaAs NWs grown under Ga-rich conditions exhibit a truncated growth interface with an inward tapered facet wetted by a catalyst droplet. Such truncated NWs have a pure ZB crystal phase because nucleation occurs away from the triple phase line where solid, liquid, and vapor phases meet.[29−32] Unfortunately, in situ TEM measurements[29,31] cannot identify the exact orientation of the small truncated facet due to the complex structure of the truncation and its fast oscillations. However, it seems reasonable that the low index (111)A and (100) can both be present in the initially truncated vertical NWs as well as in NWs reshaping under annealing.

According to the model of Tersoff,[31] the free energy change of forming an inclined facet making the angle θ_i to the vertical, of height y and length L, is given by

$$\Delta G_i = L\left[-a_i y + \left(b_i + \frac{\Delta\mu}{\Omega_{35}}\frac{\tan\theta_i}{2}\right)y^2\right] \quad (1)$$

This expression presents the free energy relative to the vertical facet and planar growth interface. Here, $-a_i$ is the surface energy change upon forming the inclined facet, which becomes negative at large enough contact angles of the droplet β ($\beta \cong 133°$ in our vertical NWs), $\Delta\mu$ is the chemical potential difference per GaAs pair in liquid and solid, $\Omega_{35} = 0.0452$ nm^3 is the elementary volume of GaAs pairs in solid, and b_i is a positive constant, which determines the facet size when $\Delta\mu = 0$. The energetically preferred facet height $y_*^{(i)}$ that minimizes ΔG_i is given by $y_*^{(i)} = a_i/[2b_i(1 + \alpha_i\Delta\mu)]$, with $\alpha_i = \tan\theta_i/(2\Omega_{35}b_i)$. According to our assumption, $a_i > 0$ for both (111)A and (100) facets, with the probability of their occurrence determining the populations of type 1 ($i = 1$) or 2 ($i = 2$) bent NW structures. We should now compare the probabilities of forming type 1 or 2 facets at a varying chemical potential $\Delta\mu$, which decreases in the annealing stage upon the growth interrupt.

The minimum free energy values at $y = y_*^{(i)}$ are given by

$$\Delta G_*^{(i)} = -\frac{a_i L}{4b_i(1 + \alpha_i\Delta\mu)} \quad (2)$$

The probability p_1 of forming type 1 structure can generally be put as

$$p_1 = \frac{\exp(-\Delta G_1^*/k_B T)}{\exp(-\Delta G_1^*/k_B T) + \exp(-\Delta G_2^*/k_B T)} \quad (3)$$

with T as the growth temperature and k_B as the Boltzmann constant. As shown in the Supporting Information, chemical potential decreases with the annealing time t approximately as

DOI: 10.1021/acs.nanolett.8b03365
Nano Lett. 2019, 19, 82−89

$$\Delta\mu = \Delta\mu_0(1 - \omega t), \quad \omega = \frac{k_B T}{\Delta\mu_0}\frac{3\Omega_3}{\Omega_{35} f(\beta)} k_{35}\frac{h}{R} \propto \frac{1}{R} \tag{4}$$

with $\Delta\mu_0$ as the initial chemical potential value at $t = 0$. The constant ω determines the rate of chemical potential decrease, with $\Omega_3 = 0.02$ nm^3 as the elementary volume of liquid Ga, $h = 0.326$ nm as the height of the GaAs monolayer, $f(\beta) = (1-\cos\beta)(2 + \cos\beta)/[(1 + \cos\beta)\sin\beta]$ as the geometrical function of the droplet contact angle β, k_{35} as the crystallization rate of GaAs pairs, and R as the NW radius (which equals the radius of the droplet base). The chemical potential decreases linearly with t, while for a given t it is higher for a larger R because larger droplets deplete more slowly with their As. Using eqs 2−4, the yield of type 1 structures is obtained in the form

$$p_1 = \frac{1}{1 + \exp\left[\Gamma\left(\frac{1}{1 + \alpha_2\Delta\mu_0(1-\omega t)} - \frac{u}{1 + \alpha_1\Delta\mu_0(1-\omega t)}\right)\right]} \tag{5}$$

with $\Gamma = [a_2^2/(4b_2)](L/k_B T)$ and $u = a_1^2 b_2/(a_2^2 b_1)$.

Using the plausible parameters of self-catalyzed growth of GaAs NWs ($\Delta\mu_0 = 0.2$ eV,[33,34] $k_{35} = 165$ s^{-1} corresponding to the mean axial growth rate of our vertical NWs of 1.06 nm/s,[22] and $\beta = 133°$), we obtain the ω values on the order of 1 min^{-1} for $R \sim 50$ nm, showing that chemical potential tends to zero after ∼1 min of annealing. According to Figure 5b,d, an almost 100% yield of type 1 NW structures is obtained after 70 s annealing and even after 45 s annealing for a smaller NW diameter of 75 nm. Shorter annealing times or larger NW diameters favor type 2 structures, which become predominant (more than 90%) for the largest NW diameters of 90−91 nm. According to the above analysis, smaller diameters or longer annealing times bring the VLS system closer to the quasi-equilibrium state at $\Delta\mu = 0$, corresponding to $\omega t = 1$ in eq 5. On the other hand, a higher $\Delta\mu$ favors type 2 structures. While the α_i and u parameters entering eq 5 are unknown, a higher yield of type 2 structures at $\Delta\mu \cong \Delta\mu_0$ (and therefore the preference of the (100) truncation in vertical NWs) transitioning to an almost 100% yield of type 1 structures at $\Delta\mu \cong 0$ requires that

$$u > 1, \quad \frac{1 + \alpha_2\Delta\mu_0}{1 + \alpha_1\Delta\mu_0} u < 1 \tag{6}$$

implying that $\alpha_1 > \alpha_2$. These two inequalities are essential for describing the observed trends in the two competing NW structures under annealing.

Using eq 6, we can quantify the yield of type 1 structures versus the NW diameter at a fixed t of 45 s. The facet length L entering the Γ parameter should be proportional to R. We can then write $\Gamma = R/R_1$ and $\omega t = R_0/R$ according to eq 5. This gives

$$p_1(R) = \frac{1}{1 + \exp\left[\frac{R}{R_1}\left(\frac{1}{1 + \alpha_2\Delta\mu_0(1 - R_0/R)} - \frac{u}{1 + \alpha_1\Delta\mu_0(1 - R_0/R)}\right)\right]} \tag{7}$$

Figure 5g shows a good fit to the data by eq 7 with $R_1 = 1.5$ nm, $R_0 = 32.5$ nm, $u = 2$, $\alpha_2\Delta\mu_0 = 1$, and $\alpha_1\Delta\mu_0 = 7$. It is seen that the transition from less than 10% to almost 100% of type 1 structures is very sharp and occurs for a relatively small diameter change from 90 to 75 nm.

Very importantly, all of the statistical data on type 1 versus type 2 NW structures shown in Figure 5a−d are qualitatively explained within our model. As discussed above, longer annealing times and smaller NW sizes decrease chemical potential and hence favor type 1 structures. Higher density NWs are ∼100 nm longer and thinner (71 nm in diameter) than the sparse ones (82 nm in diameter). Therefore, the NW density effect is the same as for the diameter series. Due to a higher fraction of re-emitted As species,[33] the local V/III flux ratio should be higher for denser NWs. A higher As flux is known to increase the axial NW growth rate and simultaneously shrink the Ga droplets, yielding thinner NWs.[35−37] Lower V/III BEP ratios lead to a steeper decrease of chemical potential in the gallium droplets[33,34] and hence favor a faster formation of type 1 structures when the growth is resumed after annealing. The only exception from this trend is the case of the highest V/III BEP ratio of 11 [see Figure 5c], where the population of type 1 structures increases even though a higher $\Delta\mu$ is expected. This may be associated with shorter incubation times, where more energetically preferred structures are formed over a given period of time. It should also be noted that nucleating the horizontal growth with an optimized V/III BEP ratio for each density (for example, V/III = 7 for the intermediate NW density) and then tuning the V/III ratio back to 9 could produce 100% yield of type 1 structures. This gives additional versatility of the growth parameters that can individually be tuned to maximize the deterministic nucleation of type 1 structures.

Based on the structural analysis of the reshaped droplet−NW interfaces and type 1 structures shown in Figures 2 and 3, type 1 structures nucleate on the (1−1−1) facet marked in Figure 2a. Simultaneously, a twin plane forms, creating a (111) B facet to oppose the (1−1−1) one. Because this twin plane is observed in both types of structures, it is most likely initiated by the triple phase line nucleation at the droplet edge opposing the reshaped (1−1−1) and (0−10) facets, where the droplet contact angle is less than 90°.[29,32] In type 1 structures, the twin plane between the (111)A and (111)B facets pins the droplet, allowing the growth to propagate in the <112> direction. Such mechanism is known as the twin-mediated growth, observed previously for Ge ingots and Au-catalyzed Ge and GaInP NWs.[38−42] However, our growth mode is different from previous observations. In our case, two different interface configurations are observed, where the flat facet dominating the droplet−NW interface may be either the upper B-polar [Figure 3c] or the lower A-polar facet [Figure 3d], and the other (111) facet is replaced by several smaller microfacets. These two morphologies present different phases of a novel type of twin-mediated growth where the flat facet dominating the growth varies periodically. Oscillations between the flat (111)A and (111)B facets during growth is supported by the periodically changing morphology of the top parts of horizontal NWs, where one half period is almost parallel to the twin plane and the other has a downward slope with respect to the twin. This fine structure can readily be seen in SEM images shown in Figure 1f and in the Supporting Information, and in more detail in the side-view TEM in Figure 3c,d. The sustainability of this oscillating twin-mediated growth mode for long horizontal sections is demonstrated in the Supporting Information by analyzing the horizontal growth rate for a V/III BEP ratio of 9. The growth rate remains constant for at least 20 min and equals the axial growth rate of vertical NWs (1.06 nm/s).

DOI: 10.1021/acs.nanolett.8b03365
Nano Lett. 2019, 19, 82−89

In relation to the surface energetics of horizontal growth, we speculated that the (111)A facets are energetically preferred to all other types of facets at low enough chemical potentials, which is why they are most representative in the reshaped droplet−NW interface. On the other hand, it is known that the (111)B plane of GaAs has a lower energy than the (111)A one (0.69 J/m^2 against 0.82 J/m^2 in contact with As-rich vapors according to ref 43). The same property should pertain when these facets are in contact with the Ga liquid, consistent with the fact that the usual NW growth direction is <111>B.[44] Our type 1 structures nucleate on a (111)A facet, which is inward tapered for vertical NWs and has a lower effective surface energy with respect to the outward tapered (111)B facet.[30] The situation changes after nucleation of a horizontal NW section, where the energetically preferred facet to introduce is the (111)B one, which allows for the stable horizontal growth of type 1 NWs. This explains the unique growth mode, whereby the horizontal growth direction is maintained by alternating the (111)A and (111)B facet and should work equally well for other III−V NWs.

In conclusion, we have demonstrated a high level of control over the growth direction of self-catalyzed GaAs NWs and found a novel type of twin-mediated growth mode, where the growth interface oscillates between the two flat (111) facets with a different polarity. By controlling the NW density, annealing time, V/III ratio during the horizontal growth, and NW diameter, we are able to obtain 100% yield of regular 90° bent NW structures, in which all of the horizontal sections start at the predetermined height. Our model describes an interesting interplay between the surface energetics and growth kinetics, whereby the horizontal growth is preferred at low chemical potentials achieved in the annealing stage. It explains all of the observed data and predicts that such morphology should be achievable for any VLS III−V NWs whose growth front is initially truncated. Detailed structural investigations reveal a high crystal quality of the obtained structures, which makes them extremely promising for quantum electronic and photonic applications.

■ ASSOCIATED CONTENT

Supporting Information

The Supporting Information is available free of charge on the ACS Publications website at DOI: 10.1021/acs.nanolett.8b03365.

SEM analysis of NW top faceting; additional SEM images to support statistical analysis of type 1 and 2 populations; description of different structures found on the sample; analysis of horizontal growth rate; evolution of type 2 downward growth; additional SEM analysis of growth interface during continued growth; additional SEM images of exceptions from type 1 and 2 growth due to short annealing or nonoptimal V/III BEP ratio; TEM analysis of NWs prior to annealing; illustrative SEM images of the horizontal plane, on which type 1 growth occurs; derivation of the chemical potential decrease under annealing (PDF)

■ AUTHOR INFORMATION

Corresponding Author

*E-mail: eero.koivusalo@tut.fi.

ORCID

Eero S. Koivusalo: 0000-0001-5029-4658

Teemu V. Hakkarainen: 0000-0001-6758-2496

Yara G. Gobato: 0000-0003-2251-0426

Vladimir G. Dubrovskii: 0000-0003-2088-7158

Mircea D. Guina: 0000-0002-9317-8187

Author Contributions

The manuscript was written through contributions of all authors. All authors have given approval to the final version of the manuscript.

Notes

The authors declare no competing financial interest.

■ ACKNOWLEDGMENTS

This work made use of the Aalto University Nanomicroscopy Center (Aalto-NMC) facilities, Tampere Microscopy Center facilities at Tampere University and Laboratory of Structural Characterization (LCE/DEMa/UFSCar). E.K, T.H., and M.G. acknowledge financial support from the Academy of Finland Projects NESP (decision no. 294630), the NanoLight (decision no. 310985), and the Vilho, Yrjö and Kalle Väisälä Foundation of the Finnish Academy of Science and Letters. H.V.A.G. and Y.G.G. acknowledge financial support from the São Paulo Research Foundation, FAPESP (decisions grant nos. 14/50513-7 and 16/10668-7). V.G.D. acknowledges the Ministry of Education and Science of the Russian Federation for financial support under grant no. 14.587.21.0040 (project ID RFMEFI58717 × 0040).

■ REFERENCES

(1) Mayer, B.; Janker, L.; Loitsch, B.; Treu, J.; Kostenbader, T.; Lichtmannecker, S.; Reichert, T.; Morkötter, S.; Kaniber, M.; Abstreiter, G.; Gies, C.; Koblmüller, G.; Finley, J. J. Monolithically Integrated High-β Nanowire Lasers on Silicon. *Nano Lett.* **2016**, *16* (1), 152−156.

(2) Tomioka, K.; Motohisa, J.; Hara, S.; Hiruma, K.; Fukui, T. GaAs/AlGaAs Core Multishell Nanowire-Based Light-Emitting Diodes on Si. *Nano Lett.* **2010**, *10* (5), 1639−1644.

(3) Svensson, C. P. T.; Mårtensson, T.; Trägårdh, J.; Larsson, C.; Rask, M.; Hessman, D.; Samuelson, L.; Ohlsson, J. Monolithic GaAs/InGaP nanowire light emitting diodes on silicon. *Nanotechnology* **2008**, *19* (30), 305201.

(4) Wallentin, J.; Anttu, N.; Asoli, D.; Huffman, M.; Åberg, I.; Magnusson, M.H.; Siefer, G.; Fuss-Kailuweit, P.; Dimroth, F.; Witzigmann, B.; Xu, H.Q.; Samuelson, L.; Deppert, K.; Borgström, M. T. InP nanowire array solar cells achieving 13.8% efficiency by exceeding the ray optics limit. *Science* **2013**, *339*, 1057.

(5) Gazibegovic, S.; Car, D.; Zhang, H.; Balk, S. C.; Logan, J. A.; de Moor, M. W. A.; Cassidy, M. C.; Schmits, R.; Xu, D.; Wang, G.; Krogstrup, P.; Op het Veld, R. L. M.; Zuo, K.; Vos, Y.; Shen, J.; Bouman, D.; Shojaei, B.; Pennachio, D.; Lee, J. S.; van Veldhoven, P. J.; Koelling, S.; Verheijen, M. A.; Kouwenhoven, L. P.; Palmstrøm, C. J.; Bakkers, E. P. A. M. Epitaxy of advanced nanowire quantum devices. *Nature* **2017**, *548*, 434.

(6) Kang, J.; Cohen, Y.; Ronen, Y.; Heiblum, M.; Buczko, R.; Kacman, P.; Popovitz-Biro, R.; Shtrikman, H. Crystal Structure and Transport in Merged InAs Nanowires MBE Grown on (001) InAs. *Nano Lett.* **2013**, *13* (11), 5190−5196.

(7) Krizek, F.; Kanne, T.; Razmadze, D.; Johnson, E.; Nygård, J.; Marcus, C. M.; Krogstrup, P. Growth of InAs Wurtzite Nanocrosses from Hexagonal and Cubic Basis. *Nano Lett.* **2017**, *17* (10), 6090−6096.

(8) Rieger, T.; Rosenbach, D.; Vakulov, D.; Heedt, S.; Schäpers, T.; Grützmacher, D.; Lepsa, M. I. Crystal Phase Transformation in Self-Assembled InAs Nanowire Junctions on Patterned Si Substrates. *Nano Lett.* **2016**, *16* (3), 1933−1941.

DOI: 10.1021/acs.nanolett.8b03365
Nano Lett. 2019, 19, 82−89

(9) Dalacu, D.; Kam, A.; Austing, D. G.; Poole, P. J. Droplet Dynamics in Controlled InAs Nanowire Interconnections. *Nano Lett.* **2013**, *13* (6), 2676−2681.
(10) Potts, H.; Morgan, N. P.; Tütüncüoglu, G.; Friedl, M.; Morral, A. F. I. Tuning growth direction of catalyst-free InAs(Sb) nanowires with indium droplets. *Nanotechnology* **2017**, *28* (5), 054001.
(11) Luo, Y.; Chi, C.; Jiang, M.; Li, R.; Zu, S.; Li, Y.; Fang, Z. Plasmonic Chiral Nanostructures: Chiroptical Effects and Applications. *Adv. Opt. Mater.* **2017**, *5* (16), 1700040.
(12) Leahu, G.; Petronijevic, E.; Belardini, A.; Centini, M.; Sibilia, C.; Hakkarainen, T.; Koivusalo, E.; Rizzo Piton, M.; Suomalainen, S.; Guina, M. Evidence of Optical Circular Dichroism in GaAs-Based Nanowires Partially Covered with Gold. *Adv. Opt. Mater.* **2017**, *5*, 1601063.
(13) Petronijevic, E.; Centini, M.; Belardini, A.; Leahu, G.; Hakkarainen, T.; Sibilia, C. Chiral near-field manipulation in Au-GaAs hybrid hexagonal nanowires. *Opt. Express* **2017**, *25* (13), 14148−14157.
(14) Kelrich, A.; Sorias, O.; Calahorra, Y.; Kauffmann, Y.; Gladstone, R.; Cohen, S.; Orenstein, M.; Ritter, D. InP Nanoflag Growth from a Nanowire Template by in Situ Catalyst Manipulation. *Nano Lett.* **2016**, *16* (4), 2837−2844.
(15) Wang, J.; Plissard, S.; Verheijen, M. A.; Feiner, L.; Cavalli, A.; Bakkers, E. P. A. M. Reversible Switching of InP Nanowire Growth Direction by Catalyst Engineering. *Nano Lett.* **2013**, *13* (8), 3802−3806.
(16) Conesa-Boj, S.; Russo-Averchi, E.; Dalmau-Mallorqui, A.; Trevino, J.; Pecora, E. F.; Forestiere, C.; Handin, A.; Ek, M.; Zweifel, L.; Wallenberg, L. R.; Rüffer, D.; Heiss, M.; Troadec, D.; Dal Negro, L.; Caroff, P.; Fontcuberta i Morral, A. Vertical "III−V" V-Shaped Nanomembranes Epitaxially Grown on a Patterned Si[001] Substrate and Their Enhanced Light Scattering. *ACS Nano* **2012**, *6* (12), 10982−10991.
(17) de la Mata, M.; Leturcq, R.; Plissard, S.; Rolland, C.; Magén, C.; Arbiol, J.; Caroff, P. Twin-Induced InSb Nanosails: A Convenient High Mobility Quantum System. *Nano Lett.* **2016**, *16* (2), 825−833.
(18) Lenrick, F.; Ek, M.; Deppert, K.; Samuelson, L.; Wallenberg, L. R. Straight and kinked InAs nanowire growth observed in situ by transmission electron microscopy. *Nano Res.* **2014**, *7* (8), 1188.
(19) Hillerich, K.; Dick, K. A.; Wen, C.; Reuter, M. C.; Kodambaka, S.; Ross, F. M. Strategies To Control Morphology in Hybrid Group III−V/Group IV Heterostructure Nanowires. *Nano Lett.* **2013**, *13* (3), 903−908.
(20) Hakkarainen, T.V.; Schramm, A.; Mäkelä, J.; Laukkanen, P.; Guina, M. Lithography-free oxide patterns as templates for self-catalyzed growth of highly uniform GaAs nanowires on Si(111). *Nanotechnology* **2015**, *26*, 275301.
(21) Koivusalo, E.; Hakkarainen, T.; Guina, M. Structural Investigation of Uniform Ensembles of Self-Catalyzed GaAs Nanowires Fabricated by a Lithography-Free Technique. *Nanoscale Res. Lett.* **2017**, *12* (1), 192.
(22) Koivusalo, E. S.; Hakkarainen, T. V.; Guina, M. D.; Dubrovskii, V. G. Sub-Poissonian Narrowing of Length Distributions Realized in Ga-Catalyzed GaAs Nanowires. *Nano Lett.* **2017**, *17* (9), 5350−5355.
(23) Colombo, C.; Spirkoska, D.; Frimmer, M.; Abstreiter, G.; Fontcuberta i Morral, A. Ga-assisted catalyst-free growth mechanism of GaAs nanowires by molecular beam epitaxy. *Phys. Rev. B: Condens. Matter Mater. Phys.* **2008**, *77*, 155326.
(24) Uccelli, E.; Arbiol, J.; Magen, C.; Krogstrup, P.; Russo-Averchi, E.; Heiss, M.; Mugny, G.; Morier-Genoud, F.; Nygård, J.; Morante, J. R.; Fontcuberta i Morral, A. Three-Dimensional Multiple-Order Twinning of Self-Catalyzed GaAs Nanowires on Si Substrates. *Nano Lett.* **2011**, *11* (9), 3827−3832.
(25) Yuan, X.; Caroff, P.; Wong-Leung, J.; Fu, L.; Tan, H. H.; Jagadish, C. Tunable Polarity in a III−V Nanowire by Droplet Wetting and Surface Energy Engineering. *Adv. Mater.* **2015**, *27* (40), 6096−6103.
(26) Wacaser, B.; Deppert, K.; Karlsson, L.; Samuelson, L.; Seifert, W. Growth and characterization of defect free GaAs nanowires. *J. Cryst. Growth* **2006**, *287* (2), 504−508.
(27) Zhang, Y.; Sun, Z.; Sanchez, A. M.; Ramsteiner, M.; Aagesen, M.; Wu, J.; Kim, D.; Jurczak, P.; Huo, S.; Lauhon, L. J.; Liu, H. Doping of Self-Catalyzed Nanowires under the Influence of Droplets. *Nano Lett.* **2018**, *18* (1), 81−87.
(28) Li, L.; Pan, D.; Yu, X.; So, H.; Zhao, J. Manipulation of morphology and structure of the top of GaAs nanowires grown by molecular-beam epitaxy. *J. Semicond.* **2017**, *38* (10), 103001.
(29) Jacobsson, D.; Panciera, F.; Tersoff, J.; Reuter, M. C.; Lehmann, S.; Hofmann, S.; Dick, K. A.; Ross, F. M. Interface dynamics and crystal phase switching in GaAs nanowires. *Nature* **2016**, *531*, 317.
(30) Dubrovskii, V. G. Development of Growth Theory for Vapor−Liquid−Solid Nanowires: Contact Angle, Truncated Facets, and Crystal Phase. *Cryst. Growth Des.* **2017**, *17* (5), 2544−2548.
(31) Wen, C.-Y.; Tersoff, J.; Hillerich, K.; Reuter, M. C.; Park, J. H.; Kodambaka, S.; Stach, E. A.; Ross, F. M. Periodically Changing Morphology of the Growth Interface in Si, Ge, and GaP Nanowires. *Phys. Rev. Lett.* **2011**, *107* (2), 025503.
(32) Glas, F.; Harmand, J.; Patriarche, G. Why does wurtzite form in nanowires of III-V zinc blende semiconductors? *Phys. Rev. Lett.* **2007**, *99* (14), 146101.
(33) Glas, F.; Ramdani, M. R.; Patriarche, G.; Harmand, J. Predictive modeling of self-catalyzed III-V nanowire growth. *Phys. Rev. B: Condens. Matter Mater. Phys.* **2013**, *88* (19), 195304.
(34) Dubrovskii, V. G. Group V sensitive vapor−liquid−solid growth of Au-catalyzed and self-catalyzed III−V nanowires. *J. Cryst. Growth* **2016**, *440* (15), 62−68.
(35) Rieger, T.; Heiderich, S.; Lenk, S.; Lepsa, M. I.; Grützmacher, D. Ga-assisted MBE growth of GaAs nanowires using thin HSQ layer. *J. Cryst. Growth* **2012**, *353* (1), 39−46.
(36) Ramdani, M. R.; Harmand, J. C.; Glas, F.; Patriarche, G.; Travers, L. Arsenic Pathways in Self-Catalyzed Growth of GaAs Nanowires. *Cryst. Growth Des.* **2013**, *13* (1), 91−96.
(37) Matteini, F.; Dubrovskii, V. G.; Rüffer, D.; Tütüncüoğlu, G.; Fontana, Y.; Fontcuberta i Morral, A. Tailoring the diameter and density of self-catalyzed GaAs nanowires on silicon. *Nanotechnology* **2015**, *26* (10), 105603.
(38) Billig, E. Growth of monocrystals of germanium from an undercooled melt. *Proc. R. Soc. London, Ser. A* **1955**, *229* (1178), 346−363.
(39) Hamilton, D. R.; Seidensticker, R. G. Propagation Mechanism of Germanium Dendrites. *J. Appl. Phys.* **1960**, *31* (7), 1165−1168.
(40) Shahani, A. J.; Voorhees, P. W. Twin-mediated crystal growth. *J. Mater. Res.* **2016**, *31* (19), 2936−2947.
(41) Gamalski, A. D.; Voorhees, P. W.; Ducati, C.; Sharma, R.; Hofmann, S. Twin Plane Re-entrant Mechanism for Catalytic Nanowire Growth. *Nano Lett.* **2014**, *14* (3), 1288−1292.
(42) Oliveira, D. S.; Tizei, L. H. G.; Li, A.; Vasconcelos, T. L.; Senna, C. A.; Archanjo, B. S.; Ugarte, D.; Cotta, M. A. Interaction between lamellar twinning and catalyst dynamics in spontaneous core−shell InGaP nanowires. *Nanoscale* **2015**, *7* (29), 12722−12727.
(43) Moll, N.; Kley, A.; Pehlke, E.; Scheffler, M. GaAs equilibrium crystal shape from first principles. *Phys. Rev. B: Condens. Matter Mater. Phys.* **1996**, *54* (12), 8844−8855.
(44) Kim, W.; Dubrovskii, V. G.; Vukajlovic-Plestina, J.; Tütüncüoglu, G.; Francaviglia, L.; Güniat, L.; Potts, H.; Friedl, M.; Leran, J.; Fontcuberta i Morral, A. Bistability of Contact Angle and Its Role in Achieving Quantum-Thin Self-Assisted GaAs nanowires. *Nano Lett.* **2018**, *18* (1), 49−57.

DOI: 10.1021/acs.nanolett.8b03365
Nano Lett. 2019, 19, 82−89

Supporting Information

Deterministic switching of the growth direction of self-catalyzed GaAs nanowires

Eero S. Koivusalo [1], Teemu V. Hakkarainen[1], Helder V. A. Galeti[2], Yara, G. Gobato[3], Vladimir G. Dubrovskii[4], Mircea D. Guina[1]*

[1] Optoelectronics Research Centre, Tampere University of Technology, P.O. Box 692, FIN-33101 Tampere

[2] Electrical Engineering Department, Federal University of São Carlos, 13565-905, São Carlos-SP, Brazil

[3] Physics Department, Federal University of São Carlos, 13565-905, São Carlos-SP, Brazil

[4] ITMO University, Kronverkskiy prospekt 49, 197101 St. Petersburg, Russia

* Email: eero.koivusalo@tut.fi

S1: SEM analysis of the NW top faceting

GaAs NWs grown for 20 min and annealed at the growth temperature for 45 s prior to cooldown without any fluxes were analyzed by SEM. Ga catalyst droplets were removed from the NWs by etching for 30 s in 10% HCl in IPA and rinsing in IPA. An in-lens detector was used to analyze the general shape of the top-facets with the highest possible resolution [Figure S1 (a)]. Based on this image it is evident that two out of six corners between NW (111)B top facet and <112> sidewall corners are reshaped during the annealing. Orientation of the facets was investigated using secondary electron (SE) detector. Images S1 (b) are taken using a low (few volts) collector bias, to increase the contribution of the backscattered electrons and brighten the facets which are tilted toward the detector. Images S1 (c) to (e) are taken using 150 V repulsive detector bias to deflect all secondary electrons and only detect the backscattered electrons. This procedure further enhances the topographical information. Image S1 f) is taken using standard 250 V collecting detector bias. Images (d) to (f) are from the same NW: (d) shows a single facet but as the contrast is increased for image (e), another facet becomes visible. Image (f) shows the full shape of the NW tip. This morphology is a clear sign of the three facets at the NW top, illustrated in the sketch in Fig. 2 (e) to (h) of the main text.

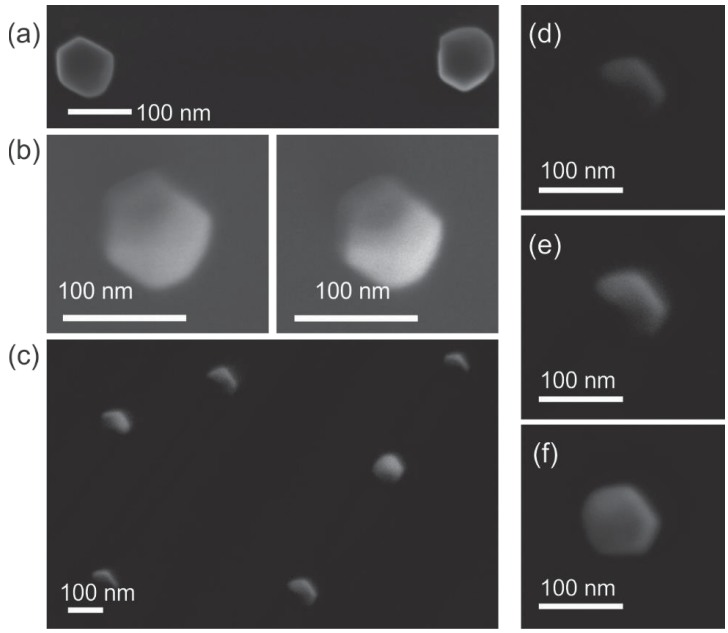

Figure S1: SEM analysis of NW top facets, with the droplets removed by HCl etching

(a) image taken with in-lens detector showing the general shape of the NW tip. (b) image taken with low (few Volt) SE detector bias (c)–(e) images taken with SE detector under repulsive bias revealing bright facets that backscatter electrons towards the detector and the shaded ones scattering electrons away from the detector. (d)–(f) analysis of a single NW with different contrasts achieved by different detector biases.

S2: Analysis of type 1 and 2 populations

The statistics were always collected from equivalent locations on different samples to avoid the effect of temperature inhomogeneity over the substrate surface. Figure S2 shows typical SEM images used

for statistical analysis. The insets more detailed views of type 1 and 2 structures. At least two similar images were analyzed from each sample representing about 100 NWs.

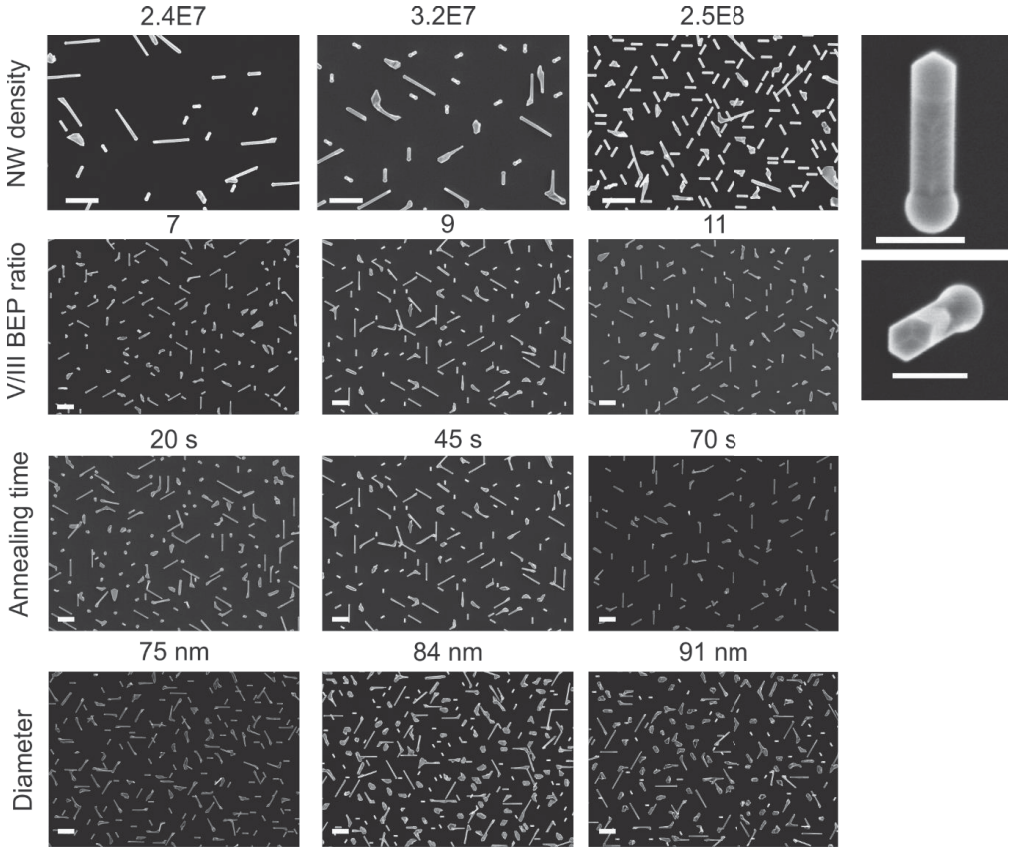

Figure S2: Analysis of type 1 and 2 populations

SEM images used to acquire statistical data for the different NW structures with the growth parameters indicated for each image. Note that the images in the center column of the three top rows are the same as they represent the intermediate data point for all the parameters investigated. Higher magnification images show the individual type 1 and type 2 NWs. Scale bars in overview images are 1 µm in the images of the NW arrays and 200 nm in the images of individual NWs.

S3: Different structures from top-view

Different types of structures found on the high-density sample with 100 % yield of growth direction switching are shown in Figure (S3). The structure labeled 1 is formed, when two type 1 bent NWs merge during the growth The structure labeled 2 is a type 1 NW, 3 is a tilted NW which has also switched the growth direction, while 4 is a parasitic growth.

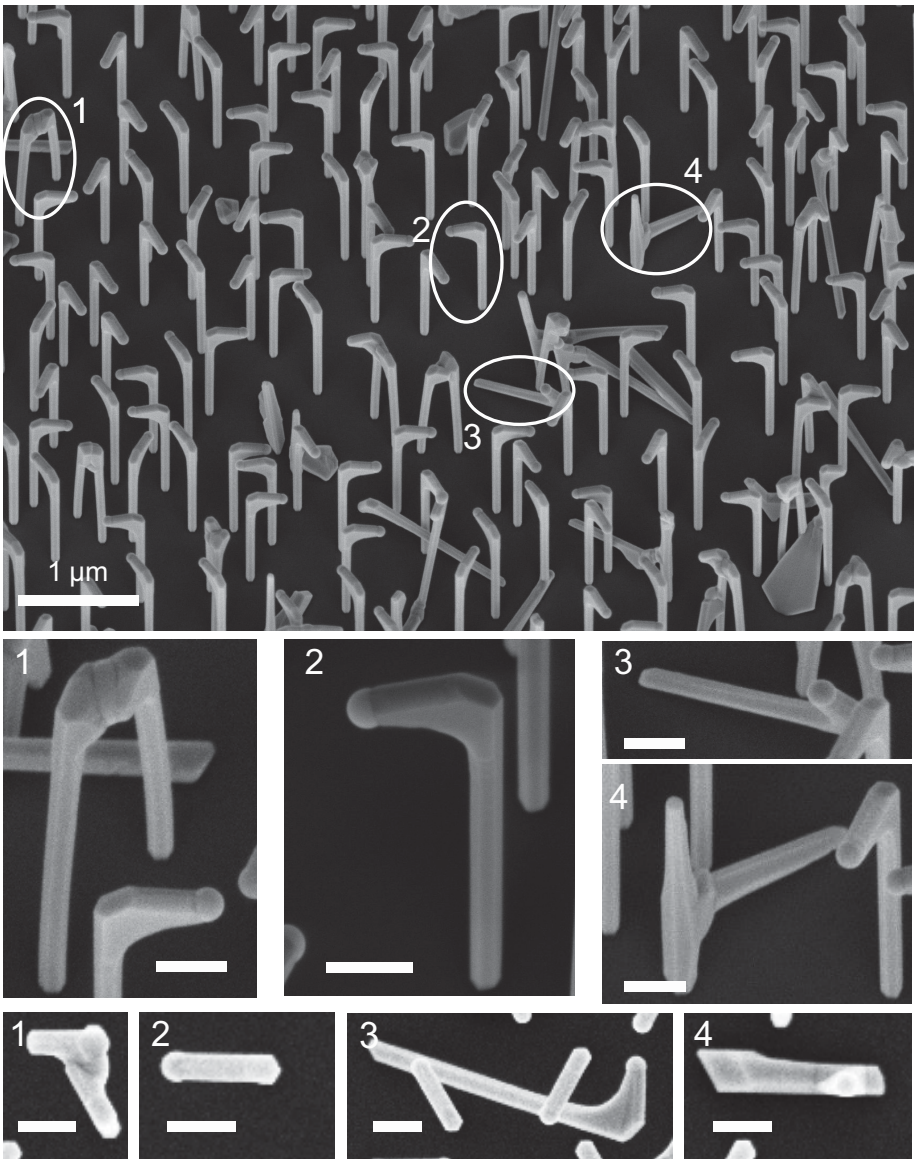

Figure S3: Different structures from top-view

Structures marked in 30° tilted view SEM images with magnifications from the same images. In the bottom row, similar types of structures are found in the top-view images used for the statistical analysis (S2). All scale bars in high magnification images are 200 nm.

S4: Type 1 horizontal growth rate

The horizontal growth rate was analyzed from top-view SEM images by measuring the length of the horizontal part and subtracting the NW diameter as measured from cross-sectional images below the tapered part. A linear fit to the time-dependent length in horizontal growths gives a growth rate of 3.8 µm/h, which is identical to the vertical growth rate determined for a growth time series from 3 to 80 min in our previous work [1]. Incubation time of 38 s was determined for the horizontal growth based on the same linear fit. Based on the linearity of the horizontal growth and the stable morphology of the NW after 20 min of horizontal growth, it can be reasonably assumed that the twin mediated oscillating growth mode is stable and can be sustained for even longer time periods if needed.

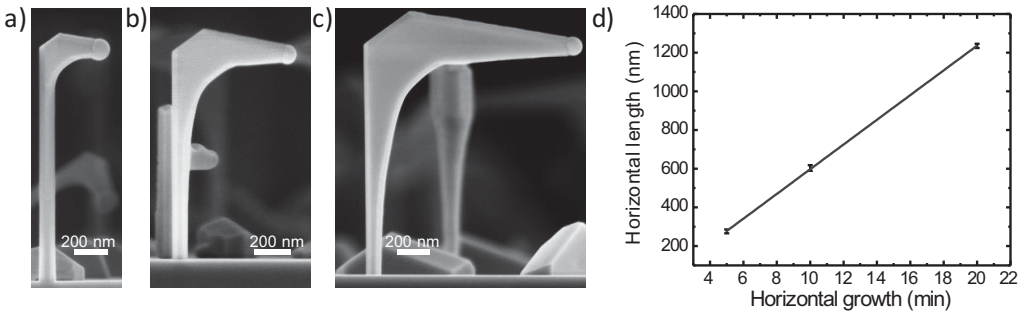

Figure S4: Analysis of type 1 horizontal growth rate

(a-c) Bent type 1 NWs after 5 (a), 10 (b), and 20 (c) min of horizontal growth; (d) Linearity of the horizontal length versus time. The mean NW diameter was subtracted from the horizontal length data after the measurements.

S5: Evolution of type 2 downward growth

Time evolution of a type 2 structure during the growth was analyzed from the same samples as in S4. The analysis further clarifies the downward nature of type 2 growth. As the growth proceeds the top of the downward section evolves faster than the original top of the vertical NW and eventually reaches it as demonstrated in Figure S5 (c).

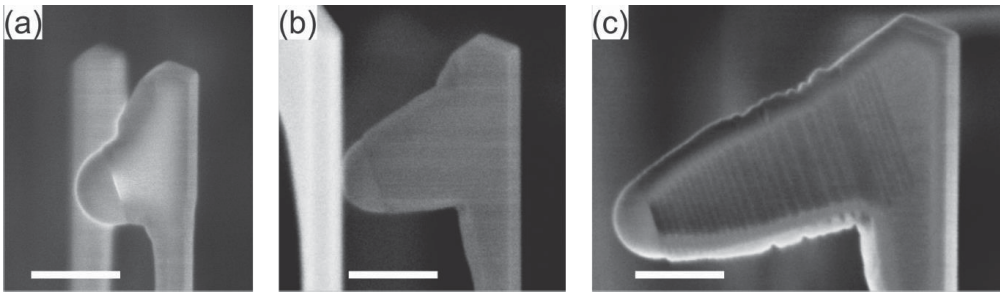

Figure S5: Analysis of type 2 downward growth

Type 2 structures after 5 (a), 10 (b) and 20 (c) min of downward growth. The scale bars are 200 nm.

S6: Additional SEM analysis of the droplet-NW interface

Droplets were removed from bent NWs with horizontal growth time ranging from 5 to 20 min similarly to S1. Type 1 NWs reveal two different morphologies of the growth interface as expected from the TEM analysis presented in Figure 3 of the main text. Type 1 NWs on the left side of Figure S5 [(a),(c),(e)] represent the facet morphology dominated by a flat B-polar (111)B facet above, and microfacetting below the twin plane. Type 1 NWs on the right side [Figure S5 (b),(d),(f)] represent morphology dominated by a flat (111)A below and microfacetting above the twin plane. Type 2 NWs in Figure S5 (g)–(h) show consistently a flat end facet.

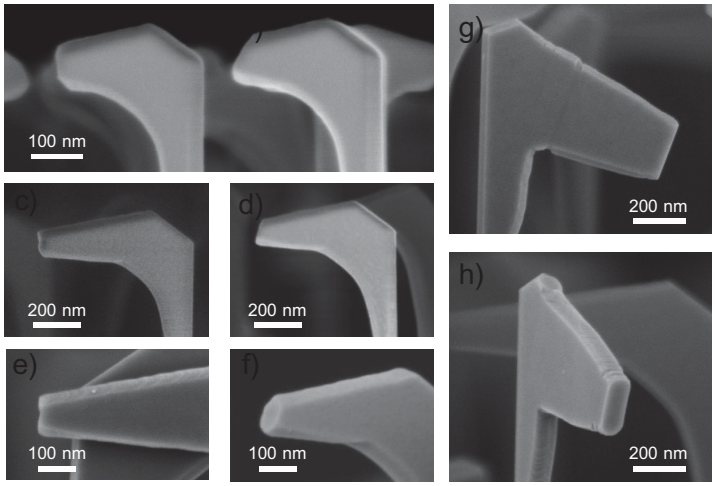

Figure S6: Facets dominating the horizontal or downward growth.

Type 1 NWs grown for 5, 10 and 20 min in (a,b), (c,d) and (e,f), respectively. Type 2 NWs in (g) and (h) with 20 min downward growth duration.

S7: Exceptions from sustainable type 1 and 2 growth

While optimizing the horizontal growth conditions for type 1 yield, several mechanism limiting the growth window for type 1 and 2 structures were found. The shortest annealing time of 20 s was found to produce a poor control of switching of the growth direction, in agreement with the model. Too short annealing leads to the formation of bulges which are shown in Figure S7 (a). Figure S7 (b) shows different stages of type 1b formation under a low V/III BEP ratio of 7. The droplets swell and start to wet the sidewalls of the horizontal NW. At a certain stage, they completely slip onto the sidewalls, terminating controlled horizontal growth. An excessive As flux with V/III BEP ratio of 11 is also problematic for sustaining the resumed growth. 40% of type 2 NWs, identified based on their characteristic shape of the top facet, eventually lose their droplets as they crystallize along the NW sidewall forming type 2b NWs as witnessed in Figure S7 (c). Simultaneously, type 1 NWs exhibit a strong tapering due to continuous shrinking of the droplet size.

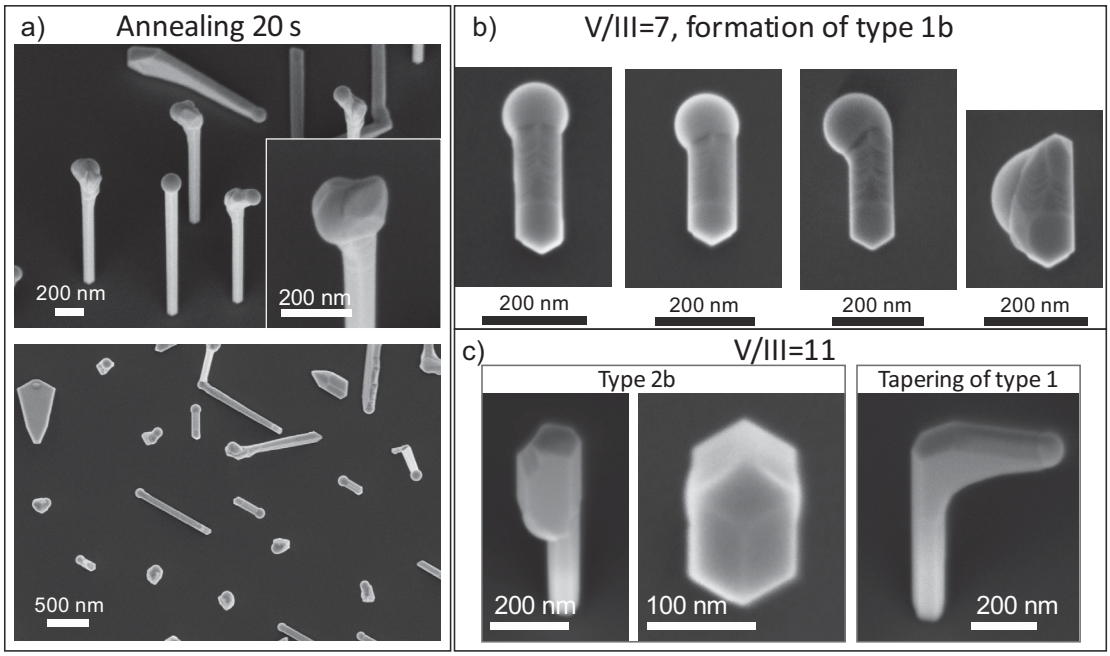

Figure S7: Loosing the stability of resumed growth

(a) NWs annealed for 20 s at the growth temperature and with 5 min resumed growth. (b) different stages of type 1b formation are illustrated. (c) NWs grown with V/III BEP ratio of 11 showing type 2b structures and continuous shrinking of the Ga droplets in type 1 structures.

S8: TEM analysis of NWs prior to annealing

A single NW from the sample without post-growth annealing was rotated from [110] ZA to [112] ZA, as shown in the SAED patterns in Figure S7. The analysis shows a pure ZB structure and minor truncation at the droplet-NW interface.

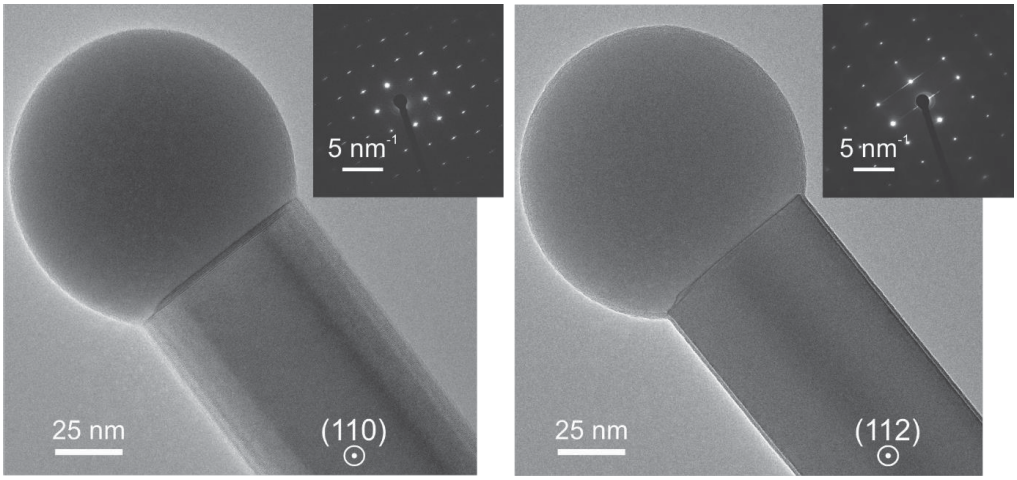

Figure S8: NWs prior to annealing

TEM images taken from the same NW in [110] and [112] ZA revealing the pure ZB structure of the NWs.

S9: Same plane of horizontal growth

All horizontal growth of type 1 occurs on the same height with respect to the substrate. This is demonstrated by the 5 min and 20 min grown horizontal sections in Fig. S9 (a) and (b), respectively.

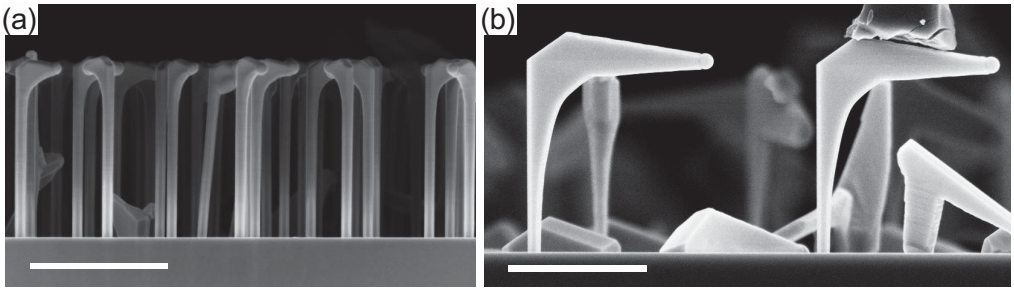

Figure S9: Same Plane of horizontal growth

Side-view SEM images of type 1 structures after 5 (a) and 20 (b) min growth of horizontal sections. The images show that the horizontal growth occurs within a constant distance from the substrate surface, i.e. in the same horizontal plane. The scale bars are 1 μm.

S10: Derivation of time-dependent chemical potential in the annealing stage

Transition from vertical to horizontal growth is induced by annealing the NWs at a growth temperature of 640 °C without any fluxes. Chemical potential in self-catalyzed growth of GaAs NWs is determined by the atomic concentration of As atoms in the Ga droplet c_5 [2]. Due to a low solubility of As in liquid Ga ($c_5 << 1$), a good approximation for chemical potential writes down as

$$\Delta\mu = const + k_B T \ln c_5 \tag{S1}$$

This c_5 can be approximated as

$$c_5 \cong \frac{N_5}{N_3}, \tag{S2}$$

where N_5 is the total number of As atoms in the droplet and $N_3 \cong const$ is the total number of Ga atoms. Assuming that N_5 decreases with time mainly due to crystallization of GaAs pairs, we can write

$$\frac{dN_5}{dt} = -\frac{\pi R^2 h}{\Omega_{35}} k_{35} c_3 c_5 \cong -\frac{\pi R^2 h}{\Omega_{35}} k_{35} c_5, \tag{S3}$$

with R as the NW radius (which equals the radius of the droplet base), h as the height of GaAs monolayer (ML), Ω_{35} as the elementary volume of solid GaAs, and k_{35} as the crystallization rate of GaAs pairs in ML/s. The last expression in (S3) is valid because the gallium concentration $c_3 = 1 - c_5 \cong 1$ at $c_5 << 1$.

Using

$$N_3 = \frac{\pi R^3 f(\beta)}{3\Omega_3}, \tag{S4}$$

with Ω_3 as the elementary volume of liquid Ga and $f(\beta)$ as the geometrical function of the contact angle β given in the main text, we can re-write Eq. (S3) in the closed form

$$\frac{dc_5}{dt} = -\frac{3\Omega_3}{\Omega_{35} f(\beta)} k_{35} \frac{h}{R} c_5 \equiv -W c_5 . \tag{S5}$$

Solving this with the initial condition $c_5(t=0) = c_5(0)$, we obtain

$$c_5(t) = c_5(0) e^{-Wt}. \tag{S6}$$

Using Eq. (S6) in Eq. (S1), we find

$$\Delta\mu(t) = \Delta\mu_0 - k_B T W t = \Delta\mu_0 (1 - \omega t), \tag{S7}$$

with ω given in Eq. (4) of the main text.

References

[1] E.S. Koivusalo, T.V. Hakkarainen, M.D. Guina, V.G. Dubrovskii, Sub-Poissonian Narrowing of Length Distributions Realized in Ga-Catalyzed GaAs Nanowires, Nano Letters, Vol. 17, Iss. 9, 2017, pp. 5350-5355, DOI: 10.1021/acs.nanolett.7b01766

[2] F. Glas, M.R. Ramdani, G. Patriarche, J. C.Harmand, Predictive modeling of self-catalyzed III-V nanowire growth, Phys. Rev. B, Vol. 88, Iss. 19, 2013, pp. 195304 DOI: https://doi.org/10.1103/PhysRevB.88.195304

PUBLICATION 4

The role of As species in self-catalyzed growth of GaAs and GaAsSb nanowires

E. Koivusalo, J. Hilska, H. V. A. Galeti, Y. G. Gobato, M. Guina, and T. Hakkarainen,

Nanotechnology, 2020
https://doi.org/10.1088/1361-6528/abac34

PUBLICATION 5

Gradients of Be-dopant concentration in self-catalyzed GaAs nanowires

M. Rizzo Piton, E. Koivusalo, T. Hakkarainen, H.V.A. Galeti, A. De Giovanni Rodrigues, S. Talmila, S. Souto, D. Lupo, Y. Galvão Gobato and M. Guina

Nanotechnology, vol. 30, no. 33, pp. 335709, 2019
https://doi.org/10.1088/1361-6528/ab1a97

Gradients of Be-dopant concentration in self-catalyzed GaAs nanowires

Marcelo Rizzo Piton[1,2], Eero Koivusalo[2], Teemu Hakkarainen[2], Helder Vinicius Avanço Galeti[3], Ariano De Giovanni Rodrigues[1], Soile Talmila[2], Sergio Souto[4], Donald Lupo[5], Yara Galvão Gobato[1,6] and Mircea Guina[2]

[1] *Physics Department, Federal University of São Carlos, São Carlos-SP, Brazil*

[2] *Optoelectronics Research Centre, Physics Unit, Tampere University, Tampere, Finland*

[3] *Electrical Engineering Department, Federal University of São Carlos, São Carlos-SP, Brazil*

[4] *FZEA/ZAB, University of São Paulo, Pirassununga-SP, Brazil*

[5] *Electronics and Communications Engineering, Tampere University, Tampere, Finland*

[6] *High Field Magnetic Laboratory, Radboud University, The Netherlands*

KEYWORDS: Nanowires, GaAs, Be doping, Concentration profiles

Abstract

Effective and controllable doping is instrumental for enabling the use of III-V semiconductor nanowires in practical electronics and optoelectronics applications. To this end, dopants are incorporated during self-catalyzed growth via vapour-liquid-solid mechanism through the catalyst droplet or by vapour-solid mechanism of the sidewall growth. The interplay of these mechanisms together with the competition between axial elongation and radial growth of nanowires can result in dopant concentration gradients along the nanowire axis. Here, we report an investigation of Be-doped p-type GaAs nanowires grown by the self-catalyzed method on lithography-free Si/SiO_x templates. The influence of dopant incorporation on the structural properties of the nanowires is analysed by scanning and transmission electron microscopy. By combining spatially resolved Raman spectroscopy and transport characterization, we are able to estimate the carrier concentration, mobility and resistivity on single nanowire level. We show that Be dopants are incorporated predominantly by vapour-solid mechanism for low Be flux, while the relative contribution of vapour-liquid-solid incorporation is increased for higher Be flux, resulting in axial dopant gradients that depend on the nominal doping level.

1. Introduction

Semiconductor III-V nanowires (NWs) have emerged due to their unique properties and development opportunities they render possible to a wide range of optoelectronics devices [1,2], such as LEDs [3,4], solar cells [5,6], and photodetectors [7]. The one-dimensional NW geometry brings specific advantages including the possibility to combine different semiconductor alloys as radial and axial heterostructures, and relaxes the lattice matching requirements; in turn, this enables III-V semiconductor NW growth on dissimilar substrates such as Si [1] which is widely used in electronics. Going into more details of the fabrication of such NWs, the self-catalyzed growth [8,9] has been adopted for direct epitaxial integration because it avoids the use of foreign catalyst metals such as Au, which is known to form deep traps in Si and therefore degenerate device performance [10]. Substantial progress has been made recently in self-catalyzed growth of GaAs NWs with high control of the size distributions and crystalline

structure [11–16]. Moreover, the ability to achieve an effective and controllable doping is essential for bringing these nanostructures to the realm of practical applications, for example enabling formation of p-n junctions without compromising the material quality of the NWs. It should be emphasized that the knowledge of the dopant incorporation in traditional thin film epitaxy cannot be directly applied to NW growth. Therefore, significant effort has been dedicated to investigate the dopant incorporation mechanisms in NW growth [17]. The dopants are incorporated in NWs either via vapor-liquid-solid (VLS) mechanism through the catalyst droplet, or via vapor-solid (VS) mechanism during the sidewall growth. The incorporation of p-type dopant Be into GaAs NWs during self-catalyzed growth has been investigated by several groups and different incorporation mechanisms have been reported. Casadei et al. reported a preferential VS Be incorporation via the NWs sidewalls [18]. Zhang et al. proposed a predominance of Be incorporation through the Ga catalyst droplets [19] and in the work of Dastjerdi et al. it was determined that Be dopants incorporated through truncated facets under the Ga droplet followed by diffusion into the core of the NWs [20]. These previous studies suggest that the Be incorporation strongly depends on the growth conditions.

Here, we report an investigation of Be-doped self-catalyzed GaAs NWs grown on lithography-free Si/SiO_x templates fabricated by droplet epitaxy and spontaneous oxidation of Si substrates [11,12]. We examine the microstructural changes caused by Be dopant incorporation and, in particular, assess the dopant concentration and its axial variations by single-NW Raman and electrical characterization techniques, respectively. We show that different axial gradients of Be concentration are formed for different Be fluxes. Our results suggest that the predominant Be incorporation mechanism is VLS for high Be flux and VS for low Be flux.

2. Experimental Methods

The self-catalyzed GaAs NWs were grown by solid-source molecular beam epitaxy (MBE) on lithography-free oxide patterns fabricated on p-Si(111) substrates by droplet epitaxy and spontaneous oxidation. GaAs droplet epitaxy was performed on oxide-free HF-etched substrates. After the droplet epitaxy, the wafers were removed from the MBE reactor, oxidized in air and loaded back to the MBE.

Prior to NW growth, the samples were annealed for 30 min at 655 °C, as determined by pyrometer, in order to evaporate the GaAs mounds and to reveal oxide-free holes for NW nucleation as described in detail in Ref. [12]. The nucleation site density of the templates used was 2×10^{8} cm^{-2}. The annealing was followed by a 60 s Ga pre-deposition at the NW growth temperature of 640 °C with Ga flux corresponding to planar 0.3 μm/h growth rate on GaAs(100). The NW growth was then initiated by providing As_2 corresponding to a V/III beam equivalent pressure ratio (BEP) of 9. The NWs were grown for 60 min and the growth was terminated by switching off all fluxes simultaneously and rapidly cooling down the sample. The NWs were doped with Be fluxes corresponding to a nominal p-type dopant concentrations of 2.0×10^{18} cm^{-3} and 2.0×10^{19} cm^{-3} for samples hereafter named Be1 and Be2, respectively. The doping levels were calibrated based on Hall measurements of three planar Be-doped GaAs(100) samples grown on semi-insulating GaAs substrates. The thin film (TF) samples were later used for comparing the carrier concentration and mobility values obtained from Raman spectroscopy and Hall measurements, and will be from now on named TF1, TF2 and TF3, in the order of increasing Be flux used during the growth.

The structural properties of NWs were characterized by scanning electron microscopy (SEM) and transmission electron microscopy (TEM). SEM characterization was performed to collect dimensional data and to obtain images of the NWs used for Raman spectroscopy and transport characterization after the measurements were carried out. TEM was used to analyze the microstructure of single NWs harvested from the as-grown samples to a carbon film of a Cu TEM grid; for the analyses we used a FEI Tecnai G2-F20 operating at 200 kV.

Room temperature Raman spectra of single NWs were obtained on backscattering geometry. The NWs were transferred to a Si substrate with a 200 nm SiO_2 thermal oxide layer. The excitation wavelength was 532 nm and a 50x magnification lens with NA=0.82 was used to obtain a spot size of <1 μm in diameter. Raman spectra with varying excitation power were first collected from test NWs to select the optimal power density that would not result in any shifts or broadening of Raman peaks due to laser-induced heating. The linear polarization of both excitation laser and scattered light were adjusted perpendicular to the NW growth axis. The TF samples were also investigated by Raman

spectroscopy with equivalent configuration of linear polarizations of excitation and detection to evaluate the methodology adopted on analysis of the Raman spectra for assessing the free carrier concentration and mobility.

For single-NW transport characterization, the NWs were first drop-casted on a p-GaAs substrate covered by a 200 nm SiO_2 layer with pre-patterned gold pads. The position of representative NWs on the substrate were identified by SEM imaging and electron beam lithography was used to fabricate electrical contacts on individual NWs. After resist development, the sample was dipped in 1:10 $HCl:H_2O$ solution for 10 s to remove the native oxide, followed by 15% ammonium polysulfide $(NH_4)2S_x$ diluted in H_2O for chemical passivation (45 °C, 3 min) of the exposed contact area of the NWs. After chemical treatments of the surface, the NWs were immediately taken to an electron beam metal evaporation equipment and a Pt/Ti/Pt/Au (5/10/10/200 nm) metallic multilayer was deposited on the sample. After lift-off of the resist, a rapid thermal annealing at 400 °C for 30 s was performed to reduce the contacts resistance. Current-voltage (IV) measurements were carried using an Agilent Source-Meter Unit.

3. Results and discussion

3.1 Structural properties

TEM and HR-TEM images from selected areas of undoped and Be-doped GaAs NWs were obtained to evaluate the influence of Be incorporation on the microstructural properties of the NWs. The results are summarized in figures. 1(a)-(d) for undoped NWs, in figures 1(e)-(h) for Be1 NWs, and in figures 1(i)-(l) for Be2 NWs. The bright-field (BF) TEM image of undoped NW in figure 1(a) shows that the twin plane density increases towards the NW/droplet interface, region at which the contact angle between the Ga droplet and NW tip decreases due to lateral growth favoring the twin plane formation [12]. HR-TEM imaging of the root region in figure 1(d) shows a 100 nm long section of stacking faults and polytypism, followed by a 2 μm long center region of pure zincblend (ZB) GaAs, as shown in figure 1(c). A short wurtzite (WZ) section (~5 nm) was formed at the interface of the Ga droplet and the NW body (figure 1(b)), which is commonly observed in self-catalyzed growth of GaAs NWs due to rapid

changes in the growth conditions after switching off the Ga and As fluxes and subsequent ramp down of the sample temperature [12].

The BF images of Be1 and Be2 NWs are shown figures 1(e) and 1(i), respectively. The twin plane density at the center-tip regions is smaller than in the undoped sample shown in figure 1(a), which has been previously reported for self-catalyzed Be-doped GaAs NWs [19]. The root regions of Be1 and Be2 NWs, shown in figures 1(h) and 1(l), are composed of ZB structure with twin planes and stacking faults due to instabilities related to early-stages of the epitaxial growth, such as Ga droplet composition. It is evident that the incorporation of Be suppresses the twin plane formation in the center [figures 1(g) 1(k)] and NW-droplet interface [figures 1(f) and 1(j)] regions when compared to the undoped sample. The formation of twin planes and WZ segments in self-catalyzed GaAs NWs is commonly attributed to the droplet contact angle [9,21,22]. However, the post growth analysis of the distributions of droplet contact angles reveals no significant difference between the Be doped and undoped NWs (See Fig. S1 in the Supplementary Data). The mean values of contact angles and the standard deviations for Be1, Be2, and undoped NWs are 123.5° ± 4.6°, 126.4° ± 6.2° and 127.8° ± 5.3°, respectively. Furthermore, Be has been reported to suppresses the formation of WZ segments during Ga droplet crystallization [23], which is another indication that the influence of Be on the ZB crystal phase purity cannot be explained merely by a change of droplet contact angle. Therefore, the reduction of twinning and WZ stacking probability in the Be-doped NWs is most likely related to a more complex change of energetics in the VLS system, leading to an increase of ZB nucleation probability over WZ stacking and twin formation. Furthermore, the NWs grown with high Be flux [Be2 in figure 1(k)] exhibit roughening of the (110) sidewall planes along the whole NW length. The selected area electron diffraction (SAED) patterns corresponding to the HR-TEM images of the bottom, center and tip regions of undoped, Be1 and Be2 NWs can be found in figure S2 in the Supplementary Data.

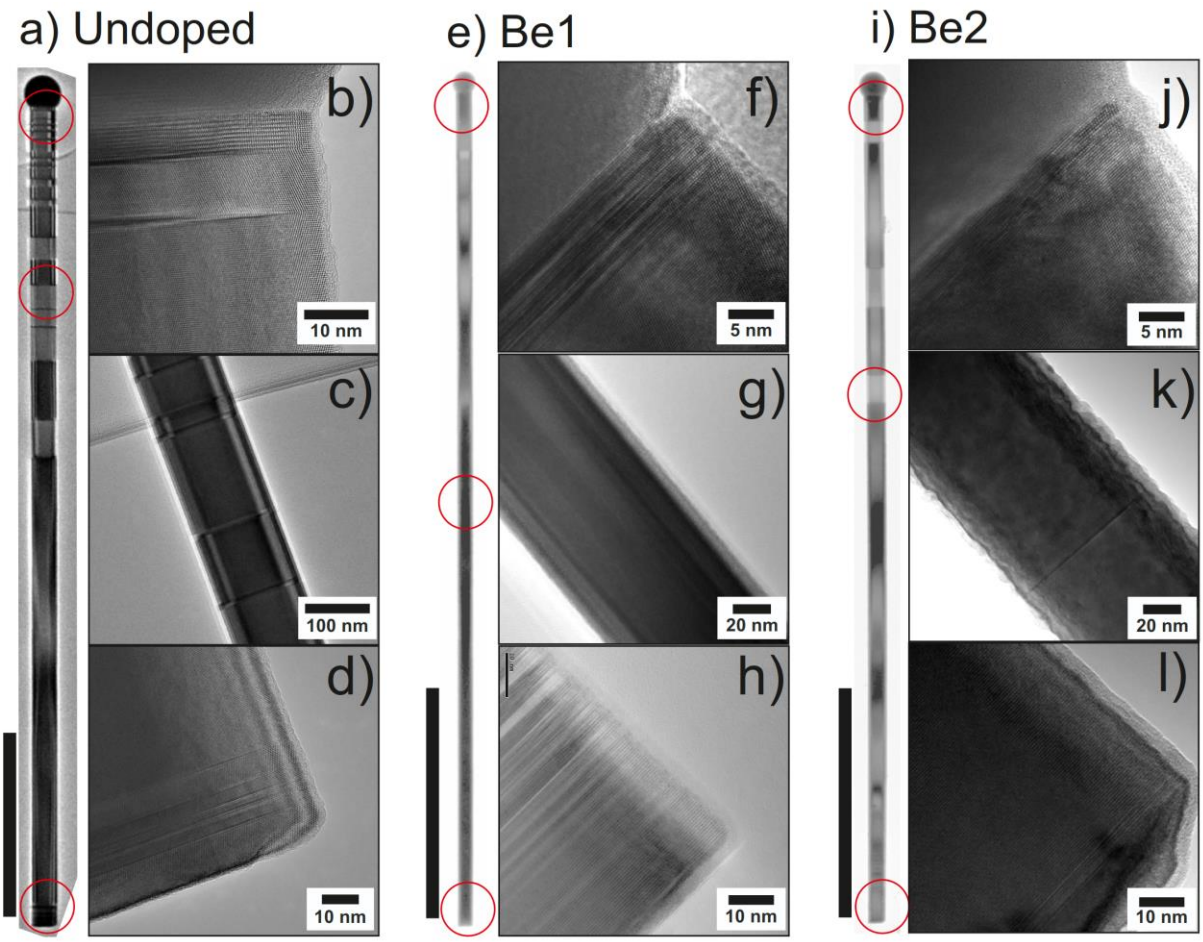

Figure 1. HR-TEM images of (a)-(d) undoped, (e)-(h) Be1, and (i)-(l) Be2 NWs. The red circles in (a), (e) and (i) indicate the different positions corresponding to the higher magnification images in (b)-(d), (f)-(h) and (j)-(l). The scale bars are 1 μm in (a), (e) and (i). The other scale bars sizes are indicated on each figure.

3.2 Raman spectroscopy

Single-NW Raman spectroscopy with microscopic resolution allows to investigate the effect of Be doping in different regions of the NW. Figure 2 shows Raman spectra of undoped, and two samples of Be-doped NWs (namely Be1 and Be2) collected from three different positions along the NW axes. The decomposition of the experimental data in Lorentzian peaks of undoped NWs in figure 2(a) reveals the transversal optical (TO), the surface optical (SO) and the longitudinal optical (LO) vibration modes of ZB GaAs centered at 268, 272 and 288 cm^{-1}, respectively. The SO modes are commonly observed in nanostructures with high surface-to-volume ratio. Its frequency depends on the surrounding medium [24] and density of defects, such as twin planes [25]. It was also reported that doping does not affect

SO mode frequency and linewidth [25]. It is worth mentioning that LO is a forbidden mode in Raman backscattering from (110) surface of ZB crystals [26], but this selection rule is relaxed to some extent for NWs due to finite size effects and hexagonal geometry of the cross section [24]. This allows to analyze the screening of the LO mode due to the presence of free carriers caused by Be incorporation on the NWs lattice [27].

In doped polar semiconductors, such as GaAs, the LO mode can couple to collective oscillations of free carriers producing a coupled-phonon-plasmon mode (CPPM) [28]. The line shape analysis of the CPPM can be used to estimate the free carriers concentrations and holes mobility for p-type GaAs epilayers [28,29] and NWs [18,27,30,31]. The Raman scattering intensity of the CPPM can be described by [32]:

$$I(\omega) = A\omega\Gamma_p\omega_p[\omega_{TO}^2(1+C) - \omega^2]^2/D \quad (1)$$

With:

$$D = \left[\omega^2(\omega_{LO}^2 - \omega^2) - \omega_p^2(\omega_{TO}^2 - \omega^2) + \gamma\Gamma_p\omega^2\right]^2 + \left[\Gamma_p\omega(\omega_{LO}^2 - \omega^2) + \gamma\omega\left(\omega_p^2 - \omega^2\right)\right]^2 \quad (2)$$

In this formulation, ω_{TO} and ω_{LO} are the TO and LO wavenumbers of an undoped reference sample respectively, A is a frequency independent parameter, C = -0.49 is the Faust-Henry coefficient for GaAs at room temperature for 532 nm laser excitation [33] and γ is the natural LO mode damping constant. The hole mobility μ_p can be calculated from the plasmon-damping constant $\Gamma_p = e/\mu_p m_p^*$ and the free carrier concentration p is obtained from the plasma oscillation frequency of the free carriers $\omega_p^2 = pe^2/\epsilon_0\epsilon_\infty m_p^*$. The remaining symbols have the usual meanings: e is the elementary electron charge, m_p* is the hole effective mass, ε_∞ is the high-frequency dielectric constant for GaAs and ε_0 is the vacuum permittivity.

Figures 2(b) and 2(c) show Raman spectra measured at three different positions of representative Be1 and Be2 NWs respectively. The figures include the spectral components related to TO, SO and CPPM modes that best fit the experimental data. On the right side are the corresponding SEM images

indicating the region of the NW from where Raman spectra were measured. The TO peak positions and linewidths are consistent with the undoped sample and the SO position is in accordance to the NW diameters and stacking faults/twin plane densities [24,25] observed in the HR-TEM images. The spectral position and linewidth of the CPPM mode is dependent on the carrier concentration and mobility [28]. The Raman peak at 256 cm^{-1} observed at the root section (P1) of Be2 NW in figure 2(c) corresponds to E_2^H TO mode of WZ phase of GaAs [34] which is consistent with the results from the HR-TEM in figure 1(l).

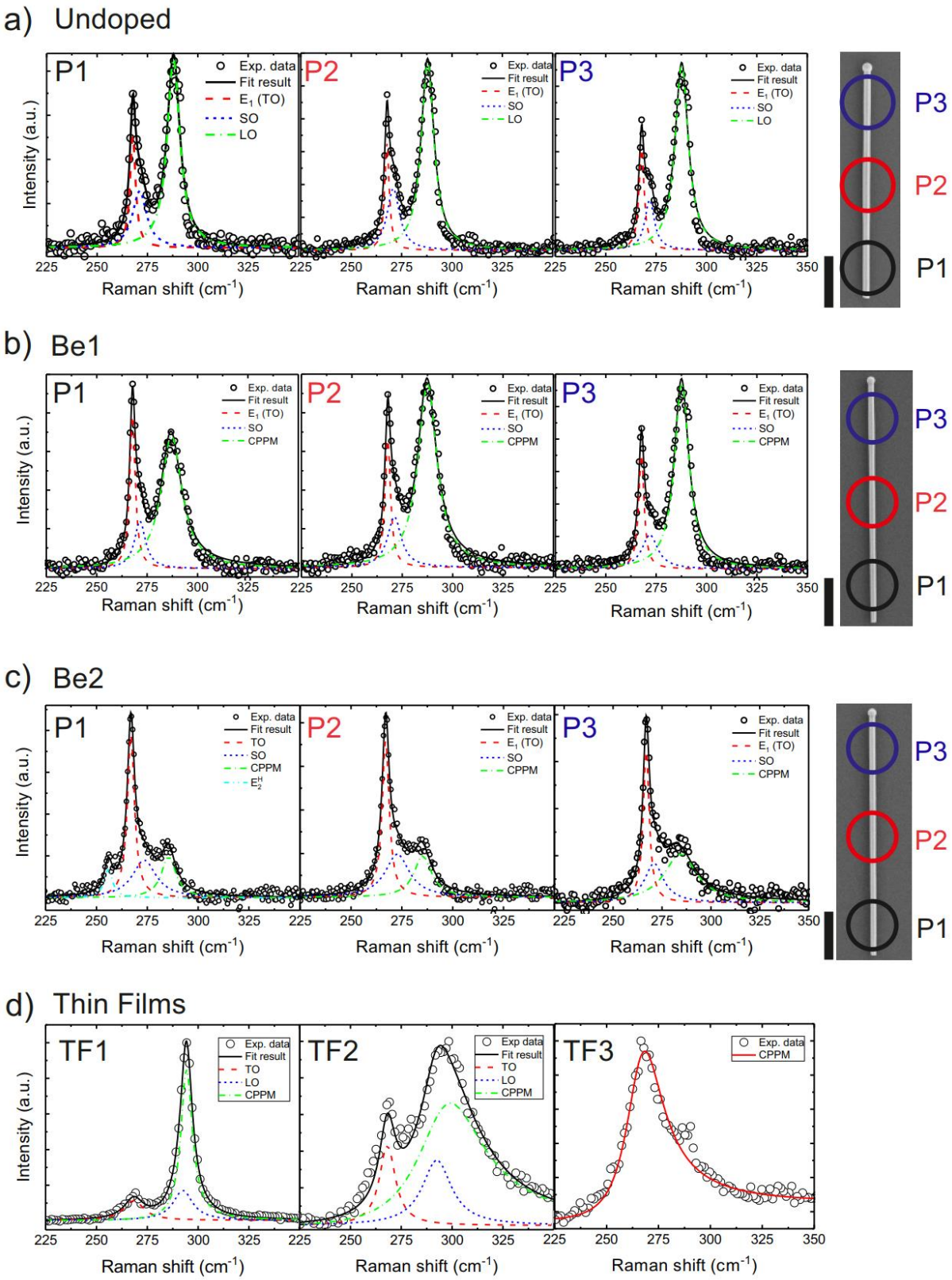

Figure 2. Raman spectra of (a) undoped, (b) Be1, (c) Be2 GaAs NWs, and (d) Be-doped GaAs TF samples. The spectra P1, P2, and P3 were collected from the regions indicated in the SEM pictures of the right sides of (a)-(c). The scale bars in the SEM pictures are 1 μm.

In order to evaluate the fit method applied to the Be1 and Be2 NWs, we analyzed the Raman spectra of TF samples considering the contribution of CPPM calculated through Eq. (1) and comparing the results with the Hall Effect data. The results are summarized in figure 3 for the carrier concentration (figure 3(a)) and the hole mobility (figure 3(b)). The carrier concentrations obtained from Raman and Hall Effect experiments in figure 3(a) are in good agreement, whereas the hole mobilities in figure 3(b) are clearly underestimated by Raman spectroscopy when compared with the Hall effect data. Similar results were previously reported for Zn-implanted GaAs [28] and p-type GaP [35]. In Ref. [35] the differences between values of hole mobility estimated by Raman and Hall effect are attributed to the contributions of several other factors that may cause an apparent decrease in the hole mobility at room temperature estimated by Raman spectroscopy, such as non-polar optical and acoustic phonons, polar optical phonons and ionized impurities [35,36].

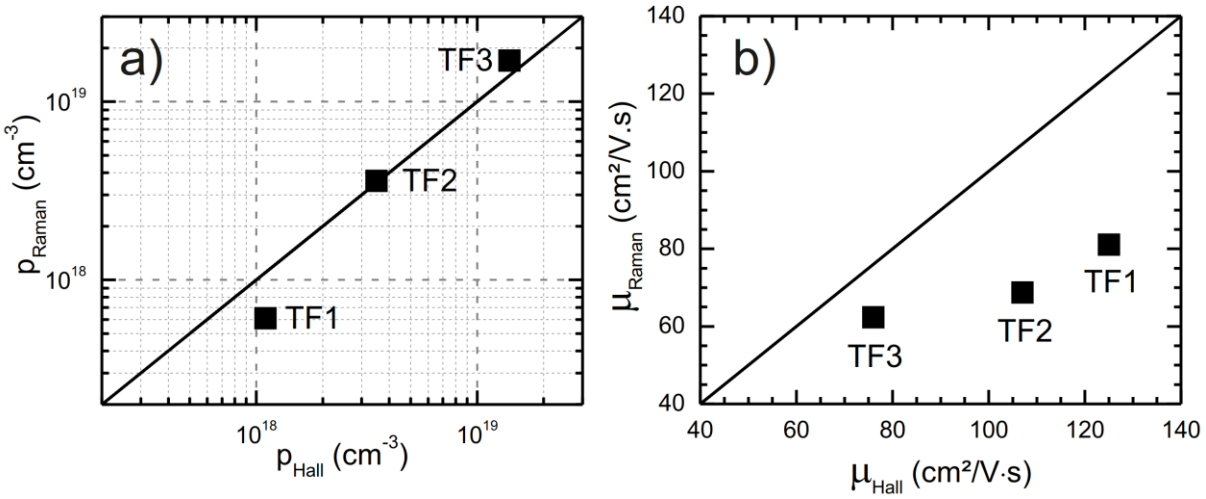

Figure 3. (a) Carrier concentration and (b) Hole mobility comparison between Hall effect data and fit of CPPM peak from Raman spectra of TF samples. The symbols represent the fit results and the solid lines, indicating one-to-one relation between Hall and Raman values, are for illustrational purposes.

By applying the same fitting procedure to the spectra in figures 2(b) and 2(c), we calculated the charge carrier concentrations and the hole mobilities of three representative NWs of each nominal doping level. The results of carrier concentration and hole mobility are presented in figures 4(a) and 4(b), respectively. The Raman spectra of the additional NWs from Be1 and Be2 samples are included in figure S3 in the Supplementary Data. The dashed lines in figure 4(a) represent the nominal doping

level of Be1 and Be2 samples. The hole concentrations from the NWs in figure 4(a) ranges from 8×10^{17} to 1.6×10^{18} cm^{-3} for Be1 NWs (nominal 2×10^{18} cm^{-3}) and from 3.4×10^{18} to 1.1×10^{19} cm^{-3} for Be2 NWs (nominal 2×10^{19} cm^{-3}). There is no consistent spatial dependence of Be concentration that would suggest a doping profile along the NW axis, but the variation of values obtained for different axial positions are rather large for all investigated NWs. Some uncertainty of the fitting results is expected due to overlapping of TO, SO and CPPM. As the dopant concentration increases, the CPPM mode gets broader and shifts to frequencies closer to the TO mode of ZB GaAs [28], which increases the uncertainty of the line shape analysis in which Eq. (1) is used as a component for spectral decomposition. Nevertheless, the fitting results were consistent with the same methodology applied to the thin film samples supported by Hall Effect measurements in figure 3.

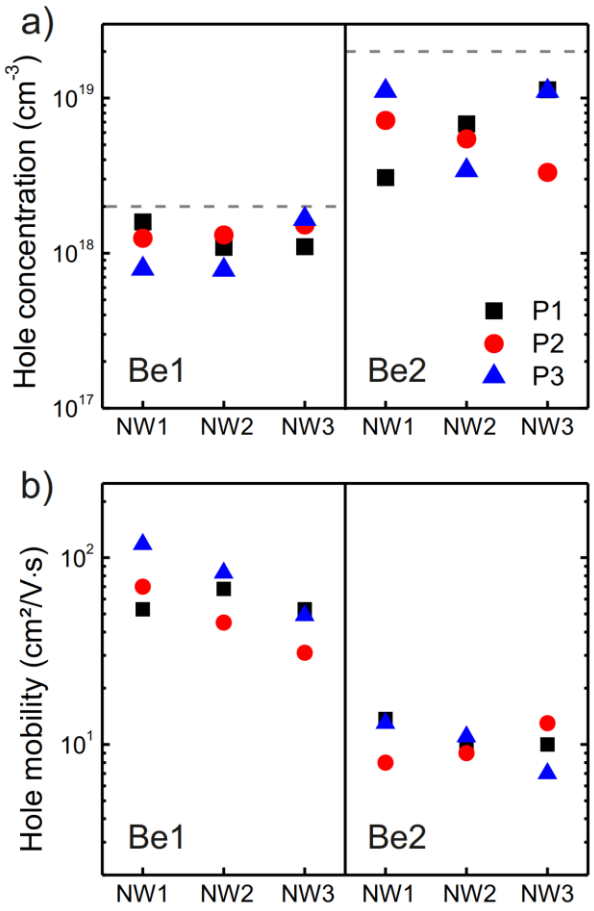

Figure 4. (a) Hole concentration and (b) hole mobility, obtained from the fit of CPPM lineshape to the Raman spectra for three different NWs extracted from Be1 and Be2 samples. The NW1 data points in (a) and (b) corresponds to the spectra presented in figures 2(b) and (c), respectively. The spectra corresponding to the NW2

and NW3 data points are shown in figure S3. The symbols represent the different positions of the NWs from which the Raman spectrum was measured: bottom region (P1), center region (P2) and tip region (P3). The grey dashed lines (a) represent the nominal Be concentration of each sample.

The carrier concentrations of Be1 and Be2 NWs are shown in figure 4(a) and are compared with the nominal dopant concentrations, which are indicated by the dashed grey lines. On average, the carrier concentration of Be1 NW is 60% from the nominal doping whereas Be2 NW present 35% of the nominal doping level. Similar incorporation efficiency of Be dopant in self-catalyzed GaAs NWs has been reported [30]. It is important to highlight that the Be fluxes used for nominal doping of the NWs are based on Hall Effect data obtained from the (100) oriented GaAs epilayers and the Be incorporation rates are expected to be different for VS incorporation at the (110) oriented NW sidewalls and for the VLS mechanism through the droplet [18–20]. Moreover, the results from Be1 and Be2 NWs suggest a reduction of the incorporation efficiency at higher Be flux. On the other hand, the hole mobilities [figure 4(b)] obtained for Be1 NW are similar to the values from Raman spectroscopy of the TF samples having similar carrier concentration. However, the values obtained for the mobility of Be2 NWs were significantly lower than what is expected for similar dopant concentration of bulk Be-doped GaAs at room temperature. Similar result was also observed in Be-doped GaAs NWs and ascribed to scattering at the surface [27] that would considerably decrease the mean free path of the carriers. It should be noted that the charge carriers in highly doped NWs are expected to be more affected by the surface due to the small depletion layer width [18].

3.3 Transport properties

The spatial dependence of the transport properties of individual Be-doped NWs was investigated by manufacturing evenly spaced contacts and analyzing the IV characteristics of each channel along the NWs. Figure 5(a) shows representative IV curves from Be1 sample and the corresponding SEM image of the device in figure 5(b). The asymmetric IV indicate a Schottky-like behavior of the metal-semiconductor contacts. The current values in different positions along the Be1 NW in figure 5(a) indicate an increase in the values of the Schottky barrier heights in the contacts from the bottom (AB

channel) to tip (CD channel) of the NW. This behavior can be associated to a dopant concentration profile which decreases from the root toward the tip of the NW. Such behavior was observed consistently for all investigated Be1 NWs, as shown in figures S4(a) and S4(e) in the Supplementary Data. It should be noted that most of the Ga droplets were removed in the contact fabrication process, unlike in the case of the NW shown in figure 5. In those cases, the bottom end of the NW was identified from the specific off-cut shape formed when the NWs were harvested from the substrate. The insets in figure 5(b) show higher magnification SEM pictures of the bottom (contact A) end with the off-cut shape and tip end (contact D) of the NW. More details can be found in figures S4, S5 and S6 in the Supplementary Data.

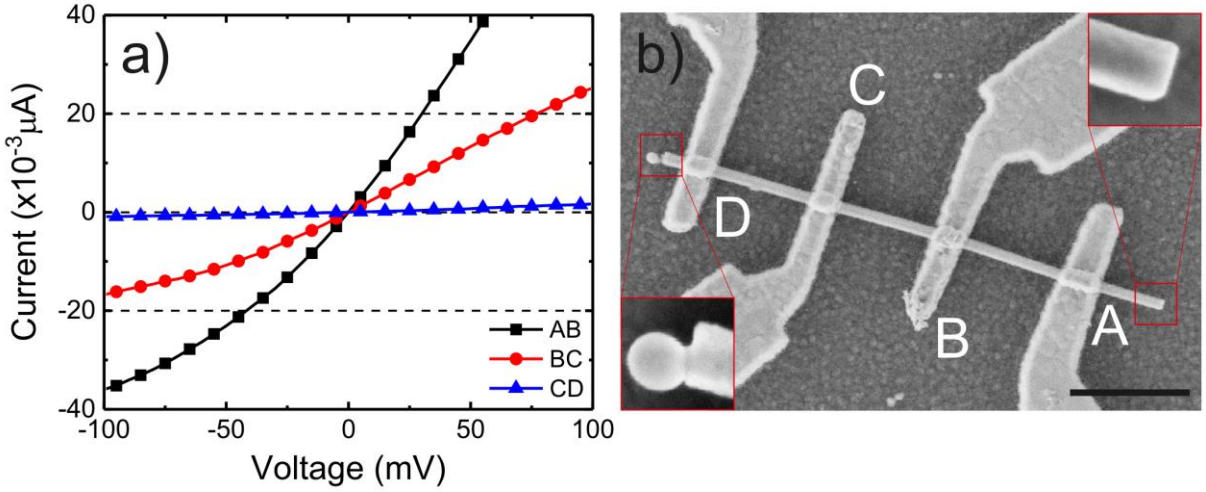

Figure 5. (a) IV characteristics of different channels along Be1 NW. (b) An SEM image of measured device. Each channel in (a) corresponds to a pair of contacts as indicated in (b), with A being at the bottom and D at the tip region of the NW. The scale bar in (b) is 1 μm. The insets in (b) show higher magnification SEM pictures of the bottom (contact A) and tip (contact D) of the NW.

Figure 6 shows similar IV curves for Be2 NWs. In contrast to Be1, the IV curves are linear and exhibit smaller differences in the current values between different channels. This also confirms that the surface passivation by ammonium polysulfide and the choice of the metal layers used for device processing were successful in achieving ohmic contacts to p-GaAs NWs. The bottom (channel AB) and tip (channel CD) parts of the NW without the Ga droplet in figure 6(b) were identified by the same method previously described. The insets in figure 6(b) show higher magnification SEM pictures of the

bottom (contact A) end with the off-cut shape and tip end (contact D) of the NW. The slope in the IV curve depends on both contact resistance and semiconductor resistivity. Therefore, in the following we present another transport experiment for distinguishing these two values.

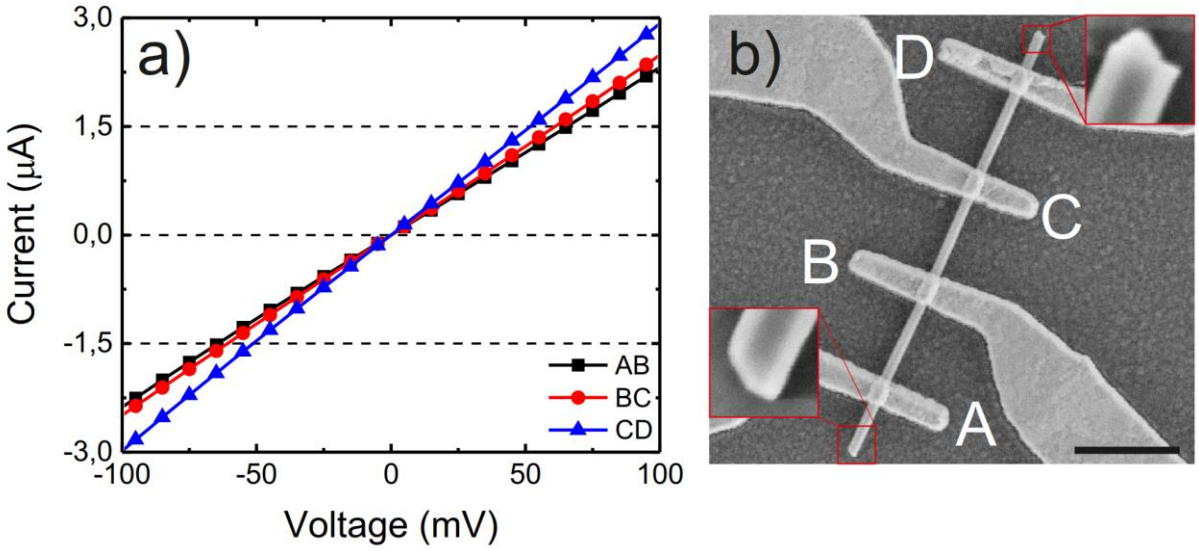

Figure 6. a) IV characteristics of different channels along Be2 NW. (b) SEM image of measured device. Each channel in (a) corresponds to a pair of contacts as indicated in (b), with A being at the bottom and D at the tip region of the NW. The scale bar in (b) is 1 μm. The insets in (b) show higher magnification SEM pictures of the bottom (contact A) and tip (contact D) of the NW.

The ohmic character of the IVs from Be2 NWs allowed us to estimate simultaneously the contact specific resistance and the semiconductor resistivity by fabricating five electrical contacts with increasing channel length along the NW axial direction, also known as transmission line model (TLM) geometry [37]. In this configuration, the total resistance R_T of each channel was obtained from the slope of the IV curves and plotted as a function of channel length, the NW resistivity ρ_s and transfer length L_T were then obtained by fitting the pairs (R_T, L) using the relation [37,38]:

$$R_T(L) = \frac{\rho_s}{\pi r^2}\left(2L_T \coth\left(\frac{W_C}{L_T}\right) + L\right) \quad (3)$$

Where W_C is the contact width and r is the NW radius obtained by SEM imaging of the devices after transport measurements. This equation format was chosen over a linear fit of the experimental points to

account for the reduced contacts width used in our devices due to NW length limitations [37]. The specific contact resistance ρ_c can be obtained from the equation:

$$\rho_c = \frac{3}{2}\frac{\rho_s}{r}L_T^2 \quad (4)$$

Where the pre-factor 3/2 accounts for the fact the metal contact layer is not covering the whole NW surface [37]. The specific contact resistance obtained from TLM devices allowed us to calculate the nanowire resistivity of the devices similar to presented in figure 6(a) by using equation (5):

$$R_T = \rho_S \frac{L}{A} + 2R_C \quad (5)$$

Where A is the hexagonal cross-section area of the NW.

Figure 7(a) shows the IV of different channel lengths of Be2 NW in the TLM geometry, the inset shows the SEM picture of the device obtained after transport measurements. The total resistance of the longer channel (L = 1.10 μm) was unexpectedly smaller than the shorter center channels most likely as a result of the contact overlap with one of the ends of the NW, resulting in smaller contact resistance. Therefore, this data point is omitted from the fitting procedure. The fitting to the experimental data in figure 6(b) resulted in nanowire resistivity of ρ_S=0.027 Ω·cm and specific contact resistance of ρ_C=4.5x10^{-6} Ω·cm², the transfer length resulting from the best-fit values was L_T = 230 nm. Based on the values of ρ_C obtained, the total contact resistance for each channel is 18 kΩ on average. Comparable results of contact resistance were previously reported for Zn-implanted p-type GaAs NWs with similar metal contact multilayer [39] and Be-doped GaAs thin films [40].

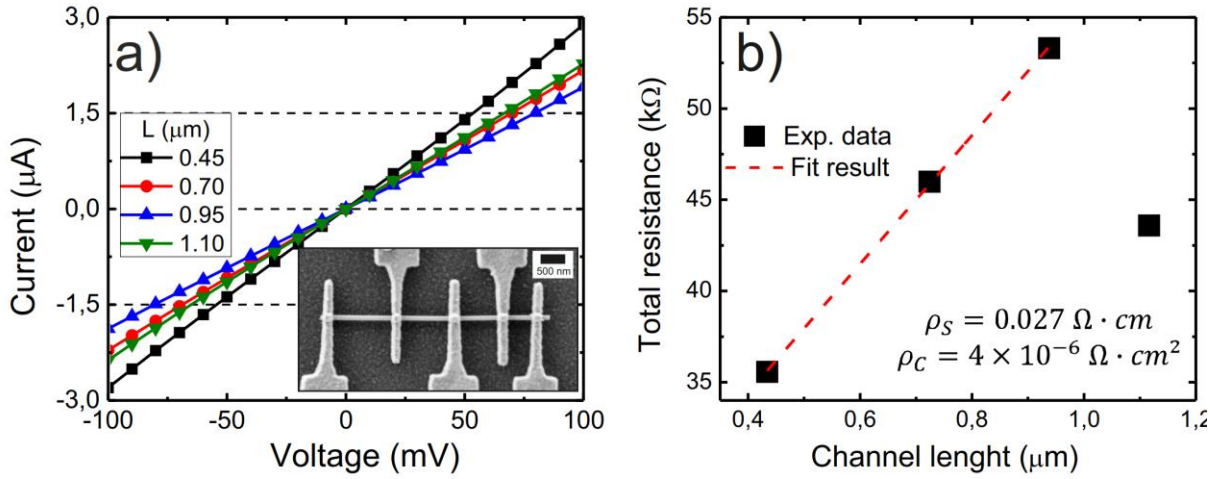

Figure 7. (a) IV characteristics of Be2 NW measured in TLM geometry. The inset shows an SEM image of the measured device. The scale bar is 500 nm. (b) Total resistances of individual channels as a function of channel length. The square points are obtained from the linear fit to the IV curves in (a) and the red dashed line is the fit result using equation (3).

With the specific contact resistance value now determined, we are able to calculate the semiconductor resistivity for each channel of the evenly spaced contacts shown in figure 6 (NW1) and other NWs from the same sample (NW2 and NW3, figure S5 of Supplementary Data) using equation (6). The NW diameters were measured by SEM images obtained after transport measurements and a hexagonal cross-section area was considered. Figure 8 shows the resistivity from channels AB (bottom region), BC (center region) and CD (tip region) of NW1, NW2 and NW3. The NW resistivity obtained from TLM is represented by the dashed line for comparison. The resistivity values range from 0.023 Ω·cm to 0.033 Ω·cm. It should be noted that the TLM calculations are based on nanowires with circular cross-sections [37] whereas the resistivity was calculated assuming more realistic hexagonal cross section for the devices with evenly spaced contacts. This explains slight deviation of the resistivity values obtained from the two methods, as can be seen from figure 8. Nevertheless, the resistivity calculated for the evenly spaced contacts allows us to investigate the Be concentration gradient in the axial direction for Be2 NWs. While there is some NW-to-NW variation in the resistivity values, we consistently observe lower resistivity for the upper part than for the lower part of the NW, indicating axial Be concentration gradient which increases towards the tip, which is contrary to what was observed for Be1.

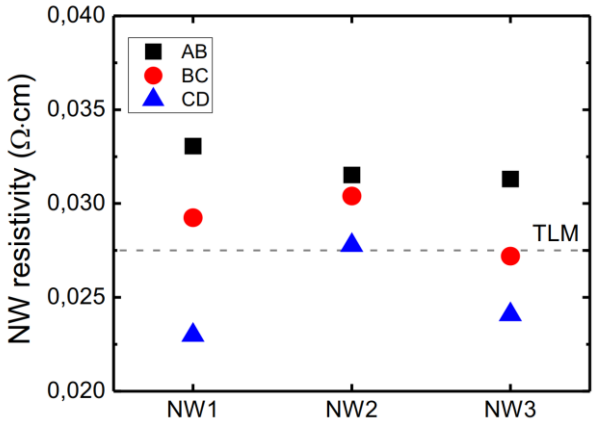

Figure 8. Nanowire resistivity of Be2 NWs from devices similar to presented in figure 6(a). The experimental points were calculated using equation (5) for each channel along the NW length, with A being at the bottom and D at the tip region of the NW. The dashed line indicates the NW resistivity value obtained by TLM.

From the IV analysis of the NW devices in figures 5(a), 6(a) and 8 it is clear that the Be dopant gradient is opposite in Be1 and Be2 samples grown with lower and higher Be flux, respectively. The IV data of Be1 indicates a dopant gradient with decreasing concentration from bottom to tip. The thickness of the VS grown shell is larger at the bottom than at the tip region of the NW, as the NWs grow constantly in thickness but are not tapered [13,41]. Thus, in sample Be1, the Be dopants incorporate predominantly through the NW sidewalls via VS growth, as reported in [18]. Predominant Be incorporation via VLS mechanism through the Ga droplet would result in a dopant gradient which increases from bottom to tip [19,20], as the thickness of the VLS grown core increases from bottom to tip [41]. This is indeed what we observe for Be2. Therefore, we conclude that the predominant dopant incorporation pathway depends on the Be flux so that lower Be fluxes favorably incorporate via VS growth and higher fluxes via VLS growth. In case of the lower Be flux, the VLS incorporation can be limited by capture of Be atoms only by direct impingement to the Ga droplet, while the axial VLS growth rate is more than 10-times larger than the nominal growth rate of 0.3 µm/h for which the nominal doping level is calibrated, thus leading the predominant VS incorporation. As for the high Be flux, it should be noted that, according to the Raman results shown in figure 4(a), the total incorporation efficiency decreases when the Be flux is increased. Therefore, the difference between the dopant gradients of Be1 and Be2 NWs is more likely due to a reduction of the VS incorporation than an increase

of the VLS incorporation when the Be flux is increased. Such saturation of the VS incorporation can be attributed to the onset of Be segregation on the GaAs surface. In the planar VS growth of Be-doped GaAs, the segregation at high Be fluxes causes an increase of surface roughness [42–44], which is indeed observed in figure 1(k) in the TEM micrographs of the NWs grown with high Be flux. When planar layers are grown by VS with typical 1 μm/h growth rates, the segregation effects are expected at high doping levels in the 10^{19}-10^{20} cm^{-3} range. However, the radial growth rate on the NW sidewalls by the VS mechanism is significantly lower and, according to the thermodynamic model presented in Ref. [43], low growth rates lead to an onset of segregation at lower doping levels. The same model also predicts that the onset of Be segregation depends on the As flux and growth temperature, which further emphasizes the influence of growth conditions on the Be incorporation in self-catalyzed GaAs NW growth.

4. Conclusions

We have investigated the effect of Be-dopant incorporation in self-catalyzed GaAs NWs using a lithography-free fabrication technique of Si/SiO_x templates. The presence of Be impurities was found to suppress the formation of twin planes and stacking faults in the NWs. Using spatially resolved single-NW Raman spectroscopy and transport characterization, we were able to assess the dopant incorporation and axial dopant gradients formed in NWs grown with higher and lower Be fluxes. We have shown that with low Be flux the dopant concentration decreases towards the NW tip, while for high Be flux the gradient is opposite. These results suggest that the Be dopants incorporate predominantly via VS growth at the NW sidewalls with low Be flux, while the relative contribution of the VLS mechanism becomes more significant when the Be flux is increased.

Acknowledgements

M.R.P. acknowledges CAPES/CNPq process 88887.100549/2015-00, H.V.A.G. and Y.G.G. acknowledge FAPESP grants 18/01808-5, 16/10668-7 and 14/50513-7. M.R.P, E.K, T.H, and M.G. acknowledge financial support from the Academy of Finland Project NESP (decision number 294630), and NanoLight (decision number 310985) and the Vilho, Yrjö and Kalle Väisälä Foundation of the

Finnish Academy of Science and Letters. This work made use of Tampere Microscopy Center facilities at Tampere University.

References

[1] Joyce H J et al 2011 III–V semiconductor nanowires for optoelectronic device applications *Prog. Quantum Electron.* **35** 23–75

[2] Zhang A, Zheng G and M. Lieber C 2016 *Nanowires: Building Blocks for Nanoscience and Nanotechnology* (New York: Springer International Publishing)

[3] Dimakis E et al 2014 Coaxial Multishell (In,Ga)As/GaAs Nanowires for Near-Infrared Emission on Si Substrates *Nano Lett.* **14** 2604–9

[4] Svensson C P T, Mårtensson T, Trägårdh J, Larsson C, Rask M, Hessman D, Samuelson L and Ohlsson J 2008 Monolithic GaAs/InGaP nanowire light emitting diodes on silicon *Nanotechnology* **19** 305201

[5] Aberg I et al 2016 A GaAs Nanowire Array Solar Cell With 15.3% Efficiency at 1 Sun *IEEE J. Photovoltaics* **6** 185–90

[6] van Dam D, van Hoof N J J, Cui Y, van Veldhoven P J, Bakkers E P A M, Gómez Rivas J and Haverkort J E M 2016 High-Efficiency Nanowire Solar Cells with Omnidirectionally Enhanced Absorption Due to Self-Aligned Indium–Tin–Oxide Mie Scatterers *ACS Nano* **10** 11414–9

[7] Thompson M D et al 2016 Low Leakage-Current InAsSb Nanowire Photodetectors on Silicon *Nano Lett.* **16** 182–7

[8] Colombo C, Spirkoska D, Frimmer M, Abstreiter G and Fontcuberta i Morral A 2008 Ga-assisted catalyst-free growth mechanism of GaAs nanowires by molecular beam epitaxy *Phys. Rev. B* **77** 155326

[9] Cirlin G E et al 2010 Self-catalyzed, pure zincblende GaAs nanowires grown on Si(111) by

molecular beam epitaxy *Phys. Rev. B* **82** 035302

[10] Bullis W M 1966 Properties of gold in silicon *Solid. State. Electron.* **9** 143–68

[11] Hakkarainen T V., Schramm A, Mäkelä J, Laukkanen P and Guina M 2015 Lithography-free oxide patterns as templates for self-catalyzed growth of highly uniform GaAs nanowires on Si(111) *Nanotechnology* **26** 275301

[12] Koivusalo E, Hakkarainen T and Guina M 2017 Structural Investigation of Uniform Ensembles of Self-Catalyzed GaAs Nanowires Fabricated by a Lithography-Free Technique *Nanoscale Res. Lett.* **12** 192

[13] Koivusalo E S, Hakkarainen T V., Guina M D and Dubrovskii V G 2017 Sub-Poissonian Narrowing of Length Distributions Realized in Ga-Catalyzed GaAs Nanowires *Nano Lett.* **17** 5350–5

[14] Tauchnitz T, Nurmamytov T, Hübner R, Engler M, Facsko S, Schneider H, Helm M and Dimakis E 2017 Decoupling the Two Roles of Ga Droplets in the Self-Catalyzed Growth of GaAs Nanowires on SiO x /Si(111) Substrates *Cryst. Growth Des.* **17** 5276–82

[15] Tan S L, Genuist Y, den Hertog M I, Bellet-Amalric E, Mariette H and Pelekanos N T 2017 Highly uniform zinc blende GaAs nanowires on Si(111) using a controlled chemical oxide template *Nanotechnology* **28** 255602

[16] Küpers H, Bastiman F, Luna E, Somaschini C and Geelhaar L 2017 Ga predeposition for the Ga-assisted growth of GaAs nanowire ensembles with low number density and homogeneous length *J. Cryst. Growth* **459** 43–9

[17] Dayeh S A, Chen R, Ro Y G and Sim J 2017 Progress in doping semiconductor nanowires during growth *Mater. Sci. Semicond. Process.* **62** 135–55

[18] Casadei A et al 2013 Doping incorporation paths in catalyst-free Be-doped GaAs nanowires

Appl. Phys. Lett. **102** 013117

[19] Zhang Y et al 2018 Doping of Self-Catalyzed Nanowires under the Influence of Droplets *Nano Lett.* **18** 81–7

[20] Dastjerdi M H T, Fiordaliso E M, Leshchenko E D, Akhtari-Zavareh A, Kasama T, Aagesen M, Dubrovskii V G and LaPierre R R 2017 Three-fold Symmetric Doping Mechanism in GaAs Nanowires *Nano Lett.* **17** 5875–82

[21] Krogstrup P, Curiotto S, Johnson E, Aagesen M, Nygård J and Chatain D 2011 Impact of the liquid phase shape on the structure of III-V nanowires *Phys. Rev. Lett.* **106** 1–4

[22] Jacobsson D, Panciera F, Tersoff J, Reuter M C, Lehmann S, Hofmann S, Dick K A and Ross F M 2016 Interface dynamics and crystal phase switching in GaAs nanowires *Nature* **531** 317–22

[23] Zhang Y et al 2017 Growth of pure zinc-blende GaAs(P) core-shell nanowires with highly regular morphology *Nano Lett.* **17** 4946–50

[24] Spirkoska D, Abstreiter G and Fontcuberta i Morral A 2008 Size and environment dependence of surface phonon modes of gallium arsenide nanowires as measured by Raman spectroscopy *Nanotechnology* **19** 435704

[25] Venkatesan S, Mancabelli T, Krogstrup P, Hartschuh A, Dehm G and Scheu C 2017 Surface optical phonon propagation in defect modulated nanowires *J. Appl. Phys.* **121** 085702

[26] Steele J A, Puech P and Lewis R A 2016 Polarized Raman backscattering selection rules for (hhl)-oriented diamond- and zincblende-type crystals *J. Appl. Phys.* **120** 055701

[27] Ketterer B, Uccelli E and Fontcuberta i Morral A 2012 Mobility and carrier density in p-type GaAs nanowires measured by transmission Raman spectroscopy *Nanoscale* **4** 1789

[28] Irmer G, Wenzel M and Monecke J 1997 Light scattering by a multicomponent plasma coupled

with longitudinal-optical phonons: Raman spectra of p-type GaAs:Zn *Phys. Rev. B* **56** 9524–38

[29] Mlayah A, Carles R, Landa G, Bedel E and Muñoz-Yagüe A 1991 Raman study of longitudinal optical phonon-plasmon coupling and disorder effects in heavily Be-doped GaAs *J. Appl. Phys.* **69** 4064–70

[30] Goktas N I, Fiordaliso E M and LaPierre R R 2018 Doping assessment in GaAs nanowires *Nanotechnology* **29** 234001

[31] Amaduzzi F et al 2016 Tuning the response of non-allowed Raman modes in GaAs nanowires *J. Phys. D. Appl. Phys.* **49** 095103

[32] Mlayah A, Carles R, Landa G, Bedel E and Muñoz-Yagüe A 1991 Raman study of longitudinal optical phonon-plasmon coupling and disorder effects in heavily Be-doped GaAs *J. Appl. Phys.* **69** 4064–70

[33] Zekeng S, Prevot B and Schwab C 1988 Raman Determination of the Faust-Henry Coefficient of GaAs in the 1.9 to 2.7 eV Range at Ordinary and Low Temperatures *Phys. status solidi* **150** 65–72

[34] Zardo I, Conesa-Boj S, Peiro F, Morante J R, Arbiol J, Uccelli E, Abstreiter G and Fontcuberta i Morral A 2009 Raman spectroscopy of wurtzite and zinc-blende GaAs nanowires: Polarization dependence, selection rules, and strain effects *Phys. Rev. B* **80** 245324

[35] Irmer G et al 1991 Determination of the hole concentration and mobility of p-GaP by hall and by raman measurements *Semicond. Sci. Technol.* **6** 1072–8

[36] Wenzel M, Irmer G, Monecke J and Siegel W 1997 Hole mobilities and the effective Hall factor in p-type GaAs *J. Appl. Phys.* **81** 7810–6

[37] Mohney S E, Wang Y, Cabassi M A, Lew K K, Dey S, Redwing J M and Mayer T S 2005 Measuring the specific contact resistance of contacts to semiconductor nanowires *Solid. State.*

Electron. **49** 227–32

[38] Park H, Beresford R, Hong S and Xu J 2010 Geometry- and size-dependence of electrical properties of metal contacts on semiconducting nanowires *J. Appl. Phys.* **108** 094308

[39] Gutsche C, Regolin I, Blekker K, Lysov A, Prost W and Tegude F J 2009 Controllable p -type doping of GaAs nanowires during vapor-liquid-solid growth *J. Appl. Phys.* **105**

[40] Stareev G 1993 Formation of extremely low resistance Ti/Pt/Au ohmic contacts to p -GaAs *Appl. Phys. Lett.* **62** 2801–3

[41] Küpers H, Lewis R B, Tahraoui A, Matalla M, Krüger O, Bastiman F, Riechert H and Geelhaar L 2018 Diameter evolution of selective area grown Ga-assisted GaAs nanowires *Nano Res.* **11** 2885–93

[42] Xu J, Towe E, Yuan Q and Hull R 1999 Beryllium doping and silicon amphotericity in (110) GaAs-based heterostructures: structural and optical properties *J. Cryst. Growth* **196** 26–32

[43] Ivanov S V, Kop'ev P S and Ledentsov N N 1991 Interplay of beryllium segregation and diffusion in heavily doped GaAs and AlGaAs grown by molecular beam epitaxy (thermodynamic analysis) *J. Cryst. Growth* **108** 661–9

[44] Pao Y C, Franklin J and Harris J S 1989 Influence of As4/Ga flux ratio on Be incorporation in heavily doped GaAs grown by molecular beam epitaxy *J. Cryst. Growth* **95** 301–4

Be-dopant gradients in self-catalyzed GaAs nanowires

Supplementary Data

Marcelo Rizzo Piton[1,2], Eero Koivusalo[2], Teemu Hakkarainen[2], Helder V. A. Galeti[3], Ariano D. Rodrigues[1], Soile Talmila[2], Sergio Souto[4], Donald Lupo[5], Yara Galvao Gobato[1,6] and Mircea Guina[2]

[1] *Physics Department, Federal University of São Carlos, São Carlos-SP, Brazil*

[2] *Optoelectronics Research Centre, Physics Unit, Tampere University, Tampere, Finland*

[3] *Electrical Engineering Department, Federal University of São Carlos, São Carlos-SP, Brazil*

[4] *FZEA/ZAB, University of São Paulo, Pirassununga-SP, Brazil*

[5] *Electronics and Communications Engineering, Tampere University, Tampere, Finland*

[6] *High Field Magnetic Laboratory, Radboud University, The Netherlands*

E-mail: marcelo.rizzopiton@tuni.fi

1. Nanowire-droplet contact angle statistics

Figure S1 shows the post growth Ga droplet contact angle statistics analysis of undoped, Be1 and Be2 NWs. The contact angles were measured from SEM images of the lateral view of 50-70 NWs from each sample. All the SEM images were obtained using the same electron acceleration voltage, working distance and magnification. The NWs were oriented in such way that the (110) facets were facing towards the in lens detector of the SEM. The mean values of contact angles and the standard deviations for undoped, Be1, and Be2 NWs are 127.8°±5.3°, 123.5°±4.6° and 126.4°±6.2° respectively.

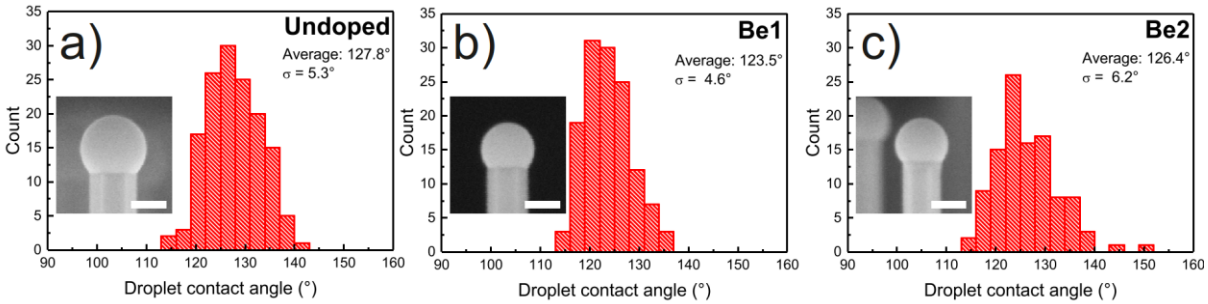

Figure S1: Droplet contact angle statistics of (a) undoped, (b) Be1 and (c) Be2 NWs. The insets show SEM images of representative NWs from each sample and the scale bars correspond to 100 nm.

2. Transmission Electron Microscopy

Figure S2 shows the selected area electron diffraction patterns (SAED) from the same position from of the HR-TEM images of undoped, Be1 and Be2 NWs in figure 1 of the main text. The SAED in figures S2(d), S2(h) and S2(l) show the high disorder of the bottom region of undoped, Be1 and Be2 NW respectively. The SAED of the center and tip regions of Be1 and Be2 NWs further confirm the lower density of twinned ZB GaAs in comparison to the undoped reference NW.

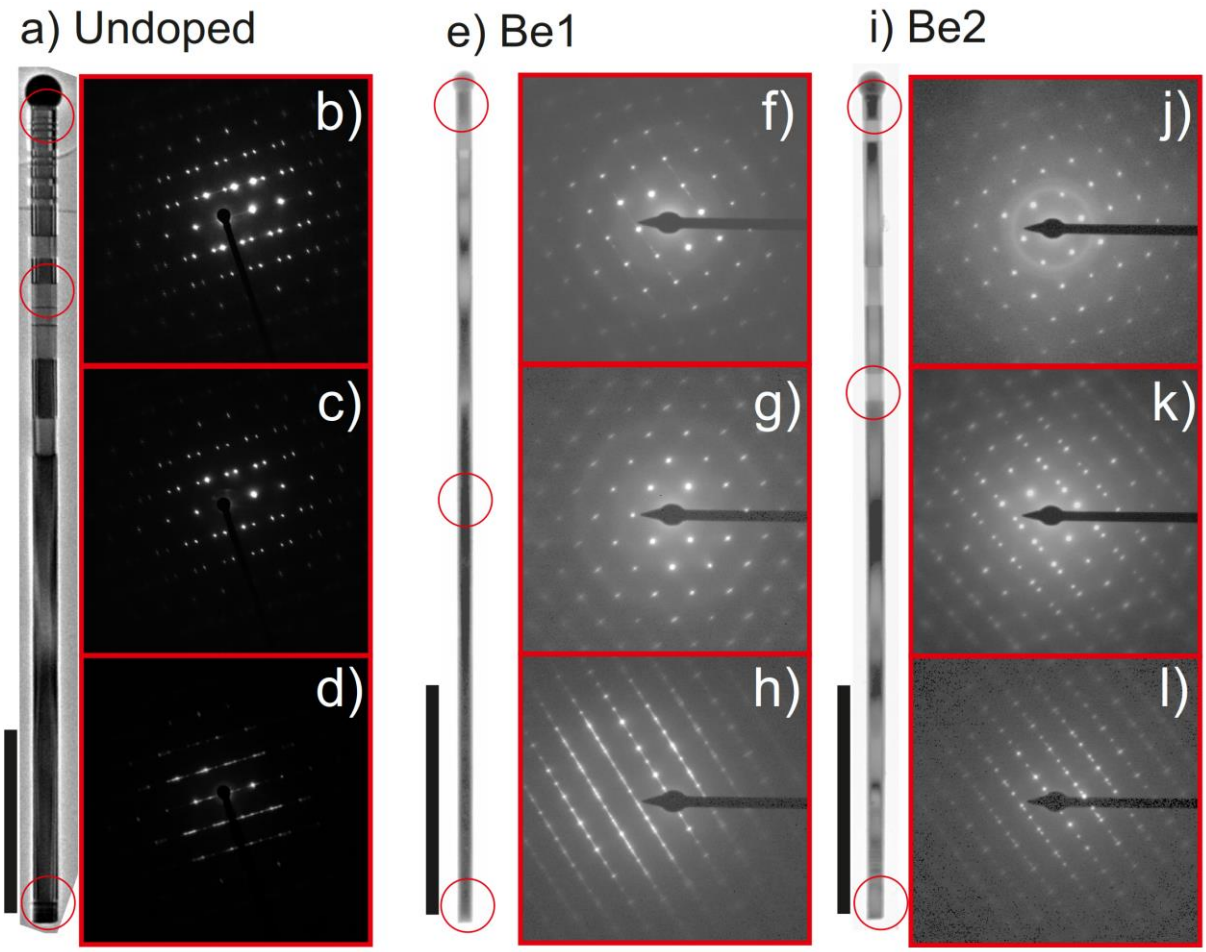

Figure S2: Low magnification HR-TEM images and SAED patterns of (a)-(d) undoped, (e)-(h) Be1 and (i)-(l) Be2 NWs. The red circles in (a), (e) and (i) indicate the position in the NW from where the SAED patterns in (b)-(d), (f)-(h) and (j)-(l) were obtained.

3. Raman spectroscopy

Figure S3 shows additional Raman data of similar Be-doped NWs. The SEM images on the right side of the spectra indicate the axial position of each NW from where the spectra were measured. The plasma frequency and damping constant obtained from the fit of the CPPM peak of each position in figure S3 were used to calculate the carrier concentrations and hole mobilities presented in figures 4(a) and 4(b) respectively.

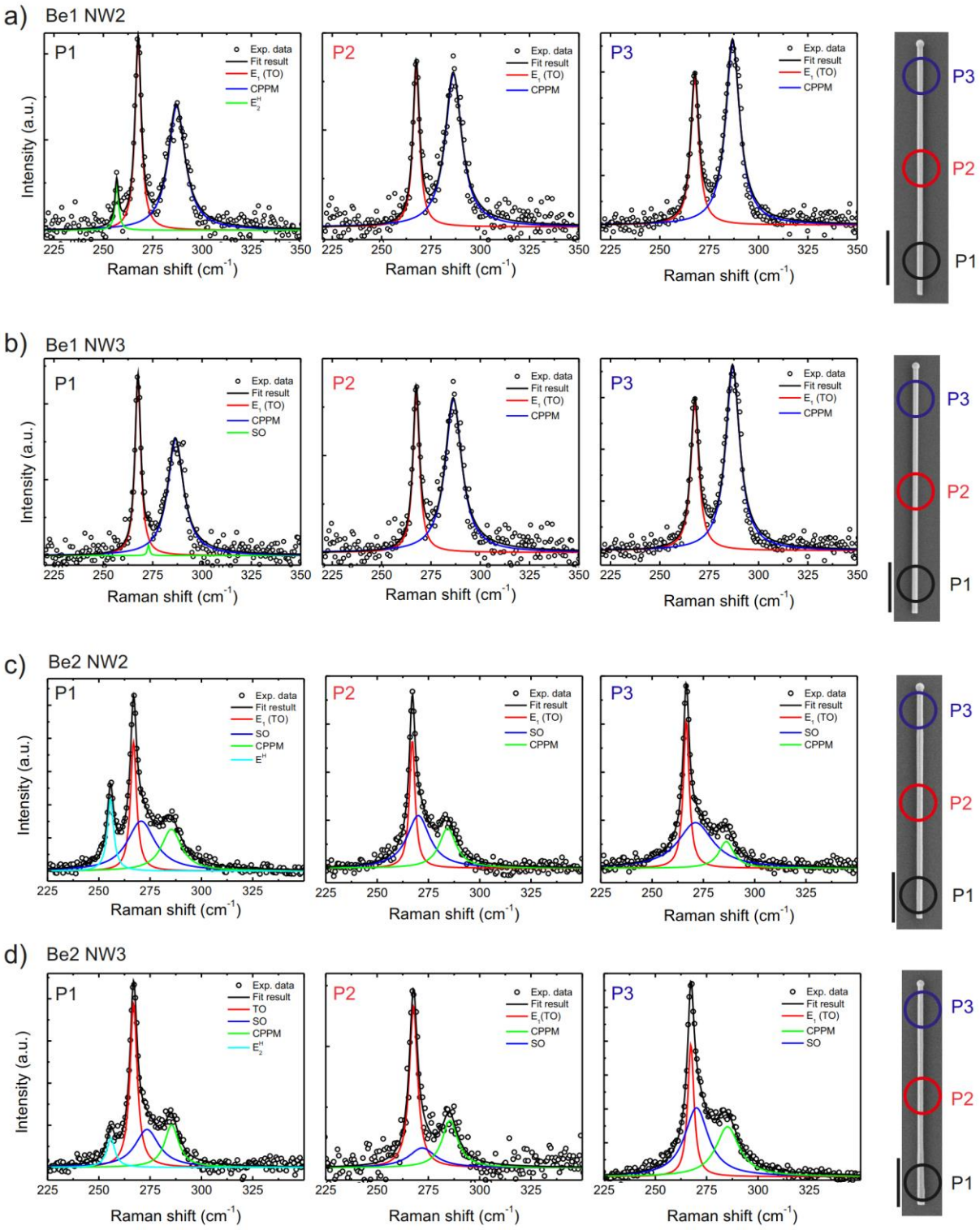

Figure S3: Raman spectra from three different axial positions of Be-doped NWs. (a) Be1 NW2, (b) Be1 NW3, (c) Be2 NW2 and (d) Be2 NW3. The spectra P1, P2, and P3 were collected from the regions indicated in the SEM pictures of the right sides of (a)-(d). The scale bars in the SEM pictures are 1 μm.

4. Transport properties

Figures S4 and S5 show additional IV and SEM data from devices with four evenly spaced contacts for NW samples Be1 and Be2, respectively. The IVs from Be1 NW2 and NW3 in figures S4(a) and S4(e) exhibit similar trend to the data presented in figure 5: asymmetric IV and different current values in different positions along the NWs. This behavior is associated to an increase in the values of the Schottky barrier heights in the metal-semiconductor contacts from bottom (AB channels) to tip (CD channels) of the NWs. Figures S5(a) and S5(e) show IV for Be2 NW2 and NW3 respectively. For these devices, the resistivity of the AB, BC, and CD channels were obtained from equation (5) and presented in figure 8.

As was discussed in Section 3.3, the Ga droplets were removed from some of the NWs during the contact fabrication process. The bottom and tip ends of the NWs in the devices shown in figures S4(b), S4(f), S5(b) and S5(f) were identified by the off-cut shape formed at the bottom end of the NWs, which was a consistent characteristic of the undoped and Be-doped NWs. This characteristic feature was observed in the TEM micrographs as well as in the SEM images of NWs used for Raman spectroscopy. Higher magnification SEM of the bottom region of the NWs are shown in figures S4(c), S4(g), S5(c), S5(g) and the tip region in figures S4(d), S4(h), S5(d) and S5(h). This trend in the NWs allowed us to identify with confidence the bottom and tip ends of the NWs, thus corroborating the results indicating different Be-dopant incorporation mechanisms discussed in the main text.

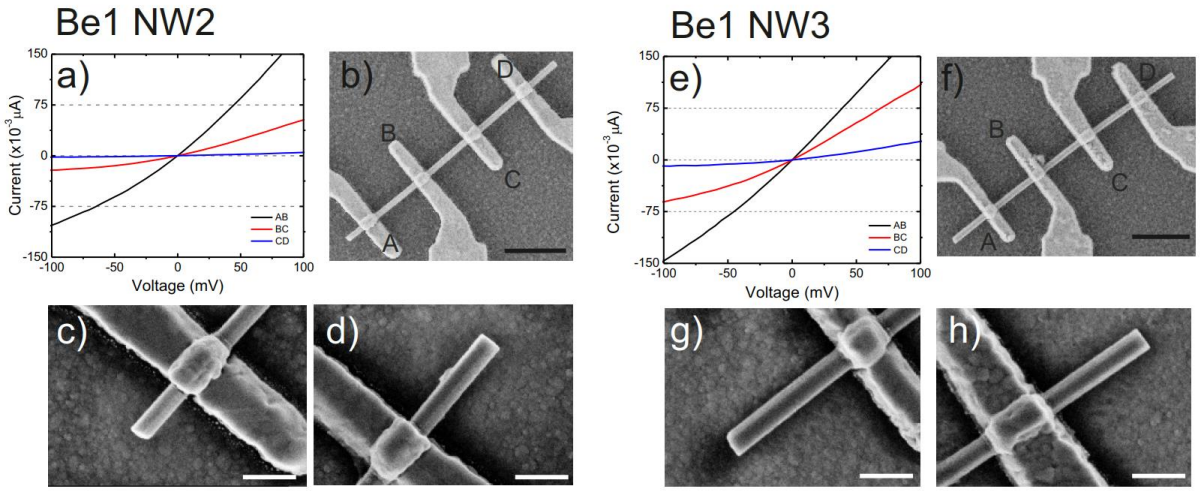

Figure S4: IV from Be1 NW2 (a) and NW3 (e) and the corresponding SEM images from the measured devices in (b) and (f). The A contact is close to the bottom and D contact close to the tip of the NW. The higher magnification SEM images of the NW ends were used to identify the bottom region of the NWs in (c),(g) and the tip region in (d) and (h). The scale bars are 1 µm in (b) and (f) and 250 nm in (c), (d), (g) and (h).

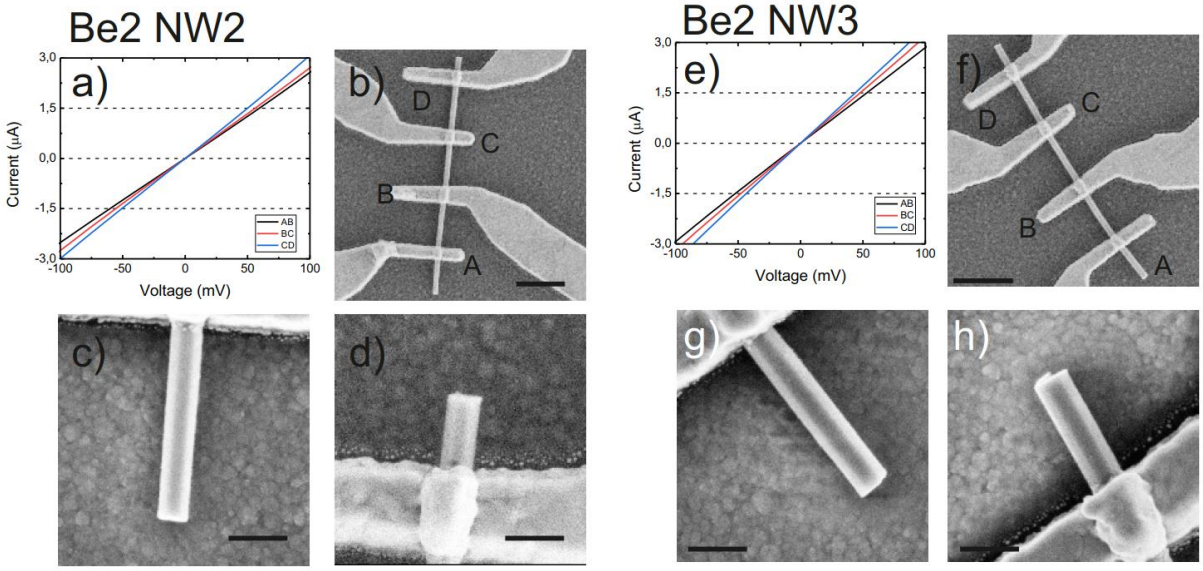

Figure S5: IV from Be2 NW2 (a) and NW3 (e) and the corresponding SEM images from the measured devices in (b) and (f). The A contact is close to the bottom and D contact close to the tip of the NW. The higher magnification SEM images of the NW ends were used to identify the bottom region of the NWs in (c),(g) and the tip region in (d) and (h). The scale bars are 1 µm in (b) and (f) and 250 nm in (c), (d), (g) and (h).

Since the off-cut at the bottom end of Be2 NW2 in figure S5(c) is not as evident as for the other NWs presented in figures S4 and S5, we show additional SEM images of Be2 NW2 from different perspectives in order to further confirm the bottom and top ends of the NW. Figures S6(a)-(d) show 30° tilted SEM pictures from a perspective perpendicular to the NW axis, obtained by properly aligning the NW in respect to the SEM detector and tilting the sample holder. From this perspective, we are able to identify the off-cut in figures S6(a) and (b) from the A contact in figure S5(b), which was ascribed to the bottom end of the NW. In contrast, figures S6(c) and (d) from D contact exhibit a flat surface at the end of the NW with residues of the Ga droplet, similar to observed in figure S5(h) from Be2 NW3, giving further confirmation that it was correctly ascribed to the top end of the NW. Figures S6(e)-(g) show additional SEM images of the bottom end (A contact), obtained by aligning the NW in a 45° in relation to the SEM detector and tilting the sample holder by 30°. The evidenced off-cut in figure S6(g) gives the necessary confirmation that the contact A indeed corresponds to the bottom end of the NW.

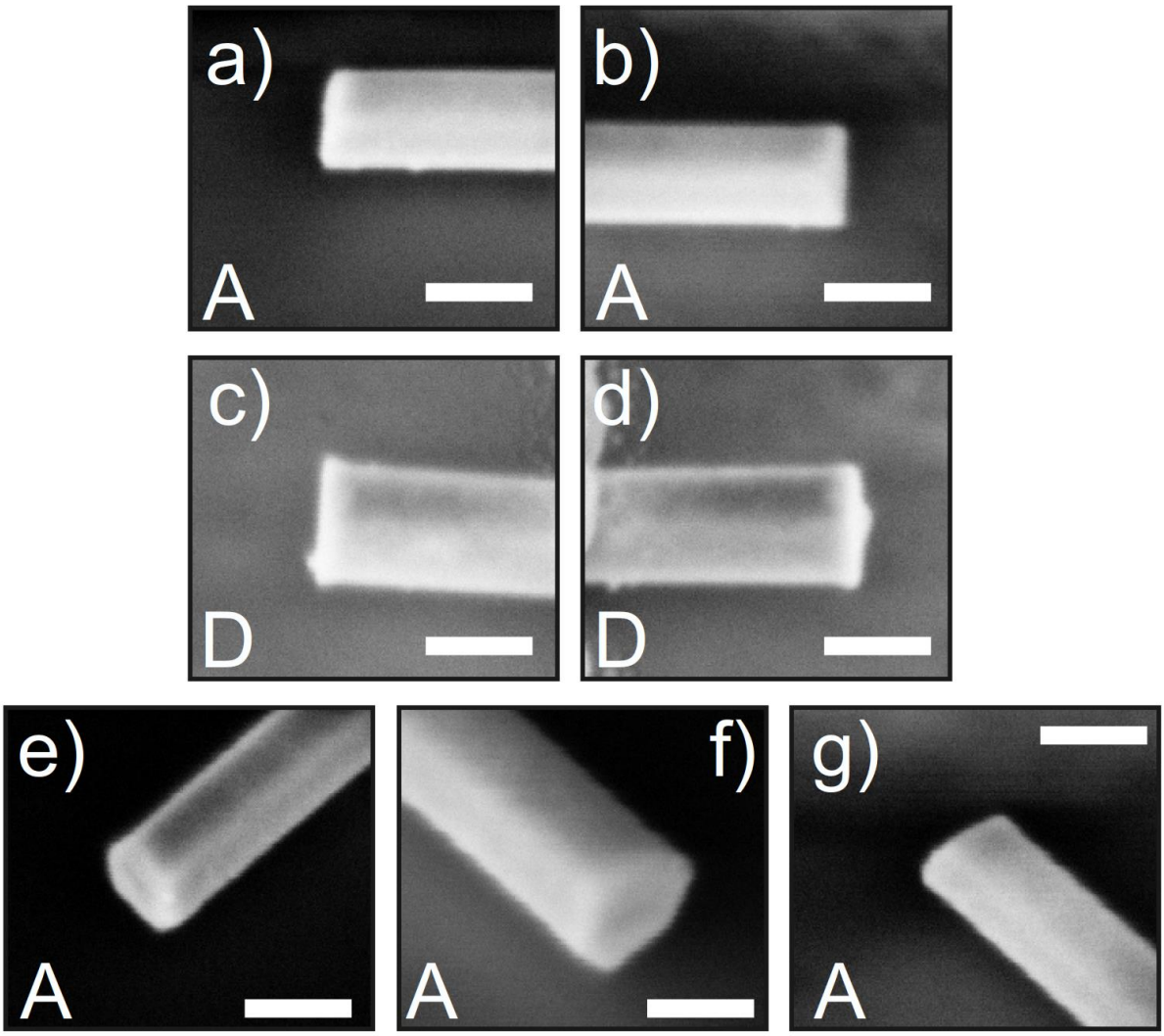

Figure S6: High magnification SEM images of NW end morphologies close to the A and D contacts of Be2 NW2 in figure S4 (a)-(d). The images were obtained from different perspectives by properly aligning the NW axis in respect to the SEM detector and tilting the sample holder by 30°. A perspective perpendicular to the NW axis is shown for the bottom region (A contact) in (a) and (b) and for the tip region (D contact) in (c) and (d). Additional perspectives on the A contact obtained by aligning the NW in a 45° angle in relation to the SEM detector and tilting the sample holder stage by 30° are shown in (e)-(g). The scale bars correspond to 100 nm.